**The Pennsylvania State University**
**The Graduate School**
**Eberly College of Science**

# BURST GRAVITATIONAL WAVE DATA ANALYSIS METHODS: DESIGN, DEVELOPMENT AND COMPARISON

A Thesis in
Physics
by
Amber L. Stuver



Submitted in Partial Fulfillment
of the Requirements
for the Degree of

Doctor of Philosophy

August 2006

LIGO-P060036-00-Z

The thesis of Amber L. Stuver was reviewed and approved* by the following:

Lee Samuel Finn
Professor of Physics and Astronomy & Astrophysics
Thesis Advisor, Chair of Committee

Pablo Laguna
Professor of Astronomy & Astrophysics and Physics

Stéphane Coutu
Associate Professor of Physics and Astronomy & Astrophysics

Steinn Sigurdsson
Associate Professor of Astronomy & Astrophysics

Jayanth R. Banavar
Professor of Physics
Head of the Department of Physics

*Signatures are on file in the Graduate School.

# Abstract

The advent of interferometric gravitational wave observatories, such as LIGO (Laser Interferometric Gravitational-wave Observatory), have promise of opening a new spectrum in astronomy. Throughout history, each time humans have looked at the universe in a different spectrum they have made discoveries that were not anticipated. With this in mind, the search for short duration gravitational wave bursts from unanticipated sources is underway. Several data analysis methods have been developed to search for these bursts which will be buried in a sea of instrumental noise. However, investigations have not been undertaken to determine if these methods are fundamentally equivalent and, if not, what are their relative strengths and weaknesses.

This work documents the results of asking the following questions of the burst gravitational wave data analysis methods: are the methods equivalent, and if they are not, what time-domain signal properties does each method favor? and are the time-domain characteristics of a signal more important to its detection by a data analysis method or are the frequency-domain characteristics more important?

To determine if the burst data analysis methods are equivalent, they were applied to LIGO science data and the results from each method were ranked by strength as measured by each method. If the methods were equivalent, then each method would see the same events and rank them in approximately the same way. This was not the case. With this knowledge, simulations with adjustable parameters were injected into a well controlled background of white noise. The efficacy of each data analysis method was probed with respect to simulation signal type, frequency, duration and amplitude. The efficiency measurements from these simulations illuminated the signal preferences of each method and served as a baseline to investigate the effect of varying the signals' time-domain properties while holding their frequency-domain magnitude constant. This evaluated the relative importance of the time-domain versus frequency-domain properties for a

signal's detection efficiency.

Ultimately, this work shows that while not fundamentally equivalent, these data analysis methods are complementary to each other in their relative strengths and features.

# Table of Contents

# List of Figures

# List of Tables

# Acknowledgments

At every step of my education, I have been blessed with only the very best of educators. The first person to formally introduce me to the elegance of physics is my high school physics teacher, **Robert Bowman**. Thank you for putting your all into teaching your students and know that even though they may not show it (or know it) at the time, they appreciate your efforts. My college experience was made whole by the mentorship of **George "Moose" Plitnik**. Thank you for supporting me when no one else in the department would and never hesitating to show me tough love when I was going soft on myself - even after I moved on to graduate school. Thank you also to **Gregory Latta** and **Robert Doyle** who were instrumental in my undergraduate success: I will forever be grateful for the support you provided me.

In graduate school, I have been blessed to have mentors who were more patient with me than they should have been. Thank you to **Gabriela González**, who I feel is wholly responsible for my admission to Penn State and who took me under her wing as my first advisor. Thank you for being just about the nicest person I have ever known, for standing up for me, for your never ending patience and for making sure that I was taken care of when you left. Thank you to **L. Sam Finn** for taking over as my advisor and teaching me how to be critical in data analysis. Thank you for putting up with all of my complaints and pushing me always forward. The highlight of my graduate career has been being a part of the Center for Gravitational Wave Physics. Thank you Sam for all of the administrative work you put into the center, for exposing me to so many other great minds and letting me be a part of something that is bigger than myself.

Being a part of a research group has shown me the true value of team work. Thank you to the post-docs who treated me like an equal while guiding me when I felt lost: **Patrick Sutton**, **John McNabb**, **Mike Ashley**, **Keith Thorne**, and **Shantanu Desai**. Special thanks go to John - thank you for always checking up

on me, having new ideas for me and for traveling to my defense even though you didn't have to. You've been a good friend to me.

I have made many good friends during my matriculation at Penn State. To my officemate and friend, **Tiffany Summerscales**, thank you for always being there to listen to me. I think that only you and my mother can listen to me complain endlessly and still have a smile on your face and seem interested. To two exceptional people who have been good friends to be since the perspective student weekend before we even decided to come to Penn State: Thank you to **Nathan Urban**, for taking the time to make sure that I always had my homework done and helping me fill any gaps my undergraduate education left me. Most of all, thank you for making sure that I didn't wash out of grad school. And thank you to **Isaac Mognet**, for giving the world *Electric Bacteria* (his old band) and always making me smile even during the many all-nighters.

To my mother, **Eileen Depcrymski**: you are the only person who has been a constant in my life; you are the reason why I have made it this far. Thank you for spoiling me with hot chocolate in the morning when I was home visiting, for helping me find my priorities in life and supporting me when following them was difficult. Thank you for making me who I am today.

And last but not least, thank you to my husband, **Derek Bridges**. Thank you for being there for me since our senior year of high school. Thank you for listening to me when I was inconsolable and for rejoicing with me in the good times. Thank you for being my fist kiss and my one true love. I will always love you unconditionally.

# Dedication

To my brothers and sisters...

♡ To **Brandi Stuver**, my guardian Angel who never got to come home,

♡ To **Ricky Stuver**, I love you for how special you are and admire your innocence and unconditional love,

♡ To **Brianne Depcrymski**, my maid-of-honor: you made me discover my love for teaching and have taught me the wonderful bond between sisters,

♡ To **Michael Depcrymski**, my ringbearer: you have shown me depths of imagination that I will always envy and have taught me that with the right encouragement, even I can play sports.

Chapter 1

# Introduction

## 1.1 Gravitational Waves

In Newtonian physics, gravity was thought to be an instantaneous 'action at a distance' - meaning that as soon as one mass moves, every other mass in the universe feels the resultant change in gravitational field immediately. This implies that changes in the gravitational field propagate though space at infinite speed. However, relativity states that nothing, including the information on mass location encoded in the gravitational field, can travel faster than the speed of light. More over, general relativity asserts that gravity is a consequence of the curvature of space-time and changes in the gravitational field will change this curvature of space-time. Therefore, a changing gravitational field will produce a ripple in space-time, propagating at the speed of light, which is referred to as a gravitational wave.

The fundamental relations in general relativity are the Einstein field equations [7]. Written as:

$$G_{\mu\nu} = 8\pi T_{\mu\nu} \tag{1.1}$$

where $G = c = 1$; these equations describe the curvature of space-time due to the distribution of mass (per the Einstein tensor, $G_{\mu\nu}$, on the left hand side of the equation) and stress-energy (per the stress-energy tensor, $T_{\mu\nu}$, on the right hand side of the equation). This relation is deceptively simple because its inherent non-linearity is concealed; $G_{\mu\nu}$ is quadratic in the metric and its first derivatives, the equations for the second derivatives of the metric are coupled and there is a

dependence on the source's 4-momentum, which in turn depends on the metric for normalization. However, if an observer is far away from the source in question, space-time is approximately flat and can be approximated by the Minkowski metric, $\eta_{\mu\nu}$. A gravitational wave, $h_{\mu\nu}$, can then be treated as a perturbation on this flat space-time yielding the following metric:

$$g_{\mu\nu} = \eta_{\mu\nu} + h_{\mu\nu} \tag{1.2}$$

Equation 1.2 is known as the weak field approximation and is used as an ansatz to solve the Einstein field equation (Equation 1.1):

$$-\bar{h}_{\alpha\beta,\mu}{}^{\mu} - \eta_{\alpha\beta}\bar{h}_{\mu\nu,}{}^{\mu\nu} + \bar{h}_{\alpha\mu,}{}^{\mu}{}_{\beta} + \bar{h}_{\beta\mu,}{}^{\mu}{}_{\alpha} = 16\pi T_{\alpha\beta} \tag{1.3}$$

where $\bar{h}_{\alpha\beta}$ is defined to be the trace-reversed metric perturbation:

$$\bar{h}_{\alpha\beta} \equiv h_{\alpha\beta} - \frac{1}{2}\eta_{\mu\nu}h \tag{1.4}$$

The first term on the left hand side of Equation 1.3 represents the flat-space wave operator and the rest of the terms on the left hand side insure gauge invariance. This can be simplified by making the gauge choice of forcing a vanishing divergence of $\bar{h}_{\mu\nu}$:

$$\bar{h}_{\mu\nu,}{}^{\nu} = 0 \tag{1.5}$$

This is known as the Lorentz gauge. In this gauge, Equation 1.3 simplifies to a wave equation:

$$-\bar{h}_{\alpha\beta,\mu}{}^{\mu} = 16\pi T_{\alpha\beta} \tag{1.6}$$

The Lorentz gauge still allows further gauge freedom. This can be exploited to choose a coordinate system where the gravitational wave is orthogonal to an observer. This gauge is known as the transverse-traceless (TT) gauge. For a wave

traveling in the $\hat{z}$ direction, the gravitational wave takes the form of:

$$h_{\mu\nu}^{TT} = \begin{pmatrix} 0 & 0 & 0 & 0 \\ 0 & h_+ & h_\times & 0 \\ 0 & h_\times & -h_+ & 0 \\ 0 & 0 & 0 & 0 \end{pmatrix} \tag{1.7}$$

with the usual basis order of $(t, x, y, z)$ and where $h_+$ and $h_\times$ are the two independent linear polarizations of the gravitational wave. $h_{\mu\nu}^{TT}$ can also be expressed as:

$$h_{\mu\nu} = \frac{2}{R}\frac{\mathrm{d}}{\mathrm{d}t^2} I_{\mu\nu}(t) \tag{1.8}$$

where $R$ is the distance between the source and the observer and $I_{\mu\nu}$ is the reduced quadrupole moment of the source.

When a gravitational wave with + polarization is perpendicularly incident on a ring of particles centered on the origin in free fall (traveling on geodesics), it will first affect them by pulling the horizontal components of the particles' vector location towards the origin and pushing their vertical component away from the origin and then alternate to pushing the horizontal component away from the origin and pulling the vertical component towards the center. The ring of particles will alternate in this pulsating manner with the same frequency as the gravitational wave and with an amplitude proportional to the strength of the quadrupole moment of the source. The situation of a gravitational wave with $\times$ polarization is much the same as the + polarization, just rotated by $45^o$. The effect of a gravitational wave's polarization is illustrated in Figure 1.1.

There is indirect evidence that gravitational waves are indeed physical. In 1974, Hulse and Taylor discovered a binary millisecond pulsar, PSR 1913+16 [8], whose orbital period was slowly decaying. The cause of this decay was investigated intensively and found to agree with the amount of energy radiated away in gravitational waves [9, 10], as shown in Figure 1.2. This discovery was the first indirect detection of gravitational waves and won the duo the Nobel Prize in Physics in 1993. Observations of this binary pulsar continue to this day and the system is expected to take about 300 million years to finally coalesce.

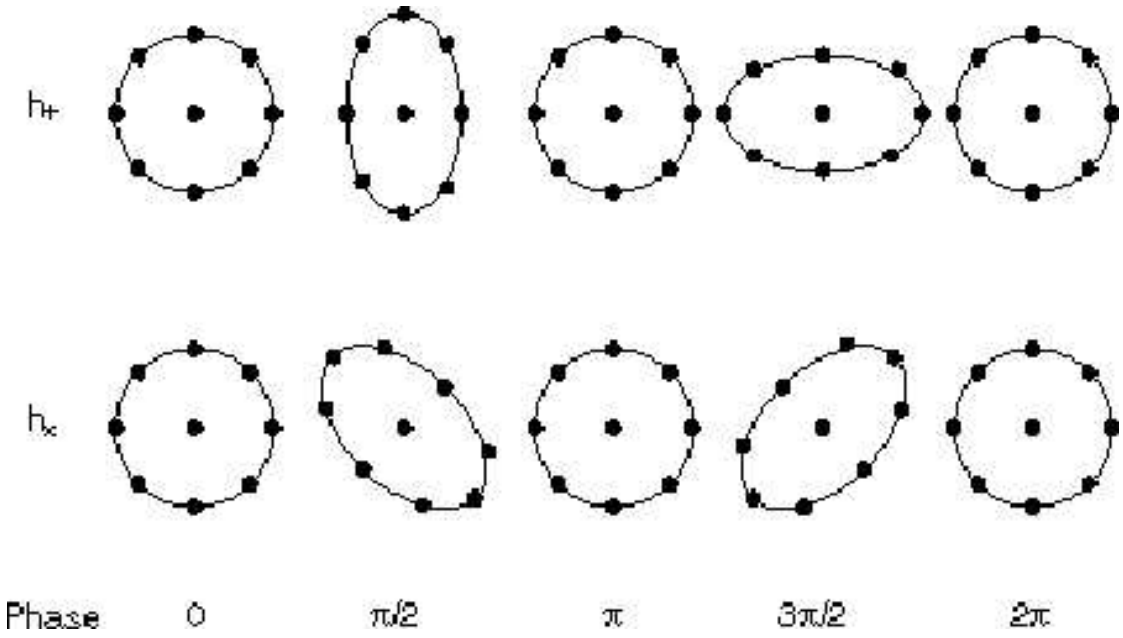


**Figure 1.1.** Illustration of the effect of the + (top) and × (bottom) polarization.

## 1.2 The Search for Gravitational Waves

### 1.2.1 Resonant Mass Detectors

The first attempt to directly detect gravitational waves was pioneered by Joseph Weber during the 1960's [11]. His apparatus consisted of high Q cylindrical aluminum bars fitted with quartz strain gauges. When a gravitational wave is incident perpendicular to the long axis of these resonant mass detectors and vibrating near the bar's resonance frequency, an acoustic wave would be generated causing vibrations in the mass that could be monitored with the strain gauges. Beginning in December of 1968 Weber claimed to have discovered the first significant gravitational wave events. The announcement caused great excitement in the physics community. Over the next few years, the rate at which these gravitational wave events were taking place increased as Weber made adjustments to his bar - from an event a day to several a day. However, energy considerations shed the first doubt on these detections. At the rate at which these events were happening and if they were really taking place in the galactic center, then the galaxy would be eating itself alive converting roughly one solar mass for every detection into pure gravitational energy. The case against these events being actual gravitational wave

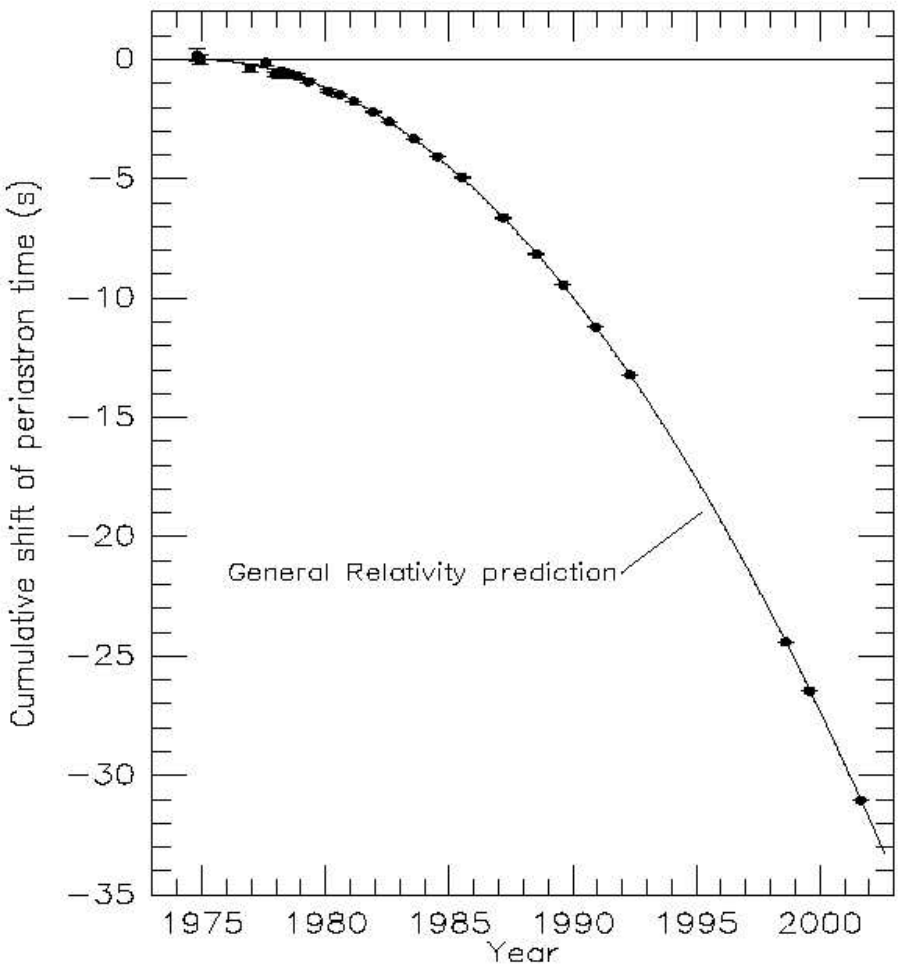


**Figure 1.2.** Plot of PSR 1913+16's cumulative shift in periastron since late 1974 as a function of time. The line passing through the data point's error bars represents the agreement with general relativity for the emission of energy in the form of gravitational waves. Image from [1].

detections became stronger when other scientists throughout the world set up their own bars and did not detect anything of significance over long periods of time.

In the end, Weber stood his ground and went to his grave claiming the first gravitational wave detections but by mid-1974 the general consensus in the scientific community was that he did not. Regardless of whether or not Weber actually detected gravitational waves, he was the ignition needed to get people thinking about detecting gravitational waves and how to push the frontiers of technology to accomplish it. Joseph Weber is truly the father of the search for gravitational

waves. Today, resonant mass detectors are still in use and include ALLEGRO [12], AURIGA [13], EXPLORER [14], NAUTILUS [15] and NIOBE [16]. These compose a worldwide network and represent great evolution to the original 'Weber bars' by employing, among other things, cryogenics to help reduce the predominant thermal noise, using SQUIDs (Superconducting QUantum Interference Devices) to detect the small vibrations of the mass and using vibration isolation systems to reduce environmental contributions to the mass' vibration. Future masses, such as TIGA (Truncated Icosahedral Gravitational-wave Antenna), will likely depart from the bar geometry in favor of spherical approximations that will improve the antenna pattern from directly above and below the detector to be nearly omnidirectional [17].

### 1.2.2 Interferometric Detectors

The current apparatus of choice in the search for gravitational waves is the interferometer. In its simplest form a beam of laser light is incident on a mirror, called the beam splitter, that transmits half of the light down one arm and reflects the other half down another arm that is usually perpendicular to the first. Both arms are the same length to a high precision; all masses are hung in pendula and can be treated as free masses above the natural frequency of the pendula. Then the light in each arm is reflected from the ends of the arms back towards the beam splitter and is allowed to interfere. If the lengths of the arms change due to an incident gravitational wave, there will be an interference pattern which contains the information on the relative difference in lengths. This quantity is called strain and is defined to be:

$$h = \frac{\Delta L}{2L} \tag{1.9}$$

where $L$ is the length of the arms, $\Delta L$ is the change in arm length and the 2 in the denominator is due to the contribution of both arms changing lengths.

The United States supports three interferometric detectors, two in Washington state at the Hanford observatory (a 2 km and a 4 km detector) and one in Louisiana at the Livingston observatory (a 4 km detector) [18, 19]. This project is dubbed LIGO, which is short for Laser Interferometer Gravitational-wave Observatory. While the basic concepts in these interferometers are the same as described pre-

viously, they also contain components to improve their performance. Fabry-Perot optical cavities are created by inserting mirrors after the beam splitter in each arm which increases the effective length of each arm, which in turn increases the time a gravitational wave has to affect the wavefronts [20]. A process called power recycling involves placing a partially reflecting mirror between the laser and the beam splitter to reflect the recombined light that does not get sent to the output photodetector. This recycles this light back into the interferometer and effectively increases the power in the detector. This optical configuration for LIGO is illustrated in Figure 1.3. Other improvements to the interferometer design planned for the next generation of LIGO detectors include inserting a partially reflecting mirror between the beam splitter and the output photodetector that creates a resonant cavity with high reflectivity at the carrier frequency of the laser. A gravitational wave signal will be outside of this resonance band and can either be recycled back into the interferometer in a process called signal recycling or 'leaked' to the output in a process called resonant sideband extraction [21].

Instrumental noise will dominate the data stream of interferometric detectors. Figure 1.4 shows the strain sensitivity limits imposed on LIGO from its various noise sources. LIGO is currently dominated by three main sources of noise. First, seismic noise from mechanical vibrations carried through the earth is caused by plate tectonics, ocean tides, logging, etc. These vibrations are then transmitted into the interferometer by way of the detector infrastructure. Second, thermal noise in the suspensions is caused by molecular motion associated with non-zero temperature. Third, shot noise is caused by the statistical fluctuations in the number of photons measuring the mirror position. Ultimately, the LIGO detector is limited by three other sources of noise: gravity gradient noise (caused by a local differential in the gravitational force), noise from stray light in the interferometer arms and noise caused by the residual gas in the arms. Figure 1.5 shows LIGO's best strain sensitivity during the timespan of the data used throughout this thesis (third science data run, called 'S3') [3]. Each science data run has resulted in improved sensitivity and stability of the detectors [22, 23, 3, 24].

There are also international interferometers in Europe and Asia. These include GEO 600 (a 600 m detector located near Hannover, Germany) [25], TAMA 300 (a 300 m detector located in Tokyo, Japan) [26], and VIRGO (a 3 km detector in

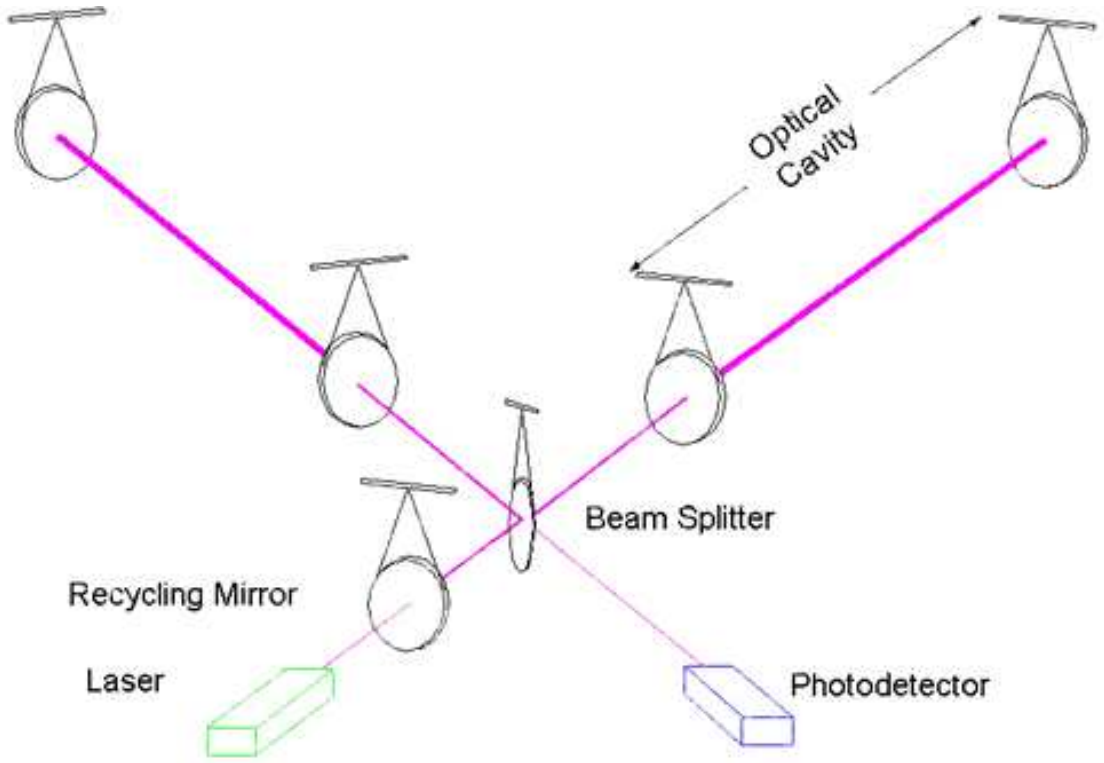


**Figure 1.3.** Illustration of the current optical configuration of the LIGO interferometers. Image from [2].

Cascina, Italy) [27]. These detectors operate much in the same way as LIGO with a few exceptions. GEO 600 already employs signal recycling but does not use Fabry-Perot cavities within its arm, choosing to simply fold light multiple times before it can recombine at the beam splitter. At the time that this thesis was completed, LIGO, GEO 600 and TAMA had successfully acquired data for scientific analysis and VIRGO was in the final stages of commissioning.

## 1.3 LIGO Science

LIGO is organized in two main groups, the LIGO Lab that is overseen by the California Institute of Technology and the Massachusetts Institute of Technology and the LIGO Scientific Collaboration (LSC), which includes members of the LIGO Lab as well as scientists from other institutions and includes the members of the GEO collaboration. The LIGO Lab sees to the administration of the observatories

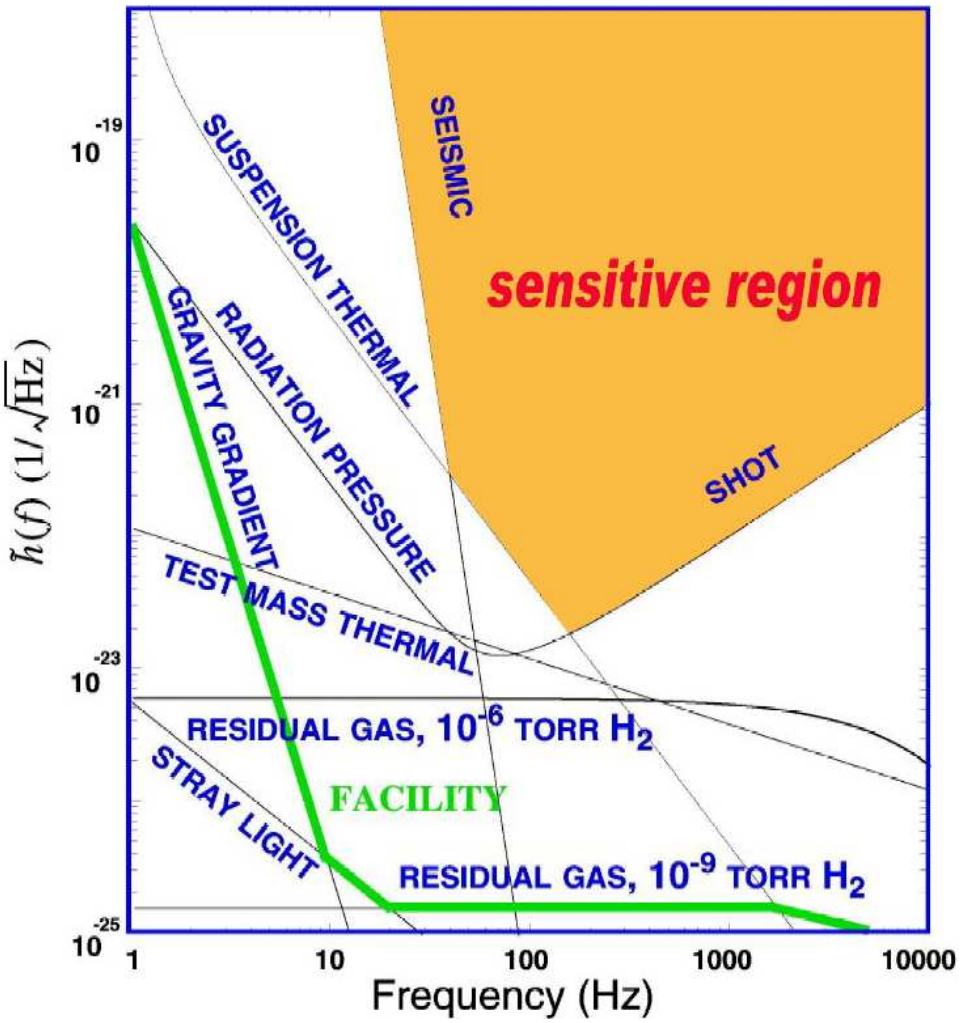


**Figure 1.4.** LIGO detector strain sensitivity limits from its various noise sources. Image courtesy of LIGO.

and the LSC is responsible for the scientific enterprises undertaken there. With the LSC there are several working groups including the Detector Characterization Working Group (which diagnoses detector issues, provides calibration data and works to improve the overall detector sensitivity), the Data Analysis Software Working Group (which maintains data analysis software repositories and oversees the validity of these programs), and four upper limit working groups which analyze data in search of gravitational waves or, in the absence of a detection, set an upper limit on the expectation of gravitational wave detection rates and strengths. The Stochastic Upper Limit Group seeks to detect primordial gravitational waves from

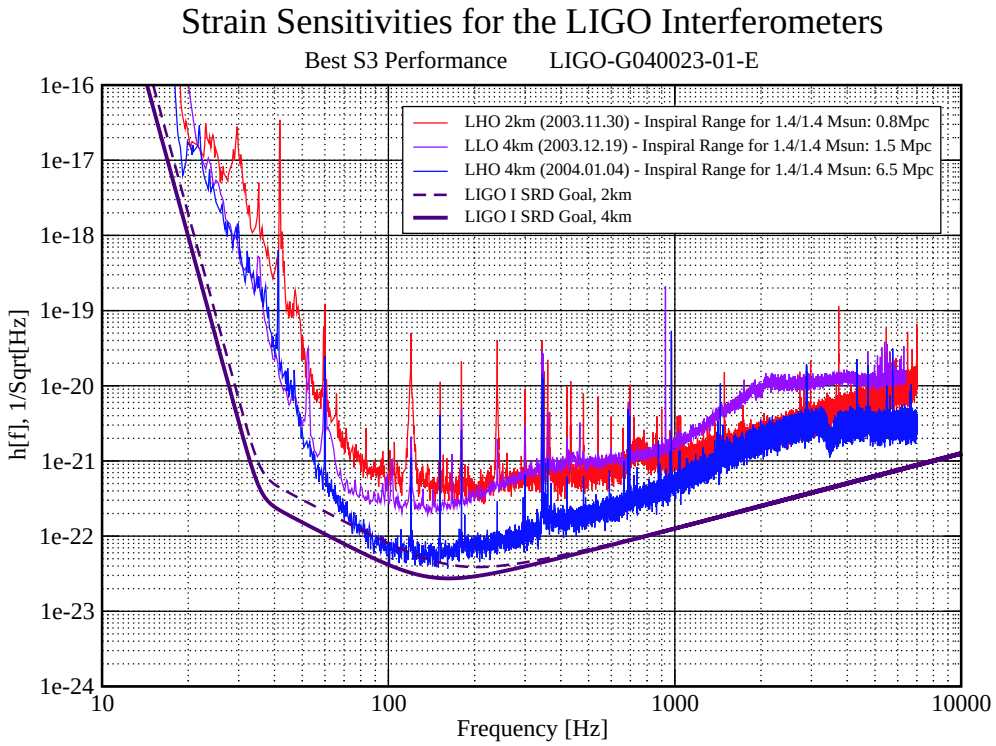


**Figure 1.5.** LIGO detector strain sensitivity during the timespan of the data used in this thesis (S3). Image from [3].

the Big Bang or continuous gravitational waves from sources that are too numerous to discern from one another. The Pulsar Upper Limit Group seeks single frequency gravitational waves from spinning pulsars. The Inspiral Upper Limit Working Group seeks gravitational waves from neutron star-neutron star, neutron star-black hole, or black hole-black hole inspirals. Finally, the Burst Upper Limit Group seeks short duration gravitational waves (less than one second) from supernovae, binary system coalescence and from unexpected sources. The work carried out throughout this thesis has been undertaken within and for the Burst Upper Limit Group. While no gravitational waves have been measured, as of the date of this writing, studies have set upper limits of the rates of gravitational waves of different strains for different sources [28, 29, 30, 31, 32, 33, 34, 35, 36, 37, 38, 39, 40, 41, 42, 43].

## 1.4 Thesis Outline

This thesis is divided into two main parts. The first part (Chapters 2 through 5) describes the design and implementation of several burst gravitational wave data analysis tools, including a gravitational wave simulation package and several burst gravitational wave data analysis methods. The second part (Chapters 6 through 8) documents some of the first head-to-head comparisons of the LIGO burst gravitational wave data analysis methods and their results.

Chapter 2 details the theory and infrastructure of a software robust gravitational wave simulation generator. Physically motivated gravitational wave signals are needed in order to study the behavior and efficacy of different data analysis methods seeking their detection. GravEn, short for Gravitational-wave Engine, is a robust software gravitational wave simulation generator developed in the MATLAB® programming environment [44]; however, the theory expounded upon in this work can be used in any programming environment. Every aspect of a desired signal can be specified, such as start time of the simulation (including inter-sample start times), maximum strain, source orientation to line-of-sight, location of the source on the sky, etc. Signals can either be generated from the supported built-in waveforms or pre-generated waveforms can be substituted. Supported interferometer detectors include LIGO, GEO, VIRGO and TAMA. Together, these features allow for the generation of coincident (within time-of-flight of a gravitational wave between detectors), physically meaningful gravitational wave simulations for multiple detectors. GravEn is currently being used within LIGO for the generation of mock data challenges to test the efficacy of burst gravitational wave data analysis methods.

Chapters 3, 4 and 5 deal with three data analysis methods geared towards the detection of burst gravitational waves within LIGO called event trigger generators (ETG). Essentially, these methods look for places in the detector output data that look different from the rest of the data and record a 'trigger' on this data as a possible gravitational wave event. These methods do not attempt to describe the trigger in any physical way but serve to mark times of interest in large data sets that are good candidates for further investigation. Three ETGs are detailed in this work: BlockNormal, SLOPE and Q Pipeline. Other ETGs that are not currently

in use for LIGO include POWER [45, 46] and TFCLUSTERS [47].

Each ETG is part of a larger data analysis pipeline. Usually, this pipeline consists of a data conditioning stage, trigger production by an ETG, temporal coincidencing between multiple detectors, energy coincidencing and measuring the statistical significance of any remaining candidate events. For all of the investigations documented in this work, only the data analysis pipeline through the trigger generation is considered. Inspecting the triggers at this point in the pipeline allows for the best comparison of the ETGs themselves without comparing the entire data analysis pipeline. The WaveBurst ETG [48, 49] is currently being used to analyze LIGO data but, since its 'triggers' cannot be analyzed before they are processed further on its pipeline, it is not included in the investigations of this thesis.

Chapter 3 describes the BlockNormal ETG which is a time-domain search for spans in the detector output where the statistical character (i.e., the mean and variance) of the data changes, which may indicate the presence of the gravitational wave signal in the detector noise. BlockNormal has two major stages, change point identification and block identification. The change point identification computes the Bayesian probability for every point in a data segment to be a point where the statistics of the data change and the point with the highest probability is considered as a candidate change point. If the probability is higher than a threshold probability, it is recorded as a change point. The change point identification is applied iteratively until there are no longer candidate change-points that exceed the threshold probability. The block identification computes a measure of relative excess power in-between two change-points based on the mean, variance and duration of the block in question, as well as the mean and variance of the larger data set which contains the block in question. If the relative excess power is larger than a threshold value, then the block is marked as a trigger.

Chapter 4 documents the redevelopment of the SLOPE ETG from its previous unsuccessful application to LIGO science data. SLOPE is a time-domain linear filter that identifies spans of time in the detector output data that are sufficiently inconsistent with Gaussian white noise. To do this, a window of data with fixed length is fit to a linear trend yielding a slope measurement. When a gravitational wave is added to the detector noise, the variance of the detector output will change since the signal is not correlated to the detector noise. SLOPE will locate these

changes by measuring the linear trend over a window length. The measured slope is then compared to the maximum slope measurement expected within a certain probability based on the Gaussian approximation for the data being analyzed. If the measurement of the slope is sufficiently unlikely, the time of the first sample in the window is recorded. The analysis window is incremented by one time sample and the algorithm applied successively. Neighboring windows with unlikely slopes, which are likely to be correlated, are clustered. The start and stop times of these clusters are recorded as triggers.

Chapter 5 describes Q Pipeline, which is a data analysis package developed by Shurov Chatterji. This ETG is a multi-resolution time-frequency search for excess power in the detector output. First, the data are whitened using zero phase linear prediction and projected onto bases that are logarithmically spaced in frequency and Q (quality factor), and linearly in time. Significant tiles are identified assuming white noise statistics and the most significant set of non-overlapping tiles are reported. This is the extent of the application of Q Pipeline in the investigations following since the investigations look at the output of the ETGs before any other processing of the triggers they produce are performed. Multi-detector coincidencing and the rejection of false triggers are also performed when Q Pipeline is applied as a full data analysis pipeline.

Chapters 6, 7 and 8 describe the methods used to compare the ETGs against each other and the results of these comparisons. Few burst gravitational wave data analysis method comparisons have been performed. Two prominent comparisons have been published [50, 51] but neither of these investigated the methods on actual detector data or focused their observations on the results of each method using the current practical application of each method.

There are three main comparisons described. First, in Chapter 6, it is investigated whether a fundamental equivalence of each method exists by studying the strongest accidental triggers that each produces from LIGO science data. This showed that the ETGs are not fundamentally equivalent. To investigate what signal properties each method favors, simulated signals of varying types, strengths and durations were injected into a background of white noise of zero mean and unit variance to measure each ETG's detection efficiency in Chapter 7. These efficiencies were then combined with appropriate population factors and integrated to give

a relative measure of detection probability. Lastly, each ETG's performance with respect to the time-domain characteristics of a signal versus the frequency-domain properties was investigated. The simulated signals from the previous investigation were projected into the time-domain and their magnitude was fixed while their phase was scrambled and projected back into the time-domain. This generated many time-domain mappings of a signal's magnitude. Injecting these time-domain mappings into a background of white noise with zero mean and unit variance allow the measurement of detection efficiency for these time-domain mappings of a fixed magnitude reference signal in Chapter 8.

Chapter 9 completes this work by summarizing the contributions made through this work, the conclusions of the investigations presented in chapters 6, 7 and 8 and suggestions for further research.

Chapter 2

# GravEn

## 2.1 Introduction

In order to adequately test the behavior and efficacies of gravitational wave data analysis methods, a simulation package that mimics expected signals must be developed. To that end, GravEn (Gravitational-wave Engine) simulates gravitational wave signals that can be added into the data stream of a gravitational wave detector. GravEn has been developed in the MATLAB® programming environment [44], however, the theory and infrastructure described in this work can be used in any programming language. The source code for this simulation package is available for download from [52] and full operational documentation can be found in [53].

Previously within LIGO, simulations were generated with ad hoc generic mathematical functions, such as Gaussian modulated sinusoids, and these waveforms were manipulated to account only for the source's sky location by calculating time delays between detectors and antenna pattern projections. GravEn allows for the specification of not only a source's sky location but also its orientation to the line-of-sight of a detector in an arbitrary gauge, projection onto the transverse-traceless (TT) gauge, polarization, and inter-sample simulation start times. With the inclusion of these features in a simulation package, even ad hoc waveforms can be manipulated in a physically meaningful way. GravEn is currently being used within LIGO for the generation of mock data challenges to test the efficacy of burst gravitational wave data analysis methods.

Simulations can be generated from within GravEn or pre-generated waveforms can be substituted. The use of pre-generated waveforms allows for the inclusion of astrophysically motivated waveforms from external numerical projects and the rapid evaluation of data analysis methods on these state-of-the-art numerical signals.

All calculations are performed in a coordinate system with the origin located at the center of the Earth. The time of flight between the center of the Earth and the detector is computed knowing the source's location on the sky and the start time of each simulation is then adjusted accordingly. This allows for the coincident (within time-of-flight) generation of simulations between any set of detectors. GravEn currently supports the LIGO, GEO, VIRGO and TAMA interferometric gravitational wave detectors.

The general operation of GravEn is summarized in Section 2.2.1 followed by a discussion of the major physical components of GravEn and their infrastructure. These include the time projection between the center of the Earth and detector (q.v. Section 2.3), metric perturbation generation (q.v. Section 2.4), TT gauge projection (q.v. Section 2.5), and detector projection (q.v. Section 2.6). Finally, this overview concludes with a commentary on injecting software simulation signals into actual detector data along with an outline on how to perform the needed calibrations for LIGO data in Section 2.7.

## 2.2 Driver Function - `graven`

### 2.2.1 Structure of the Driver

There are four modes of operation for GravEn: 1) the simulation information is read line-by-line from a file, 2) the simulation information is read by making multiple random draws on the lines of a file, 3) the driver takes the simulation information directly from the inputs and does not need to read a file and 4) a pre-generated waveform is pushed through the driver. The first three modes generate original waveforms from within GravEn, while the last takes its waveform data from an external source.

#### 2.2.1.1 Generate Original Waveforms

First, the driver decides what mode to operate in based on the number of input variables and then assigns them accordingly. The appropriate variables are then used as input into the list function for the generation of the master simulations list (each line contains the information for one simulation).

With the list made, the driver initiates a loop to make simulations by going line-by-line through this master simulations list. For each simulation, the information from one line of the simulations list is read and variables are assigned.

Knowing the source location on the sky and which detector this simulation uses, the driver calls a function, `ifodelay`[1], that calculates the appropriate number of samples to add to the start time to account for the difference in arrival time of a gravitational wave between the center of the Earth and the detector.

The driver then calls a function, `makeh`, to create the desired metric perturbation and then feeds this perturbation into the TT gauge projector, `makett`. With the metric perturbation in the TT gauge, the $+$ and $\times$ polarizations are returned and then fed into the detector projector, `detproj`. This projects the gravitational wave on the antenna pattern of the detector at the center of the Earth.

The detector projector returns the timeseries in units of strain. This may or may not then need to be converted into detector output units so that the simulation may be added to the data stream. A discussion on the use of simulated strain data is contained in Section 2.7. The final timeseries, in units of detector output, is saved along with the start time of the simulation at the detector. Information for the simulation is also saved to a log file so that the log file can be used as the input file for the list function to recreate the waveform. The loop then increments and goes through the next line of the master simulations list.

#### 2.2.1.2 Use Pre-generated Waveforms

The structure of the driver is exactly the same for pre-generated waveforms, except that once the pre-generated waveform is read from a file, the metric perturbation creation function, `makeh`, and the TT gauge projector, `makett` are bypassed along with rounding the start time of the simulation at the detector to the nearest sample,

[1] Function names are specified in `fixed width font` throughout this work.

since inter-sample start times for pre-generated waveforms are not yet supported.

Several assumptions are made about the pre-generated waveform:

- The waveform is in the TT gauge
- The waveform is evenly sampled at the same rate as the detector[2]

It is important to make sure that the sampling frequency input into GravEn matches that of the pre-generated waveform and the detector for accurate results, however GravEn does take into account the different sampling rate of VIRGO (20 kHz) versus the other interferometric detectors (16,384 Hz).

### 2.2.2 Outputs

The output of `graven` consists of the name of the simulation, the start time of the simulation in whole samples at the detector, the simulation time series, the start time of the simulation in seconds and nanoseconds at the detector, and the time of maximum strain in seconds and nanoseconds at the detector. This information, along with the start time of the simulation at the center of the Earth, the maximum allowable strain and other source orientation input variables are recorded in a log file that can be used as an input file to generate coincident simulations between detectors or recreate simulations for a single detector.

## 2.3 Time Projector Between the Center of the Earth and the Detector - `ifodelay`

GravEn supports the generation of coincident simulations between multiple detectors by defining the time of arrival of the gravitational wave at the center of the Earth. Then, for each detector, the time lapse between the arrival at the center of the Earth and the arrival at the location of the detector is calculated. This lapse is added to the arrival at the center of the Earth and recorded as the appropriate injection time for the specified detector. This gives a common coordinate system to multiple detectors so that coincident simulations between multiple detectors can

[2]e.g. The original Ott, et al. waveforms are not evenly sampled [54].

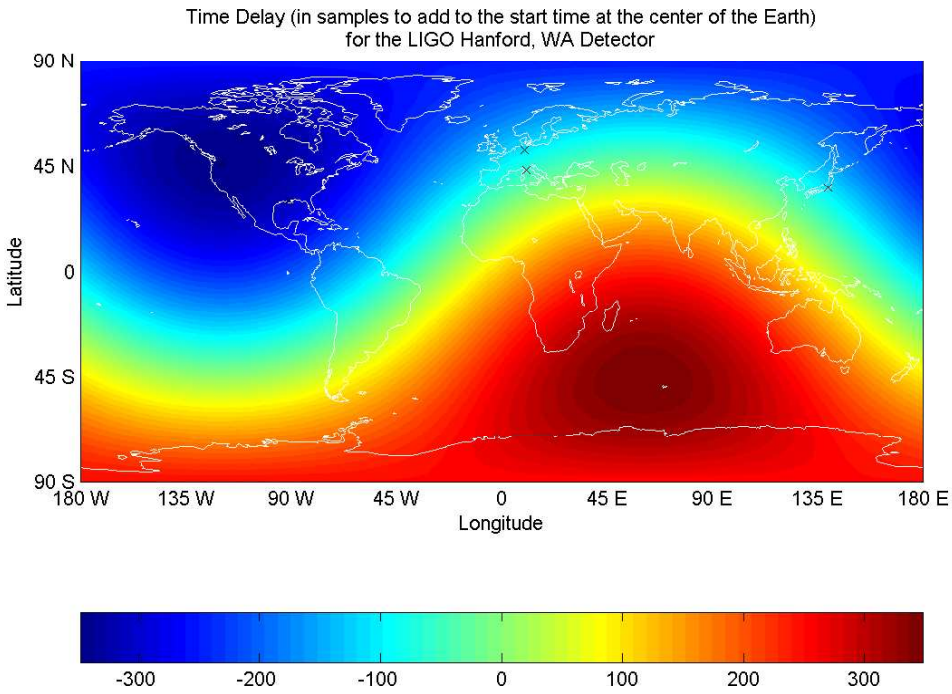


**Figure 2.1.** The number of samples to add to signal start time with respect to the source sky location for the LIGO Hanford Observatory (sampling frequency = 16,384 samples/sec)

be produced. The end result is a timeseries in units of detector output that can be directly added to existing data from a detector.

The time lapse is computed knowing the location of the detector on the surface of the Earth ($\vec{V}_{det}$), the unit vector of the sky location of the source ($\vec{V}_{GW}$) and the speed of light ($c$):

$$t = \frac{\vec{V}_{det} \cdot \vec{V}_{GW}}{c} \tag{2.1}$$

Example time projections for the LIGO Hanford Observatory, WA are shown in Figure 2.1 and the LIGO Livingston Observatory, LA in Figure 2.2. Similar plots for GEO, VIRGO and TAMA are found in Appendix A.

Given the WGS-84 (World Geodetic System dated 1984 [55]) coordinates for the beam splitter and the LIGO sampling frequency of 16,384 samples per second, the maximum number of samples to add for the LIGO Hanford Observatory is approximately 347.9687 samples and the maximum number of samples to add for LIGO Livingston Observatory is approximately 348.2718 samples.

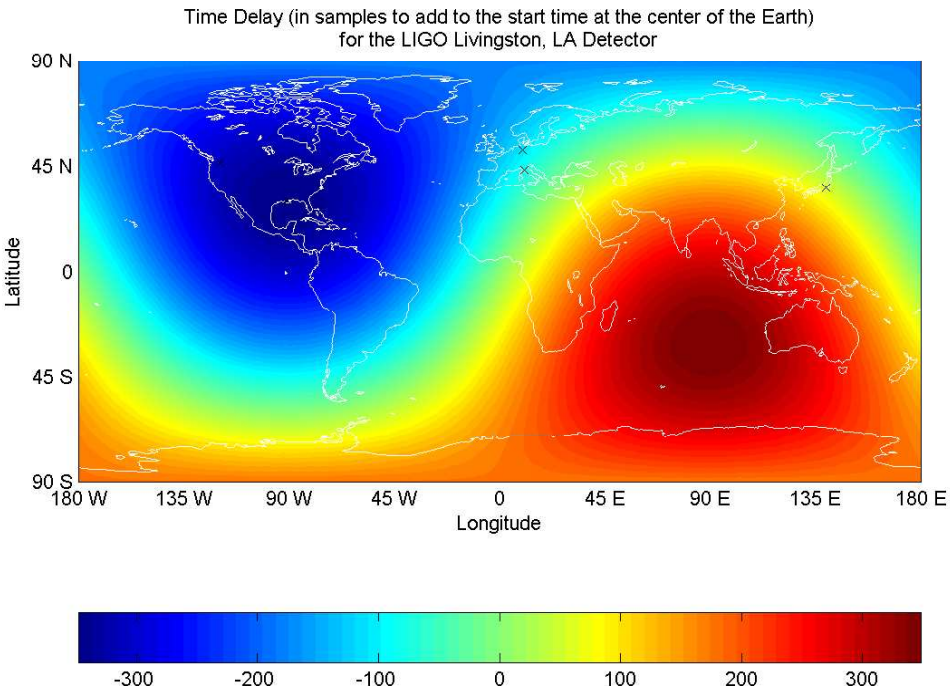


**Figure 2.2.** The number of samples to add to signal start time with respect to the source sky location for the LIGO Livingston Observatory (sampling frequency = 16,384 samples/sec)

## 2.4 Metric Perturbation Function - `makeh`

Currently supported waveforms include Gaussians (Equation 2.2a), sine-Gaussians (Equation 2.2b), cosine-Gaussian (Equation 2.2c), sinc's (Equation 2.2d) and black hole ringdowns (Equation 2.2e) of the following form:

$$h_{ij}^{G}(t,\tau) = h_{max} \exp\left(-\frac{t}{\tau}\right)^2 \begin{pmatrix} -1 & 0 & 0 \\ 0 & -1 & 0 \\ 0 & 0 & 2 \end{pmatrix} \tag{2.2a}$$

$$h_{ij}^{SG}(f,t,\tau) = h_{max} \sin(2\pi f t) \exp\left(-\frac{t}{\tau}\right)^2 \begin{pmatrix} -1 & 0 & 0 \\ 0 & -1 & 0 \\ 0 & 0 & 2 \end{pmatrix} \tag{2.2b}$$

$$h_{ij}^{CG}(f,t,\tau) = h_{max} \cos(2\pi f t) \exp\left(-\frac{t}{\tau}\right)^2 \begin{pmatrix} -1 & 0 & 0 \\ 0 & -1 & 0 \\ 0 & 0 & 2 \end{pmatrix} \tag{2.2c}$$

$$h_{ij}^{SINC}(f,t) = h_{max}\frac{\sin(\pi f t)}{\pi f t}\begin{pmatrix} -1 & 0 & 0 \\ 0 & -1 & 0 \\ 0 & 0 & 2 \end{pmatrix} \quad (2.2d)$$

$$h_{ij}^{BH}(f,t,\tau) = h_{max}\exp\left(-\frac{t}{\tau}\right)\begin{pmatrix} \sin(2\pi f t) & \cos(2\pi f t) & 0 \\ \cos(2\pi f t) & \sin(2\pi f t) & 0 \\ 0 & 0 & 0 \end{pmatrix} \quad (2.2e)$$

where $h_{max}$ is the desired maximum amplitude of the waveform, $f$ is the frequency of the signal, $\tau$ is the Gaussian time scale and $t$ is time. In addition to these waveforms, sine waves, cosine waves, linear chirps[3], Gaussian modulated linear chirps, square waves, Gaussian modulated square waves, sawtooth waves, Gaussian modulated sawtooth waves and Gaussian modulated white noise can be generated similarly to the ones described above.

The form of the matrix applied to all of the signals described above (with the exception of the black hole ringdown) is derived from the notation for the metric perturbation ($h_{jk}$) as described in [56]. The metric perturbation is given by:

$$h_{ij} = h(t)\mathcal{Y}_{ij}^{l=2,m=0} \quad (2.3)$$

where $h(t)$ is a strain timeseries and $\mathcal{Y}_{ij}^{l=2,m=0}$ is the $l=2, m=0$ symmetric trace-free tensor of rank 2 (STF-$l$). Because there is a one-to-one mapping between STF-$l$ and the spherical harmonics, they can be used interchangeably in calculations. The form of $Y^{l=2,m=0}$ in Cartesian coordinates is:

$$Y^{l=2,m=0} = \frac{1}{4}\sqrt{\frac{5}{\pi}}\left(\frac{3z^2}{x^2+y^2+z^2} - 1\right) \quad (2.4)$$

Therefore, the matrix form of every supported metric perturbation generated from within GravEn, excluding black hole ringdowns is:

$$\mathcal{Y}_{ij}^{l=2,m=0} \propto \begin{pmatrix} -1 & 0 & 0 \\ 0 & -1 & 0 \\ 0 & 0 & 2 \end{pmatrix} \quad (2.5)$$

[3]The linear chirp begins at 0 Hz and sweeps up to the frequency specified.

The output of `makeh` is a timeseries of the 3×3 metric perturbation time evolution.

## 2.5 TT Gauge Projector - `makett`

Given the metric perturbation timeseries output by `makeh` and the orientation of the source to the line-of-sight ($\theta_{int}$, $\varphi_{int}$), `makett` projects the metric perturbation onto the TT gauge. The source is defined to be in a right-handed Cartesian coordinate system with the rotation of the source in the $XY$ plane and the angular momentum in the $Z$ direction ($\hat{z} = \hat{x} \times \hat{y}$). $\theta_{int}$ is the angle the line-of-sight makes with the source's axis of angular momentum and $\varphi_{int}$ is the angle between the source's X-axis and the projection of the line-of-sight on the rotation plane, measured counterclockwise in radians. $\cos(\theta_{int})$ describes the projection of $\hat{n}$ along $+\hat{z}$ and $\cos(\varphi_{int})$ describes the projection of $\hat{n}$ along $+\hat{x}$ ($\hat{n}$ points in the direction of the line-of-sight, from the source to the Earth) [57], q.v. Figure 2.3.

A rotation of the source's coordinate system is needed so that $\hat{z}$ coincides with $\hat{n}$. This is done by rotating about $\hat{z}$ through an angle $\varphi$ counterclockwise and then rotating about the new $\hat{y}$ counterclockwise through an angle $\theta_{int}$:

$$\begin{pmatrix} \hat{e}_x \\ \hat{e}_y \\ \hat{n} \end{pmatrix} = \begin{pmatrix} \cos(\varphi)\cos(\theta_{int}) & \sin(\varphi)\cos(\theta_{int}) & -\sin(\theta_{int}) \\ -\sin(\varphi) & \cos(\varphi) & 0 \\ \cos(\varphi)\sin(\theta_{int}) & \sin(\varphi)\sin(\theta_{int}) & \cos(\theta_{int}) \end{pmatrix} \begin{pmatrix} \hat{x} \\ \hat{y} \\ \hat{z} \end{pmatrix} \tag{2.6}$$

where $\varphi$ is $\varphi_{int}+\pi$ so that the orientation of $\hat{x}$ and $\hat{y}$ that span the polarization plane are same here as in `detproj`, q.v. Section 2.6.1.

The + and × polarization bases are constructed as follows:

$$\hat{e}_+ = \hat{e}_x \otimes \hat{e}_x - \hat{e}_y \otimes \hat{e}_y \tag{2.7a}$$

$$\hat{e}_\times = \hat{e}_x \otimes \hat{e}_y + \hat{e}_y \otimes \hat{e}_x \tag{2.7b}$$

$h_+$ and $h_\times$ are then formed by contracting the metric perturbation with the appropriate basis:

$$h_+ = \frac{1}{2} h^{ij} \hat{e}_{+\ ij} \tag{2.8a}$$

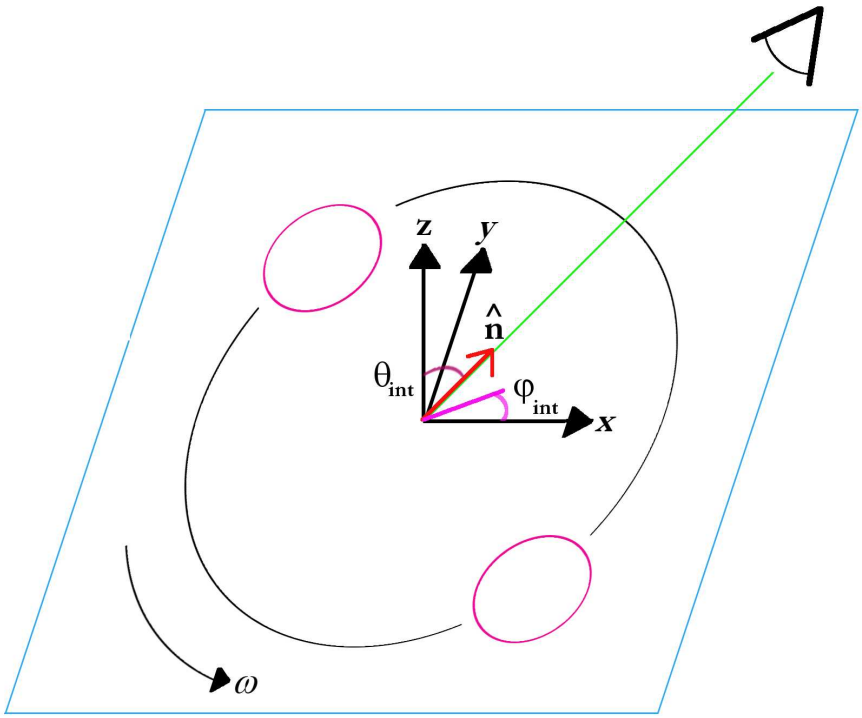


**Figure 2.3.** Illustration of source internal angles

$$h_\times = \frac{1}{2} h^{ij} \hat{e}_{\times\ ij} \tag{2.8b}$$

`makett` outputs a timeseries for both the + and × polarizations.

## 2.6 Detector Projector - `detproj`

Given the output of `makett` (or a pre-generated waveform), a detector and the orientation of the source on the sky ($\theta_{ext}$, $\varphi_{ext}$, $\psi$), `detproj` projects the TT gauge waveform onto the antenna pattern of the detector. $\theta_{ext}$ is the source's co-declination sky location as projected onto Earth's fixed coordinates, $\varphi_{ext}$ is the source's sky location longitude as projected onto Earth's fixed coordinates (in radians) and $\psi$ is the source's polarization angle in radians, defined in Section 2.6.1. The detector is assumed to be the origin of a coordinate system with $\hat{Z}$ pointing toward the North Pole, $\hat{X}$ pointing toward the intersection of the Prime Meridian and the Equator, and $\hat{Y} = \hat{Z} \times \hat{X}$; the gravitational wave is assumed to

be a plane wave.

A rotation of Earth's axes is needed so that $\hat{Z}$ points towards the source along the line-of-sight:

$$\begin{pmatrix} \hat{e}_x \\ \hat{e}_y \\ \hat{n} \end{pmatrix} = \begin{pmatrix} \cos(\varphi_{ext})\cos(\theta_{ext}) & \sin(\varphi_{ext})\cos(\theta_{ext}) & -\sin(\theta_{ext}) \\ -\sin(\varphi_{ext}) & \cos(\varphi_{ext}) & 0 \\ \cos(\varphi_{ext})\sin(\theta_{ext}) & \sin(\varphi_{ext})\sin(\theta_{ext}) & \cos(\theta_{ext}) \end{pmatrix} \begin{pmatrix} \hat{X} \\ \hat{Y} \\ \hat{Z} \end{pmatrix} \tag{2.9}$$

Since both the source's and Earth's Z axes now lie on the line-of-sight, the + and × polarization basis can be defined in the source frame:

$$\hat{e}_+ = \hat{e}_x \otimes \hat{e}_x - \hat{e}_y \otimes \hat{e}_y \tag{2.10a}$$

$$\hat{e}_\times = \hat{e}_x \otimes \hat{e}_y + \hat{e}_y \otimes \hat{e}_x \tag{2.10b}$$

Now define the + and × polarization basis in the detector frame:

$$\hat{e}'_+ = \cos(2\psi)\hat{e}_+ + \sin(2\psi)\hat{e}_\times \tag{2.11a}$$

$$\hat{e}'_\times = \cos(2\psi)\hat{e}_\times - \sin(2\psi)\hat{e}_+ \tag{2.11b}$$

where $\psi$ is the polarization angle as described in Section 2.6.1.

The antenna projection matrix is formed by:

$$D = \hat{V} \otimes \hat{V} - \hat{W} \otimes \hat{W} \tag{2.12}$$

where $\hat{V}$ and $\hat{W}$ are the unit vectors for the X and Y arms of the detector in the WGS-84 coordinate system.

The beam pattern functions are defined to be:

$$F_+ = \frac{1}{2} D^{ij} \hat{e}'_{+\ ij} \tag{2.13a}$$

$$F_\times = \frac{1}{2} D^{ij} \hat{e}'_{\times\ ij} \tag{2.13b}$$

[3] A short discussion of the WGS-84 coordinate system as well as the official location and orientation of the LIGO interferometers in this system can be found in [58]. Location and orientation coordinates of GEO, VIRGO and TAMA can be found in [45] but a swapping of the GEO X and Y arms is need to correct a mislabeling in this paper (confirmed by [59]). Full documentation for the WGS-84 coordinate system can be found in [55].

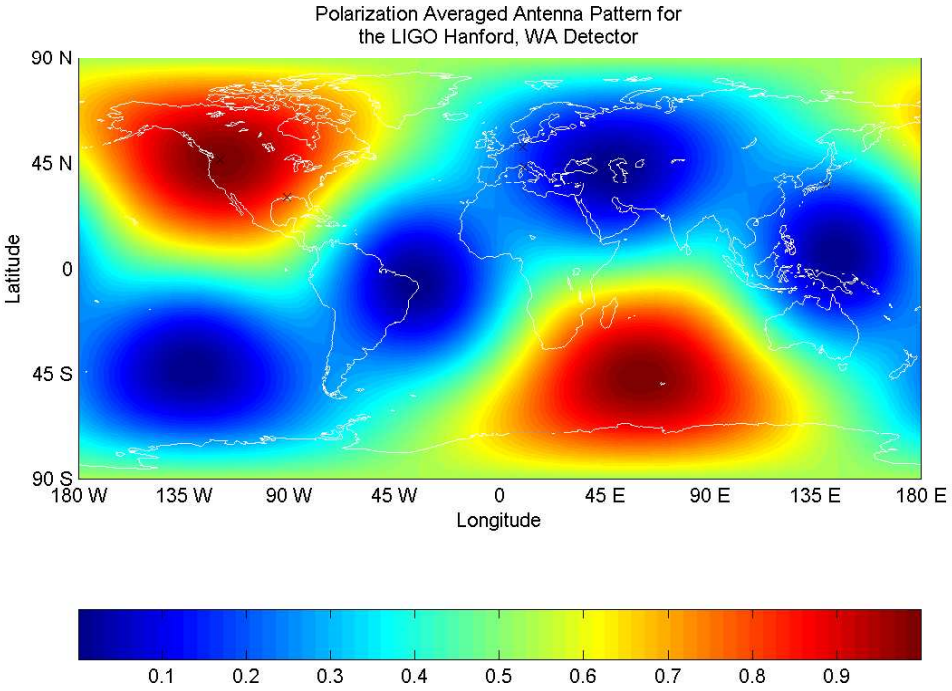


**Figure 2.4.** Antenna pattern for the LIGO Hanford Observatory, WA

The polarization averaged antenna pattern is defined to be [60, 57]:

$$\rho^2 = F_+^2 + F_\times^2 \tag{2.14}$$

Example data for the antenna pattern for the LIGO Hanford Observatory, WA is in Figure 2.4 and the antenna pattern for the LIGO Livingston Observatory, LA is in Figure 2.5.

Antenna patterns for GEO, VIRGO and TAMA can be found in Appendix A.

The final detector projection, which combines the $+$ and $\times$ polarizations into units of strain as seen by the detector, is then:

$$h = F_+ h_+ + F_\times h_\times \tag{2.15}$$

The timeseries in units of strain as seen by the detector is output by `detproj`.

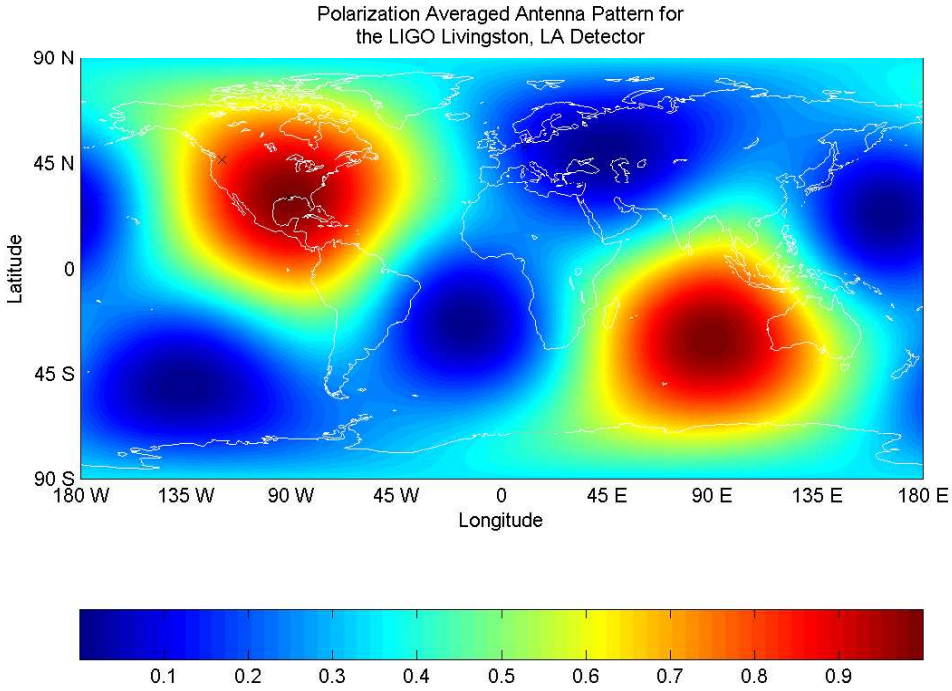


**Figure 2.5.** Antenna pattern for the LIGO Livingston Observatory, LA

### 2.6.1 Definition of the Polarization Angle $\psi$

The transverse plane of the TT gauge is defined as a coordinate plane between the Earth and the source that is perpendicular to the line-of-sight. $\hat{n}$ is defined to be the unit vector pointing from the center of the Earth to the source and $\hat{k}$ is defined to be the unit vector pointing from the center of mass of the source to the Earth, q.v. Figure 2.6.

Determine the projection of the source's Z-axis and the Earth's Z-axis onto the transverse plane, $\vec{\xi}_s$ and $\vec{\xi}_\oplus$ respectively:

$$\vec{\xi}_s = \hat{z}_s - \hat{k}(\hat{k} \cdot \hat{z}_s) \tag{2.16a}$$

$$\vec{\xi}_\oplus = \hat{Z}_\oplus - \hat{n}(\hat{n} \cdot \hat{Z}_\oplus) \tag{2.16b}$$

$\psi$ is defined to be the angle between $\vec{\xi}_s$ and $\vec{\xi}_\oplus$, q.v. Figure 2.6:

$$\psi = \cos^{-1}\left[\frac{\hat{Z}_\oplus - \hat{n}(\hat{n} \cdot \hat{Z}_\oplus)}{|\hat{Z}_\oplus - \hat{n}(\hat{n} \cdot \hat{Z}_\oplus)|} \cdot \frac{\hat{z}_s - \hat{k}(\hat{k} \cdot \hat{z}_s)}{|\hat{z}_s - \hat{k}(\hat{k} \cdot \hat{z}_s)|}\right] \tag{2.17}$$

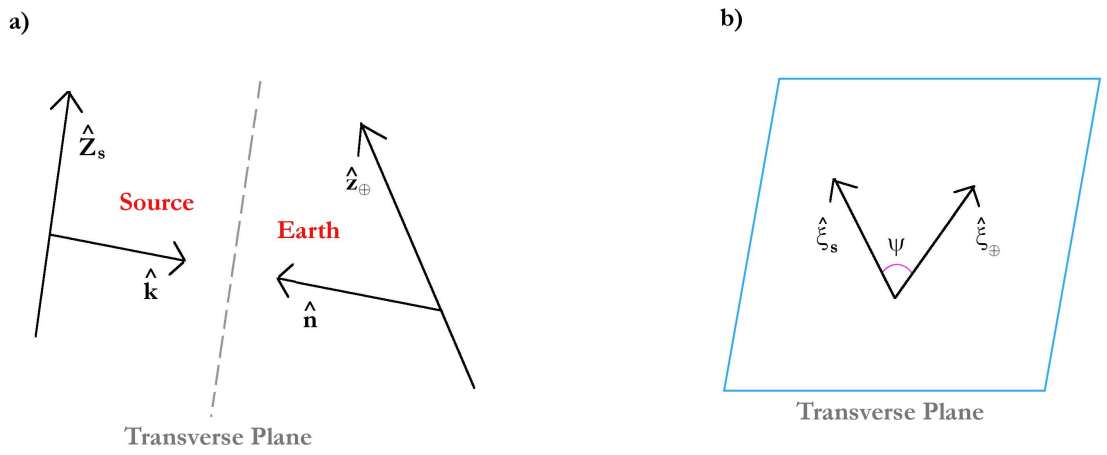


**Figure 2.6.** a) Definition of the transverse plane between the source and Earth coordinate systems. b) Definition of the polarization angle $\psi$ as seen on the transverse plane.

Since:

$$\hat{k} \cdot \hat{z}_s = \cos(\theta_{int}) \tag{2.18a}$$

$$\hat{n} \cdot \hat{Z}_\oplus = \cos(\theta_{ext}) \tag{2.18b}$$

$$\hat{k} = -\hat{n} \tag{2.18c}$$

$\psi$ is then:

$$\psi = \cos^{-1}\left[\frac{\hat{Z}_\oplus - \hat{n}\cos(\theta_{ext})}{|\hat{Z}_\oplus - \hat{n}\cos(\theta_{ext})|} \cdot \frac{\hat{z}_s + \hat{n}\cos(\theta_{int})}{|\hat{z}_s + \hat{n}\cos(\theta_{int})|}\right] \tag{2.19}$$

When the Earth's Z-axis is parallel or anti-parallel to the line-of-sight, $\psi$ is measured as the angle between $\hat{X}_\oplus$ and $\vec{\xi}_s$:

$$\psi = \cos^{-1}\left[\hat{X}_\oplus \cdot \frac{\hat{z}_s + \hat{n}\cos(\theta_{int})}{|\hat{z}_s + \hat{n}\cos(\theta_{int})|}\right] \tag{2.20}$$

When the source's Z-axis is parallel or anti-parallel to the line-of-sight, $\psi$ is measured as the angle between $\vec{\xi}_\oplus$ and $\hat{x}_s$:

$$\psi = \cos^{-1}\left[\frac{\hat{Z}_\oplus - \hat{n}\cos(\theta_{ext})}{|\hat{Z}_\oplus - \hat{n}\cos(\theta_{ext})|} \cdot \hat{x}_s\right] \tag{2.21}$$

When both the Earth's and the source's Z-axes are parallel or anti-parallel to the line-of-sight, $\psi$ is measured as the angle between $\hat{X}_{\oplus}$ and $\hat{x}_s$:

$$\psi = \cos^{-1}\left[\hat{X}_{\oplus} \cdot \hat{x}_s\right] \tag{2.22}$$

## 2.7 Injecting Simulated Strain Data Into the Detector Data

The scope of any gravitational wave simulation package extends to the generation of a strain timeseries as seen by the detector. The conversion of this strain to the appropriate detector output units, if needed, is an instrumentation issue dealing with the measurement of detector calibration functions. For detectors whose output is a direct measurement of strain (e.g., GEO) the simulated strain produced by GravEn may be directly added to the detector data.

Since LIGO records such things as voltages measured by photodiodes after interference and calibration signals that are injected into the detector hardware separately, calibration information must be used to convert the simulated strain signal into units of detector output before it can be added to the detector data.

### 2.7.1 Inverse Calibrator - `calibsimfd`

#### 2.7.1.1 Calibrations

In LIGO, calibrations are measured to convert the detector output into strain. Of interest here is converting strain into detector output. In this sense, an inverse calibration is being performed.

In order to measure the LIGO detector's response to an external disturbance, such as a gravitational wave, it is parameterized as a feedback loop, $G(f)$ (shown in Figure 2.7) consisting of the cavity response or 'sensing' function $C(f)$, a digital filter function $D(f)$ and an actuation function $A(f)$ [61, 4, 62, 63]. The sensing function describes the response of the optical cavities of the interferometer while the digital filter describes the digital filtering used in the feedback loop and the actuation function describes the mechanical response of the suspended test masses

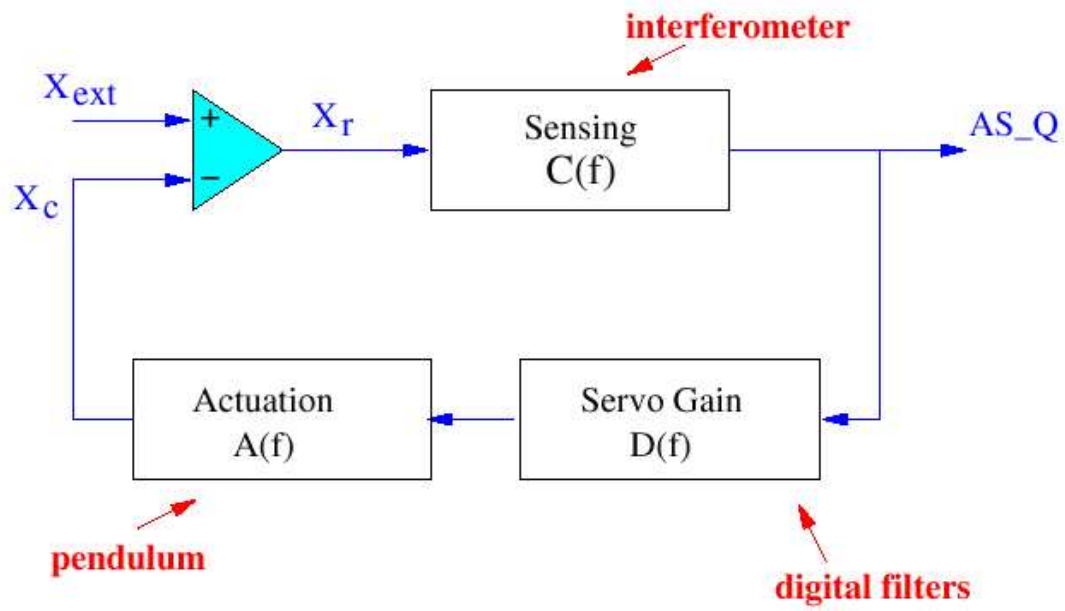


**Figure 2.7.** Diagram of the feedback loop used to measure the response of the LIGO interferometer to an external disturbance. Image from [4].

due to the feedback loop. These combine to form the feedback loop by:

$$G(f) = C(f)A(f)D(f) \tag{2.23}$$

The strain of the interferometer at time $t_0$ is related to the detector output ($AS\_Q$) by:

$$h(f, t_0) = \frac{1 + G(f, t_0)}{C(f, t_0)} AS\_Q(f, t_0) \tag{2.24}$$

Setting $R(f, t_0) = \frac{1+G(f,t_0)}{C(f,t_0)}$ gives us a new function called the response function for the detector. This function essentially represents the calibration function at a given time. The evolution of the detector calibration is assumed to be linear. Therefore, the sensing function and digital filter functions are parameterized by:

$$C(f, t) = \alpha(t)C(f, t_0) \tag{2.25a}$$
$$D(f, t) = \beta(t)D(f, t_0) \tag{2.25b}$$

where $\alpha(t)$ and $\beta(t)$ are frequently measured parameters and generalize the ref-

erence $C$ and $D$ at time $t_0$ to time $t$. The variations in the sensing function are measured by applying sinusoidal excitations to one of the end test masses of the interferometer and monitoring its amplitude as a function of time. These sinusoidal excitations are known as calibration lines and are either removed or otherwise avoided when analyzing the data for the detection of gravitational waves.

LIGO calculates the response function in units of strain/detector output at a given time $t$ as:

$$R(f,t) = \frac{1 + \alpha(t)\beta(t)G(f,t_0)}{\alpha(t)C(f,t_0)} \tag{2.26}$$

As can be seen here, the response function is easily separated into the time dependent sum of two fixed filters:

$$\frac{1 + \alpha(t)\beta(t)G(f)}{\alpha(t)C(f)} = \frac{1}{\alpha(t)C(f)} + \frac{\beta(t)G(f)}{C(f)} \tag{2.27}$$

The inverse calibration cannot be separated so easily:

$$\frac{\alpha(t)C(f)}{1 + \alpha(t)\beta(t)G(f)} \neq \frac{\alpha(t)C(f)}{1} + \frac{C(f)}{\beta(t)G(f)} \tag{2.28}$$

This property has created difficulties in producing the inverse calibration in the time domain. However, the frequency-domain calibration has proved effective with the caveat that it cannot be done 'on-the-fly.'

#### 2.7.1.2 Frequency Domain Inverse Calibrator

Given the output of `detproj`, the detector, start time of the simulation at the detector, and the detector's sampling frequency, `calibsimfd` converts the strain time-series into detector output units. Doing the inverse calibration is rather straightforward. First, the strain data is Fourier transformed using the FFT algorithm, then multiplied by the response function in units of detector output/strain:

$$R^{-1}(f,t) = \frac{\alpha(t)C(f)}{1 + \alpha(t)\beta(t)G(f)} \tag{2.29}$$

and the resultant is inverse Fourier transformed back into the time domain. The time-domain series is now in units of detector output and can be added directly

into the data stream.

Chapter 3

# BlockNormal

## 3.1 Introduction

With the development of international efforts to make the first direct observation of gravitational waves, the need for robust data analysis methods to pull signals from a sea of detector noise has become apparent. There are sources of gravitational waves whose waveforms can be well characterized and detection methods can be specially tailored for these sources. For example, banks of templates can be generated for use in matched filtering techniques for inspiralling binaries. However, there lies great potential in unknown (burst) sources of gravitational waves to unveil new science, but their detection will require robust data analysis techniques that assume little about the waveforms. An assumption that can be made is that a burst signal will be uncorrelated with the detector noise. From this, it is known that the character of the data will change from when it is only detector noise to when it is a combination of detector noise and a signal; specifically, the variance of the data when there is no signal present will change when there is a signal present while the mean may or may not change, depending on the signal. Places in the data where these statistics change are called *change-points*. Described here is the data analysis method that looks for such change-points called BlockNormal

This Event Trigger Generator (ETG) assumes the data to be analyzed is stationary (no long term drifts in mean or variance) and white (equal power over the frequency bandwidth). Therefore, the data conditioning stage for these ETGs consists of frequency banding (to avoid strong instrumental artifacts), removal of

weak instrumental artifacts within the bandwidth, data whitening and stationary segment determination. Documentation of this data conditioning is found in [64] and an overview of the entire BlockNormal data analysis pipeline is found in [65]. The source code for this ETG and its accompanying pipeline is available for download from [66].

BlockNormal has two major stages: change point identification and block identification. The change point identification computes the Bayesian probability for every point in a data segment to be a point where the statistics of the data change; the point with the highest probability is considered as a candidate change point. If the probability is higher than a threshold probability, it is recorded as a change point. The change point identification is applied iteratively until there are no longer candidate change-points that exceed the threshold probability. The block identification computes a measure of relative excess power in-between two change-points based on the mean, variance and duration of the block in question, as well as the mean and variance of the larger data set which contains the block in question. If the relative excess power is larger than a threshold value, then the block is marked as a trigger.

This chapter begins by outlining the theory used by BlockNormal in Section 3.2. The theory is then applied to the search for one change-point (q.v. Section 3.2.1) and then multiple change-points (q.v. Section 3.2.2). With BlockNormal described, the larger data analysis pipeline where it is applied is outlined in Section 3.3. Finally, the tuning of the ETG parameters that will be used in the ETG comparisons investigated in subsequent chapters is illustrated in Section 3.4.

## 3.2 Theory

Before setting out to develop a data analysis technique, it should be defined exactly what is being asked of the data. There are two schools of thought on how to answer this question: the Frequentist and Bayesian perspectives [67, 68]. A Frequentist assigns a confidence in the procedure for making a decision on the posed question. Therefore, the confidence in a Frequentist's conclusion is an assessment of the rule's average performance. The Bayesian measures the degree of belief that a proposition is true in light of an observation.

Since burst sources are unmodeled and there are no observations to average a data analysis' performance, it makes sense to approach the data from the Bayesian perspective. That still leaves the question of what is being asked of the data. Since the object is to find the points in the data where the statistics change, the probability is investigated that, at a given point, the data before it was drawn from one normal distribution and the data after it from another. A method similar to the one outlined here was presented by A. F. M. Smith in 1975 [69] and is analogous to the photon counting studies by J. Scargle [70].

At a given point, the probability that the data before it was drawn from one normal distribution and the data after it from another is investigated.

Let $\mathcal{M}_j$ be a set of models. To distinguish between them for a given observation $X_N$, define the odds ratio:

$$\rho_j = \frac{P(\mathcal{M}_j|X_N)}{P(\mathcal{M}_1|X_N)} \tag{3.1}$$

where the standard notation that $P(A|B)$ is the probability of $A$ given that condition B holds is adopted. For a particular observation $X_N$, $\rho_j > \rho_k$ if and only if $\mathcal{M}_j$ is more likely than model $\mathcal{M}_k$; similarly, $\rho_j > 1$ if and only if model $\mathcal{M}_j$ is more likely than $\mathcal{M}_1$.

The odds ratio $\rho_j$ can be written in terms of the sampling distribution for $X_N$ assuming model $\mathcal{M}_j$ and $\mathcal{M}_1$ and the *a priori* likelihood of these two models:

$$\rho_j = \frac{P(X_N|\mathcal{M}_j)P(\mathcal{M}_j)}{P(X_N|\mathcal{M}_1)P(\mathcal{M}_1)} \tag{3.2}$$

The *a priori* odds ratio

$$\gamma_j = \frac{P(\mathcal{M}_j)}{P(\mathcal{M}_1)} \tag{3.3}$$

depends only on the predisposition regarding the relative likelihood of the different models $\mathcal{M}_j$ (i.e., it is independent of the observations). $\gamma_j$ will be addressed further in Section 3.2.1.2.

### 3.2.1 Searching for One Change-point

Let $X_N$ be an observation consisting of N consecutive samples at the output of the detector

$$X = \{x[k] : k = 0, ..., N-1\} \tag{3.4}$$

where the $x[k]$ are the individual output samples. Further, assume that the data is filtered so that the noise is uncorrelated among the samples.

Consider a specific class of models $\mathcal{M}_j$ which suppose that the data are drawn piecewise from $j$ normal distributions; i.e., model $j$ includes all data $X_N$ where samples $x[k_l]$ through $x[k_l + 1]$ are drawn from the particular normal distribution with:

$$(\mu_l, \sigma_l) \neq (\mu_{l+1}, \sigma_{l+1}) \tag{3.5a}$$

$$0 = k_0 < k_1 < \ldots < k_l < k_l + 1 < \ldots N \tag{3.5b}$$

$P(X_N|\mathcal{M}_2)$ is given by:

$$P(X_N|\mathcal{M}_2) = \sum_{j=1}^{N-1} P(X_j|\mathcal{M}_1)P(X_{N-j}|\mathcal{M}_1) \tag{3.6}$$

where $X_N$ is the concatenation of $X_j$ and $X_{N-j}$, and similarly for $P(X_N|\mathcal{M}_j)$ for $j < N$.

Now consider $P(X_N|\mathcal{M}_1)$, from which any of the $P(X_N|\mathcal{M}_j)$ can be constructed:

$$P(X_N|\mathcal{M}_1) = \int \mathrm{d}\sigma \int \mathrm{d}\mu \, \left(2\pi\sigma^2\right)^{-\frac{N}{2}} P(\mu, \sigma) \prod_{k=0}^{N-1} \exp\left(\frac{-\left(x[k] - \mu\right)^2}{2\sigma^2}\right) \tag{3.7}$$

where $P(\mu, \sigma)$ is the *a priori* probability for $\mu$ and $\sigma$.

A position of ignorance is adopted with regards to $\mu$ and $\sigma$. The sampling distribution for $x[k]$ (the normal distribution) is form invariant under translations in $\mu$ and scaling of $\sigma$; correspondingly, adopt the prior distributions

$$P(\mu) = \alpha \tag{3.8a}$$

$$P(\sigma) \;=\; \frac{\beta}{\sigma} \tag{3.8b}$$

where $\alpha$ and $\beta$ are constants. Both these priors are improper (i.e., non-normalizable); however, they lead to a finite odds ratio $P(\mathcal{M}_j|X_N)/P(\mathcal{M}_1|X_N)$. The constants $\alpha$ and $\beta$ are introduced to account for the unknown scales introduced by these priors and will be discussed further in Section 3.2.1.2.

With these priors, the integrals in Equation 3.7 are analytic:

$$P(X_N|\mathcal{M}_1) = \frac{\alpha\beta}{\sqrt{N}}\left(2\pi N\left(\overline{x^2}-\overline{x}^2\right)\right)^{-\frac{N-1}{2}} I_{N-2} \tag{3.9}$$

where:

$$I_N = \begin{cases} \sqrt{\left(\frac{\pi}{2}\right)} & N=0 \\ (N-1)!! & \text{N odd} \\ \sqrt{\left(\frac{\pi}{2}\right)}(N-1)!! & \text{N even} \end{cases} \tag{3.10}$$

(q.v. Appendix B for the complete derivation.)

Now consider the odds ratio $\rho_2$,

$$\rho_2 \;=\; \frac{P(\mathcal{M}_2|X_N)}{P(\mathcal{M}_1|X_N)} \tag{3.11a}$$

$$\;=\; \frac{P(X_N|\mathcal{M}_2)}{P(X_N|\mathcal{M}_1)}\gamma_2 \tag{3.11b}$$

$$= \alpha\beta\gamma_2\sqrt{2\pi}\sum_{k=1}^{N-1}\sqrt{\frac{N}{(N-k)k}}\frac{I_{k-2}I_{N-k-2}}{I_{N-2}}\frac{[NY_{0,N}]^{(N-1)/2}}{[kY_{0,k}]^{(k-1)/2}\,[(N-k)Y_{k,N-k}]^{(N-k-1)/2}} \tag{3.11c}$$

where:

$$Y_{j,k} \;=\; \overline{x_{j,k}^2} - \overline{x_{j,k}}^2 \tag{3.12a}$$

$$\overline{x_{j,k}} \;=\; \frac{1}{k}\sum_{l=0}^{k-1} x[j+l] \tag{3.12b}$$

$$\overline{x_{j,k}^2} \;=\; \frac{1}{k}\sum_{l=0}^{k-1} x[j+l]^2 \tag{3.12c}$$

Equation 3.11c gives the probability that $X_N$ is drawn piecewise from two

normal distributions yielding a single change-point.

#### 3.2.1.1 The $\rho_2$ Figure of Merit

Equation 3.11c yields an overall probability measurement that there is one change point in a segment of data. However, information on the location of the change-point is also needed. To achieve this, the $\rho_2$ figure of merit, $\rho_{2,k}$ is introduced. This calculates the probability that each point in the data, $k$, is a change-point. Therefore, the $\rho_2$ figure of merit is composed of the individual components within the summation expression in Equation 3.11c:

$$\rho_2 = \alpha\beta\gamma_2\sqrt{2\pi}\sum_k \rho_{2,k} \tag{3.13}$$

The most likely location for a change-point is then the $k$ which makes $\rho_{2,k}$ the largest. Figure 3.1 graphically shows the $\rho_2$ figure of merit for a simulated data segment that has a change in mean directly in the middle of the data length.

#### 3.2.1.2 Constants $\alpha$, $\beta$ and $\gamma_2$

To evaluate the odds ratio $\rho_2$, it was needed to introduce prior probabilities reflecting the expectations regarding $\mu$, $\sigma$, the probability that the segment under consideration has a single change point and the probability that it has one change point:

$$P(\mu) = \alpha \tag{3.14a}$$

$$P(\sigma) = \frac{\beta}{\sigma} \tag{3.14b}$$

$$\frac{P(\mathcal{M}_2|N)}{P(\mathcal{M}_1|N)} = \gamma_2 \tag{3.14c}$$

The expectations concerning the particular $\mu$ or $\sigma$ that apply to a particular sample are independent of the number of samples examined; correspondingly, $\alpha$ and $\beta$ are truly constants. The probability ratio $\gamma_2$, however, does depend on $N$.

Suppose that the rate of triggers, each of which involves at least two change-points (one for the onset of a signal and another for its conclusion), is $R$. Let the detector sample rate be $f_s$. The probability that there are no triggers in $N$

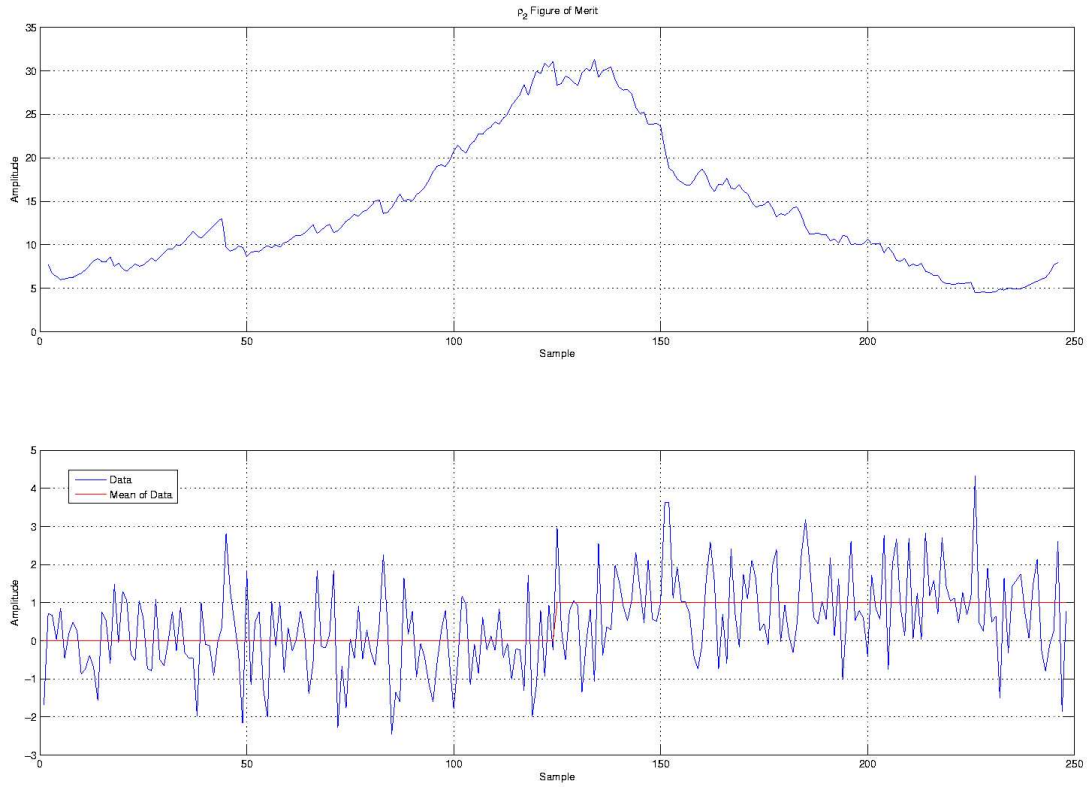


**Figure 3.1.** The $\rho_2$ figure of merit is shown in the top plot for each point in the timeseries data shown in the bottom plot.

samples is the probability that neither a trigger start nor a trigger end occurs in the $N$ samples. Assuming that triggers are Poisson distributed and that the interval covered by the $N$ samples is much longer than the duration of a trigger this probability is:

$$P(\mathcal{M}_1|N) = \exp\left(-N\frac{R}{f_s}\right) \tag{3.15}$$

Supposing that $N\frac{R}{f_s}$ is very much less than unity gives:

$$P(\mathcal{M}_1|N) \simeq 1 - N\frac{R}{f_s} \tag{3.16}$$

Correspondingly,

$$P(\mathcal{M}_2|N) < 1 - \exp\left(-N\frac{R}{f_s}\right) \tag{3.17}$$

When triggers are rare (i.e., $N\frac{R}{f_s}$ very much less than unity):

$$\gamma_2 = \frac{P(\mathcal{M}_2|N)}{P(\mathcal{M}_1|N)} < N\frac{R}{f_s} \tag{3.18}$$

which is directly proportional to $N$.

It is assumed here that $\gamma_2$ is proportional to this bound: i.e., that it is proportional to $N$.

### 3.2.2 Searching for More Than One Change-point

Since burst gravitational waves are expected to have short durations, it is expected that a signal may very well begin and end within the same data segment. Therefore, methods of applying the BlockNormal theory to the search for more than one change-point is vital to effective data analysis.

There are two methods for seeking multiple change-points. The first is the utilization of $\rho_{3+}$ and the second is the iterative application of $\rho_2$ between change-points. This section develops both methods and discusses their strengths and weaknesses for practical data application.

#### 3.2.2.1 $\rho_3$

Perhaps the more theoretically sound method for searching for two change-points is the construction of $\rho_3$. Begin by defining $\rho_3$ similarly to $\rho_2$:

$$\rho_3 = \gamma_3\frac{P(X_N|\mathcal{M}_3)}{P(X_N|\mathcal{M}_1)} \tag{3.19}$$

$P(X_N|\mathcal{M}_3)$ describes the probability that a data segment is composed of data drawn piecewise from three different normal distributions. Logically, these segments of data should not overlap but should be consecutive to each other. Therefore the indexing for these segments should be:

$$j : 1 \to N-2 \tag{3.20a}$$

$$k : j+1 \to N-1 \tag{3.20b}$$

$P(X_N|\mathcal{M}_3)$ is then given by:

$$P(X_N|\mathcal{M}_3) = \sum_{j=1}^{N-2} \sum_{k=j+1}^{N-1} P(X_j|\mathcal{M}_1)P(X_{k-j}|\mathcal{M}_1)P(X_{N-k}|\mathcal{M}_1) \tag{3.21}$$

Each of the probabilities in the double sum corresponds to a segment of data (where $X_j$, $X_{k-j}$ and $X_{N-k}$ are concatenated to form $X_N$). Using the definition for $P(X_N|\mathcal{M}_1)$ from Equation 3.9 yields:

$$\rho_3 = \gamma_3(\alpha\beta)^2 2\pi \sum_{j=1}^{N-2} \sum_{k=j+1}^{N-1} \frac{\sqrt{N}}{\sqrt{j}\sqrt{k-j}\sqrt{N-k}} \frac{I_{j-2}I_{k-j-2}I_{N-k-2}}{I_{N-2}} \cdots \times \frac{[NY_{0,N}]^{\frac{N-1}{2}}}{[jY_{0,j}]^{\frac{j-1}{2}}[(k-j)Y_{j,k-j}]^{\frac{k-j-1}{2}}[(N-k)Y_{k,N-k}]^{\frac{N-k-1}{2}}} \tag{3.22}$$

This will yield a figure of merit that is a two dimensional array (matrix) with zeros on the diagonal and all components below.

#### 3.2.2.2 How to Interpret the $\rho_3$ Figure of Merit

Similar to the $\rho_2$ figure of merit, the $\rho_3$ figure of merit measures the probability that every point $j$ is the location of the first change-point in the data segment and that every subsequent point $k$ is the location of the second change-point. This will yield a figure of merit that is a two-dimensional array (matrix) with zeros on the diagonal as well as in all components below. The columns of each row contain the probabilities that the location of the second change-point is at column index $k$ assuming that the first change-point is located at the row index.

For example, consider examining row 3 where there will be non-zero values in columns 4 to $N-1$. The column index that has the maximum value for that row is where the most likely second change-point is assuming the first change-point is at row index 3. The $\rho_3$ figure of merit is shown in Figure 3.2 for data that has a change in mean that begins a third of the way into the data and ends two-thirds of the way into the data, as shown in Figure 3.3.

Ultimately, the location of the two most likely change-points are of interest. Each of the elements in the figure of merit represents the probability that the first change-point is located at index 'row' and the second change-point is located

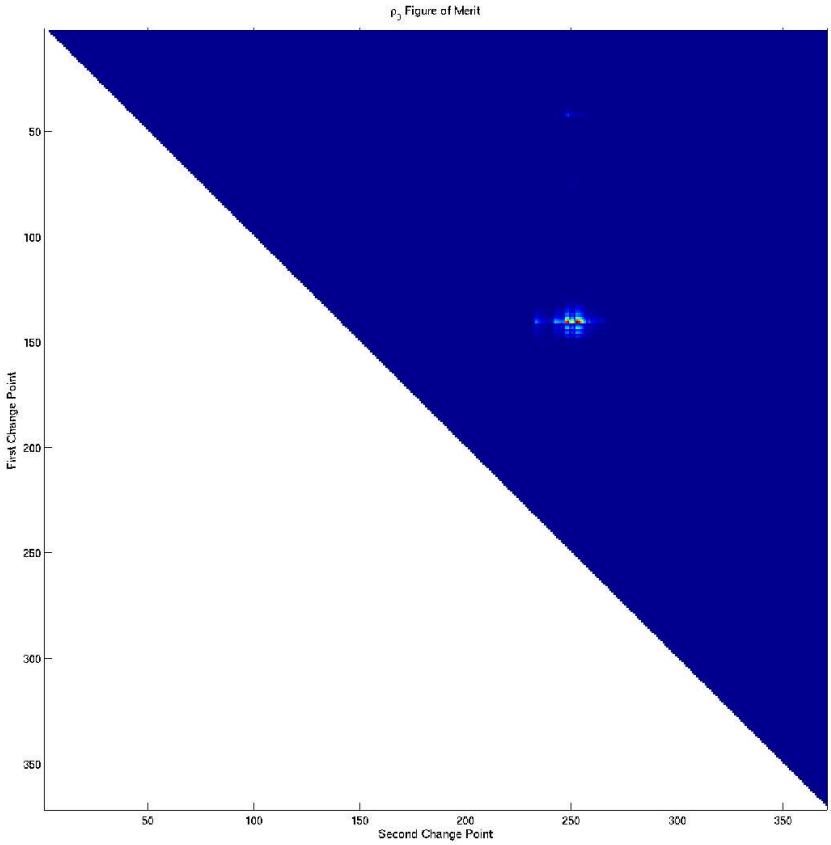


**Figure 3.2.** The $\rho_3$ figure of merit. Blue regions represent indices with low probability of change-point location while red regions represent higher probability. White regions are indices where the figure of merit is not calculated (i.e., zero) since they are not included in the double sum in Equation 3.22.

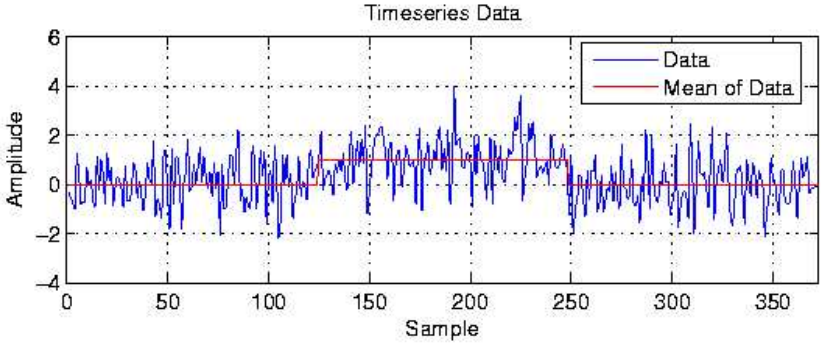


**Figure 3.3.** Timeseries data containing a change in mean that begins a third of the way into the data and ends two-thirds of the way into the data.

at index 'column.' Therefore, the component of the figure of merit that has the largest value tells us where the most likely change-points are located.

Another roughly equivalent method for determining the location of two change-points is to sum the values in each row and each column independently and identify the row with the largest value as being the location of the first change-point and the column with the largest value as being the location of the second.

#### 3.2.2.3 Iterative $\rho_2$

Since the computation time of $\rho_3$ is on the order of $N^2$ (because $\rho_3$ contains a double sum), the search for multiple change-points can quickly become computationally expensive. This situation only worsens for the search of 3 change-points (which scales as $N^3$ since it is composed from a triple sum) or more. However, $\rho_2$ can be applied to the entire timeseries and split into two smaller data segments at the change-point. $\rho_2$ can then be run on each of these smaller segments to further break them down. This process is known as binary segmentation and was studied in general by Vostrikova [71] who proved its consistency.

## 3.3 BlockNormal Data Analysis Pipeline

BlockNormal forms a piece of a much larger data analysis pipeline; the pipeline begins by analyzing a single detector by fetching its data from a database, performing data quality measures (to make sure the data is designated science data with no known contaminants or flaws), data conditioning (q.v. Section 3.3.1), trigger generation (q.v. Section 3.3.2), and veto generation (to reject triggers that are correlated to instrumental or environmental artifacts that have been detected at the same time). Triggers that survive the single detector pipeline are pooled together and compared for temporal coincidence in triggers between detectors within the expected time-of-flight of a gravitational wave between the detectors (which is a maximum time of about 10 ms between the LIGO Hanford, WA detectors and the LIGO Livingston, LA detector). This data analysis pipeline is illustrated in Figure 3.4. Triggers that survive the data analysis pipeline are called events and are considered candidate gravitational wave detections. The investigations throughout this work will look only at ETG triggers.

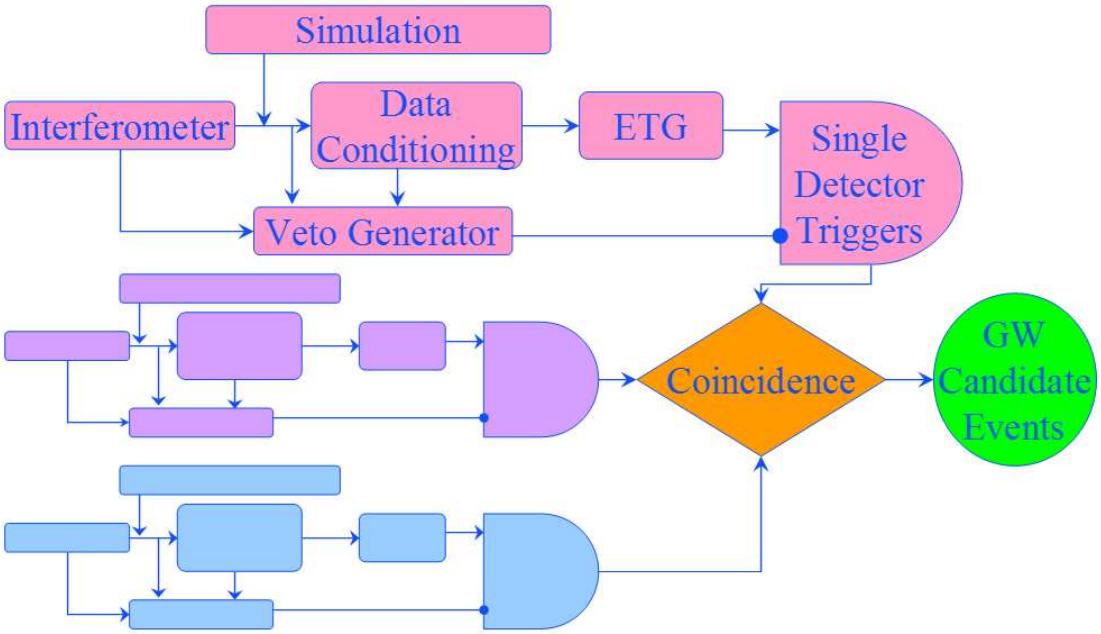


**Figure 3.4.** Graphical representation of the BlockNormal data analysis pipeline.

### 3.3.1 Data Conditioning

BlockNormal assumes that the detector output data has no correlations within it, meaning that the data has equal power at all frequencies (this is called white data). However, this is not the case for the LIGO interferometers. There are many localized frequency features, called lines, that are instrumentally and environmentally induced. An example of instrumental lines in the data is the vibration of the mirror suspensions at their resonant modes. An environmental line is induced at the 60 Hz fundamental frequency caused by the coupling of the detector electronics and the United States alternating current power grid. Also, low frequencies are dominated by seismic noise (caused by such things as the ocean beating of the shores) and shot noise (caused by the discrete nature of photons).

A data conditioning procedure has been developed by Tiffany Summerscales and is described in detail in [64]. This procedure removes lines, whitens the data and breaks the data into frequency bands. These frequency bands aid in data conditioning since they reduce the number of features that need to be addressed at one time and also improve data analysis performance by increasing the speed of BlockNormal as well as giving some knowledge of the frequency characteristics

of the resulting triggers based on the band in which it was found.

### 3.3.2 BlockNormal Event Trigger Generator

The BlockNormal event trigger generator (ETG) is built on a modified iterative $\rho_2$ method. First, the data are subtended into fixed length intervals (in practice, these intervals are about 10 s). Then, $\rho_2$ is computed for the first fixed length interval. If the value of $\rho_2$ is above a threshold amount $\rho_A$ (called the change-point add threshold), the highest value in the $\rho_2$ figure of merit is recorded. Then, beginning at the first determined change-point, $\rho_2$ is calculated again and the change-point add threshold applied again. If no change-point is determined at this stage, another fixed length of data is appended and the $\rho_2$ calculation repeated. This entire process is repeated until the end of the data set is reached. Each of the intervals between change-points are then searched iteratively using binary segmentation until no further change-points above the $\rho_A$ value are detected.

This method was adopted in favor of the pure binary segmentation method described in Section 3.2.2.3 because of an excess of false change-points detected near the end points of the fixed data widths which caused subsequent false coincident events between detectors.

Because of the iteration on progressively smaller data segments, some change-points may be identified due to small sample statistics that are not stable when analyzed in a larger data segment. Therefore, each change-point is reprocessed using the data after the previous change-point and before the next. If the $\rho_2$ value is not higher than the change-point drop threshold, $\rho_D$, the change-point in question is removed from the candidate trigger change-point list. It has been observed that there is little effect on the removal of unstable change-points when $\rho_D$ is slightly larger or smaller than $\rho_A$. Therefore, they are set to be equal to each other in practice and will be referred to as $\rho_T$ and called the change-point threshold.

The next step in the BlockNormal ETG is to identify significant blocks of data as defined by change-points. The significance is a measure of how different the mean and variance inside the block is compared to the larger data set from which it was drawn. Therefore, the block's mean and variance, $\mu_B$ and $\nu_B$, are measured

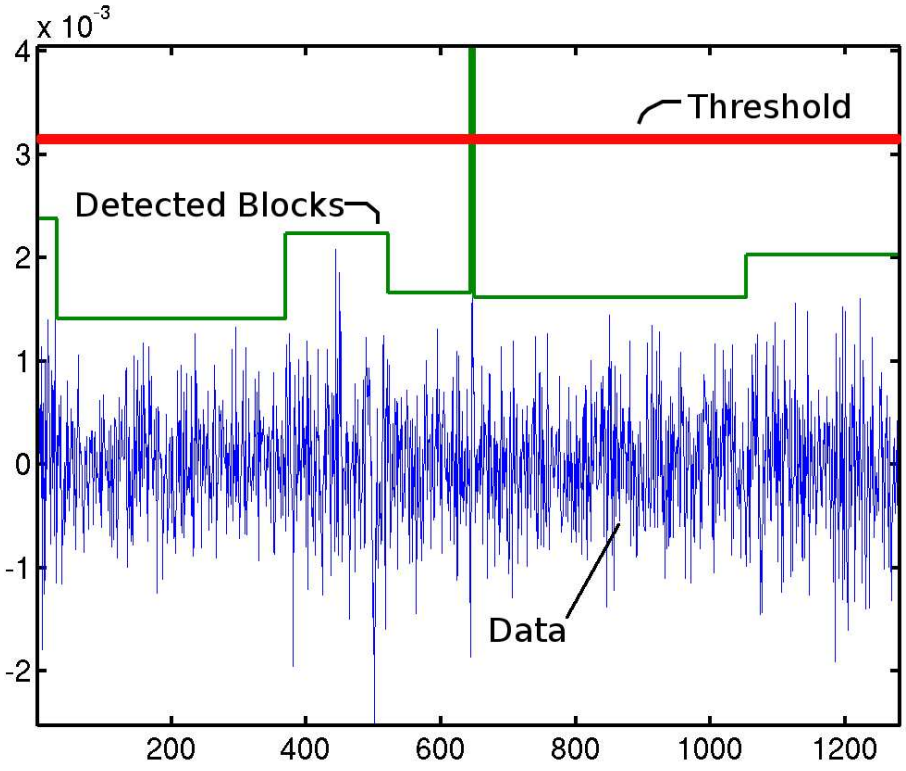


**Figure 3.5.** Illustration of BlockNormal thresholding on a timeseries. The magnitude of a detected block's variance is shown in green. Only the block whose magnitude is greater than the shown threshold (in red) is admitted as a trigger.

along with the mean and variance from the large data set, $\mu_0$ and $\nu_0$. These are then combined to give a measure of the block's excess 'power' relative to the statistics of the larger data set:

$$\mathcal{P} = \frac{(\mu_B - \mu_0)^2}{\nu_0} + \frac{t-1}{t}\left(\frac{\nu_B - \nu_0}{\nu_0}\right) \tag{3.23}$$

A block is admitted as a trigger if $\mathcal{P} > \epsilon$ where $\epsilon$ is the threshold value on the relative excess power of the block $\mathcal{P}$. This thresholding method is illustrated in Figure 3.5.

## 3.4 Tuning BlockNormal on the S3 Playground Data Set

The criteria for tuning the BlockNormal parameters ($\rho_T$ and $\epsilon$) on LIGO science data is to set an average trigger duration and an average accidental rate (also known as the false rate). To do this, BlockNormal was run over an evenly spaced subset of data from the third science data run (S3) called the playground data set (q.v. Appendix C). This data set is composed of evenly spaced, triple coincidence data that is set aside for tuning ETGs such as BlockNormal and is not included in the science analysis after the ETG parameters are set. Any triggers from this data set are assumed to be accidental.

In order to determine the average duration of triggers and the false rate from this playground data set, BlockNormal was run on the data iteratively for many combinations of $\rho_T$ and $\epsilon$ ($\rho_T$: 100 linear spacings between 0 and 10, $\epsilon$: 30 linear spacings between 1 and 30). The average duration results for the playground triggers are shown in Figure 3.6 and the average trigger rate results are shown in Figure 3.7.

With this information, parameter sets that met the desired average duration of between 20 ms and 40 ms and an average false rate of between 0.25 triggers per second and 0.75 triggers per second were selected. These parameter sets are shown in Figure 3.8.

Of the parameters that met all of the tuning criteria, the $\rho_T$ and $\epsilon$ that best matched the SLOPE trigger duration and false rate (q.v. Section 4.5) were selected. A $\rho_T$ of 3.2 and an $\epsilon$ of 1 sample were selected and yielded an average trigger duration of about 0.0221 s and an average trigger rate of about 0.312 triggers per second.

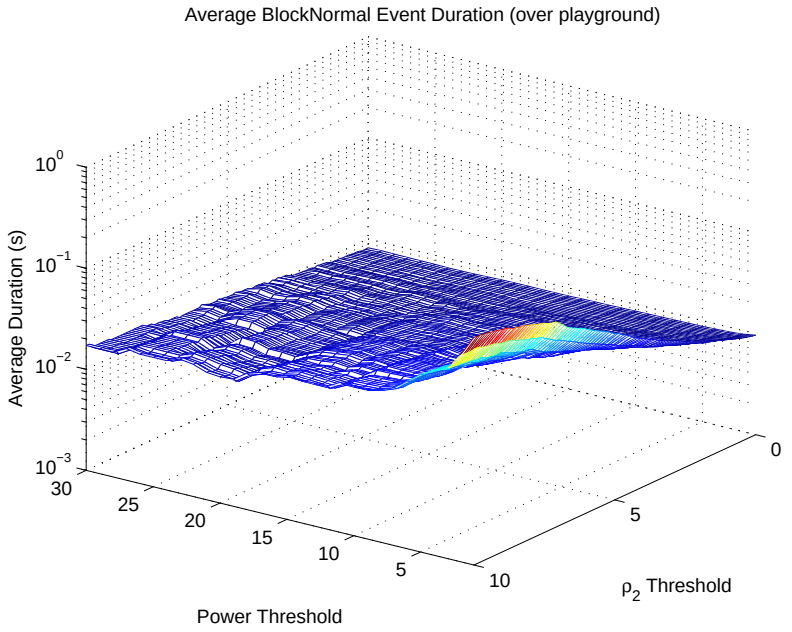


**Figure 3.6.** BlockNormal trigger average duration, on the Hanford S3 playground between 512 Hz and 640 Hz, with respect to BlockNormal change-point threshold ($\rho_T$) and relative excess power threshold ($\epsilon$).

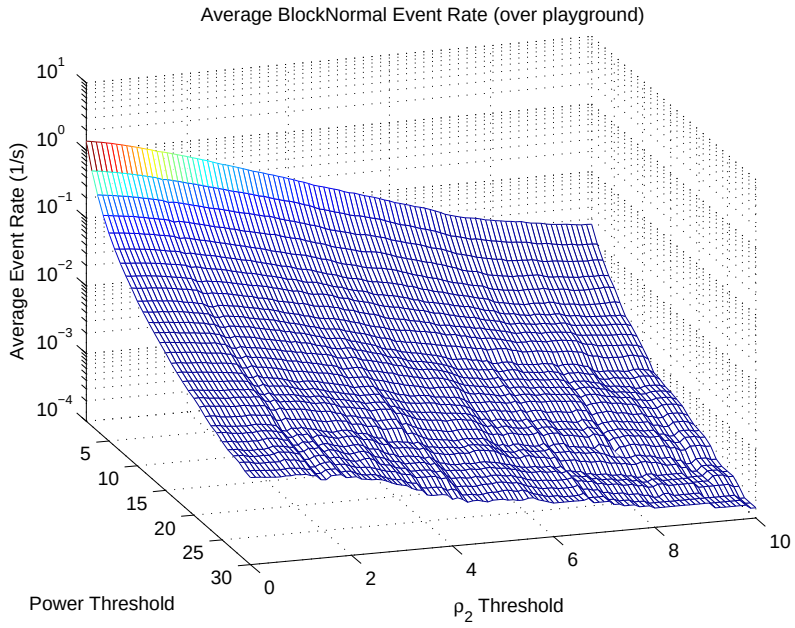


**Figure 3.7.** BlockNormal trigger rate, on the Hanford S3 playground between 512 Hz and 640 Hz, with respect to BlockNormal change-point threshold ($\rho_T$) and relative excess power threshold ($\epsilon$).

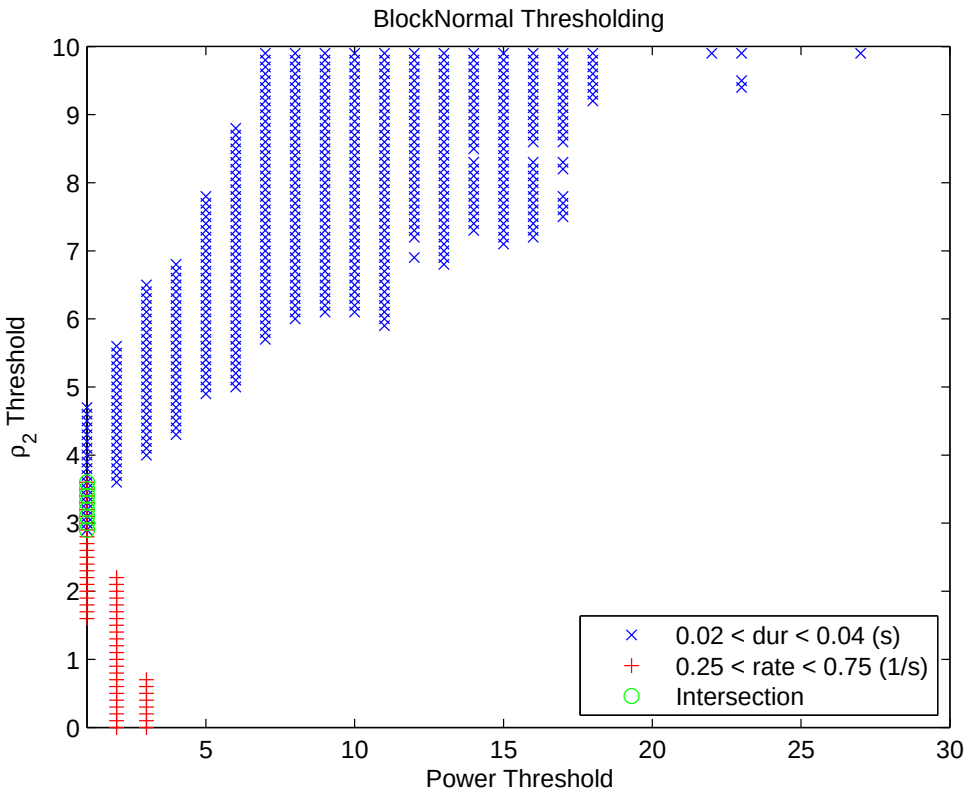


**Figure 3.8.** BlockNormal change-point ($\rho_T$) and relative excess power thresholds ($\epsilon$) that meet the criteria of having an average duration between 0.02 and 0.04 seconds and/or a rate between 0.25 and 0.75 Hz.

Chapter 4

# SLOPE

## 4.1 Introduction

The SLOPE event trigger generator (ETG) is a time-domain linear filter that identifies spans of time in prefiltered (with data conditioning identical to BlockNormal's, q.v. Section 3.3.1) gravitational wave data that are sufficiently inconsistent with Gaussian white noise. To do this, a window of data with fixed length is fit to a linear trend yielding a slope measurement. When a gravitational wave is added to the detector noise, the variance of the detector output will change since the signal is not correlated to the detector noise. SLOPE will locate these changes by measuring the linear trend over a window length. The measured slope is then compared to the maximum slope measurement expected within a certain probability based on the Gaussian approximation for the data being analyzed. If the measurement of the slope is sufficiently unlikely, the time of the first sample in the window is recorded. The analysis window is incremented by one time sample and the algorithm applied successively. Neighboring windows with unlikely slopes, which are likely to be correlated, are clustered. The start and stop times of these clusters are recorded as triggers. The source code for this ETG is available for download from [72].

This chapter begins by describing the underlying theory of the SLOPE ETG and the first application of SLOPE to LIGO science data in Section 4.2. The theoretical basis for SLOPE is outlined in Section 4.3 and with the knowledge of SLOPE's previous weaknesses, I describe my work on restructuring the ETG's

application in Section 4.4. Specifically, SLOPE's restructuring consists of new thresholding (q.v. Section 4.4.1) and temporal trigger clustering (q.v. Section 4.4.2) techniques. Finally, the tuning of the ETG parameters that will be used in the ETG comparisons investigated in subsequent chapters is illustrated in Section 4.5.

## 4.2 Previous Application of SLOPE to the S1 LIGO Data

SLOPE has previously been applied to LIGO data during the first science data run in 2002. Ultimately, unfortunate choices in SLOPE's application, as well as immature data conditioning, led to SLOPE being excluded from the burst gravitational wave upper limit calculation [31].

The first LIGO data acquisition for scientific results, abbreviated S1, took place between August 23 and September 9, 2002. This run resulted in 95.7 hours of coincident data between the three LIGO interferometers. Before data was processed by ETGs, it was high-pass filtered above 150 Hz and whitened. The high-pass filtering served to suppress large noise fluctuations which dominated the lower frequencies and the whitening flattened the noise spectrum of the remaining bandwidth. The whitening filters were different for each interferometer and fixed just prior to the S1 data run. Also, there was no effort made to remove known spectral lines from the data or otherwise prevent the ETGs from triggering because of these lines.

The SLOPE ETG calculated the slope fit inside of moving windows 10 samples long (610 $\mu$s). The threshold value on the slope measurements was determined in a two part investigation [5]. This consisted of measuring the frequency of slope amplitudes on a subset of raw data with and without added simulations given a preliminary threshold. The subset data, referred to as the playground data set, consisted of evenly spaced segments of triple coincidence data between 300 and 600 seconds long and comprised about 10% of the triple coincident data. It is assumed that there are no (or very few) real gravitational wave bursts in the playground data. The preliminary thresholds were 8,000 for the Hanford 4 km interferometer (H1), 12,800 for the Hanford 2 km interferometer (H2) and 4,000 for

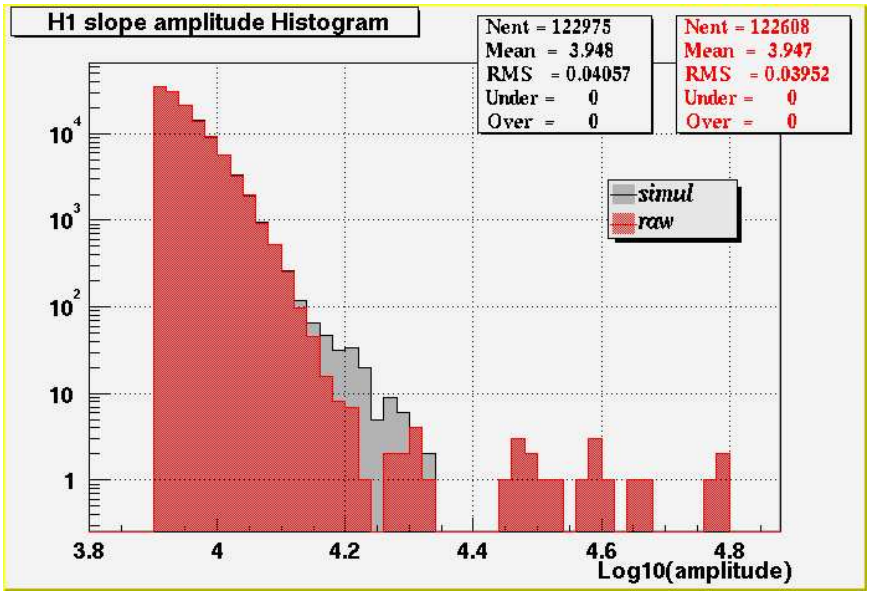


**Figure 4.1.** H1 measured slope frequency on S1 raw data with and without simulations. Image courtesy of Laura Cadonati for the LIGO Burst Group [5].

the Livingston 4 km interferometer (L1). The simulations used were sine-Gaussians with a frequency of 554 Hz and a strain of $3 \times 10^{-18}$ (this was the weakest strain detected by SLOPE). The results of this stage of the SLOPE thresholding are shown in Figures 4.1, 4.2 and 4.3. The H2 amplitude histogram shows that it was broad enough to cover the simulation triggers with the initial threshold. Because of this and because further investigation showed that changes in the H2 threshold yielded no changes in the raw data histogram and only served to reduce efficiency of detecting simulations, the H2 SLOPE threshold was fixed at 12,800.

The second stage of thresholding was to determine the triple coincident rate upper limit for one interferometer while holding the thresholds on the other interferometers fixed. The final threshold would be the threshold that minimizes the upper limit for the most simulated signal strains. This is in accordance with the assumption that there were no (or very few) real gravitational wave bursts in the playground data.

The upper limit for various SLOPE thresholds for H1 and L1, using sine-Gaussians with a frequency of 554 Hz and strains of $2 \times 10^{-18}$, $3 \times 10^{-18}$, $5 \times 10^{-18}$ and $7.5 \times 10^{-18}$, are shown in Figures 4.4 and 4.5. Ultimately, the thresholds were set at 10,000 for H1, 12,800 for H2 and 6,000 for L1.

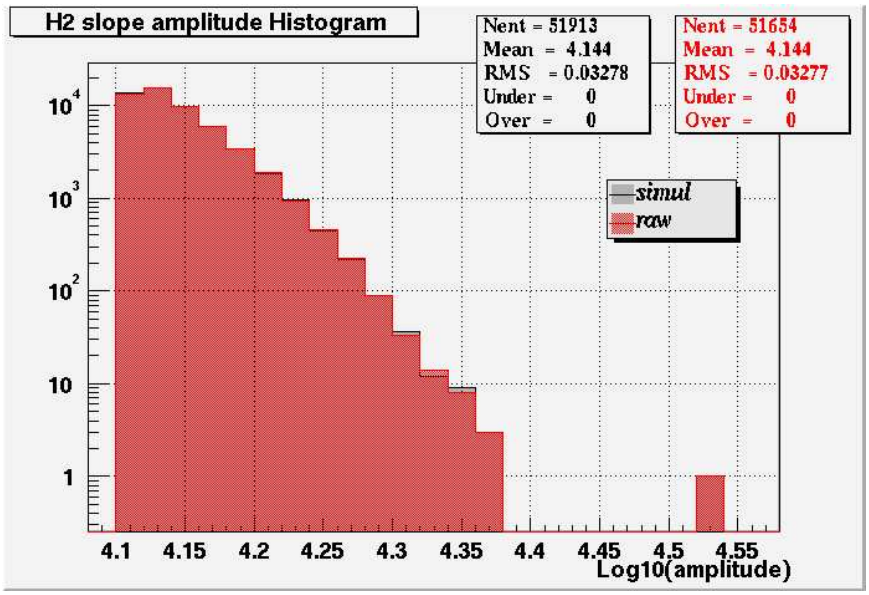


**Figure 4.2.** H2 measured slope frequency on S1 raw data with and without simulations. Image courtesy of Laura Cadonati for the LIGO Burst Group [5].

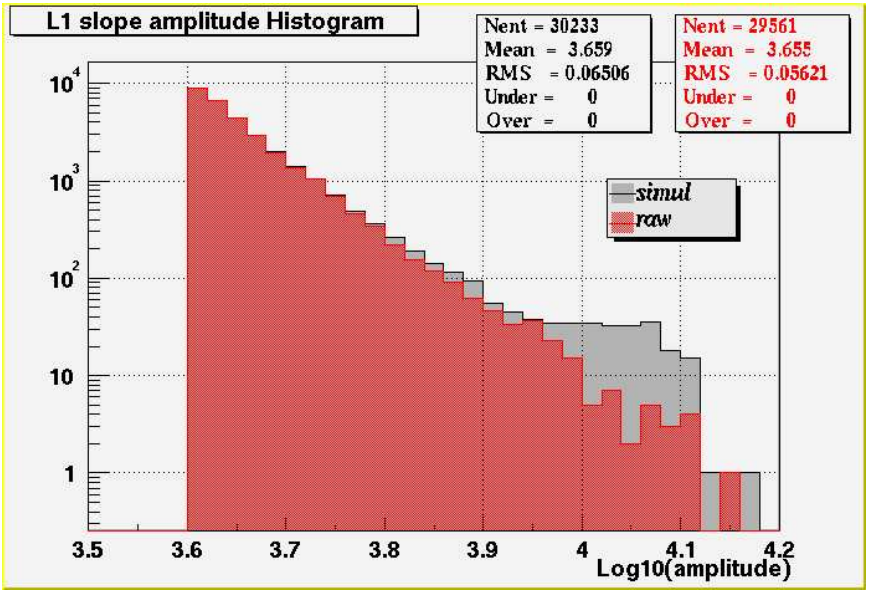


**Figure 4.3.** L1 measured slope frequency on S1 raw data with and without simulations. Image courtesy of Laura Cadonati for the LIGO Burst Group [5].

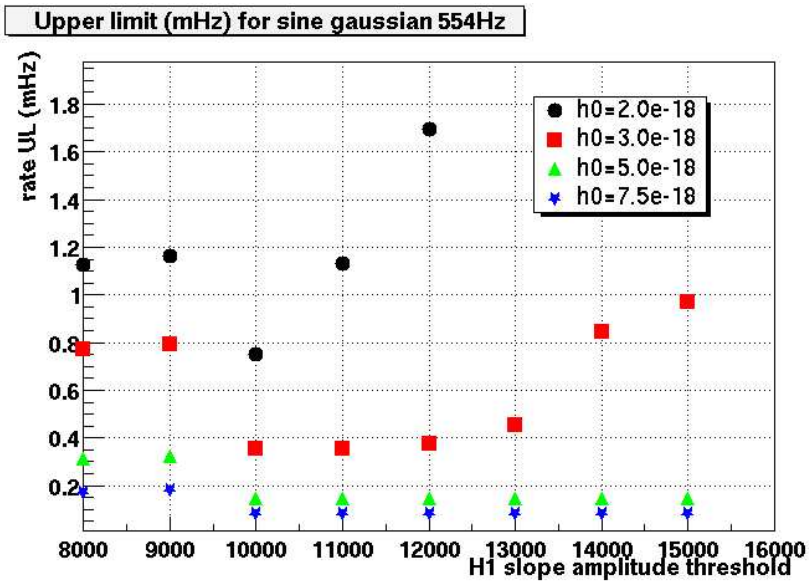


**Figure 4.4.** SLOPE upper limit of triple coincident triggers, with respect to threshold, for H1 with the H2 threshold held at 12,800 and the L1 threshold held at 6,000. Image courtesy of Laura Cadonati for the LIGO Burst Group [5].

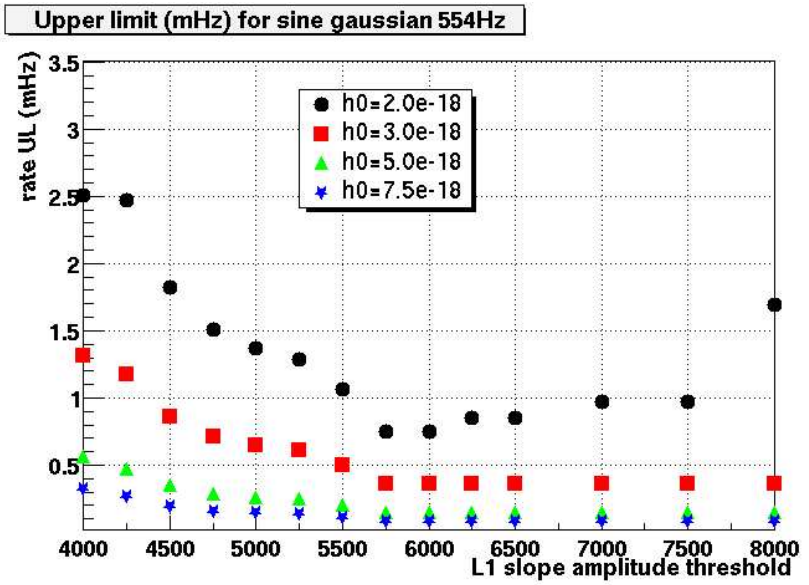


**Figure 4.5.** SLOPE upper limit of triple coincident triggers, with respect to threshold, for L1 with the H1 threshold held at 10,000 and the H2 threshold held at 12,800. Image courtesy of Laura Cadonati for the LIGO Burst Group [5].

It is important to note that these thresholds are fixed and did not change as the noise level in the detector changed. Therefore, any change in the noise level of the data caused the ETG's performance to change. Also, the prefilter applied to the data had an impulse response that caused a strong ringing in the data extending about 40 ms. This is sufficiently larger than the light travel time between the two interferometers and caused a cluster of triple coincident events around this impulse. The sensitivity to changes in the noise level was very evident in background event estimation. A background event is defined to be an event that is accidentally triple coincident and is measured by time shifting the different detector data streams relative to one another. This is important for the estimation of when an excess of events is statistically significant. Ultimately, the non-stationarity of the data and the non-adaptive thresholding of SLOPE led it to have a wildly varying single interferometer trigger rate, varying by more than a factor of one thousand on timescales of 10 seconds or less. This led the background rate estimation for SLOPE to be deemed unreliable and excluded it from the upper limit calculation for gravitational wave bursts on the S1 data run. However, the publication on the S1 gravitational burst search [31] did not completely discredit SLOPE's use as an ETG in future science data runs:

> *"... we intend to continue to employ and improve the SLOPE pipeline in future analyses."*

The rest of this chapter documents the redevelopment of SLOPE to overcome its previous shortcomings.

## 4.3 Theory

The basic SLOPE theory used in S1 and further developed here is derived from [73]. A data set is divided into sliding windows in time with $N$ samples. This is the order of the SLOPE ETG. Fitting the data, $x(t)$, to a straight line $(at + b)$ yields the slope $a$ and offset $b$:

$$a = \frac{< tx > - < t >< x >}{< t^2 > - < t >^2} \tag{4.1a}$$

$$b = < x > - a < t > \tag{4.1b}$$

where $< x >= \frac{1}{N}\sum_{i=1}^{N} x_i$ is the arithmetic mean of $x$ in the interval of length $N$. Also, $t_i = \frac{i}{f_{data}}$ is the $i^{th}$ sampled time and $x_i$ is the $i^{th}$ sampled detector output at sampling frequency $f_{data}$ [73]. The offset parameter $b$ is *not* used in the SLOPE ETG. Using the identities:

$$\sum_{i=1}^{N} i = \frac{N(N+1)}{2} \tag{4.2a}$$

$$\sum_{i=1}^{N} i^2 = \frac{N(N+1)(2N+1)}{6} \tag{4.2b}$$

Equation 4.1a becomes:

$$a = \frac{12}{\tau N(N^2-1)}\left(\sum_{j=1}^{N} j x_j - \frac{N+1}{2}\sum_{k=1}^{N} x_k\right) \tag{4.3}$$

where $\tau = \frac{1}{f_{data}}$. This is the computational basis of the SLOPE ETG.

### 4.3.1 SLOPE in Terms of Finite Differences

Slopes are the basis for computationally solving differential equations, therefore one can ask how SLOPE works in terms of finite differences in order to gain a better intuition for Equation 4.3. The first forward derivative (measuring the slope between samples by comparing one sample to the sample directly afterward) is defined as:

$$\triangle^1 f_k = f_{k+1} - f_k \tag{4.4}$$

where $f_k$ is the $k^{th}$ sample from the timeseries $f$. The first centered derivative (measuring the slope between samples by comparing the sample directly before and after the sample of interest) is defined similarly:

$$\delta^1 f_k = f_{k+\frac{1}{2}} - f_{k-\frac{1}{2}} = \frac{f_{k+1} - f_{k-1}}{2} \tag{4.5}$$

Consider SLOPE with an order of 2 ($N$=2):

$$a = \frac{2}{\tau}\left(x_2 - \frac{1}{2}[x_1 + x_2]\right) \tag{4.6a}$$

$$= \frac{x_2 - x_1}{\tau} \tag{4.6b}$$

This is exactly the first forward derivative. When SLOPE has an order of 3 ($N$=3), the first centered derivative is produced:

$$a = \frac{1}{2\tau}(x_2 + 2x_3 - [x_1 + x_2 + x_3]) \tag{4.7a}$$

$$= \frac{x_3 - x_1}{2\tau} \tag{4.7b}$$

Now consider higher orders of SLOPE.

$N$=4:

$$a = \frac{9}{10}\left(\frac{x_4 - x_1}{3\tau}\right) + \frac{1}{10}\left(\frac{x_3 - x_2}{\tau}\right) \tag{4.8}$$

$N$=5:

$$a = \frac{4}{5}\left(\frac{x_5 - x_1}{4\tau}\right) + \frac{1}{5}\left(\frac{x_4 - x_2}{2\tau}\right) \tag{4.9}$$

$N$=6:

$$a = \frac{25}{35}\left(\frac{x_6 - x_1}{5\tau}\right) + \frac{9}{35}\left(\frac{x_5 - x_2}{3\tau}\right) + \frac{1}{35}\left(\frac{x_4 - x_3}{\tau}\right) \tag{4.10}$$

A pattern is becoming evident: for even order, SLOPE is a series of weighted forward derivatives, centered on the data length with increasing weights moving out from the center; for odd order, SLOPE is a series of weighted centered derivatives, centered on the data length with increasing weights moving out from the center.

## 4.4 Redevelopment of the SLOPE ETG

The goal for this redevelopment of SLOPE is to bring the ETG into a consistently functioning order so that it may be effectively applied to LIGO data again. There are several key areas of improvement that are outlined here. The first is the development of a thresholding method that is less sensitive to the non-stationarity of the background noise and the second is a development of meaningful single detector trigger clusters. Also, the data conditioning developed and used for Block-

Normal (as described in Section 3.3.1) is applied to the data before the SLOPE ETG is applied.

### 4.4.1 Thresholding

The threshold on the absolute value of the magnitude of the slope (this is valid since, as seen later, the mean of the SLOPE distribution is zero, yielding an even Gaussian distribution) will be determined based on the probability of measuring a slope greater than the current slope. This probability of measuring a slope greater than the absolute value of a measured slope $a$ given the variance and mean of the SLOPE filter, $\sigma_a$ and $\mu_a$, is [73]:

$$P(>|a| \mid a, \sigma_a, \mu_a) = 1 - 2\int_0^{|a|} \frac{1}{\sqrt{2\pi}} \exp\left(\frac{(|a'| - \mu_a)^2}{2\sigma_a^2}\right) \mathrm{d}a' \tag{4.11}$$

$\mu_a$ and $\sigma_a^2$ are given by:

$$\sigma_a^2 = \frac{12 f_{data}^2}{N(N^2-1)} \sigma_{data}^2 \tag{4.12a}$$

$$\mu_a = 0 \tag{4.12b}$$

where $\sigma_{data}^2$ is the variance of the data being analyzed by SLOPE. These also approximate the data as Gaussian.

In order to save computation time, the probability that a slope is sufficiently unlikely to be significant is not computed; rather the absolute value of the minimum slope needed to pass threshold, which will be known as the threshold slope ($a_{thresh}$), is computed once and absolute values of the slopes computed from the data are compared to this threshold slope. The threshold slope is computed using the cumulative distribution function:

$$D(a_{thresh}) = \frac{1}{2}\left[1 + \mathrm{erf}\left(\frac{a_{thresh} - \mu_a}{\sigma_a\sqrt{2}}\right)\right] = \int_{-\infty}^{a_{thresh}} P(a'|\sigma_a, \mu_a)\mathrm{d}a' \tag{4.13}$$

where $D$ is the probability of measuring a slope between $-\infty$ and $a_{thresh}$ and $P$ is the normal probability distribution of slope measurements given $\sigma_a$ and $\mu_a$. Since the mean of this distribution is zero (since $\mu_a = 0$), $P$ is an even function with

respect to the measured slopes and comparing the absolute values of the slopes to the threshold slope is justified. $\Sigma$ is identified as the confidence that a measured slope is not accidental:

$$\Sigma = 2D - 1 = \text{erf}\left(\frac{|a_{thresh}|}{\sigma_a\sqrt{2}}\right) \tag{4.14}$$

Solving for $|a_{thresh}|$ yields the expression for the threshold slope:

$$|a_{thresh}| = \sigma_a\sqrt{2}\text{erf}^{-1}(\Sigma) \tag{4.15}$$

An example signal with thresholding illustrated is shown in Figure 4.6. Here, a cosine-Gaussian has been injected into a background of white noise and is shown in blue. The slope measurements are shown in red and the threshold slope shown in green. Any slope measurement above the top green line and below the bottom green line is a trigger. It can be seen here that the cosine-Gaussian has been well detected.

Defining the signal to noise ratio (SNR) as in Pradier, et al. [73]:

$$\text{SNR} = \frac{a}{\sigma_a} \tag{4.16}$$

we can also express $a_{thresh}$ in terms of a minimum SNR needed to pass threshold:

$$\text{SNR}_{thresh} = \sqrt{2}\text{erf}^{-1}(\Sigma) \tag{4.17}$$

Using probabilities to threshold SLOPE allows one to tune the threshold directly on false rates *before* the triggers are clustered. For example, $\Sigma = 0.99$ implies that there is only a 1% probability that a slope that passes threshold is accidental. Therefore, the expectation is to trigger on one window for every 100 windows SLOPE is applied. The number of windows is determined by the number of data points and the order:

$$W = N_{tot} - N + 1 \tag{4.18}$$

where $W$ is the number of windows and $N_{tot}$ is the total number of points in the

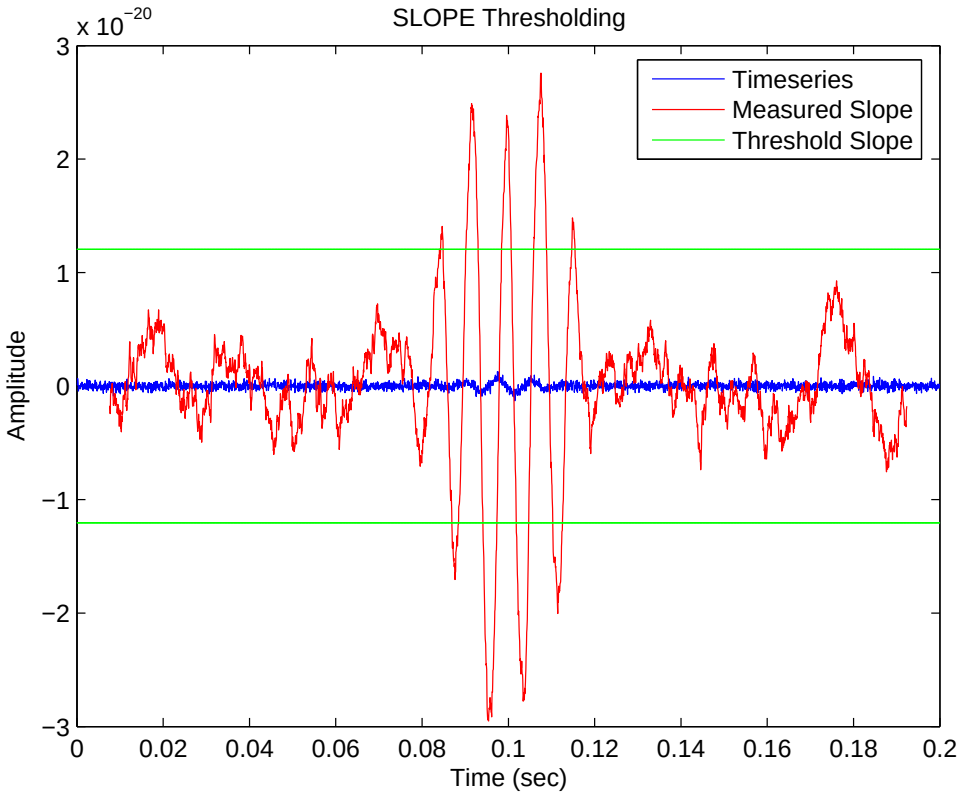


**Figure 4.6.** Illustration of SLOPE thresholding on a timeseries.

data set. Therefore, the expected number of triggers from this data set is:

$$N_{triggers} = (1 - \Sigma)(N_{tot} - N + 1) \tag{4.19}$$

This can then be expressed in terms of the expected accidental rate given the sampling frequency of the data:

$$\frac{\mathrm{d}N_{triggers}}{\mathrm{d}t} = (1 - \Sigma)\frac{N_{tot} - N + 1}{f_{data}} \tag{4.20}$$

### 4.4.2 Temporal Slope Clustering

When applying successive windows to the data, a phenomenon known as multi-windowing occurs. Multi-windowing is when a single anomaly may be triggered on multiple times by SLOPE because at least part of the trigger is included in multiple successive slope calculations. Therefore, slopes that have passed threshold

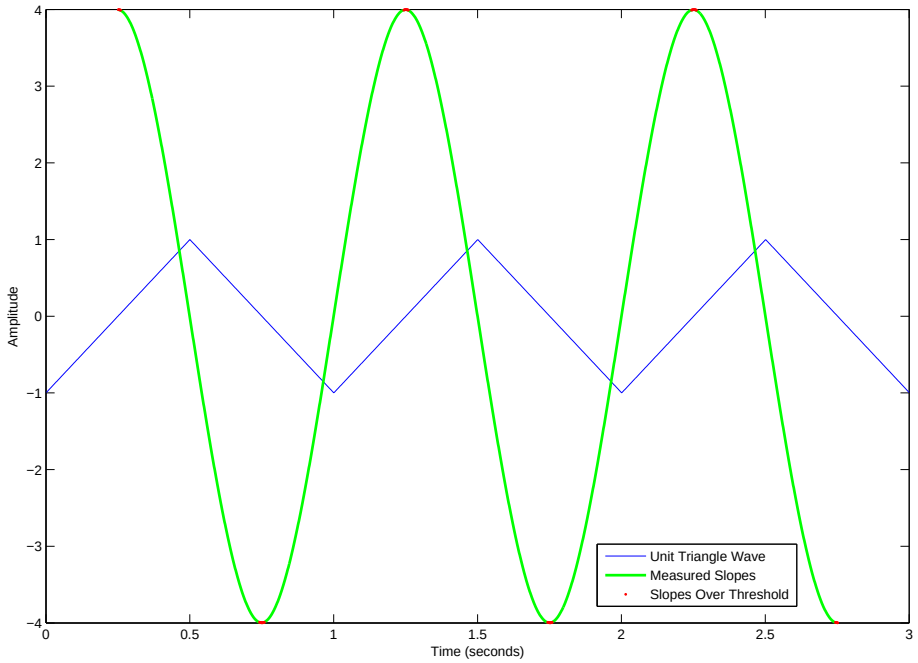


**Figure 4.7.** Unit triangle wave and measured slopes

are clustered together on the condition that they are separated by an order or less - any less and many shorter duration triggers are expected and any longer would risk clustering uncorrelated triggers together.

To justify the clustering criteria, consider running SLOPE with a unit amplitude and frequency triangle wave. Selecting an order equal to exactly half the period of the wave yields a maximum slope measurement of $a_{max} = 4$ (as in Figure 4.7). Assume that the entire data set, of which this waveform is a part, has a variance near:

$$\sigma_{data} = \frac{N(N^2-1)|a_{max}|}{12\sqrt{2}f_{band}^2 \mathrm{erf}^{-1}(\Sigma)} \tag{4.21}$$

This will make $|a_{thresh}|$ near $|a_{max}|$. It is clear, from inspection of the waveform, that the clustered slopes should encompass the entire duration of the triangle wave. This can only happen when the clustering distance is the same size as the order - any less and many shorter duration triggers are expected and any longer would risk clustering uncorrelated triggers together. A comparison between clustering within a full order and a half an order is shown in Figure 4.8.

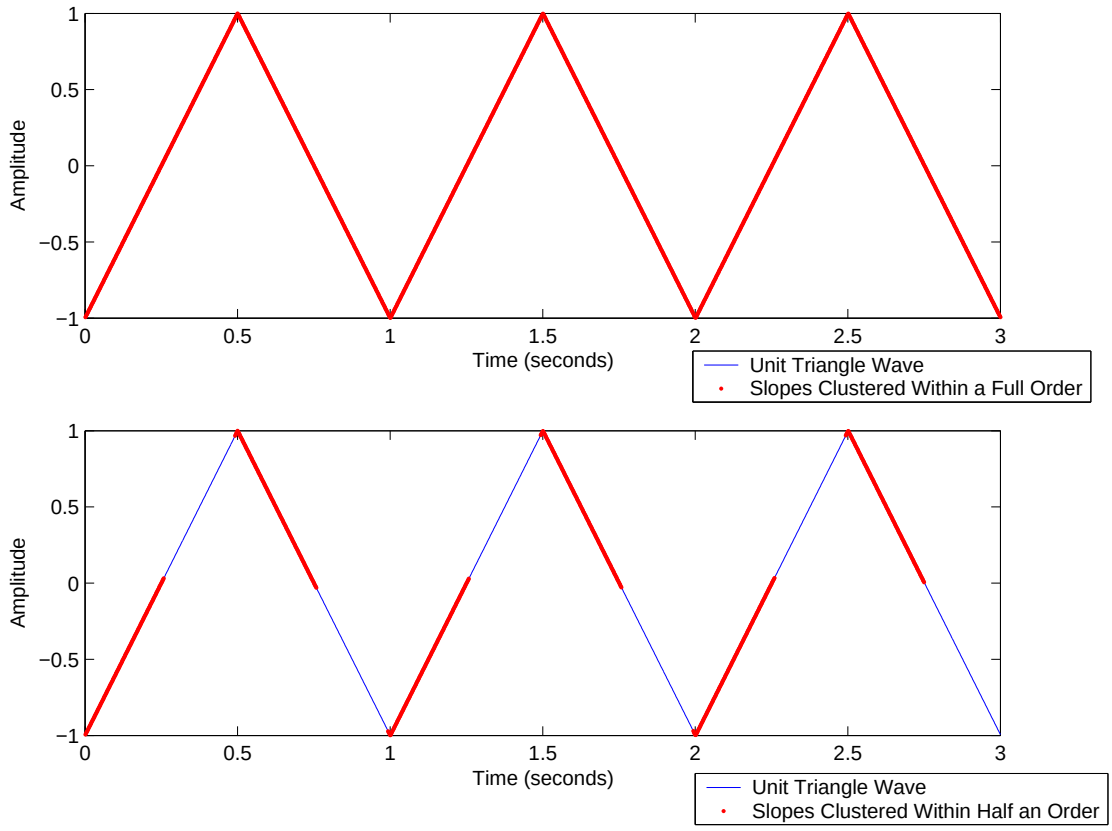


**Figure 4.8.** Unit triangle wave and clustered SLOPE triggers using the clustering criteria of a full order (top) and a half an order (bottom).

## 4.5 Tuning SLOPE on the S3 Playground Data Set

The criteria for tuning the SLOPE parameters ($\Sigma$ and $N$) on LIGO science data is to set an average trigger duration and an average accidental rate (also known as the false rate). To do this, SLOPE was run over an evenly spaced subset of data from the third science data run (S3) called the playground data set (q.v. Appendix C). This data set is set aside for tuning ETGs such as SLOPE and is not included in the science analysis after the ETG parameters are set, just as had been done for S1 (q.v. Section 4.2). Any triggers from this data set are assumed to be accidental.

In order to determine the average duration of triggers and the false rate from this playground data set, SLOPE was run on the data iteratively for many combinations of $\Sigma$ and N ($\Sigma$: 20 logarithmic spacings between 1 and 0.01, $N$: 100 linear

spacings between 2 and 102). The average duration results for the playground triggers are shown in Figure 4.9 and the average trigger rate results are shown in Figure 4.10.

With this information, parameter sets that met the desired average duration of between 20 ms and 40 ms and an average false rate of between 0.25 triggers per second and 0.75 triggers per second were selected. These parameter sets are shown in Figure 4.11.

Of the parameters that met all of the tuning criteria, the $\Sigma$ and N that best matched the BlockNormal trigger duration and false rate (q.v. Section 3.4) were selected. A $\Sigma$ of 0.99 and an $N$ of 4 were selected and yielded an average trigger duration of about 0.0214 s and an average trigger rate of about 0.313 triggers per second.

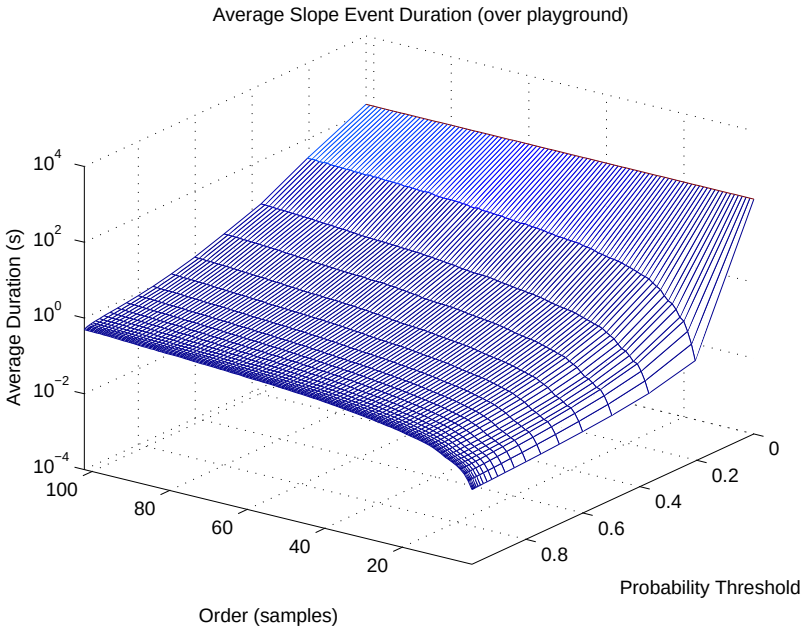


**Figure 4.9.** SLOPE trigger average duration, on the Hanford S3 playground between 512 Hz and 640 Hz, with respect to SLOPE order ($N$) and probability threshold ($\Sigma$).

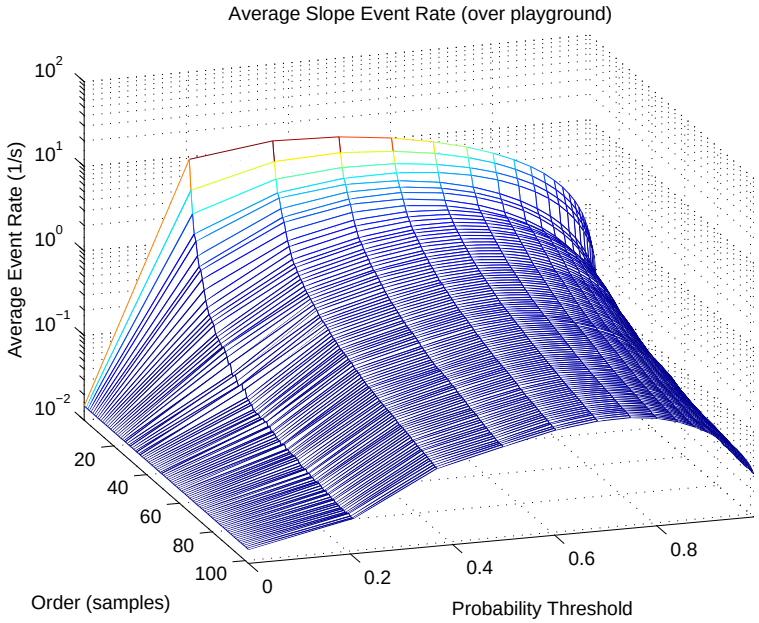


**Figure 4.10.** SLOPE trigger rate, on the Hanford S3 playground between 512 Hz and 640 Hz, with respect to SLOPE order ($N$) and probability threshold ($\Sigma$).

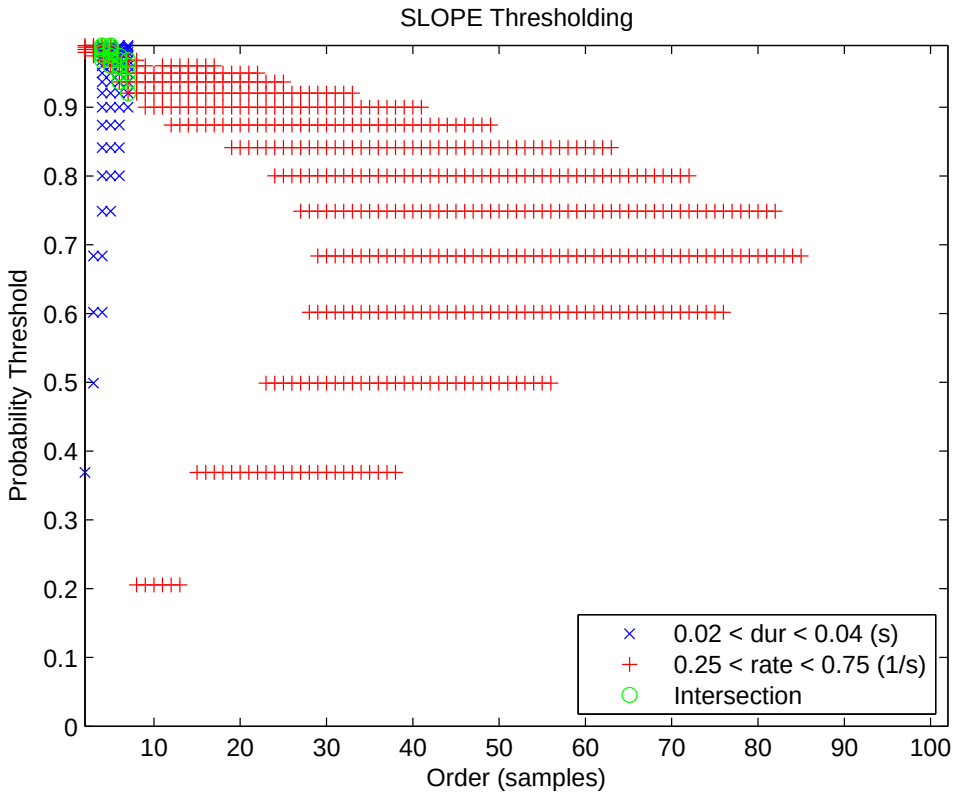


**Figure 4.11.** SLOPE order ($N$) and probability thresholds ($\Sigma$) that meet the criteria of having an average duration between 0.02 and 0.04 seconds and/or a rate between 0.25 and 0.75 Hz.

Chapter 5

# Q Pipeline

## 5.1 Introduction

BlockNormal and SLOPE are just a couple of the event trigger generators (ETG) that have been developed by LIGO in pursuit of burst gravitational wave detection. This chapter outlines another of the prominent ETGs that are currently applied called Q Pipeline. This ETG is merely outlined here so that the fundamental theory of its application may be understood since I had no hand in the development of this ETG or in shaping its application. The Q Pipeline programs used in the investigations of the Chapters 6, 7 and 8 were taken directly from the work done by Shourov Chatterji and the following descriptions are adapted from his Ph.D. thesis [6]. The source code for this ETG is available for download from [74].

Both BlockNormal and SLOPE are examples of data analysis methods that operate solely in the time-domain in that they directly process timeseries data. There are also effective methods that incorporate analysis in the frequency-domain [75]. To that end, Q Pipeline is a multi-resolution time-frequency domain search for excess power in the detector output. First, the data are whitened using zero phase linear prediction (q.v. Section 5.2) and projected onto bases that are logarithmically spaced in frequency and Q (quality factor) and linearly in time (q.v. Section 5.3). Significant tiles are identified assuming white noise statistics and the most significant set of non-overlapping tiles are reported. This is the extent of the application of Q Pipeline in the investigations following since the investigations look at the output of the ETGs before any other processing of the triggers they produce

are performed. For the purpose of the investigations in this work, Q Pipeline is applied through the trigger identification in Section 5.4. When Q Pipeline is applied as the full data analysis pipeline that it is, multi-detector coincidencing and the rejection of false triggers are also performed (q.v. Section 5.5). This chapter concludes with a description of the parameters used by Q Pipeline and how it is tuned (q.v. Section 5.6).

Q Pipeline also differs from BlockNormal and SLOPE in that it incorporates a full data analysis pipeline starting from the conditioning of the data for analysis to multi-detector coincidencing. BlockNormal and SLOPE were both parts of a pipeline; Q Pipeline is a full-fledged data analysis pipeline. As such, it is more than a simple ETG which can be interchanged in a larger data analysis pipeline. In this description, the extent of its application and any special consideration for it is described.

## 5.2 Data Conditioning

The data conditioning step for Q Pipeline consists of applying a zero phase high-pass filter to the detector data and then whitening the data using zero phase linear prediction. Any time that filters are applied to data, a certain amount of dispersion results and is manifested as a relative timing error (which can be dangerous when applying multi-detector coincidencing to ETG triggers). Using a zero phase filter simply implies that the timing error is corrected for by convolving the data with the impulse response of the filter and then convolving the resulting data with the time reversed response of the same filter. The zero phase high pass filter removes the dominant low frequency noise in the data. Next, the data are whitened using zero phase linear prediction. Whitening seeks to remove the contribution of the environment and the detector to the data.

## 5.3 Discrete Q Transform

The discrete Q transform projects the whitened data onto bases of windowed sinusoids with constant quality factory, Q. The bases are chosen to cover a specific finite region of time, frequency and Q space so that the energy loss due to any

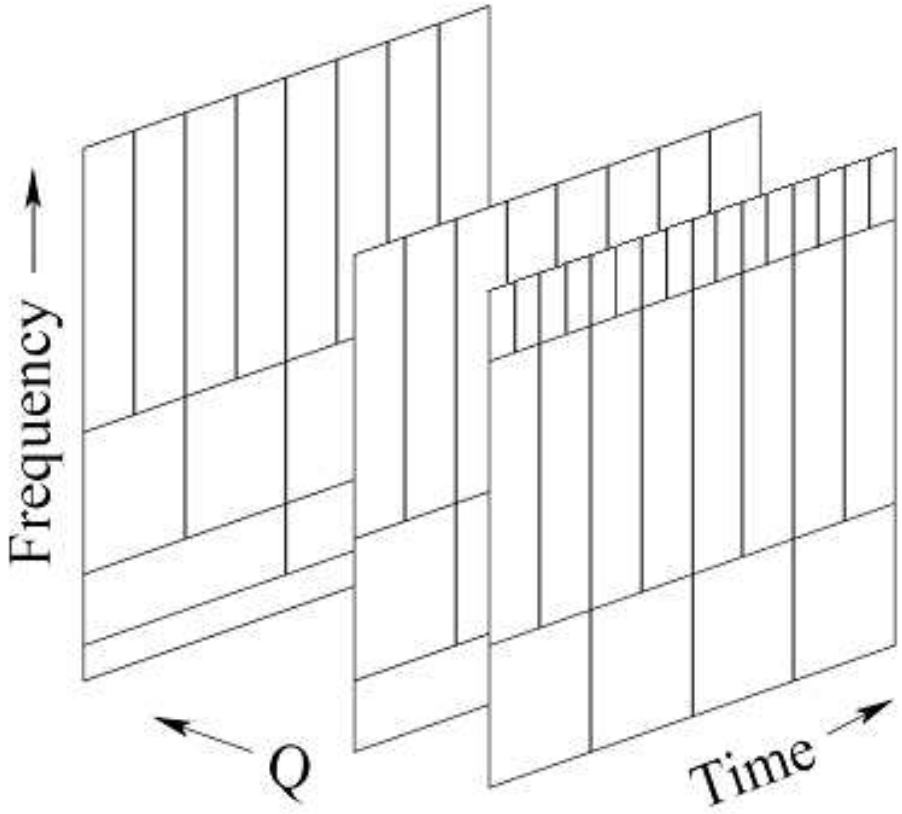


**Figure 5.1.** Illustration of the time-frequency domain bases onto which Q Pipeline projects a timeseries. These bases are logarithmically spaced in frequency and Q, and linearly in time. Image from [6].

mismatch between an arbitrary signal and a basis function is not greater than a specified amount and are logarithmically spaced in frequency and Q, and linearly in time. These bases are illustrated in Figure 5.1. A discrete time, frequency and Q region is known as a 'tile.'

Although there are considerations to be taken into account for the practical application of the discrete Q transform, the continuous Q transform illustrates the operation of the discrete version well. That is, the projection of the continuous time series $x(t)$ onto windowed complex exponentials of center frequency $\phi$ and quality factor $Q$ is given mathematically by:

$$X(\tau, \phi, Q) = \int_{-\infty}^{+\infty} x(t)\omega(t-\tau, \phi, Q)\exp(-i2\pi\phi t)\mathrm{d}t \tag{5.1}$$

where $\omega(t - \tau, \phi, Q)$ is a time-domain window centered on time $\tau$ with a duration that is proportional to $Q$ and inversely proportional to the frequency $\phi$ under consideration.

## 5.4 Trigger Identification

The mean energy for each tile in the base planes is calculated. The probability of measuring an energy greater than the measured energy for the tile is calculated based on a target false rate assuming the data being analyzed is stationary white noise. This threshold is applied to the Q transform tiles to produce the set of triggers for the data set.

It is common for the set of triggers produced to result in multiple overlapping tiles that pass the thresholding to generate triggers. Therefore, only the most significant of overlapping triggers are selected to provide the best parameterization of localized transients within the targeted range of time, frequency and Q.

## 5.5 Candidate Event Identification

The single detector triggers of multiple detectors are compared for a potential time coincidence given the expected time of flight of a gravitational wave between the detectors. Coincident triggers are then assigned a joint significance based on the assumption that the detectors have independent stationary white noise. Candidate events are then selected from these triggers based on the targeted false rate for coincident events. Nearby redundant events are excluded based on their joint significance. Finally, candidate events that coincide with times that auxiliary interferometer and environmental channels identify as times of likely data contamination are rejected. This decreases the probability of false identification of gravitational waves.

## 5.6 Parameters and Tuning

There are several parameters Q Pipeline needs before it can analyze data and these parameters are selected to have the same values as currently used in its practical

application on advice from this ETG's author. Most are relatively straightforward such as the data sampling frequency (16,384 sample/sec for LIGO), the Q range to investigate (4-64), the frequency range (512-640 Hz) and the duration of data segment to investigate at one time (64 seconds). Other parameters have more impact on the data analysis goals at hand: the minimum block overlap (10 seconds) specifies how much the blocks of data should overlap to remove data conditioning transients and still evaluate all of the data, the maximum mismatch parameter (0.2) specifies the fractional loss in squared signal energy due to mismatch and the outlier factor (2.0) specifies the Tukey whisker[1]multiplier used for outlier rejection.

Q Pipeline is a unique ETG in that it is self-tuning. BlockNormal and SLOPE need to be run over a subset of data with various parameter settings in order to determine the thresholds that best fit the data analysis goals. But for Q Pipeline, specifying a target false (accidental) trigger rate allows it to self-tune since it uses the probability of measuring an energy greater than a measured energy for a tile. Therefore, this ETG simply needs a target false rate specified without any laborious tuning investigations. For the investigations carried out in the rest of this thesis, Q Pipeline's false trigger rate was set to the average false rate of BlockNormal and SLOPE which is 0.313 triggers per second (q.v. Sections 3.4 and 4.5).

[1]The Tukey whisker is derived from the box-and-whisker plot which draws a box between the first and third quartiles of a distribution, marks the statistical median within it and then draws whiskers to identify outliers. 'Whiskers' are lines that are drawn from the ends of the box to the farthest points that are not outliers, usually defined by $\frac{3}{2}$ of the range spanned by the box [76, 77, 78].

Chapter 6

# Analysis I: Characterization of the Strongest Accidental Triggers

The investigations described in this chapter seek to determine if the event trigger generators (ETGs) described previously give fundamentally equivalent results. Since the theory applied in each is different, one can think of each ETG as a different set of spectacles with different lenses. If each set of spectacles are equivalent, then they should see the same things in the same way. Similarly, if each ETG is equivalent, then they should detect the same triggers in the same way. The observations and conclusions of this chapter and those following are important for the LIGO collaboration to address since, if one or more of the ETGs are equivalent, the parallel application of them on data would be redundant and wasteful of the limited available computer resources. But if they are not equivalent, then the common characteristics of the strongest accidental triggers need to be known.

This chapter seeks to identify if the strongest accidental (false) triggers on LIGO science data from each ETG are the same or similar and, if they are not, what differences exist between them. Section 6.1 outlines the methodology used to generate the strongest accidental triggers. The temporal location of the top 10 triggers within each data segment is discussed in Section 6.2 followed by an evaluation of the strongest triggers' timeseries as ranked on entire dataset in Section 6.3. Since no equivalence is established between the ETGs at this level, a comparison of the triggers that were identified by multiple ETGs is undertaken in Section 6.4. Finally, the observations made through this investigation are summarized in

Section 6.5.

## 6.1 Methodology

Each ETG was used to analyze a subset of evenly spaced data segments from the third LIGO science data run (called S3, which took place between October 31, 2003 and January 9, 2004 [43, 79, 80]) ranging between 300 seconds and 600 seconds in duration. This data set is called the S3 playground data [81] and is cataloged in Appendix C. It is assumed that there are no or very few gravitational wave events contained in this data set and that all of the triggers produced by the ETGs are accidental. Only data from the LIGO Hanford, WA 4 km interferometer were analyzed in the frequency band between 512 Hz and 640 Hz. Other detectors and frequency bands were not analyzed since a fundamental equivalence of ETGs is assumed not to be detector or bandwidth dependent. The data were conditioned as appropriate for the ETG and each ETG was *tuned using the specific criteria used in its current practical application.* This choice of tuning is important since it is of the most interest to LIGO and, as will be seen in Section 7.4, the choice in tuning can significantly impact an ETG's performance. Each data segment was then processed by each ETG. A measure of trigger strength was given to each trigger based on the criteria each ETG uses to identify a trigger: relative excess power of a trigger compared to the larger data set for BlockNormal , energy (measured as the root-sum-squared of the slopes within a trigger for SLOPE and normalized energy for Q Pipeline. The triggers from each ETG and data segment are then ranked based on this strength and a large number of these triggers (greater than or equal to the total number of strongest triggers that are of interest to investigate from the entire S3 playground data set) are admitted to the larger pool of triggers from all data segments. The strongest triggers from all of the data segments are then ranked against each other based on their strength. These triggers are investigated by comparing the temporal locations of the strongest triggers identified within a signal data set, by comparing the timeseries characteristics of the strongest triggers from all of the data segments and then by comparing the ranks between ETGs for triggers that multiple ETGs identified.

123 S3 playground data segments (also known as *locks*) were analyzed and the

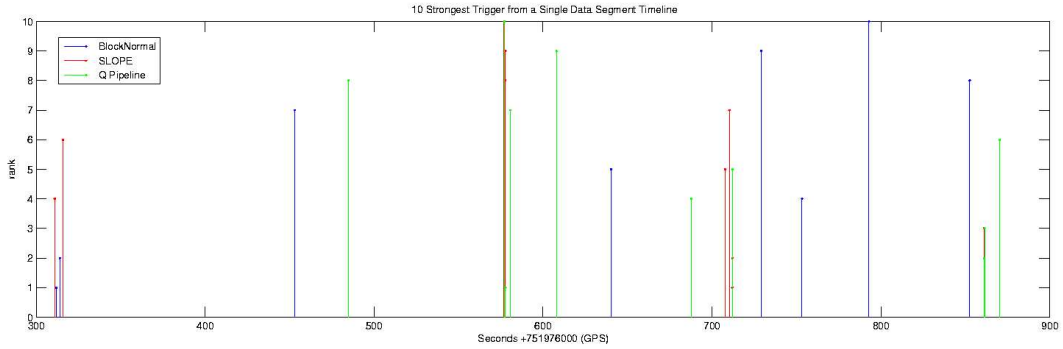


**Figure 6.1.** Timeline of the top 10 strongest triggers from a single data segment for BlockNormal, SLOPE and Q Pipeline.

100 strongest triggers from each data segment were admitted for consideration (S3 playground segment GPS times are listed in Appendix C). Every data segment contributed the maximum 100 strong triggers from each ETG for a total pool of triggers for consideration being 12,300 triggers for each ETG.

## 6.2 Temporal Location of Strongest Triggers

Investigating the temporal location of the strongest triggers from each of the ETGs will give a very preliminary answer to the question of equivalence between the methods. If the ETGs are indeed fundamentally equivalent, it is expected that a trigger by one ETG would be seen by the others and its strength would be ranked roughly the same between them.

Figure 6.1 shows the temporal locations of the strongest ten triggers from a single data set as measured by each ETG and is representative of the results from all of the playground data segments. The height of the stem for each trigger indicates the rank of the trigger, 1 being the strongest trigger and 10 being the $10^{\text{th}}$ strongest trigger. As is evident here, the ETGs usually do not identify the same triggers in the same way. For example, there is a cluster of 7 triggers around the GPS time of 75198177 containing BlockNormal, SLOPE and Q Pipeline triggers. However, the range of ranks runs the gambit of 1 through 10 and, even though these triggers are closely spaced, there is no overlap of triggers between ETGs. That suggests that, while there is likely some noise artifact in this area that caused this

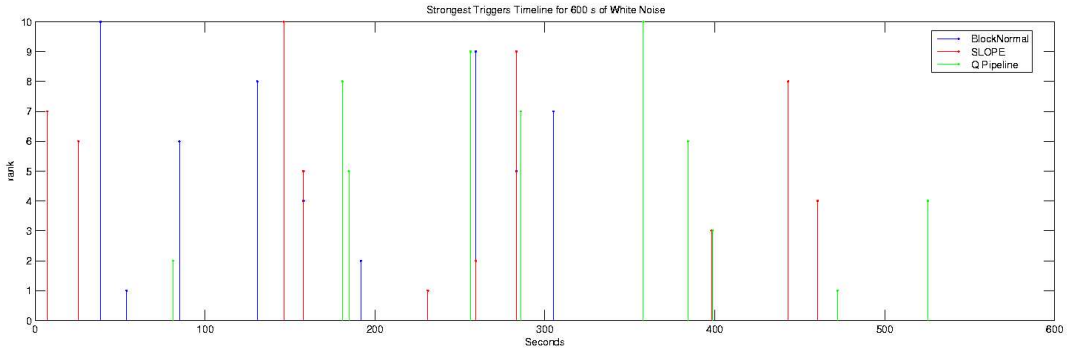


**Figure 6.2.** Timeline of the top 10 strongest triggers from a single white noise data segment for BlockNormal, SLOPE and Q Pipeline.

cluster of triggers, the ETGs did not process it equivalently. Looking at all of the strongest triggers from this data segment shows that, while there are clusters of triggers around certain times, there are isolated triggers. It is especially true of BlockNormal and Q Pipeline. This suggests that the ETGs do not identify the same triggers in the same way.

This investigation was also performed on simulated data sets composed of only white noise of zero mean and unit variance to see if the ETGs would still identify different strong triggers. Figure 6.2 shows the temporal locations of the strongest ten triggers from a single white noise data segment and is representative of the results from the other simulated data segments. As can be seen here, the observation made for Figure 6.1 that the ETGs do not identify the same triggers in the same way is also valid in the case of data composed of only white noise and therefore implies that this phenomenon is not a behavior specific to the data set being considered.

## 6.3 Timeseries Comparison of Strongest Triggers

With the apparent nonequivalence of the ETGs on short time scales, the question is raised as to whether or not this phenomenon is observed over longer timescales. That is, for the triggers that are ranked to be among the strongest single ETG triggers from the entire playground data set, do the other ETGs identify similar triggers as strong? To answer this question, the timeseries of the strongest triggers

from each ETG are characterized.

### 6.3.1 BlockNormal

The strongest BlockNormal triggers tend to be localized around times of rapid, sudden changes that are easily picked out of the data stream by eye. These triggers will colloquially be called 'glitches' since such triggers are almost certainly instrumentally induced. The triggers are often isolated (within the $\pm$ 1 second neighborhood of the trigger) but when they are not, these strongest triggers were also obviously stronger than the other 'glitches' in the neighborhood. These strongest triggers also tend to have greater absolute values of the local maximum of the trigger than the absolute value of the local minimum of the trigger. All together, these observations point to an overall greater mean of the strongest triggers compared to the whole data set as well as a larger variance. The power spectral densities (PSDs) of the triggers as well as the larger data set it was drawn from were calculated. Due to the short duration of the triggers yielding ill-defined PSDs, the PSD of the triggers' $\pm$1 second neighborhood was calculated. Even then, the resolution of the trigger's PSD was not sufficient enough to reveal any significant differences from the larger data set. (The top three BlockNormal triggers (in red) are shown in Figures 6.3, 6.4 and 6.5.)

### 6.3.2 SLOPE

The strongest SLOPE triggers were longer in duration than the BlockNormal triggers. Whereas the strongest BlockNormal triggers had a short impulsive quality to them, the strongest SLOPE triggers have a more defined evolution. They tend to quickly grow in amplitude and then immediately decay; they are much stronger than anything else in the $\pm$ 1 second neighborhood and are almost always isolated within that neighborhood. The absolute value of the local minimum of the trigger is often greater than the absolute value of the trigger's local maximum. These observations suggest that the mean of the strongest triggers will tend to be negative and have a larger variance than the larger data set. Again, due to the short duration of the strongest triggers, neither the PSDs of the trigger nor the $\pm$ 1 second neighborhood of the trigger were well enough resolved to reveal any

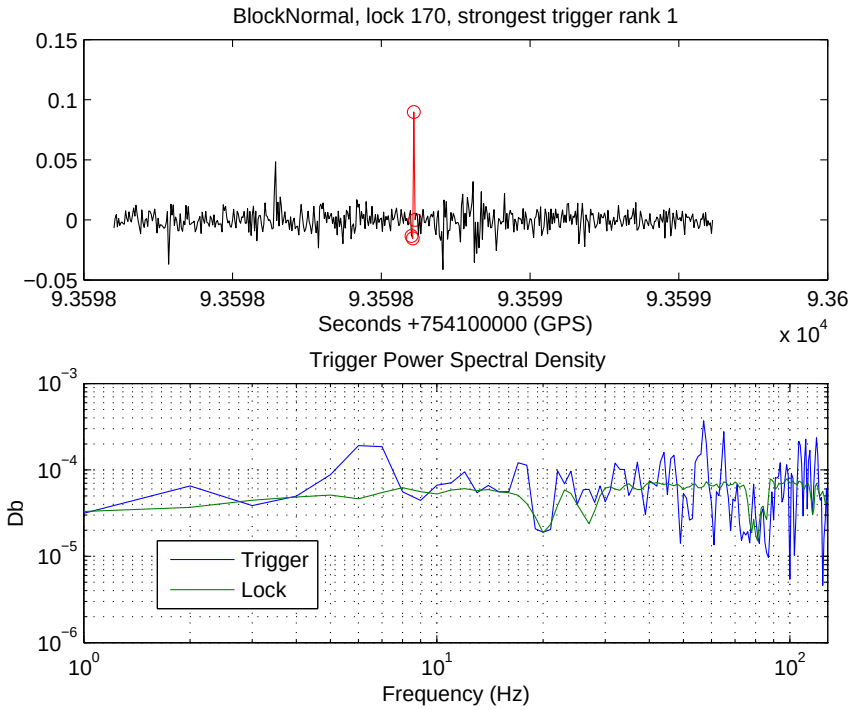


**Figure 6.3.** Strongest BlockNormal trigger from all S3 playground data segments.

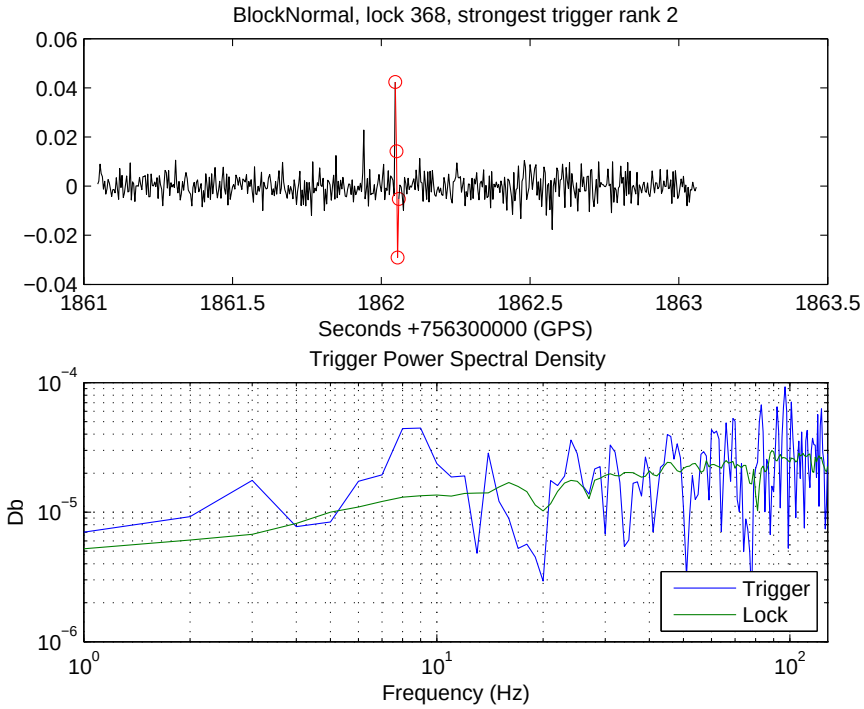


**Figure 6.4.** Second strongest BlockNormal trigger from all S3 playground data segments.

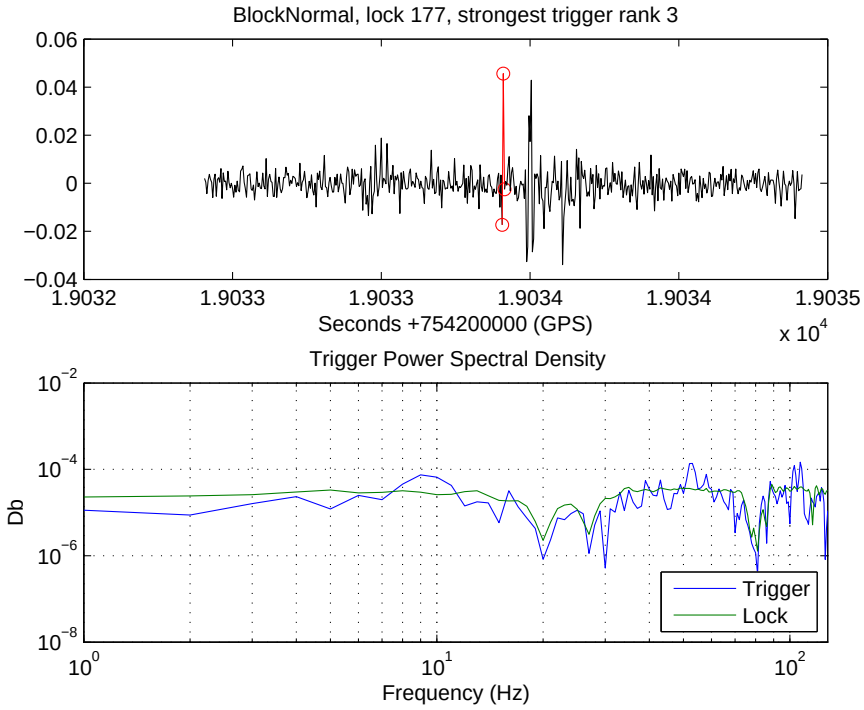


**Figure 6.5.** Third strongest BlockNormal trigger from all S3 playground data segments.

significant differences from the larger data set. (The top three SLOPE triggers (in red) are shown in Figures 6.6, 6.7 and 6.8.)

### 6.3.3 Q Pipeline

Characterizing the timeseries of Q Pipeline triggers is a bit more complicated than for BlockNormal and SLOPE since Q Pipeline triggers are determined in the frequency-domain. These triggers do not have a well-defined duration, but the central time of the triggers is reported. The strongest Q Pipeline triggers within the neighborhood are easily picked out by the eye as being different from the rest of the data; these times will again be referred to as 'glitches.' The reported time usually does not coincide with the maximum or minimum of the glitch but shortly after the peak. The resolution of the PSD of the neighborhood around the reported trigger time did not have sufficient resolution to reveal any differences from the larger data set. (The top three Q Pipeline triggers (in red) are shown in Figures 6.9, 6.10 and 6.11.)

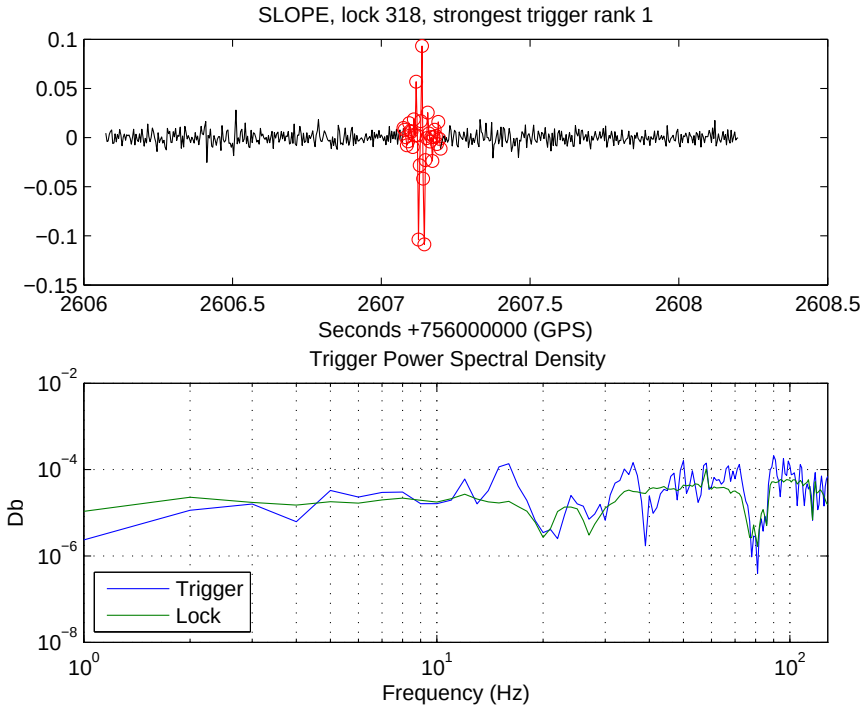


**Figure 6.6.** Strongest SLOPE trigger from all S3 playground data segments.

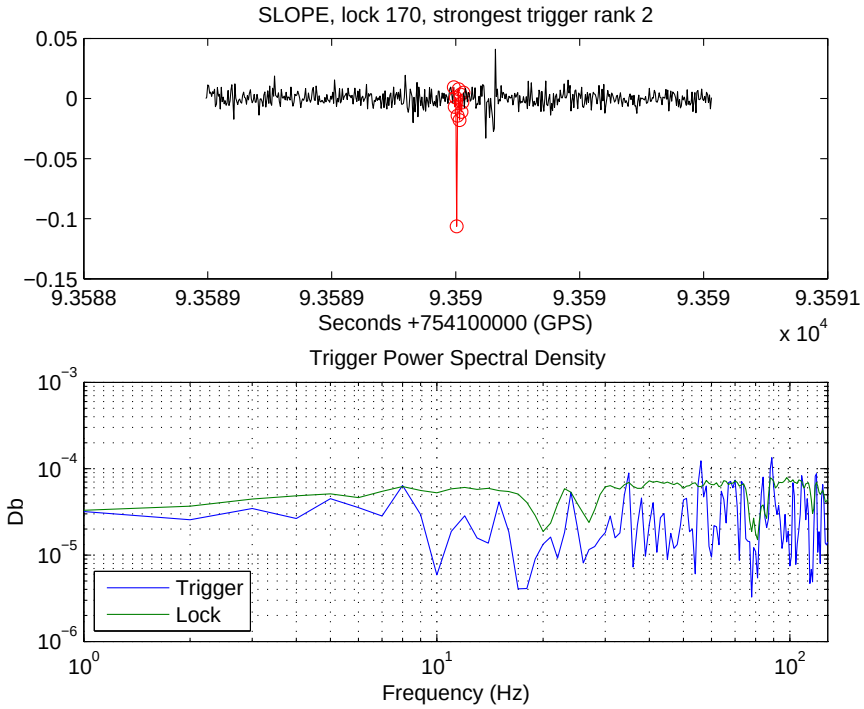


**Figure 6.7.** Second strongest SLOPE trigger from all S3 playground data segments.

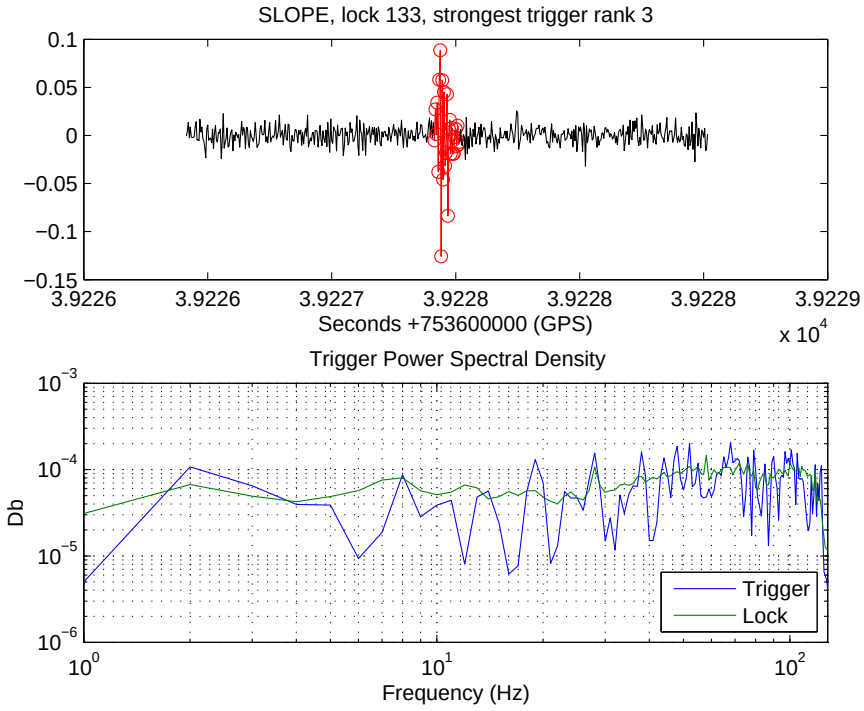


**Figure 6.8.** Third strongest SLOPE trigger from all S3 playground data segments.

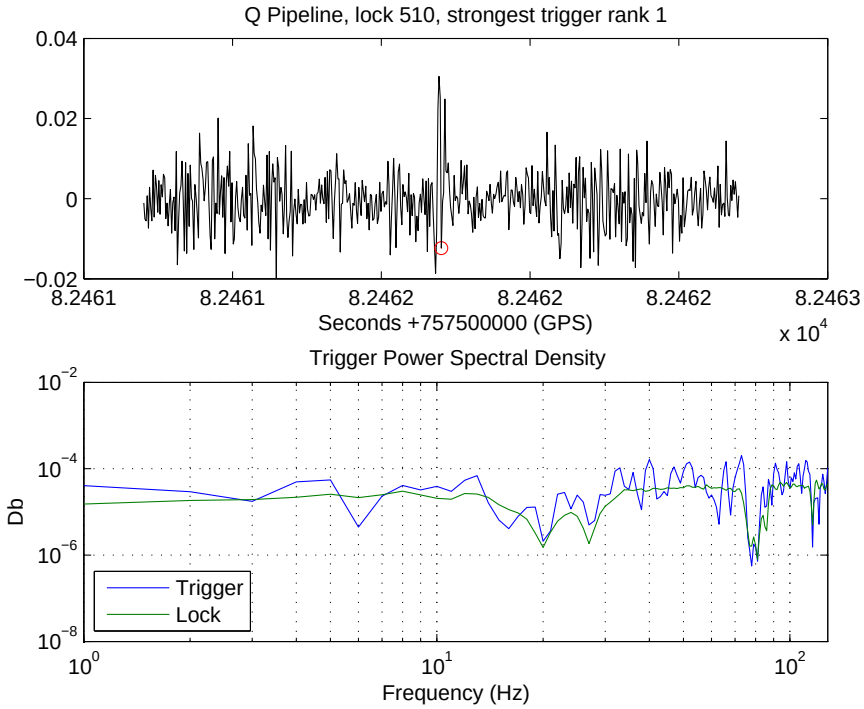


**Figure 6.9.** Strongest Q Pipeline trigger from all S3 playground data segments.

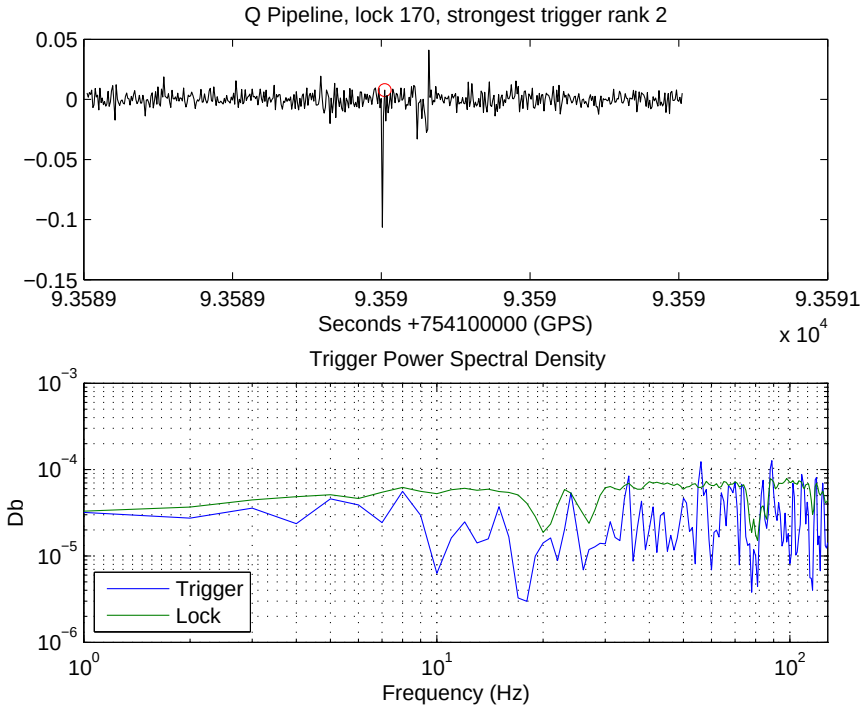


**Figure 6.10.** Second strongest Q Pipeline trigger from all S3 playground data segments.

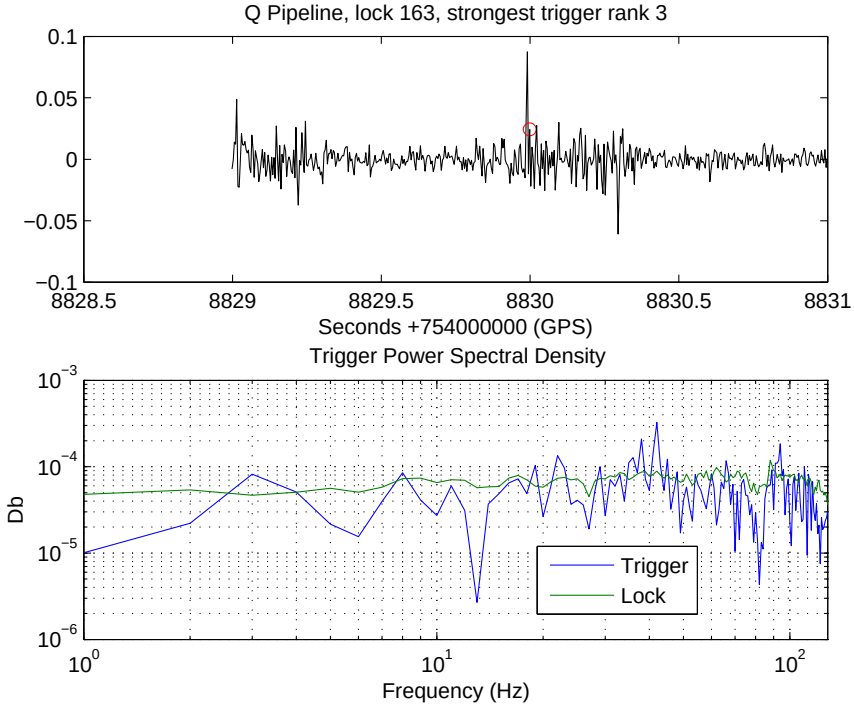


**Figure 6.11.** Third strongest Q Pipeline trigger from all S3 playground data segments.

The mean and variance from the strongest 10 triggers for BlockNormal and SLOPE are summarized in Table 6.1. Because Q Pipeline is a frequency-domain ETG and does not have a well-defined trigger duration, the mean and variance of the trigger in the time-domain is not well defined.

| **10 Strongest Triggers** | BlockNormal | SLOPE | Q Pipeline |
|---|---|---|---|
| Average duration | 15.625 msec | 101.2 msec | N/A |
| Average mean | $6.2151 \times 10^{-3}$ | $-9.5922 \times 10^{-4}$ | N/A |
| Average variance | $1.0776 \times 10^{-3}$ | $8.8155 \times 10^{-4}$ | N/A |

**Table 6.1.** Characteristics of the data within the 10 strongest triggers from all playground data segments (since Q Pipeline is a frequency-domain ETG, the duration of a trigger is not well defined, and therefore neither is the mean or variance of the trigger). The average mean and variance of all of the playground data sets is $8.4369 \times 10^{-7}$ and $3.4959 \times 10^{-5}$, respectively.

Again, these observations also apply to the strongest triggers produced on pure white noise (q.v. Appendix D for complete documentation).

## 6.4 Rank Comparison of Triggers Identified by Multiple ETG's

Since there are no specific obvious similarities or differences in the timeseries properties of the strongest ETG triggers, any correlation between the triggers that were detected by two or more ETGs is investigated. To do this, consider the top 100 triggers produced by each playground data segment and identify any triggers between the ETGs that share at least one data sample in common. When one trigger is identified as also being a trigger in another ETG, the data segment number is recorded along with the rank *as measured within a single data segment* by each ETG. If there is an equivalence between the ETGs on this level, the rank of the multiply detected triggers will be roughly the same in each ETG, producing a clustering along the diagonal of a scatter plot of the rank in one ETG to the rank in another.

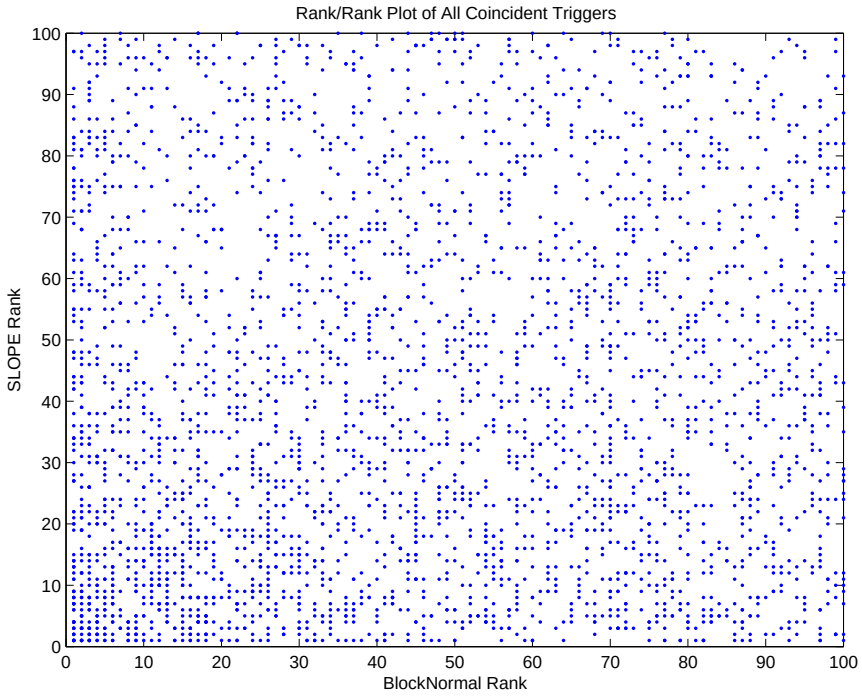


**Figure 6.12.** Scatter plot showing the rank of a 2-ETG trigger detected in the BlockNormal ETG to the rank as detected in the SLOPE ETG. There is a total of 3172 2-ETG triggers between BlockNormal and SLOPE.

### 6.4.1 2-ETG Triggers

First, let us consider the triggers that were detected by two of the three ETGs. These triggers will be referred to as 2-ETG triggers. Figure 6.12 shows the scatter plot of the rank of BlockNormal 2-ETG triggers to the rank of the corresponding SLOPE 2-ETG triggers. Similarly, Figure 6.13 shows the scatter plot for the 2-ETG triggers for BlockNormal and Q Pipeline and Figure 6.14 for SLOPE and Q Pipeline 2-ETG triggers.

Two observations are readily made: there is no clustering along the diagonal of these plots to suggest an equivalence between the ETGs and there are many more triggers that both BlockNormal and SLOPE identified compared to those that Q Pipeline and BlockNormal or Q Pipeline and SLOPE identified. This is attributed to the fact that there is not a well-defined trigger duration from Q Pipeline since it analyzes data in the frequency-domain. Therefore, the triggers it produces are only a single time sample and have a smaller chance of being coincident with a trigger from another ETG. The fraction of triggers that are coincident with another ETG

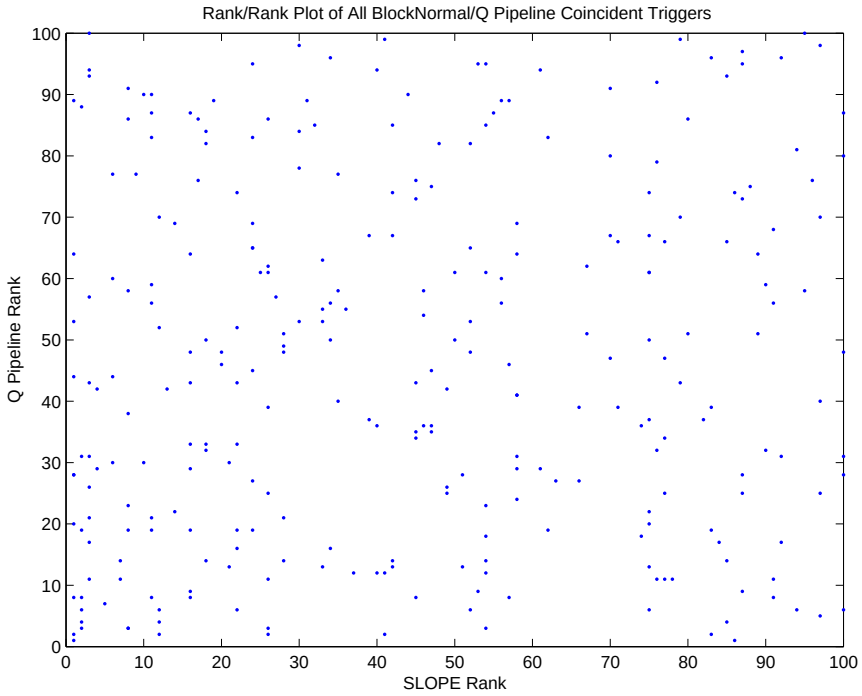


**Figure 6.13.** Scatter plot showing the rank of a 2-ETG trigger detected in the BlockNormal ETG to the rank as detected in the Q Pipeline ETG. There is a total of 288 2-ETG triggers between BlockNormal and Q Pipeline.

is summarized in Table 6.2.

| **2-ETG Triggers** | Fraction of total triggers | Total triggers |
|---|---|---|
| BlockNormal and SLOPE | 0.2579 | 3172 |
| BlockNormal and Q Pipeline | 0.02341 | 288 |
| SLOPE and Q Pipeline | 0.04350 | 535 |

**Table 6.2.** Fraction of 2-ETG triggers between BlockNormal , SLOPE and Q Pipeline. The total number of triggers admitted from each ETG from all of the playground data segments is 12,300.

There does seem to be some correlation of rank between the SLOPE and BlockNormal 2-ETG triggers and SLOPE and Q Pipeline 2-ETG triggers. Specifically, it appears that the higher ranking (ranks closer to 1) a 2-ETG trigger is in SLOPE, the more likely it is to be seen by the other ETGs at any rank. Conversely, this implies that the lower ranking a trigger is in SLOPE, the less likely it is to be seen at all by the other ETGs. This is visually more pronounced when looking at the SLOPE and Q Pipeline 2-ETG triggers as shown in Figure 6.14. It is less obvious

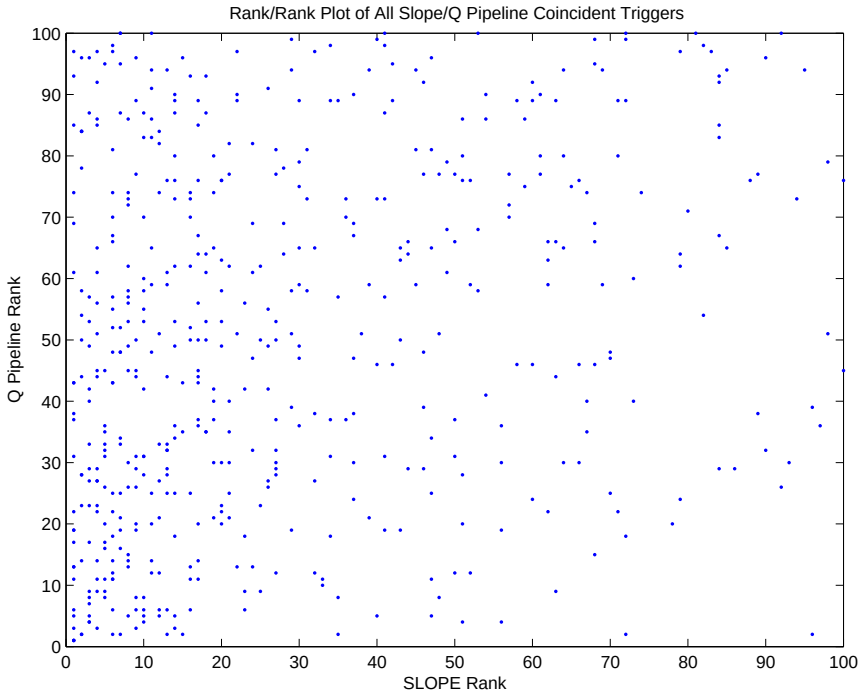


**Figure 6.14.** Scatter plot showing the rank of a 2-ETG trigger detected in the SLOPE ETG to the rank as detected in the Q Pipeline ETG. There is a total of 535 2-ETG triggers between SLOPE and Q Pipeline.

between SLOPE and BlockNormal 2-ETG triggers (Figure 6.12) because of the large number of these particular 2-ETG triggers lead to the 'stacking' of triggers with the same ranks between the ETG's - this is just a shortcoming of using a scatter plot to illustrate these triggers.

To test the strength of this correlation, the Spearman rank correlation coefficient [82] is calculated. The higher the absolute value of this coefficient, the stronger the correlation, while its sign represents a positive or negative correlation, i.e. a positive correlation would be observed when the number of 2-ETG triggers increases in another ETG as the SLOPE rank approaches 1 and a negative correlation when the number of 2-ETG triggers decreases in another ETG as the SLOPE rank increases.

To calculate this correlation, state the null hypothesis ($H_0$) for any given ETG and the correlation hypothesis that is to be tested ($H_1$):

> **$H_0$**: There is no correlation between the strength of a trigger in one ETG and it likelihood to be detected in another ETG.

$\mathbf{H}_1$: The stronger the trigger is in one ETG, the more likely it is to also be detected by another ETG.

To illustrate the methodology for calculating the Spearman rank coefficient, consider investigating the correlation between the strength of a SLOPE 2-ETG trigger to the number of times it was selected by another ETG at any rank. For every SLOPE rank, count the number of triggers that were also detected by BlockNormal or Q Pipeline. Then the number of triggers detected in BlockNormal or Q Pipeline is ranked (with rank 1 being the greatest number of triggers, 2 the next greatest and so on). This will be called the trigger number rank. If several SLOPE ranks have the same number of triggers in BlockNormal or Q Pipeline, then they receive the average rank of the trigger number ranks they span. The Spearman rank correlation coefficient is computed by comparing the SLOPE rank to the trigger number rank for BlockNormal and Q Pipeline.

The Spearman rank correlation coefficient $R^2$ is given by:

$$R^2 = 1 - \frac{6}{N^3 - N} \sum_{k=1}^{N} d_k^2 \tag{6.1}$$

$$R^2 \in [1, -1] \tag{6.2}$$

where $d$ is the difference between the SLOPE rank and trigger number rank, and $N$ is the number of SLOPE ranks. For this investigation, $N$ will always be 100. The variance in $R^2$ is given by:

$$\sigma^2 = \frac{1}{X - 1} \tag{6.3}$$

where $X$ is the number of 2-ETG triggers being considered. Therefore, the error in the Spearman rank correlation coefficient will be estimated by the standard deviation, $\sigma$:

$$\sigma = \pm\sqrt{\sigma^2} = \pm\frac{1}{\sqrt{X - 1}} \tag{6.4}$$

Table 6.3 shows the Spearman rank correlation coefficient between the rank of an ETG (rows) and the number of times that rank is observed, with respect to another ETG, for each 2-ETG combination (columns). $\mathrm{H}_1$ is confirmed for SLOPE since the coefficients in the SLOPE row are significantly greater than the

coefficients in other rows.

| **2-ETG Correlation Coefficients** | BlockNormal & SLOPE | BlockNormal & Q Pipeline | SLOPE & Q Pipeline |
|---|---|---|---|
| BlockNormal | $0.5249 \pm 0.0178$ | $0.2018 \pm 0.0590$ | N/A |
| SLOPE | $0.8923 \pm 0.0178$ | N/A | $0.8319 \pm 0.0433$ |
| Q Pipeline | N/A | $0.2129 \pm 0.0590$ | $0.1234 \pm 0.0433$ |

**Table 6.3.** Spearman rank correlation coefficient between the rank of a 2-ETG trigger in one ETG (rows) and the number of times that rank is observed in another ETG for each 2-ETG combination (columns).

### 6.4.2 3-ETG Triggers

Finally, let us consider the triggers that were detected by BlockNormal, SLOPE and Q Pipeline. These triggers will be referred to as 3-ETG triggers. Figure 6.15 shows the scatter plot of the rank of the 3-ETG triggers in BlockNormal to their rank in SLOPE. Similarly, Figure 6.16 shows the 3-ETG trigger rank in BlockNormal to their rank in Q Pipeline and Figure 6.17 shows the same for SLOPE and Q Pipeline. There are 253 3-ETG triggers which are 2.057% of the triggers admitted by each ETG. However, there is a multi-triggering issue with Q Pipeline; that is, since Q Pipeline produces single points where the trigger is localized, there is a higher probability that there can be more than one Q Pipeline trigger contained in either a BlockNormal or SLOPE trigger. There are 233 unique 3-ETG triggers between BlockNormal and SLOPE and 253 unique 3-ETG triggers between BlockNormal and Q Pipeline, and SLOPE and Q Pipeline. Regardless, the small percentage of 3-ETG triggers compared to the overall number of triggers from each ETG reinforces that there is not an equivalence between the ETG in the triggers that they all identify.

Again, there is no clustering along the diagonals of these scatter plots to suggest that there is a correlation between the ETGs seen in the triggers that they all detect. However, there appears to be a similar correlation between the strength of a SLOPE 3-ETG trigger and the number of times it is detected in the other ETGs.

Table 6.4 shows the Spearman rank correlation coefficient between the rank of an ETG and the number of times that rank is observed, with respect to another

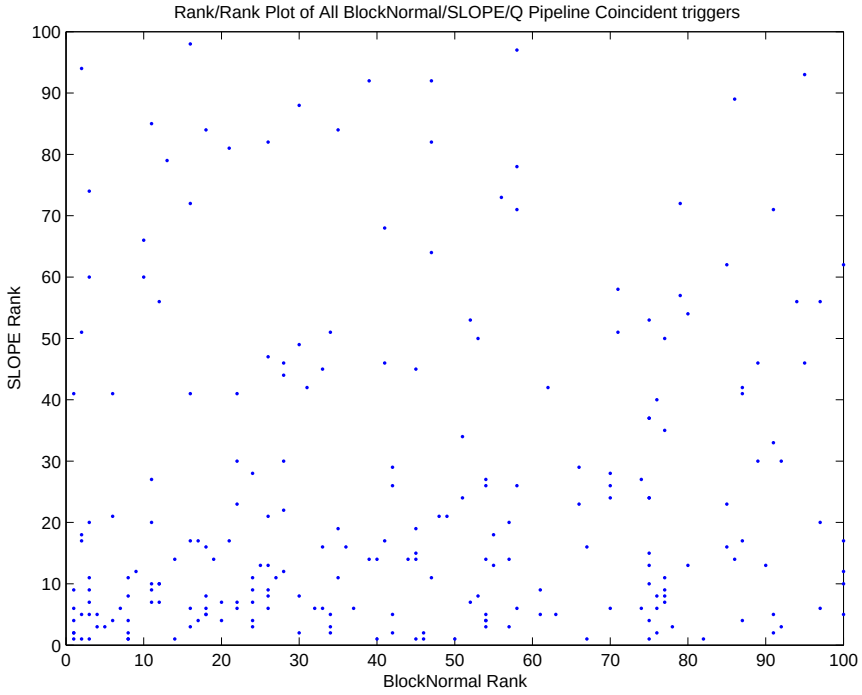


**Figure 6.15.** Scatter plot showing the rank of a 3-ETG trigger in the BlockNormal ETG to the rank as detected in the SLOPE ETG.

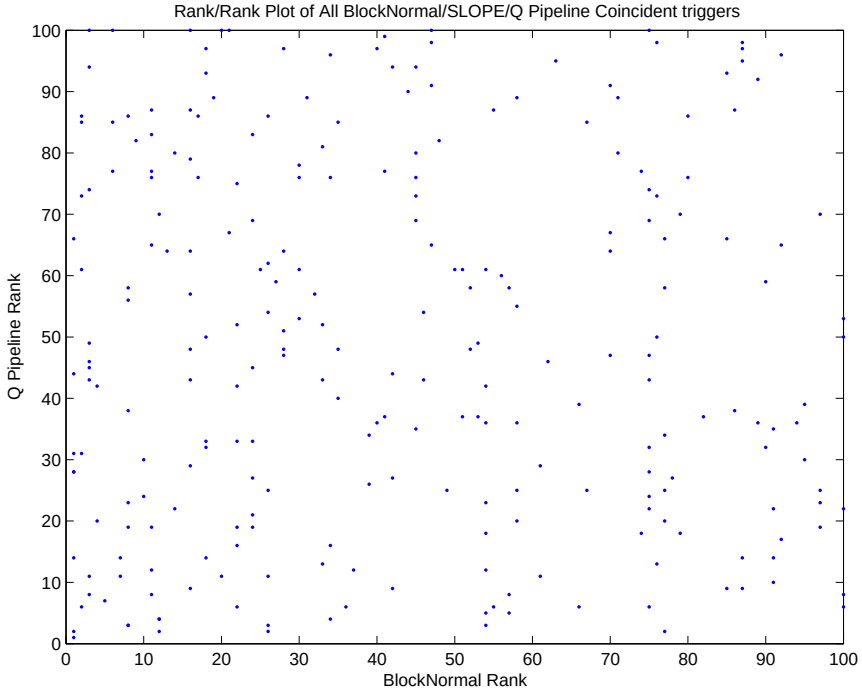


**Figure 6.16.** Scatter plot showing the rank of a 3-ETG trigger in the BlockNormal ETG to the rank as detected in the Q Pipeline ETG.

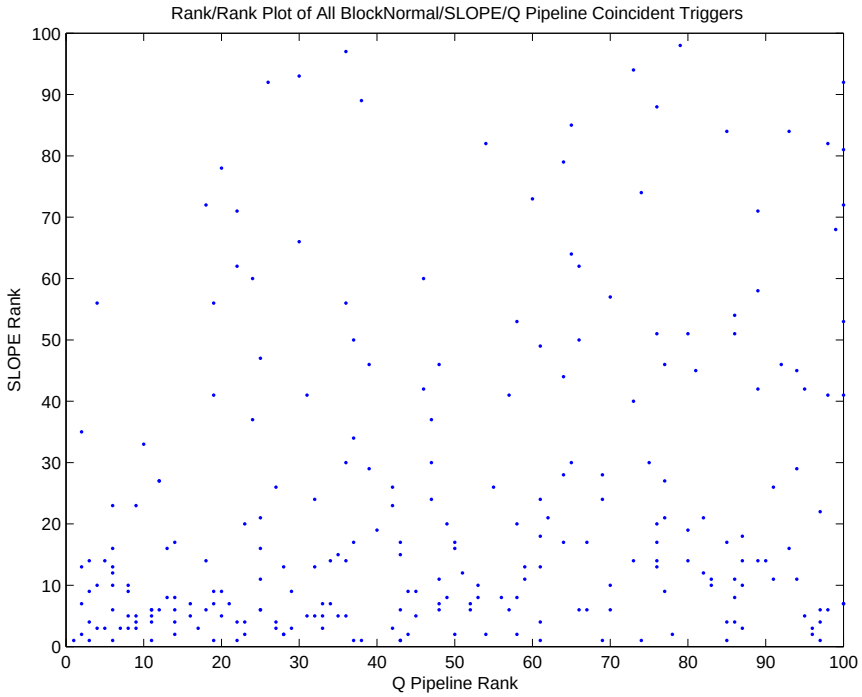


**Figure 6.17.** Scatter plot showing the rank of a 3-ETG trigger in the SLOPE ETG to the rank as detected in the Q Pipeline ETG.

ETG, for each ETG. These numbers represent the mean coefficient when the different combinations of unique 3-ETG combinations are calculated to account for the multi-triggers phenomenon of Q Pipeline. The coefficients used for each mean were all well within the standard error.

| BlockNormal | SLOPE | Q Pipeline |
|---|---|---|
| $0.2892 \pm 0.0657$ | $0.6608 \pm 0.0657$ | $0.1494 \pm 0.0630$ |

**Table 6.4.** Spearman rank correlation coefficient between the rank of an ETG and the number of times that rank is observed, with respect to another ETG, for 3-ETG triggers.

## 6.5 Observations

This investigation sought to determine if several LIGO burst ETGs were fundamentally equivalent in the strongest accidental triggers they produced even though each method used a different theory to process the data. Initial inspection of the temporal locations of the strongest triggers in individual data sets proved that the

ETGs will often identify different times for strongest triggers and even triggers from multiple ETGs that were localized around a specific time rarely overlapped in their trigger time or ranked the trigger with equivalent strength. Looking at the few triggers that each ETG identified as a top 100 trigger from an individual data segment, there is no fundamental equivalence between the ETGs in the strength that each ranked the trigger. However, there was a correlation between the strength of the trigger as SLOPE identified it to the likelihood that the trigger would be seen by other ETGs.

Chapter 7

# Analysis II: Characterization of the ETGs' Performance With Respect to Specific Signals

Since there were no obvious similarities or differences in the strongest trigger properties between the ETGs to suggest a fundamental equivalence, how each ETG performs with respect to specific signal properties such as signal type, frequency, amplitude and duration is investigated. This is done by taking a specific signal type, injecting it many times into base data for various amplitudes and durations and measuring the fraction of injected signals detected by an ETG. Comparing the results of the detection fraction from different signal types will yield more specific information on what signal properties each ETG favors.

Section 7.1 outlines the methodology used to measure the detection efficiency profiles (the detection fraction sampled at various amplitudes and durations). These profiles usually resemble sigmoid functions of amplitude. Two important parameters of a sigmoid are the 50% efficiency mark and the steepness of the transition region between the minimum and maximum efficiencies. These are discussed for the different ETGs in Section 7.2. These profiles are then further analyzed in Section 7.3 by applying them to an astrophysical population and numerically integrating the result. This volume represents the relative probability of detection of a signal from that population and gives a single quantity that can be used to compare ETG performances. Both the efficiency profiles and population compari-

son were also done on BlockNormal and SLOPE with an erroneous tuning. These results are shown in Section 7.4. Finally, this chapter concludes by summarizing the observations of this investigation in Section 7.5.

## 7.1 Methodology

For this investigation, simulated signals are injected into a base data of white noise with zero mean and unit variance. The reason for departure from actual LIGO science data is to avoid contamination from external instrumental sources in this efficacy investigation of an ETG's performance with respect to specific, well defined signal properties. A base of white noise allows for every aspect of this investigation to be controlled. This data is specified to have the same sampling frequency (256 samples/second) as the genuine LIGO data used in the strongest accidental trigger investigation and, since the data conditioning applied by each of the ETGs has a whitening component, the generic white base data does make for a reasonable idealization. Because this base data is already white, no data conditioning is performed by any of the ETGs.

There are three main categories of signals used in this investigation: non-impulsive white noise signals, non-impulsive single frequency signals and impulsive single frequency signals. The non-impulsive white noise signals are composed of Gaussian modulated white noise; the non-impulsive single frequency signals are Gaussian modulated sinusoids of a specific frequency and the impulsive single frequency signals are modeled as exponentially decaying harmonic oscillators with a specific frequency.

Injecting signals into data is a delicate undertaking especially when the thresholding of the data analysis methods depends on the properties of the data itself. Too many injected signals in a span of data will result in changing the way the ETGs see the larger data set as a whole so that the simulated signals look more and more like the background. Injecting signals into a background of white noise has two distinct advantages: 1) the true mean and variance of the base data is well defined and 2) as much data as is needed to insure proper spacing of the signals can be generated on-the-fly. This allows for the background mean and variance of the data to be forced to the base data mean and variance (making the smaller data

segment being analyzed by the ETG appear to be part of a larger data set) and avoids the need to iterate over a small piece of genuine data multiple times to inject the desired number of signals. Simulations are injected every 15 $\pm 1$ seconds for a total of 100 injections. The same ETG tuning is applied here as in the previous investigations.

While the base data does indeed change the performance of the tuning, the performance is proportional between the ETGs. For BlockNormal, the previous tuning gave a false trigger rate of 0.3122 triggers/sec and the new false rate on white noise data is 2.461 triggers/sec; for SLOPE the previous tuning gave a false trigger rate of 0.3131 triggers/sec and the new false rate on the white noise data is 2.1873 triggers/sec. The measured false detection fraction (the fraction of zero amplitude signals detected), $\alpha$ gives the probability that any one point will be within a false trigger and is estimated by the measured false trigger rate ($\frac{\Delta N_{trigger}}{\Delta t}$) and average trigger duration ($\bar{t}_{trigger}$):

$$\alpha = \frac{\Delta N_{trigger}}{\Delta t}\bar{t}_{trigger} \tag{7.1}$$

Since the average trigger duration is not measured through this investigation, it can be estimated from the measurement of $\alpha$ which is measured to be 0.0426 for BlockNormal and 0.0725 for SLOPE. This yields an average trigger duration of 0.0173 seconds for BlockNormal and 0.0332 seconds for SLOPE. This is not a large departure from the tuned performance of 0.0221 seconds for BlockNormal and 0.0214 seconds for SLOPE. Since Q Pipeline tunes itself based on a desired false rate, it was manually set to have a new false rate similar to the rates observed in BlockNormal and SLOPE at 2.169 triggers/sec.

For these investigations, the amplitude of a simulated signal is defined to be the root-sum-square (RSS) of the entire signal and is given by:

$$A_{RSS} = \sqrt{\int_{-\infty}^{\infty} |A(t)|^2} \tag{7.2}$$

where $A(t)$ is the timeseries of the simulation.

### 7.1.1 Non-impulsive, White Noise Signals

Gravitational wave bursts are from unanticipated sources of which there is little to no knowledge. Because of this, there is no reason to expect well-defined signal properties from a burst. Therefore, Gaussian modulated white noise will be used for a baseline ETG characterization of a simulated gravitational wave signal:

$$A(t) = A_0 \exp\left(-\frac{t}{\tau}\right)^2 \text{ multiplied by white noise} \tag{7.3}$$

where $A_0$ is the maximum desired amplitude of the simulated signal and $\tau$ is the Gaussian timescale. The $A_{RSS}$ is approximated the by RSS value of a pure Gaussian and is given by:

$$A_{RSS} = A_0 \sqrt[4]{\frac{\pi\tau^2}{2}} \tag{7.4}$$

### 7.1.2 Non-impulsive, Single Frequency Signals

With the baseline characterization of the ETGs to a signal with no specific frequency complete, how the ETGs perform to similar signals with a specific frequency is investigated. To do this, the ETGs' response to Gaussian modulated sinusoids (sine-Gaussians) with a frequency of 16 Hz and then 64 Hz will be characterized. These frequencies were chosen to investigate low frequency and mid-range frequency characteristics of the ETGs; since the sampling frequency of the base data is defined to be 256 samples/second, the Nyquist frequency (the frequency where aliasing becomes an issue) is 128 Hz.

The Gaussian modulated sinusoids of frequency $f$ are given by:

$$A(t) = A_0 \sin(2\pi f t) \exp\left(-\frac{t}{\tau}\right)^2 \tag{7.5}$$

The $A_{RSS}$ is then given by:

$$A_{RSS} = A_0 \sqrt[4]{\frac{\pi\tau^2}{8}} \tag{7.6}$$

### 7.1.3 Impulsive, Single Frequency Signals

Impulsive signals are of interest to gravitational wave data analysis since these signals are not only expected to approximate the waveform of a black hole ringdown but can also be instrumentally induced by a 'ringing' of a digital filter (e.g., if a calibration line as described in Section 2.7.1.1 were to suddenly fail to be actuated, there would be an impulse in the feedback loop of the interferometer that would induce a signal in the detector output similar to a damped harmonic oscillator). Again, low (16 Hz) and mid-range (64 Hz) frequencies are characterized.

The impulsive, single frequency signals are given by:

$$A(t) = A_0 \exp\left(-\frac{t}{\tau}\right) \cos(2\pi f t) \tag{7.7}$$

The $A_{RSS}$ is then:

$$A_{RSS} = A_0 \sqrt{\frac{\tau}{4} \frac{(2\pi f t)^2 + 2}{(2\pi f t)^2 + 1}} \tag{7.8}$$

## 7.2 ETG Detection Efficiency Profiles

Measuring the efficiency of a signal of varying amplitude and duration produces a three dimensional surface which can be compared between ETGs. These surfaces will be known as *efficiency profiles*. For BlockNormal and SLOPE, a detection is defined by a trigger overlap with the time of maximum simulation absolute amplitude; for Q Pipeline, detection is credited if the strongest trigger in $\pm 1$ second of the maximum simulation absolute amplitude is also within $\pm 0.1$ seconds of the simulation time of maximum absolute amplitude. In general, the shape of this surface is approximately a sigmoid function of amplitude with minor parameter changes with respect to duration. These parameters are the false detection fraction ($\alpha$), the maximum efficiency plateau ($\gamma$), the 50% detection efficiency ($A_{50}$) and the steepness of the approximately linear transition between $\alpha$ and $\gamma$ ($s$). These combine to form the detection efficiency sigmoid, $\epsilon(A)$:

$$\epsilon(A) = \alpha + (1 - \alpha)\frac{\gamma}{2}\left(1 + \tanh\left[s \ln\left(\frac{A}{A_{50}}\right)\right]\right) \tag{7.9}$$

For these investigations, amplitude is logarithmically sampled between 0.1 and

50 with 100 intervals and the exponential timescale, $\tau$ (signal duration), is linearly sampled between $7.5 \times 10^{-4}$ and 0.5 seconds with 50 samples. A baseline efficiency profile is established for each ETG using the Gaussian modulated white noise signals. These profiles are shown in Appendix E in Figures E.1 and E.2 for BlockNormal, in Figures E.3 and E.4 for SLOPE and in Figures E.5 and E.6 for Q Pipeline. For BlockNormal and SLOPE, the profile is roughly a sigmoid, with $\gamma$ approaching unity with respect to amplitude and over the entire duration range. However, Q Pipeline is roughly a sigmoid with $\gamma$ nearing unity for $\tau < 1$ but as $\tau$ increases the $\gamma$ decays to about 0.6 as $\tau$ approaches 0.5 seconds. The low detection fraction for all ETGs at extremely short durations ($\tau < 0.025$ seconds) regardless of amplitude is due to simulations that are only a few samples in duration which look more like random statistical fluctuations than candidate triggers.

Since none of these profiles is truly a sigmoid and curve fitting tools are too sensitive to these departures to give reliable parameter measurements, $\alpha$ is measured by determining the accidental detection fraction (by injecting signals with zero amplitude into the white noise background and measuring the fraction of detected signals), $\gamma$ is set to near unity by default, and $A_{50}$ and $s$ are derived from a linear fit to the central transition region, as a function of amplitude. The 50% detection fraction has been a standard performance measure for ETGs within the LIGO burst group and so the derived $A_{50}$ points for each signal type is plotted for each ETG along with plots of the sigmoid steepness, $s$. 3-dimensional surfaces and contour plots for each efficiency profile discussed in this section can be found in Appendix E.

### 7.2.1 BlockNormal

Figure 7.1 shows the measured $A_{50}$ for BlockNormal which had an observed false detection fraction ($\alpha$) of 0.0426. Here it is observed that the Gaussian modulated white noise simulations ('White') are comparable to the sine-Gaussian simulations ('SG16' and 'SG64') with a mid-range ($\tau = 0.25$ sec) $A_{50}$ of about 0.6. The impulsive signals ('BH16' and 'BH64') are also comparable to each other and have an $A_{50}$ that tends to be about 20% lower than the other signals at large $\tau$ with mid-range $A_{50}$'s of about 0.5. This implies that BlockNormal has a slight preference

to impulsive signals than those that have continuous waveforms. Overall, the $A_{50}$ increases as the signal duration increases (about 80% over the $\tau$ range of 0.05 to 0.5 seconds for the impulsive signals and about 128% for the Gaussian modulated signals) suggesting a moderate preference for shorter duration signals.

Another important component of the sigmoid is the steepness of its transition region. This describes how rapidly a signal's detection efficiency increases. Figure 7.2 shows the measured sigmoid slopes ($s$) for BlockNormal. In general, the lower the $A_{50}$ measurement, the greater the sigmoid slope, and vice versa. That implies that a signal with a low $A_{50}$ will have increased rapidly between its $\alpha$ and $\gamma$ and a signal with a higher $A_{50}$ will have a more gradual increase in detection efficiency. This is interesting because it implies that even though a signal may have a high $A_{50}$, it may still have a better efficiency at lower amplitudes than a signal with a lower $A_{50}$. Ultimately, it is seen here that the most significant difference between the Gaussian modulated signals (since there was not much difference in their $A_{50}$ performance) is the steepness of their sigmoid slopes. This also applies for the impulsive signals. Close inspection of the sigmoid slope plots shows that there is a slight difference in sigmoid slope steepness with respect to signal frequency. The higher frequency signals have steeper slopes, the lower frequency signals have shallower slopes and the broadband signal has about the average performance of the two frequencies.

### 7.2.2 SLOPE

Figure 7.3 shows the measured $A_{50}$ for SLOPE which had an observed false detection fraction ($\alpha$) of 0.0725. Here it is observed that the Gaussian modulated white noise simulations ('White') have a consistent average performance to the other signal types. The best performing signal type is the impulsive 64 Hz signals ('BH64') with a mid-range ($\tau = 0.25$ sec) $A_{50}$ of about 0.4 (about 33% lower than the baseline signal) followed by the sine-Gaussian signals of 64 Hz ('SG64') with an $A_{50}$ just about 17% lower than the baseline over the entire $\tau$ range. The next best performing signal type after the baseline is the impulsive 16 Hz signals ('BH16') with an $A_{50}$ just a few percent above the baseline followed but the sine-Gaussian signals of 16 Hz ('SG16') with an $A_{50}$ about 33% higher than the baseline over

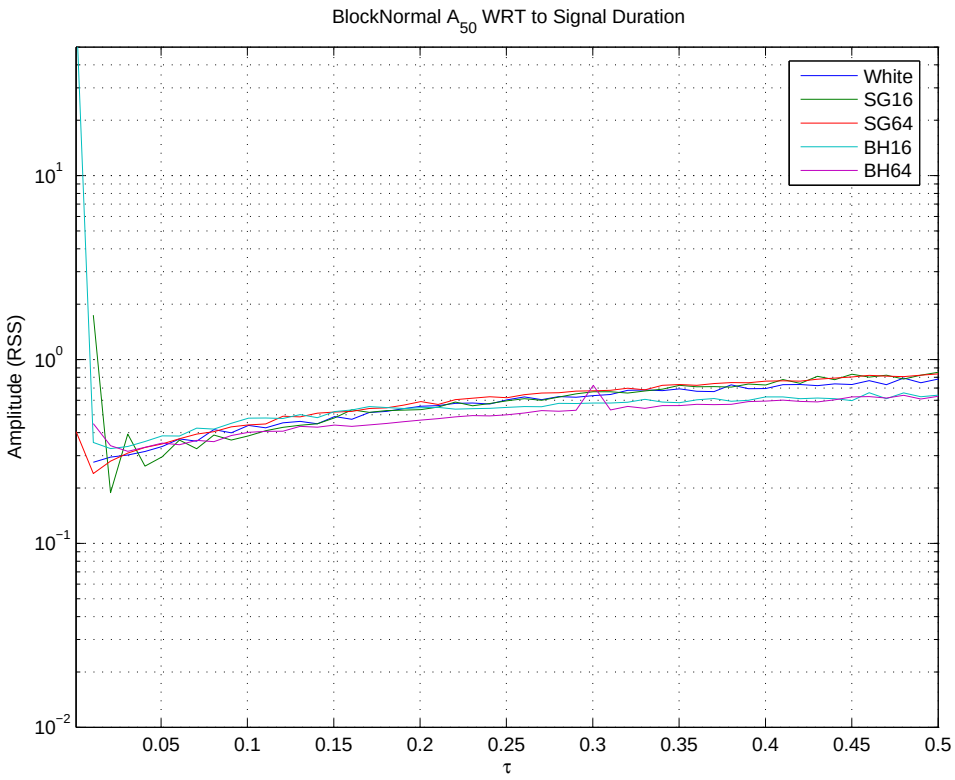


**Figure 7.1.** 50% efficiency curves for BlockNormal with respect to signal type, amplitude and duration.

the entire $\tau$ range. These observations suggest that SLOPE will have a lower $A_{50}$ for signals with higher frequency components and a higher $A_{50}$ for lower frequency components. Broadband frequency signals represented by the baseline Gaussian modulated white noise, will have an average performance of the high and low frequency performances. Regardless of signal frequency, SLOPE performs better to impulsive signals than those that have continuous waveforms. Overall, the $A_{50}$ increases as the signal duration increases (about 170% over the $\tau$ range of 0.05 to 0.5 seconds) suggesting a moderate preference for shorter duration signals.

Figure 7.4 shows the measured sigmoid slopes ($s$) for SLOPE. As was observed in the BlockNormal sigmoid slope measurements, the lower the measured $A_{50}$ results in a greater sigmoid slope measurement and the higher the frequency of the signal, the steeper its slope.

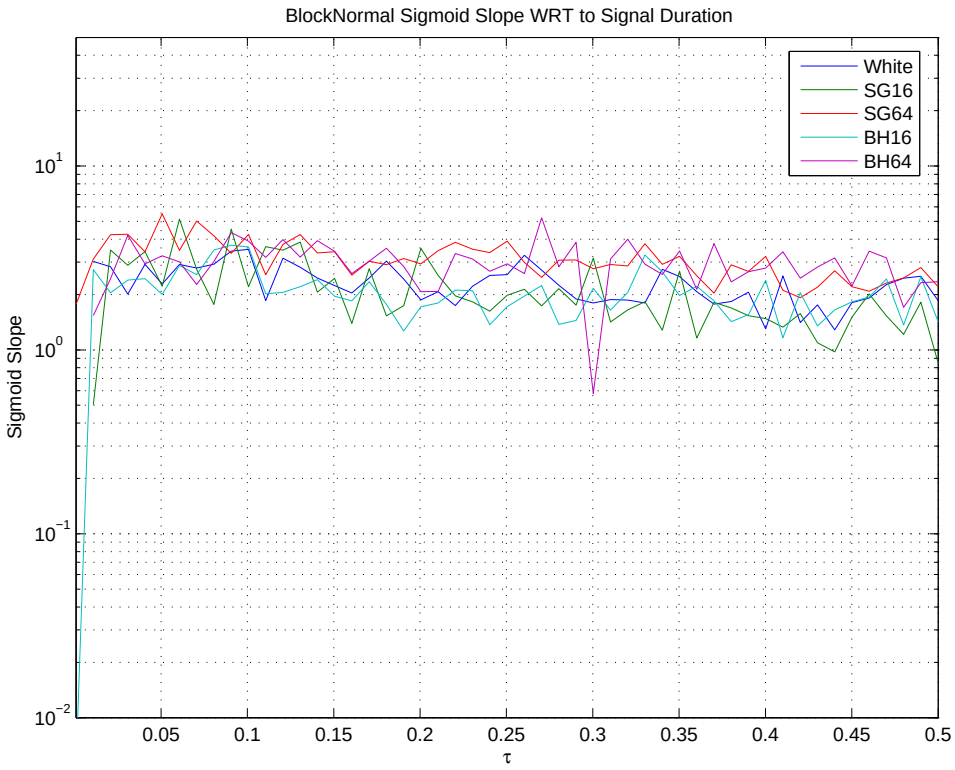


**Figure 7.2.** Sigmoid steepness curves for BlockNormal with respect to signal type, amplitude and duration.

### 7.2.3 Q Pipeline

Figure 7.5 shows the measured $A_{50}$ for Q Pipeline which had an observed false detection fraction ($\alpha$) of 0.1130. There was a minor change in parameter settings for this investigation from those described in section 5.6; because of an observed periodic detection failure of large amplitude signals (every $7^{th}$ injection and its $\pm 1$ neighbor), the minimum block overlap parameter was changed from 10 seconds to 32 seconds. Also, the minimum and maximum frequency range has been changed from 512 Hz to 640 Hz in the previous investigation to 0 Hz to 128 Hz for this investigation.

For the first time in any of these ETGs, an increase in $A_{50}$ as both $\tau$ duration and amplitude increase, is observed. This very well may be the case for BlockNormal and SLOPE, but the current investigation ranges are not large enough to observe this phenomenon (which will be referred to as *turning*). Since the $A_{50}$ is no longer a sigmoid function of amplitude, the 50% efficiency point seeking was

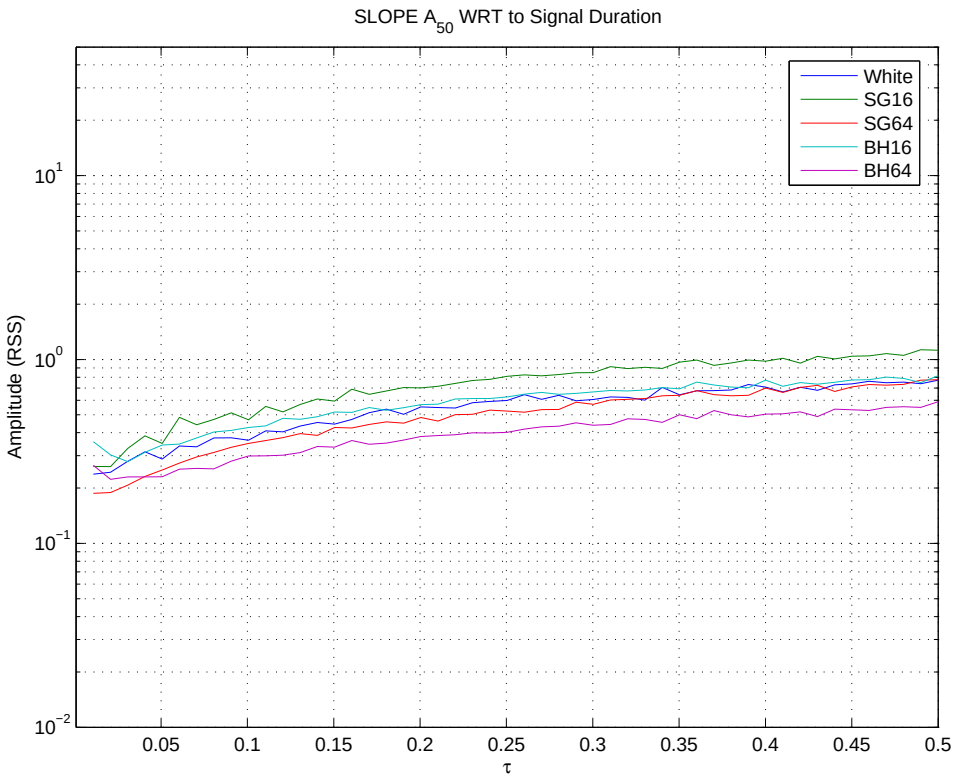


**Figure 7.3.** 50% efficiency curves for SLOPE with respect to signal type, amplitude and duration.

performed along both the amplitude and $\tau$ axes. The baseline signal of Gaussian modulated white noise ('White') turns asymptotes slightly above the maximum $\tau$ of 0.5 seconds. Even at lower $\tau$ durations ($<\sim$ 0.15 seconds) this signal has on average the highest $A_{50}$ of the signal types investigated as well as the greatest increase in $A_{50}$ and $\tau$ increases. The other signals that clearly show this phenomenon within the investigation range are the impulsive signal of 16 Hz ('BH16') which turns to asymptotes at about $\tau = 0.16$ seconds. At lower $\tau$ durations ($<\sim$ 0.15 seconds) this signal closely tracked the performance of the impulsive signal of 64 Hz ('BH64') which also shows the trend of rapid increase in $A_{50}$ as $\tau$ increases suggestion that this too will turn outside of the investigation range. These impulsive signals both had greater $A_{50}$ values than the sine-Gaussian signals ('SG16' and 'SG64'). At lower $\tau$ durations ($<\sim$ 0.15 seconds) these signals closely tracked each other (just as the impulsive signals had) but as $\tau$ increases, the 64 Hz signal is the first to show signs this signal will also turn outside of the investigation range. The most

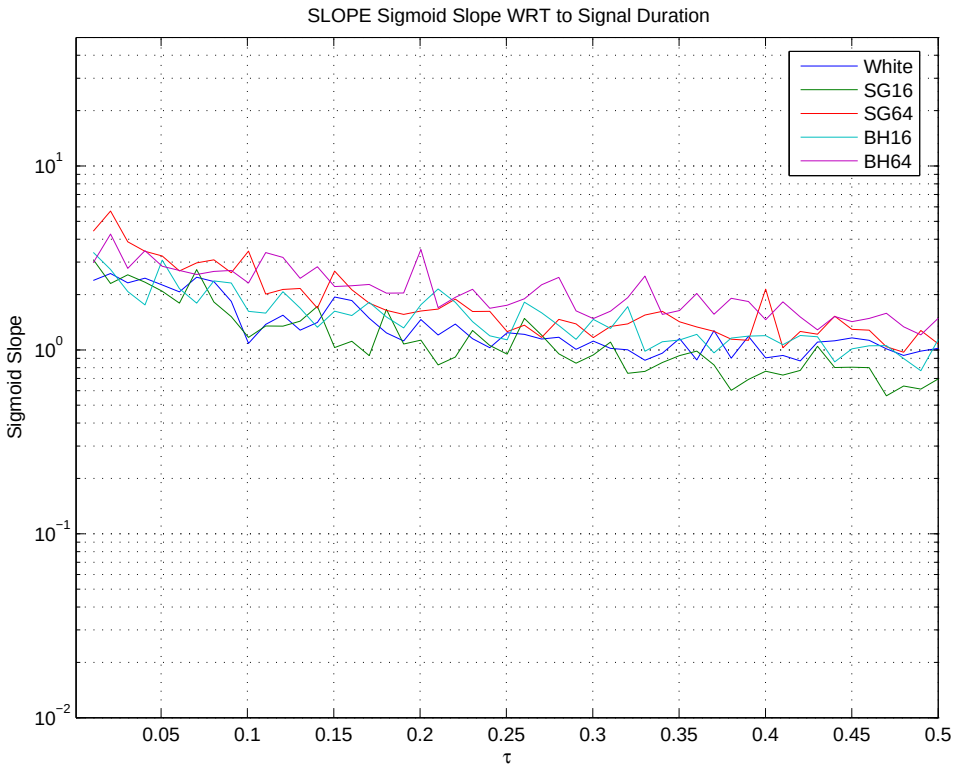


**Figure 7.4.** Sigmoid steepness curves for SLOPE with respect to signal type, amplitude and duration.

consistent of these signals is the sine-Gaussian of 16 Hz which only increases in $A_{50}$ about 35% over the $\tau$ range and, with an average $A_{50}$ of about 0.25, is the best performing signal in any ETG. This turning phenomenon shows that Q Pipeline has a strong preference to short duration signals.

Figure 7.6 shows the measured sigmoid slopes ($s$) for Q Pipeline. $s$ was only measured when the $A_{50}$ was still a function of amplitude since this is the only time that the sigmoid slope is well defined. It is again observed here that the lower the measured $A_{50}$ results in a greater sigmoid slope measurement and the higher the signal frequency, the steeper the slope (for measurements made before the turn).

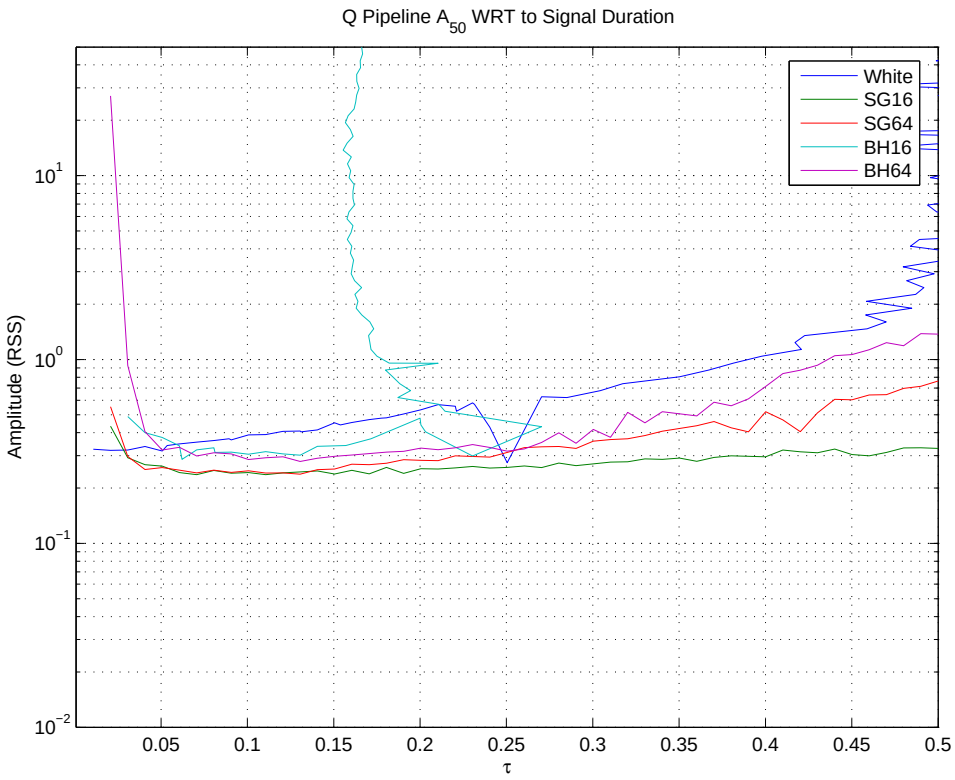


**Figure 7.5.** 50% efficiency curves for Q Pipeline with respect to signal type, amplitude and duration.

## 7.3 Relative Probability of Detection with Respect to an Astrophysical Population

While the measurement of the $A_{50}$ values gives information on the performance of an ETG, it does not give a complete description of its performance. For example, two ETGs can have identical $A_{50}$ performances, but if one ETG has a steep slope to its sigmoid transition and the other has a shallow slope, then the ETG with the shallow slope will have a much better performance to low amplitude signals than the ETG with the steep slope. When these ETGs are applied to real data, the shallow slope ETG would be preferred to the steep slope ETG since there is a better chance to detect the weak signals that may be in the data.

It would be helpful to be able to quantify the overall performance an ETG in a signal quantity; this quantity should physically relate to the data analysis objective. Here, the objective for the burst ETGs is to detect short duration

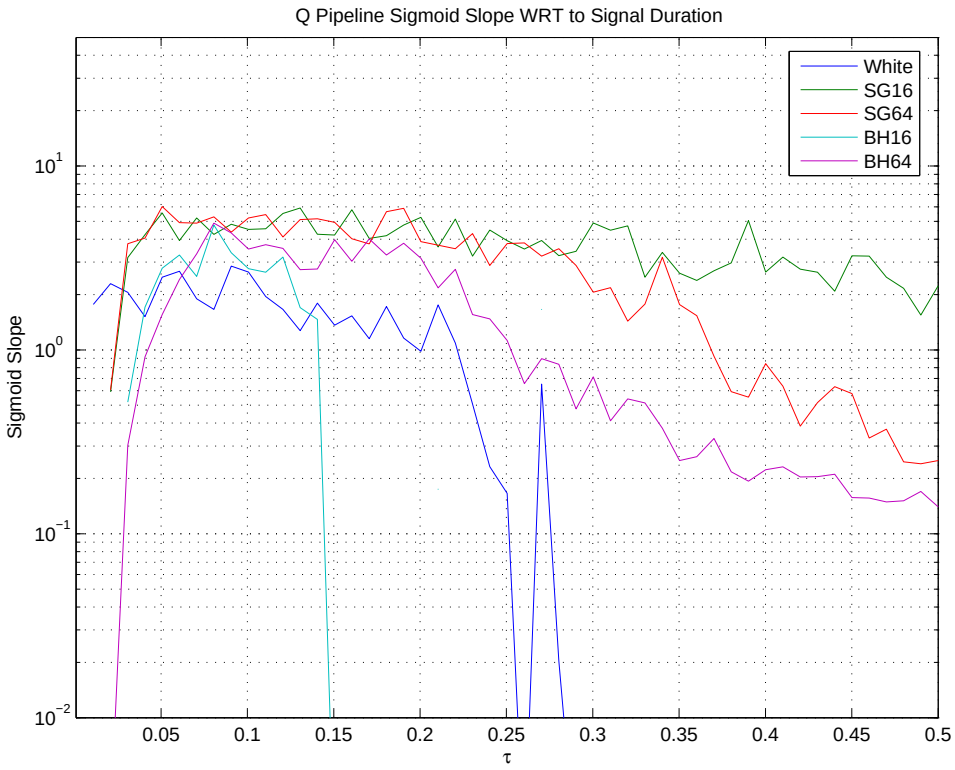


**Figure 7.6.** Sigmoid steepness curves for Q Pipeline with respect to signal type, amplitude and duration.

gravitational waves from astrophysical sources. So, a quantity which describes the relative probability of an ETG to detect a gravitational wave signal with respect to an astrophysical population is described here.

Consider a population composed of an infinitely thin disk of uniformly distributed standard candles. The number of sources in each infinitesimal ring of width $\mathrm{d}r$ at radius $r$ is:

$$N(r) = 2\pi r \mathrm{d}r \tag{7.10}$$

Also known is that the strain, $h$, falls off as the inverse of the location radius of the source:

$$h(r) = \frac{k}{r} \tag{7.11}$$

where $k$ is a proportionality constant.

The measure of the probability of detection with respect to the measured strain at the detector is proportional to the efficiency of the detector and the number of

sources with that strain, both as a function of strain. Therefore, a change in variable must be made to Equation 7.10 using Equation 7.11:

$$r = \frac{k}{h} \tag{7.12a}$$

$$\mathrm{d}r = -\frac{k}{h^2}\mathrm{d}h \tag{7.12b}$$

Substitution yields:

$$N(h) = -2\pi\frac{k^2}{h^3}\mathrm{d}h \tag{7.13}$$

Similarly, the number of isotropically distributed standard candles in an infinitesimal shell of depth $\mathrm{d}r$ at location radius $r$ is given by:

$$N(r) = 4\pi r^2 \mathrm{d}r \tag{7.14}$$

Making the substitutions of Equation 7.12a and 7.12b yields:

$$N(h) = -4\pi\frac{k^3}{h^4}\mathrm{d}h \tag{7.15}$$

Therefore, the number of sources for each population is proportional to:

$$N(h) \propto \begin{cases} h^{-3}, & \text{for disk population} \\ h^{-4}, & \text{for isotropic population} \end{cases} \tag{7.16}$$

With this population knowledge, the detection efficiency surfaces with respect to amplitude and duration can be multiplied by the appropriate population to produce the probability of detection for a specific population:

$$P(\text{detection}|A_{rss},\tau) \propto \ldots \begin{cases} \int_0^{A_{rss}^{max}} \int_0^{\tau_{max}} \epsilon(A_{rss},\tau) A_{rss}^{-3} \mathrm{d}A_{rss}\mathrm{d}\tau, & \text{disk population} \\ \int_0^{A_{rss}^{max}} \int_0^{\tau_{max}} \epsilon(A_{rss},\tau) A_{rss}^{-4} \mathrm{d}A_{rss}\mathrm{d}\tau, & \text{isotropic population} \end{cases} \tag{7.17}$$

where $\epsilon$ is the detection efficiency and the amplitude $A_{rss}$ is identified as the strain $h$.

Due to there being a non-zero false detection fraction ($\alpha$), $\epsilon(A_{rss},\tau)$ must have its false rate removed. Once this direct, element by element, subtraction is com-

pleted, $\gamma$ will no longer approach unity. This will have little effect on the integral since $\epsilon(A_{rss}, \tau)$ is multiplied by at least the inverse cube of the amplitude and maximum efficiency elements will contribute only a small portion of the total volume. Nonetheless, the false detection removed $\epsilon(A_{rss}, \tau)$ is normalized to restore the maximum efficiency to its original value (after all, for very large amplitude signals, detection efficiencies near unity are expected regardless of $\alpha$):

$$\epsilon^N(A_{rss}, \tau) = \frac{1}{1-\alpha}\left[\epsilon(A_{rss}, \tau) - \alpha\right] \tag{7.18}$$

where $\epsilon^N$ is the false removed, normalized detection efficiency.

Integration is performed numerically by summing the volumes of columns whose height is estimated to be the mean of the highest corner and the lowest corner ($\bar{\mathcal{D}}$, where $\mathcal{D} = \epsilon^N(A_{rss}, \tau)$ multiplied by the appropriate population factor) and whose cross sectional area is the product of the appropriate spacing in $A_{rss}$ and $\tau$ ($\Delta A_{rss}\Delta\tau$):

$$\int_0^{A_{rss}^{max}} \int_0^{\tau_{max}} \mathcal{D}\mathrm{d}A_{rss}\mathrm{d}\tau \simeq \sum_{A_{rss}} \sum_{\tau} \bar{\mathcal{D}}_{(A_{rss},\tau)} \Delta A_{rss} \Delta\tau \tag{7.19}$$

Once $\mathcal{D}$ is integrated for each ETG and signal, a number that represents the relative probability of detection for that signal with respect to that population is obtained. This quantity can be compared across ETGs. Since the extremely short duration signals' poor detection efficiency is likely due to simulations of only a few samples in length, the integration bounds for $\tau$ are 0.030705 to 0.5 seconds and the amplitude bounds include the full range investigated (0.01 to 50).

### 7.3.1 Disk Population

Table 7.1 shows the relative probability of detection with respect to a disk population for BlockNormal, SLOPE and Q Pipeline, normalized to the BlockNormal Gaussian modulated white noise value. Here it is observed that each of the ETGs perform approximately as well as one another for the baseline signal of Gaussian modulated while noise. BlockNormal has the most consistent performance across signal types and frequencies but does show a slight preference to lower fre-

| **Disk Population** | BlockNormal | SLOPE | Q Pipeline |
|---|---|---|---|
| Gaussian modulated white noise | 1.000 | 1.315 | 0.8537 |
| Sine-Gaussians, 16 Hz | 1.113 | 0.6134 | 5.113 |
| Sine-Gaussians, 64 Hz | 0.6741 | 1.409 | 3.501 |
| Black hole ringdowns, 16 Hz | 1.409 | 1.072 | 1.900 |
| Black hole ringdowns, 64 Hz | 1.333 | 2.229 | 2.614 |

**Table 7.1.** Relative probability of detection for each ETG with respect to a disk population (normalized to the BlockNormal probability for Gaussian modulated white noise).

quency signals and shows a moderate preference for impulsive signals. SLOPE's performance varies more than BlockNormal's. It shows a moderate preference to impulsive signals but, unlike BlockNormal, shows a strong preference to higher frequency signals. Q Pipeline shows the largest range in performances: it shows a preference to the sine-Gaussian signals over the impulsive signals but not to the broadband Gaussian modulated white noise. Within the sine-Gaussian signals, there is a strong preference to the lower frequency signals while there is a moderate preference to the higher frequency signals for the impulsive signals. It is also noted that Q Pipeline has higher performance numbers than the other ETGs. While these are impressive, one cannot completely rely on this ETG for detection purposes since it is unlikely that a strong impulsive gravitational wave with a $\tau$ of 0.3 seconds and an RSS amplitude of 10 would be detected at all.

### 7.3.2 Isotropic Population

| **Isotropic Population** | BlockNormal | SLOPE | Q Pipeline |
|---|---|---|---|
| Gaussian modulated white noise | 1.000 | 1.709 | 0.8895 |
| Sine-Gaussians, 16 Hz | 1.241 | 0.4966 | 12.75 |
| Sine-Gaussians, 64 Hz | 0.4974 | 1.796 | 7.324 |
| Black hole ringdowns, 16 Hz | 1.971 | 1.192 | 4.645 |
| Black hole ringdowns, 64 Hz | 1.542 | 3.471 | 4.915 |

**Table 7.2.** Relative probability of detection for each ETG with respect to an isotropic population (normalized to the BlockNormal probability for Gaussian modulated white noise).

Table 7.2 shows the relative probability of detection with respect to an isotropic population for BlockNormal, SLOPE and Q Pipeline, normalized to the BlockNor-

mal Gaussian modulated white noise value. This echoes the same undertones as the observations made for the disk population: BlockNormal shows a moderate preference to impulsive signals and signals with lower frequency, SLOPE has a strong preference to higher frequency signals and a moderate preference to impulsive signals, Q Pipeline still prefers sine-Gaussian signals over impulsive signals and broadband signals, and prefers lower frequency sine-Gaussians and higher frequency impulsive signals. While the degree of preference has changed between the disk population and this population, these observations are consistent.

## 7.4 Comparison to Previous Results

Before the results discussed in this chapter were obtained, this investigation was performed on BlockNormal and SLOPE with an incorrect tuning (an error in the parameter tuning programming produced tunings that did not reflect the tuning objectives of average trigger rate and duration and an error in the SLOPE clustering programming resulted in a low measurement of trigger duration). The resultant tuning parameters were set for BlockNormal at $\rho_T = 4$ and $\epsilon = 1$ (q.v. Section 3.4) and $\Sigma = 27$ and $N = 0.99$ (q.v. Section 4.5). This resulted in a false rate of 1.521 triggers/sec for BlockNormal and 0.8742 triggers/sec for SLOPE and an $\alpha$ of 0.0205 for BlockNormal and 0.2067 for SLOPE. Deriving the average trigger duration from Equation 7.1 yields an average trigger duration of 0.0135 seconds for BlockNormal and 0.236 seconds for SLOPE. The results of this investigation are included here to observe the effect of ETG tuning on the detection efficiency. 3-dimensional surfaces and contour plots for each efficiency profile discussed in this section can be found in Appendix F.

### 7.4.1 ETG Detection Efficiency Profiles

#### 7.4.1.1 BlockNormal

Figure 7.7 shows the measured $A_{50}$ for BlockNormal. Here it is observed that the Gaussian modulated white noise simulations ('White') are comparable to the sine-Gaussian simulations ('SG16' and 'SG64'). The impulsive signals ('BH16' and 'BH64') are also comparable to each other and have an $A_{50}$ that is overall

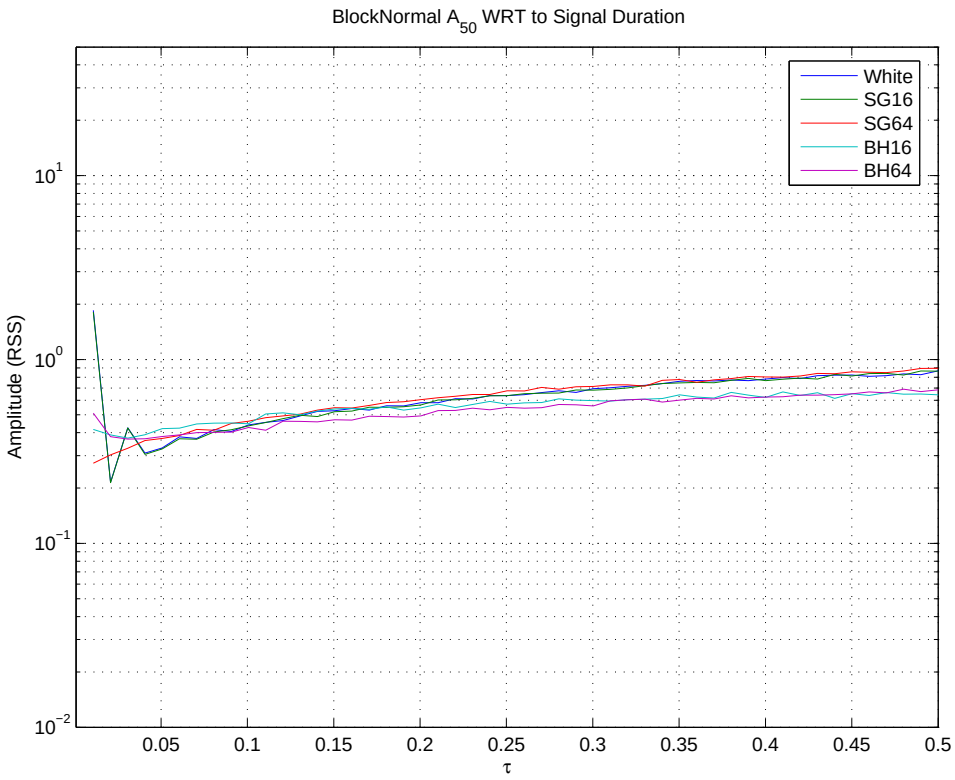


**Figure 7.7.** 50% efficiency curves for BlockNormal with respect to signal type, amplitude and duration using an alternative tuning.

about 10% lower than the other signals. This implies that BlockNormal still has a slight preference to impulsive signals than those that have continuous waveforms. Overall, the $A_{50}$ increases as the signal duration increases (about 75% over the $\tau$ range of 0.05 to 0.5 seconds for the impulsive signals and about 125% for the Gaussian modulated signals) suggesting a moderate preference for shorter duration signals. These observations are similar to those made with the correct tuning.

#### 7.4.1.2 SLOPE

Figure 7.8 shows the measured $A_{50}$ for SLOPE. Here it is observed that the Gaussian modulated white noise simulations show the highest performance over other signal types along with the 16 Hz sine-Gaussian simulations. Comparable to these performances are the 16 Hz impulsive signals. Showing a much higher $A_{50}$ (about 185%) are the 64 Hz sine-Gaussian signals and the 64 Hz impulsive signals. This suggests that SLOPE has a strong preference to signal frequency but, unlike the

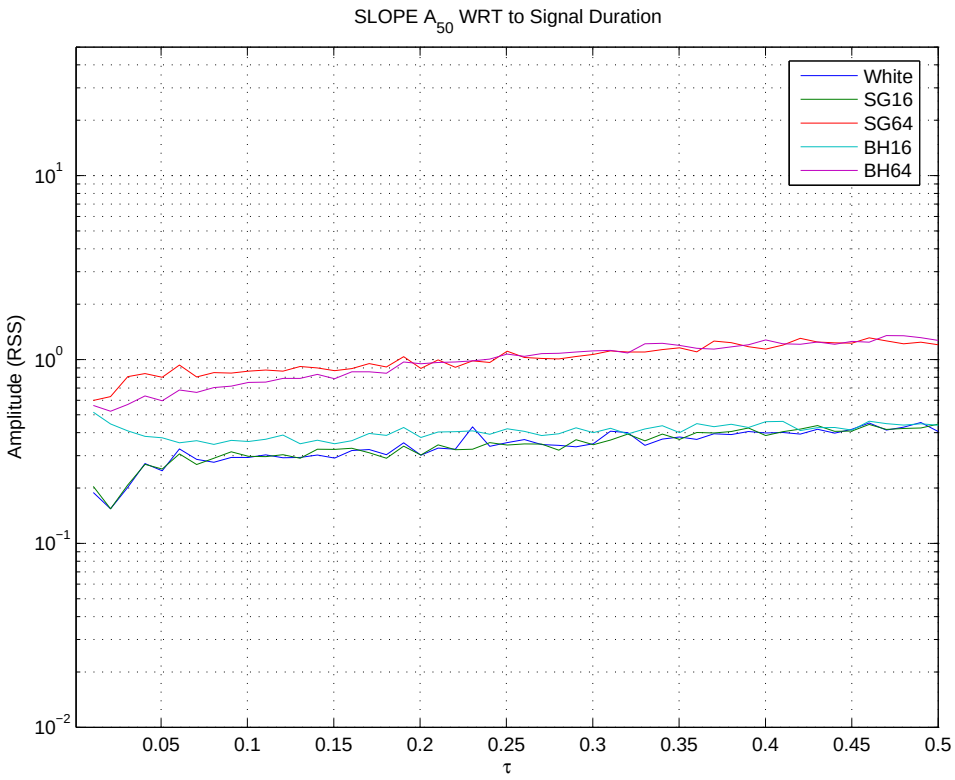


**Figure 7.8.** 50% efficiency curves for SLOPE with respect to signal type, amplitude and duration using an alternative tuning.

results with the correct tuning, the preference has changed from high frequency to low frequency. SLOPE still exhibits the tendency of the $A_{50}$ to grow larger as the signal duration increases (about 33% for the low frequency signals and Gaussian modulated white noise and about 80% for the high frequency signals). This also suggests a slight to moderate preference for shorter duration signals.

### 7.4.2 Relative Probability of Detection with Respect to an Astrophysical Population

#### 7.4.2.1 Disk Population

Table 7.3 shows the relative probability of detection with respect to an disk population for BlockNormal, and SLOPE normalized to the BlockNormal Gaussian modulated white noise value. When comparing the normalization factors between the Gaussian white noise quantities from the correct tuning to this tuning, the

current normalization factor is roughly 120% of what it was previously. The observations for BlockNormal are again similar to the observations made with the correct tuning: there is a relatively consistent performance between signal types with a slight preference to lower frequency signals and impulsive signals. SLOPE, on the other hand, has changed drastically with much wider variation in performance between signals and a reversal in frequency preference from higher frequencies to lower frequencies and from impulsive signals to Gaussian modulated signals.

| **Disk Population** | BlockNormal | SLOPE |
|---|---|---|
| Gaussian modulated white noise | 1.000 | 2.326 |
| Sine-Gaussians, 16 Hz | 0.9515 | 2.566 |
| Sine-Gaussians, 64 Hz | 0.6347 | 0.2951 |
| Black hole ringdowns, 16 Hz | 1.292 | 1.797 |
| Black hole ringdowns, 64 Hz | 1.115 | 0.2880 |

**Table 7.3.** Relative probability of detection for each ETG with respect to a disk population (normalized to the BlockNormal probability for Gaussian modulated white noise) using an alternate tuning.

#### 7.4.2.2 Isotropic Population

Table 7.4 shows the relative probability of detection with respect to an isotropic population for BlockNormal, and SLOPE normalized to the BlockNormal Gaussian modulated white noise value. When comparing the normalization factors between the Gaussian white noise quantities from the correct tuning to this tuning, the current normalization factor is roughly 145% of what it was previously. Again, BlockNormal's performance remains comparable to the observations from the disk population with this tuning and with the population results with the correct tuning. SLOPE has changed to have an even more exaggerated variance in performance between signals and shows and even stronger preference for lower frequency signals.

## 7.5 Observations

This investigation sought to establish the differences in ETG efficiency with respect to different signal types, frequencies, amplitudes and durations. This was done by

| **Isotropic Population** | BlockNormal | SLOPE |
|---|---|---|
| Gaussian modulated white noise | 1.000 | 3.518 |
| Sine-Gaussians, 16 Hz | 0.9018 | 4.206 |
| Sine-Gaussians, 64 Hz | 0.4326 | 0.1674 |
| Black hole ringdowns, 16 Hz | 1.562 | 2.407 |
| Black hole ringdowns, 64 Hz | 1.080 | 0.1507 |

**Table 7.4.** Relative probability of detection for each ETG with respect to an isotropic population (normalized to the BlockNormal probability for Gaussian modulated white noise) using an alternate tuning.

injecting simulations into a base of white noise. It was observed that the change in base data from LIGO science data produced a proportional change in tuning performance between BlockNormal and SLOPE. Since Q Pipeline tunes itself based on a target false rate, it was not affected by the base data change except that its false rate was reset to match those of BlockNormal and SLOPE.

Inspection of the efficiency profile $A_{50}$ measurements generated for BlockNormal shows a slight preference to impulsive signals. SLOPE showed a strong preference to high frequency signals and a slight preference to impulsive signals. Q Pipeline showed a *turning* phenomenon (an increase in $A_{50}$ as both $\tau$ duration and amplitude increase) which caused a departure from the sigmoid efficiency observed in the other ETGs. It is not known if this also occurs at higher durations not investigated here for the other ETGs. Q Pipeline performed better for sine-Gaussian signals by having lower $A_{50}$'s and less turning. All of the ETGs showed preference to shorter duration signals as illustrated by the upward trend of $A_{50}$ measurements as $\tau$ increased. In general, the lower the measured $A_{50}$ or the higher the signal frequency, the steeper the measured slope of the sigmoid.

In order to more accurately portray the performance of an ETG, the entire shape of its efficiency profile must be considered. This can be quantified by applying a population to the profiles and integrating. This volume is proportional to the relative probability of detecting a signal from this population. Considering the disk population, BlockNormal had the most consistent performance over signal type and frequency but had a slight preference towards impulsive signals, SLOPE prefers high frequency and impulsive signals and Q Pipeline prefers sine-Gaussian signals and is biased against signals with broadband spectrum. Q Pipeline can

outperform both BlockNormal and SLOPE but has a large variance in performance with respect to signal type and frequency. When considering an isotropic population, the same observations can be made and are only exaggerated.

Looking at the results for BlockNormal and SLOPE with an erroneous tuning has shown that tuning can have a strong effect on ETG performance, especially for SLOPE which has a reversal in frequency preference and signal type, now preferring low frequency signals and sine-Gaussians. BlockNormal's performance was relatively consistent with the result from the correct tuning but it also had a much smaller change in its tuning performance from Section 3.4.

Chapter 8

# Analysis III: Effect of Time-Domain vs. Frequency-Domain Properties on ETG Performance

In Chapter 7 the performance of the ETGs to different signal types and frequencies was investigated. These signals had well defined and specific timeseries properties. However, since gravitational wave bursts come from unanticipated sources, it cannot be assumed that burst signals will have well defined waveforms. Therefore, it is interesting to investigate the performance of signals similar to those that have already been characterized but with modified time-domain properties. That is, are the ETGs sensitive to the specific time-domain properties of a signal or are they sensitive to the frequency-domain signal magnitude?

This chapter begins by describing the modifications to the investigation of the last chapter needed to characterize the effect of holding the frequency-domain signal magnitude constant in Section 8.1. This investigation produces similar figures of merit as those discussed in Chapter 7 and the detection efficiency profiles for each ETG are discussed in Section 8.2 as is their performance with respect to an astrophysical population in Section 8.3. These results are summarized in Section 8.4.

## 8.1 Methodology

To investigate the ETG sensitivities to fixed frequency-domain magnitude signals compared to the original specific time-domain signals, the signal set used in the previous chapter (Gaussian modulated white noise, Gaussian-modulated sinusoids of 16 Hz and 64 Hz and exponentially decaying harmonic oscillators of 16 Hz and 64 Hz) is mapped into the frequency-domain and the signal phase is randomized while the magnitude is held constant. This is done many times to make multiple time-domain mappings of a single frequency-domain magnitude. Other than this modification to the simulated signals, this investigation proceeds in the same way as described in Section 7.1 including injecting simulations into a base of white noise and the tuning parameters used for each ETG.

Simulation generation begins by Fourier transforming a time-domain signal ($x(n)$) into the frequency domain:

$$\tilde{X}(k) = \sum_{n=1}^{N} x(n) \exp\left(-i2\pi(k-1)\frac{n-1}{N}\right) \tag{8.1}$$

for $1 \leq k \leq N$ and where $N$ is the length of the time-domain signal in samples and $\tilde{X}(k)$ is the complex frequency-domain signal. Since $\tilde{X}$ is complex, it can also be expressed as a combination of magnitude ($m$) and phase ($\theta$):

$$\tilde{X} = m \exp(i\theta) \tag{8.2}$$

The magnitude is expressed by:

$$m = \tilde{X}^* \tilde{X} = (\Re(\tilde{X}) + \Im(\tilde{X}))(\Re(\tilde{X}) - \Im(\tilde{X})) \tag{8.3}$$

where $^*$ indicates the complex conjugate and $\Re$ and $\Im$ indicate the real and imaginary parts of a complex number. The phase is given by:

$$\theta = \tan^{-1}\left(\frac{\Im(\tilde{X})}{\Re(\tilde{X})}\right) \tag{8.4}$$

To generate many time-domain mappings of a frequency-domain signal, hold

the magnitude of the frequency-domain signal constant and allow the phase to vary:

$$m = \Re(\tilde{X})^2 + \Im(\tilde{X})^2 = \text{constant} \tag{8.5a}$$

$$\tilde{X}' = m\exp(i\theta') \tag{8.5b}$$

where $'$ indicates modified values from those given in Equation 8.2. Holding the magnitude constant and manipulating the phase requires that both the real and imaginary parts of the frequency-domain signal be manipulated. To do this, every sample in the magnitude $m$ is multiplied by random numbers with values $\in [-1, 1]$ and set equal to the new real part of $\tilde{X}$. The imaginary part is then determined to insure that the magnitude remains unchanged:

$$\Im(\tilde{X}') = \pm\sqrt{m - \Re(\tilde{X}')^2} \tag{8.6}$$

where the sign is randomly determined for each sample. With the new real and imaginary parts of the modified frequency-domain signal determined, it is then transformed back into the time domain:

$$x'(n) = \frac{1}{N}\sum_{k=1}^{N}\tilde{X}'(k)\exp\left(i2\pi(k-1)\frac{n-1}{N}\right) \tag{8.7}$$

where $1 \leq n \leq N$. This resulting time-domain signal ($x'(n)$) has the same frequency-domain magnitude as the original signal ($x(n)$) as well as the same $A_{RSS}$.

As in the last chapter, 100 of these time-domain mappings are injected into the base of white noise with zero mean and unit variance every $15 \pm 1$ seconds and then processed by each ETG to measure the fraction of signals that are then detected.

## 8.2 ETG Detection Efficiency Profiles

Recall that measuring the efficiency of a signal with varying amplitude and duration produces a three dimensional surface which can be compared between ETGs. Previously, the baseline that all other signals were compared to was the Gaus-

sian modulated white noise signals; for the purposes of this investigation, the efficiency profiles from the previous investigation serve as the base for comparison. 3-dimensional surfaces and contour plots (except for Q Pipeline, q.v. Section 8.2.3) for each efficiency profile discussed in this section can be found in Appendix G.

### 8.2.1 BlockNormal

Figure 8.1 shows the measured $A_{50}$ for BlockNormal which had the same observed false detection fraction ($\alpha$) as seen in Section 7.2.1 (0.0426). Overall, the $A_{50}$ for each signal type increased over the entire $\tau$ duration range while the general shape of the plots remained the same. The worst performing of the signals is the Gaussian modulated white noise ('White') since it is not well defined in the frequency domain. Its mid-range ($\tau = 0.25$ sec) $A_{50}$ is about 1.1. All of the other signals ('SG16', 'SG64', 'BH16' and 'BH64') are comparable to each other with mid-range $A_{50}$'s of about 0.9 (at shorter durations the impulsive signals have a slightly higher $A_{50}$ than the sine-Gaussian signals). This represents about 80% degradation in $A_{50}$ for the impulsive signals, about 50% degradation for the sine-Gaussian signals and about 83% degradation for the Gaussian modulated white noise signals. Previously, BlockNormal showed a slight preference toward impulsive signals by needing a slightly lower $A_{50}$ but that is no longer the case here. Also, the $A_{50}$ of all signals increase (about 100% over the $\tau$ range of 0.05 to 0.5 seconds) as the signal duration increases suggesting a moderate preference for shorter duration signals.

Figure 8.2 shows the measured sigmoid slopes for BlockNormal. As was observed in the last investigation, higher the $A_{50}$ measurements give shallower sigmoid slope measurements. This is exemplified here by the worst performing signal (Gaussian modulated white noise, 'White') having consistently the shallowest slopes compared to the other signals. Because the rest of the signals had roughly equivalent performances, the distinguishing feature in their slope measurements is their frequency dependence. As noted in the last investigation and is observed here, the higher the signal frequency, the steeper the slope and the lower the signal frequency the shallower the slope. Since the $A_{50}$ for each signal increased in this investigation, the measured sigmoid slopes are also expected to decline. This is

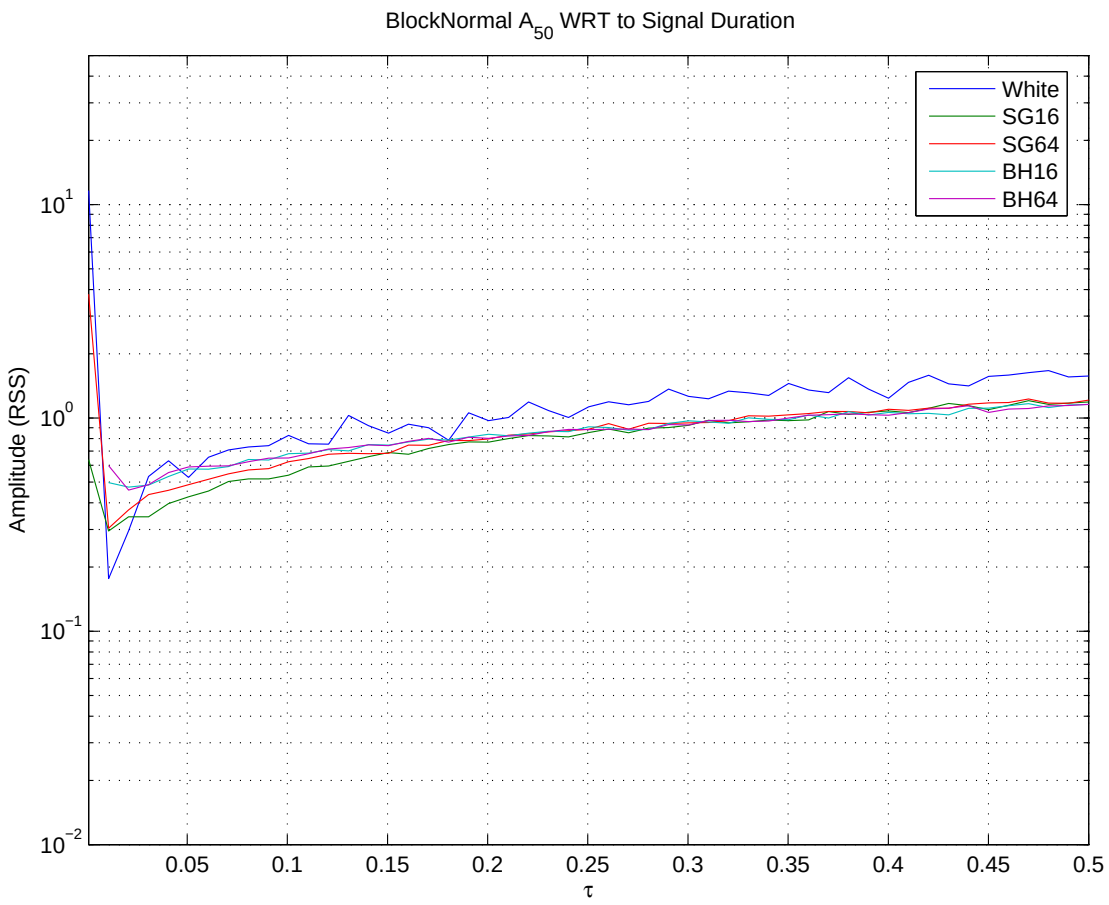


**Figure 8.1.** 50% efficiency curves for BlockNormal with respect to signal type, amplitude and duration using constant frequency-domain magnitude signals.

observed as well. Previously, the mid-range slope measurements were about $2.5 \pm 1$ while this investigations mid-range measurements are about $1.5 \pm 0.5$.

### 8.2.2 SLOPE

Figure 8.3 shows the measured $A_{50}$ for SLOPE which had the same observed false detection fraction ($\alpha$) as seen in Section 7.2.2 (0.0725). It is again observed that the $A_{50}$ for each signal type increased over the entire $\tau$ duration range while the general shape of the plots remained the same. Where, in the last investigation, it was the frequency of the signal that determined how well it performed, signal type is now the dominating factor in this investigation. Sine-Gaussians perform worse than the impulsive signals ('BH16' and 'BH64') which are comparable to

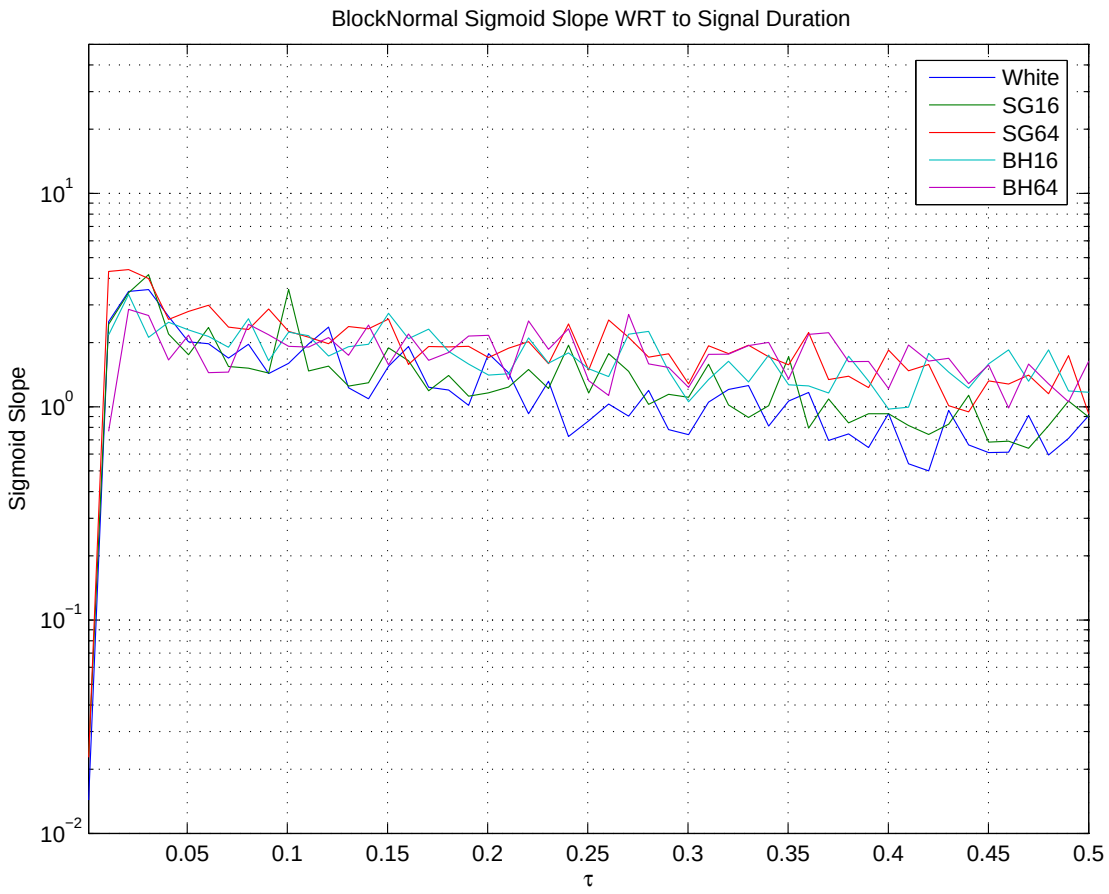


**Figure 8.2.** Sigmoid steepness curves for BlockNormal with respect to signal type, amplitude and duration using constant frequency-domain magnitude signals.

each other; the 16 Hz sine-Gaussian signals ('SG16') perform comparably to the Gaussian modulated white noise signals ('White') and both are significantly worse than the sine-Gaussian of 64 Hz ('SG64'). Compared to the last investigation, the mid-range ($\tau = 0.25$ sec) $A_{50}$'s are estimated to have increased from 0.6 to 1.1 (83%) for the Gaussian modulated white noise signals, from 0.8 to 1.05 (31%) for the 16 Hz sine-Gaussians, from 0.5 to 0.8 (60%) for the 64 Hz sine-Gaussians, from 0.6 to 0.75 (25%) for the 16 Hz impulsive signals and from 0.4 to 0.7 for the 64 Hz impulsive signals. Also, the $A_{50}$ of all signals increase (about 150% over the $\tau$ range of 0.05 to 0.5 seconds) as the signal duration increases suggesting a moderate preference for shorter duration signals.

Figure 8.4 shows the measured sigmoid slopes for SLOPE. As was observed in the last investigation, higher $A_{50}$ measurements give shallower sigmoid slope

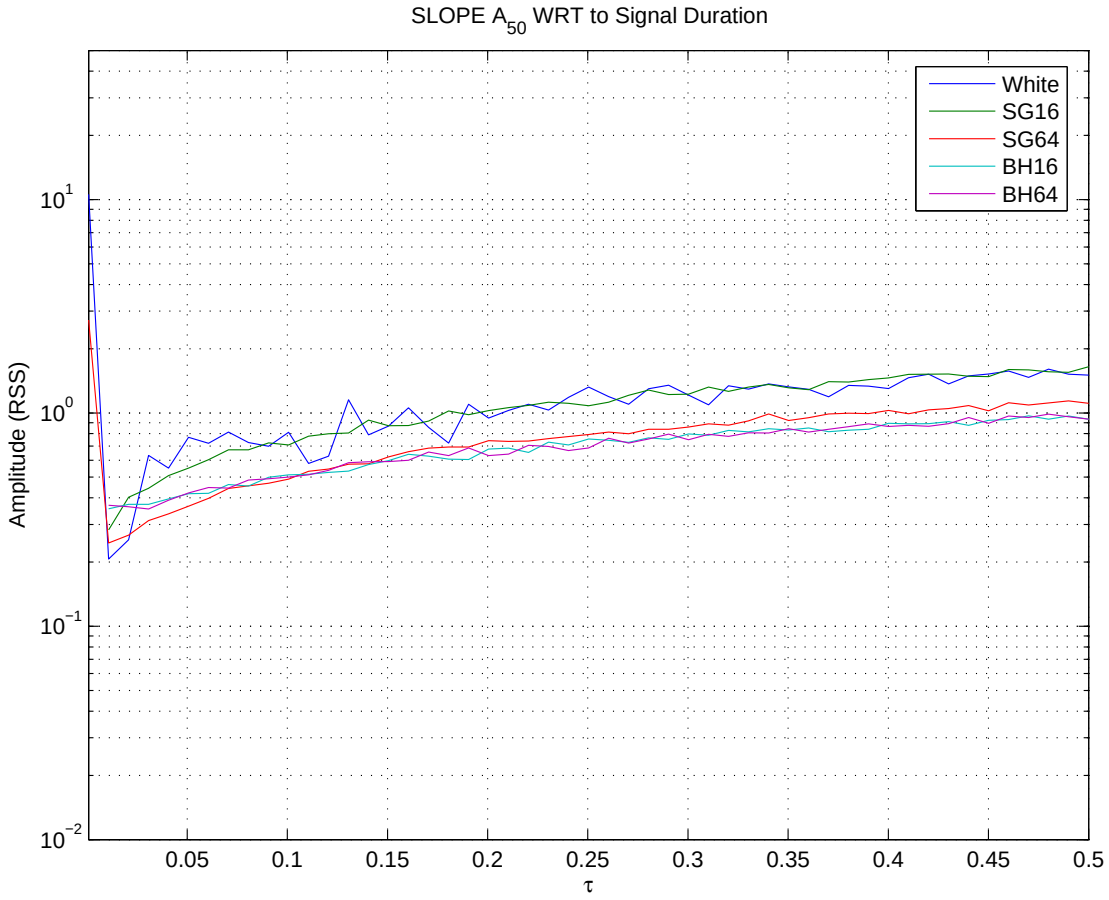


**Figure 8.3.** 50% efficiency curves for SLOPE with respect to signal type, amplitude and duration using constant frequency-domain magnitude signals.

measurements. This is exemplified here by the worst performing signals (Gaussian modulated white noise, and the 16 Hz sine-Gaussians) which consistently have the shallowest slopes. Since the $A_{50}$ for each signal increased in this investigation, the measured sigmoid slopes are also expected to decline. This is observed as well. Previously, the mid-range slope measurements were about $1.5 \pm 0.5$ while this investigation's mid-range measurements are about $0.8 \pm 0.2$.

### 8.2.3 Q Pipeline

For Q Pipeline, the effect of using time-domain mappings of frequency-domain magnitudes is so severe that the calculation of $A_{50}$ values is not possible for all signal types and frequencies. Therefore, the general characteristics of each signal

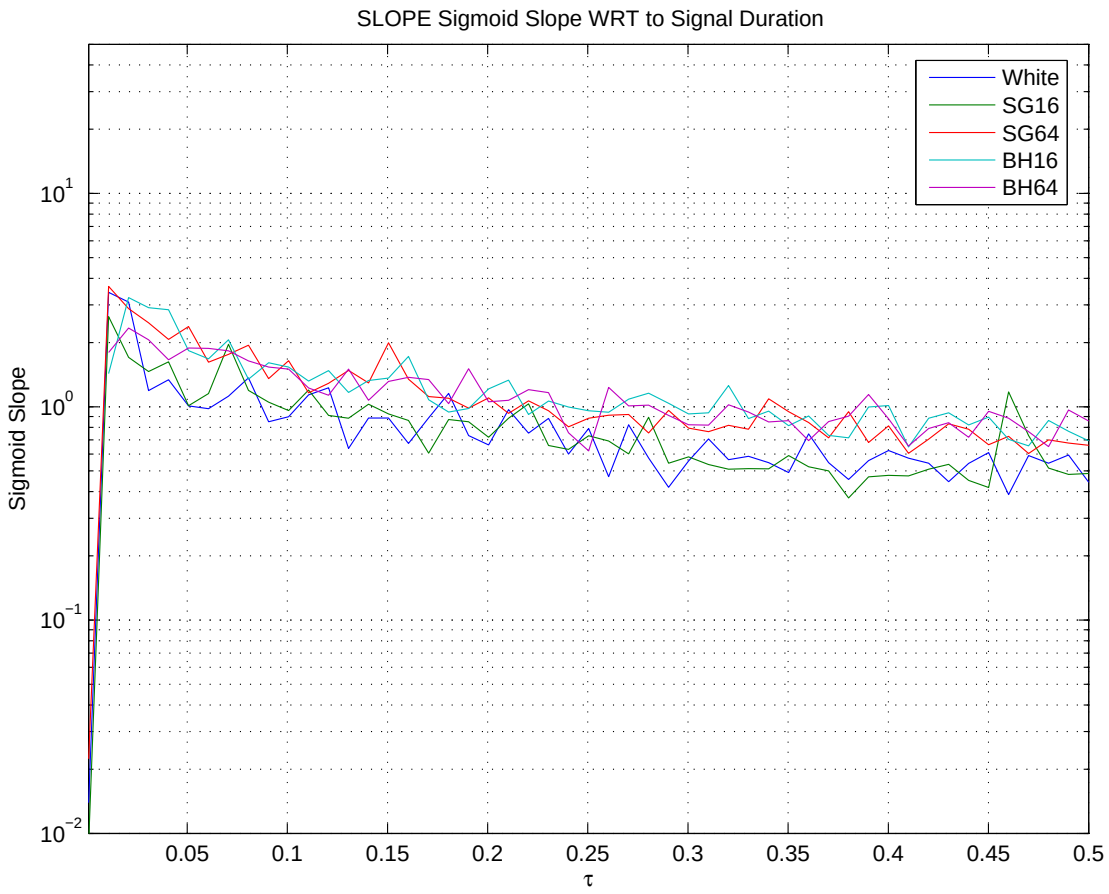


**Figure 8.4.** Sigmoid steepness curves for SLOPE with respect to signal type, amplitude and duration using constant frequency-domain magnitude signals.

are discussed in reference to the contour plots of their efficiency surfaces (the label '[const. magnitude]' is applied to the figure captions to distinguish them from the figures in Appendix E.). Corresponding 3-dimensional surfaces of these contours are found in Appendix G. The false detection fraction ($\alpha$) remained unchanged from the last investigation at 0.1130 (q.v. Section 7.2.3).

From the results of BlockNormal and SLOPE, it is not surprising that the worst performing signal is the Gaussian modulated white noise. As discussed in the last investigation (q.v. Section 7.2.3), there is a phenomena called *turning* observed where there is an increase in $A_{50}$ as both $\tau$ duration and amplitude increase. Whereas the turning point in the previous investigation was often near the maximum $\tau$ of 0.5 seconds, the turning point here is very sharp at $\tau = 0.02$ seconds with a minimum $A_{50}$ of about 0.3, as seen in Figure 8.5. While the

maximum efficiency ($\gamma$) is near unity for extremely short durations, $\gamma$ is nearer to 0.8 for the area inside the turn.

16 Hz sine-Gaussians, as seen in Figure 8.6, exhibit similar turning phenomena at about $\tau = 0.25$ seconds with a minimum $A_{50}$ of about 0.3 and a $\gamma$ of about 0.9 but also shows a secondary peak in efficiency (tending towards 0.9) at longer durations (about $\tau = 0.45$ seconds) with a larger minimum $A_{50}$ (about 0.6). This has not been observed before as there was no turning observed for this signal in the last investigation. It is unlikely that this can be observed for other signals, in general, at longer durations than those investigated here since the Gaussian modulated white noise signals have a sharper turn at shorter durations but do not show any tending towards a secondary peak at longer durations. The 64 Hz sine-Gaussians, as seen in Figure 8.7, also shows the turning phenomena but it is more gradual than the 16 Hz sine-Gaussians. The turning point is at about 0.4 seconds (with a minimum $A_{50}$ of about 0.35 and a $\gamma$ of about 0.9) and there does not appear to be a trend towards a secondary peak in efficiency at longer durations.

The 16 Hz impulsive signals as shown in Figure 8.8 not only show the turning phenomena (with a turning point at about 0.2 seconds, a minimum $A_{50}$ of about 0.5 and a $\gamma$ of near 0.9) but also show the beginnings of a secondary peak in efficiency in the amplitude 7, $\tau = 0.45$ seconds area. The minimum $A_{50}$ of this peak is also larger (about 2) than the primary peak. Finally, the 64 Hz impulsive signals show the familiar sigmoid function of amplitude but the $\gamma$ tends to about 0.85 instead of unity. The mid-range $A_{50}$ is about 0.6, increased 70% from the previous investigation from about 0.35. There does not appear to be evidence of imminent turning in the efficiency, but there is a gradual trend towards higher $A_{50}$'s as the $\tau$ duration increases which is similar to the results of the other ETGs in this investigation as well as the last. This general behavior is also clear in all of the other signal types and frequencies. Besides the obvious favoritism towards short duration signals as seen in the turning phenomena, there is also a general bias towards higher frequency signals.

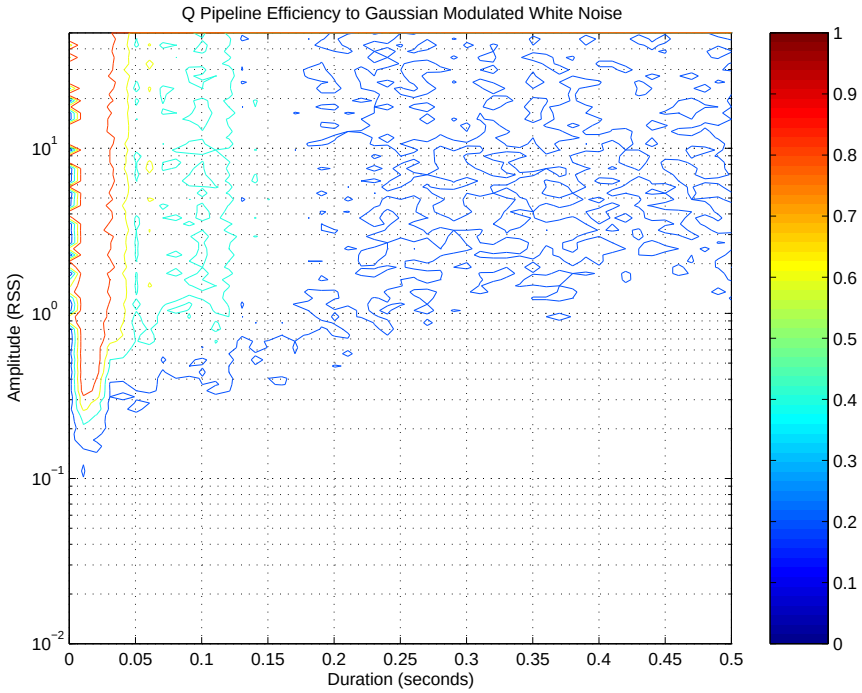


**Figure 8.5.** Q Pipeline efficiency to Gaussian modulated white noise with varying amplitude and duration (shown as a contour plot) [const. magnitude].

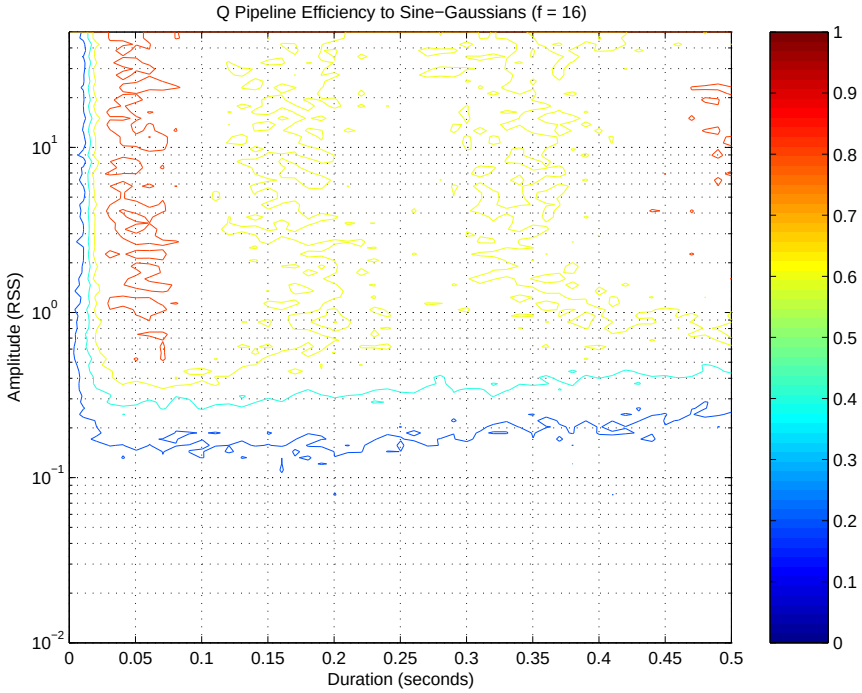


**Figure 8.6.** Q Pipeline efficiency to 16 Hz sine-Gaussians with varying amplitude and duration (shown as a contour plot) [const. magnitude].

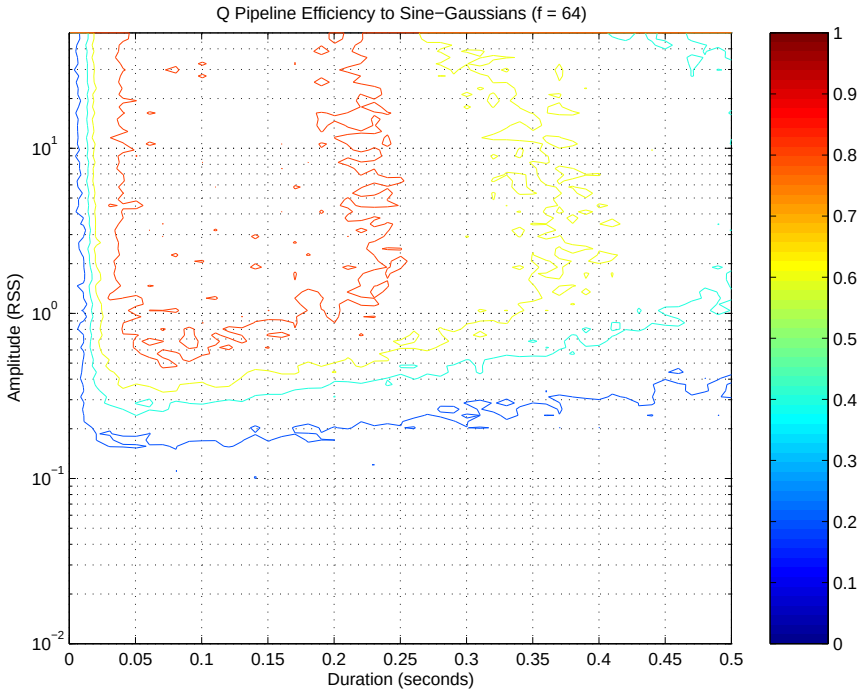


**Figure 8.7.** Q Pipeline efficiency to 64 Hz sine-Gaussians with varying amplitude and duration (shown as a contour plot) [const. magnitude].

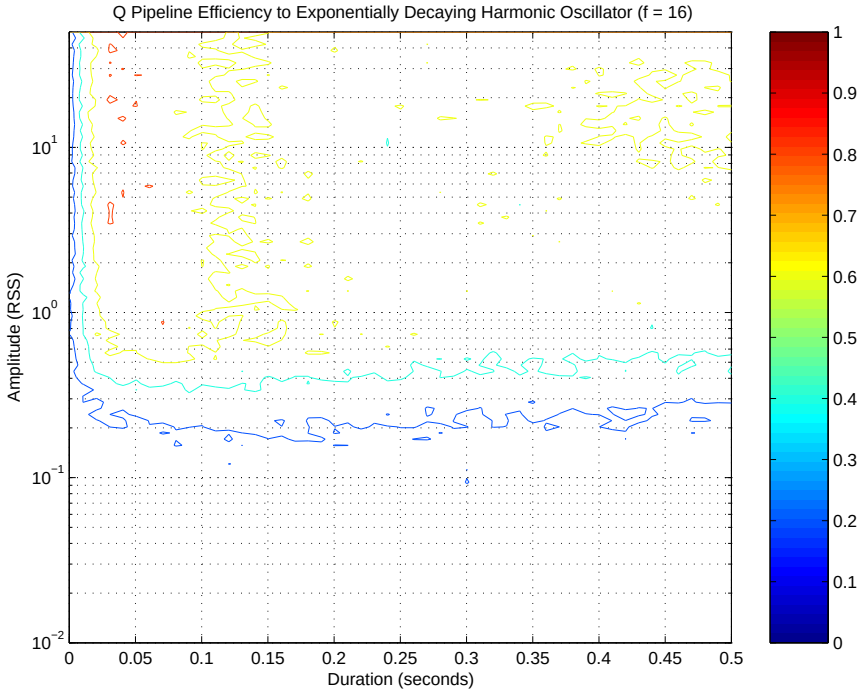


**Figure 8.8.** Q Pipeline efficiency to exponentially decaying harmonic oscillators of 16 Hz with varying amplitude and duration (shown as a contour plot) [const. magnitude].

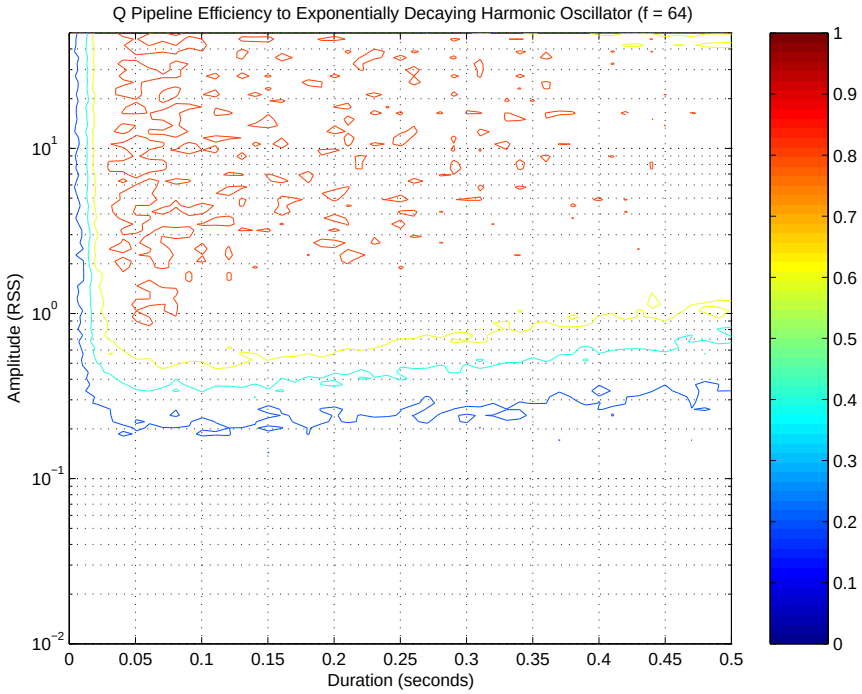


**Figure 8.9.** Q Pipeline efficiency to exponentially decaying harmonic oscillators of 64 Hz with varying amplitude and duration (shown as a contour plot) [const. magnitude].

## 8.3 Relative Probability of Detection with Respect to an Astrophysical Population

The efficiency profiles from this investigation are applied to astrophysical populations in the same way as described in Section 7.3: the elements of the efficiency profile, false detection fraction removed and normalized, are multiplied by the appropriate factor ($A^{-3}$ for a disk population and $A^{-4}$ for an isotropic population), and numerically integrated. The resulting values are then normalized to the BlockNormal quantity for Gaussian modulated white noise for comparison. Because of Q Pipeline's severely degraded performance, the probability of detection was not computed; suffice it to say that the quantities are substantially smaller than those for BlockNormal and SLOPE.

### 8.3.1 Disk Population

Table 8.1 shows the relative probability of detection with respect to a disk population for BlockNormal and SLOPE normalized to the BlockNormal Gaussian modulated white noise value. When comparing the normalization factors between the Gaussian white noise quantities from the last investigation to this investigation, the current normalization factor is roughly 28% of what it was previously. This implies that even though the quantities may have a greater variance between signal types, the probability of detection is still less than the respective probability from the last investigation.

| **Disk Population** | BlockNormal | SLOPE | Q Pipeline |
|---|---|---|---|
| Gaussian modulated white noise | 1.000 | 1.034 | N/A |
| Sine-Gaussians, 16 Hz | 3.149 | 1.155 | N/A |
| Sine-Gaussians, 64 Hz | 1.154 | 3.767 | N/A |
| Black hole ringdowns, 16 Hz | 1.584 | 5.227 | N/A |
| Black hole ringdowns, 64 Hz | 1.296 | 4.681 | N/A |

**Table 8.1.** Relative probability of detection for each ETG with respect to a disk population using constant frequency-domain magnitude signals (normalized to the BlockNormal probability for Gaussian modulated white noise).

BlockNormal had similar frequency dependence to the previous results in that the 16 Hz signals performed better than their 64 Hz counterparts. However, there is no longer a preference to impulsive signals as seen in the previous results. Overall, BlockNormal's results are fairly consistent over each signal type and frequency. SLOPE showed a greater change from the results of the last investigation. Previously, it was observed that the higher frequency signals outperformed lower frequency signals with only a slight preference to impulsive signals. Here, it is observed that impulsive signals outperform the sine-Gaussian signals regardless of their frequency but the lower frequency impulsive signals now outperform the higher frequency signals. Between BlockNormal and SLOPE, SLOPE consistently outperforms BlockNormal but has a greater variability in its performance over different signal types and frequencies.

### 8.3.2 Isotropic Population

Table 8.2 shows the relative probability of detection with respect to a disk population for BlockNormal and SLOPE normalized to the BlockNormal Gaussian modulated white noise value. When comparing the normalization factors between the Gaussian white noise quantities from the last investigation to this investigation, the current normalization factor is roughly 15% of what it was previously. Again, this implies that the probability of detection is still less than the respective probability from the last investigation.

| **Isotropic Population** | BlockNormal | SLOPE | Q Pipeline |
|---|---|---|---|
| Gaussian modulated white noise | 1.000 | 0.9958 | N/A |
| Sine-Gaussians, 16 Hz | 2.081 | 1.069 | N/A |
| Sine-Gaussians, 64 Hz | 1.185 | 2.359 | N/A |
| Black hole ringdowns, 16 Hz | 1.426 | 2.892 | N/A |
| Black hole ringdowns, 64 Hz | 1.279 | 2.718 | N/A |

**Table 8.2.** Relative probability of detection for each ETG with respect to an isotropic population using constant frequency-domain magnitude signals (normalized to the BlockNormal probability for Gaussian modulated white noise).

The measured probabilities of this population have the same general trend as for the disk population: BlockNormal shows a preference to lower frequency signals but shows consistent performance regardless of signal type or frequency and SLOPE shows a stronger dependence on signal type, preferring impulsive signals, than frequency. SLOPE still consistently outperforms BlockNormal to a lesser extent and has a more consistent variance than the disk population measurements.

## 8.4 Observations

This investigation sought to determine if it was the specific time-domain properties of a signal that each ETG were sensitive to or if it was sensitive to the frequency-domain magnitude of that signal. This was done by performing the same methodology described in Section 7.1 with the modification of transforming the time-domain signal into the frequency-domain, fixing the magnitude while randomizing the phase and transforming the signal back into the time-domain.

The overall performance of each ETG was degraded in this investigation. For BlockNormal and SLOPE, the measured $A_{50}$ for each signal type increased over the entire $\tau$ duration range while the general shape of the plots remained the same. Q Pipeline, however, showed a general breakdown of the usual sigmoid efficiency profile. For each ETG, the Gaussian modulated white noise signals were the worst performing in each (while it had about average performance in the previous investigation). For BlockNormal and SLOPE, there is still a preference towards shorter duration signals as shown by the general upward trending of the measured $A_{50}$ as $\tau$ increases. The sigmoid slopes also have the same general shape as the ones from the last investigation except the slopes are overall shallower. Since the sigmoid shape disintegrated for Q Pipeline, no measurements of the sigmoid slope were possible.

The slight preference that BlockNormal had to impulsive signals no longer exists as impulsive signals had comparable performance to sine-Gaussian signals. For SLOPE, the dominant preference for high frequency signals was replaced with the preference for impulsive signals. Q Pipeline continued to show the turning phenomena but the turns now occur at lower durations and are much more sudden than they were before. Besides this, the development of a secondary peak in efficiency was also observed for 16 Hz sine-Gaussians and the 16 Hz impulsive signals. None of the signals achieved a $\gamma$ of unity, asymptoting instead at 0.9. It is not known at the time of this writing exactly what has caused the dramatic decline in Q Pipeline performance.

Considering the efficiency profiles with respect to a disk population shows an overall decrease in performance compared to the last investigation and the normalization factor is significantly reduced. Again, since there was a dramatic decline in Q Pipeline's performance, it was not included in the population comparisons. BlockNormal's preference to low frequency signals (which was not clear from the inspection of its $A_{50}$ and sigmoid slope plots) is clear and similar to the previous investigation. SLOPE again showed its new preference to impulsive signals over signals with high frequency and while it consistently outperforms BlockNormal, it has a greater variability in performance over the different signal types and durations. Whereas the application of the isotropic population served to exaggerate differences in the last investigation, here it served to even out the differences between

the ETGs and reduce the variability in SLOPE's performance. Both BlockNormal and SLOPE have shown a bias against the Gaussian modulated white noise signals, in both populations, which is consistent with the observations made here of the $A_{50}$ and sigmoid slope plots.

Chapter 9

# Conclusions

The work documented in this thesis describes the development of original software tools to simulate gravitational waves and to search for gravitational wave bursts in the noise dominated detector data. Along with a redeveloped data analysis tool and another from a third party, these methods were compared head-to-head to test if they were fundamentally equivalent, what specific signal properties each were sensitive to and how each ETG responded to changing the specific time-domain properties of a signal while holding the frequency-domain magnitude constant.

This chapter outlines the conclusions of these investigations (q.v. Section 9.1), the summary of contributions made by this work (q.v. Section 9.2) and the suggestions on furthering this research in the future (q.v. Section 9.3).

## 9.1 Conclusions

Investigating the strongest accidental triggers from each ETG generated from the S3 playground data has shown that **the burst ETGs are *not* fundamentally equivalent**. Very few triggers were coincident between multiple ETGs and, for those that were, the significance of the triggers as identified by the ETGs were uncorrelated.

Since there were no obvious differences in the characteristics of the strongest accidental triggers, well controlled signals were injected into a base of white noise. Investigating the change in tuning performance of BlockNormal and SLOPE has shown that **once BlockNormal and SLOPE are tuned to the same criteria,**

**changing the 'white' data that they analyze will induce a proportional change in their tuning performance**. Since Q Pipeline self-tunes based on a desired trigger rate, its tuning was manually changed to match the new performance of BlockNormal and SLOPE. The efficiency profiles (detection efficiency with respect to amplitude and duration) generated through this investigation have shown that **there are signal properties that distinguish the preferences of each ETG**. These are summarized in Table 9.1.

| **Signal Preference** | BlockNormal | SLOPE | Q Pipeline |
|---|---|---|---|
| Signal Type | Slight to Impulsive | Moderate to Impulsive | Strong to Single Frequency and Non-impulsive |
| Signal Frequency | Slight to Low Frequency | Strong to High Frequency | No Preference |
| Signal Duration | Moderate to Short Duration | Strong to Short Duration | Very Strong to Short Duration |
| Consistency Rank | 1 | 2 | 3 |

**Table 9.1.** Summary of ETG preference to different signal properties. The consistency rank rates each ETG's performance over different signal types as measured in Section 7.3 with rank 1 being the most consistent.

The relative performance of each ETG to each signal type was parametrized by calculating a relative probability of detection with respect to two astrophysical populations. These have been shown to give a more general measure of ETG performance than considering the 50% efficiency measurements alone; therefore, **the *overall* shape of the efficiency profile is more meaningful for describing an ETG's performance than just its $A_{50}$ curve**.

This investigation was also performed with an erroneous tuning for BlockNormal and SLOPE. While these results do not specifically apply to this investigation, they do show that **changing the tuning of BlockNormal and SLOPE affects their overall sensitivities and can dramatically change their signal property preferences**. This was especially evident in SLOPE (whose tuning was most different from the correct tuning) and was suggested by the results of BlockNormal as seen here and investigated previously in [83].

Using the same infrastructure developed in the previous investigation, how each ETG responded to changing the specific time-domain properties of a signal while

holding the frequency-domain magnitude constant was investigated. The most evident conclusion from this evaluation was that the efficiency profiles usually retained their general shape while needing larger amplitudes to reach their prior efficiencies (except for Q Pipeline, which showed dramatic disintegration of its efficiency profiles); therefore, **the specific time-domain properties of a signal are important to its detection but are not the only factors contributing to the signal's detectability**.

Ultimately, **the comparison of the performances of these ETGs shows that they are complementary to each other**. That is, there is not a single ETG that is optimal for use in detecting burst gravitational waves nor any ETG that is without unique signal preferences and features. While the strengths of the ETGs can be used to search for specific classes of bursts, they also represent a bias in the accidental triggers they are likely to produce.

## 9.2 Summary of Contributions

Through research documented in this thesis I have contributed both original tools and methods that are of special interest to the LIGO collaboration. **A robust software gravitational wave simulator has been developed** which is currently being used by the LIGO Science Collaboration for the evaluation of burst ETGs. I also **performed the first development of the BlockNormal ETG** based on theory presented to me by Lee Samuel Finn and **redeveloped the SLOPE ETG** to address shortcomings illustrated in its application to the first LIGO science data set.

I have also **developed several original methods to compare burst ETGs** including investigating the strongest accidental triggers produced on actual detector data, comparing the detection efficiency with respect to specific signals and astrophysical populations, and comparing the detection efficiencies to fixed frequency-domain magnitude properties. With these comparison methods, I then **performed the first head-to-head comparison of burst ETGs on actual detector data with current practical tunings**. The results of these investigations can be used to tailor ETG application for specific purposes as well as suggest signals that are likely to be accidental.

## 9.3 Directions for Future research

While this research has provided new insights into the burst ETGs, it has also generated issues that require further research:

- **Include the WaveBurst** [48, 49] **ETG in these investigations** to investigate its strengths and weaknesses compared to BlockNormal, SLOPE and Q Pipeline.
- **Perform these investigations on other detectors, data runs and frequency bands.** The results presented in this work focus on results from the LIGO 4 km interferometer in Hanford, WA from the S3 playground data set in the frequency band 512-640 Hz.
- Deeper investigation into **how the tuning parameters change the performance of each ETG** will also yield more information on the overall performance of each ETG. For example, this research focused only on the current practical tuning of the ETGs but it is very possible that this is not the 'optimal' tuning. What is the 'optimal' tuning and how would this tuning change these results?
- Section 6.4 showed a correlation between the rank of a SLOPE trigger and its likelihood of being seen by the other ETGs at all. **What is the nature of this correlation?**
- **Repeat the investigation in Chapter 7 with an increased range in duration** $\tau$ in order to investigate if there is a 'turn' in the $A_{50}$ curves like those observed in Q Pipeline (q.v. Section 7.2.3).
- **Investigate the overall deterioration of the Q Pipeline efficiency profile when holding the frequency-domain magnitude of a signal constant** as observed in Chapter 8.
- **Study the practicality of the amplitudes needed to achieve high detection efficiency for each ETG and signal type** by converting the $A_{RSS}$ values to corresponding strains for S3 and characterize what astrophysical sources would be likely targets.

Appendix A

# GravEn Illustrations for Other Interferometric Gravitational Wave Observatories

## A.1 Time Projection Between the Center of the Earth and Other Interferometric Gravitational Wave Observatories

Figures A.1, A.2 and A.3 are graphical representations of the number of samples to add to a start time to account for the time of flight from the center of the Earth to the detector given the source's sky location for gravitational wave observatories other than LIGO. The theory behind these plots is explained in Section 2.3.

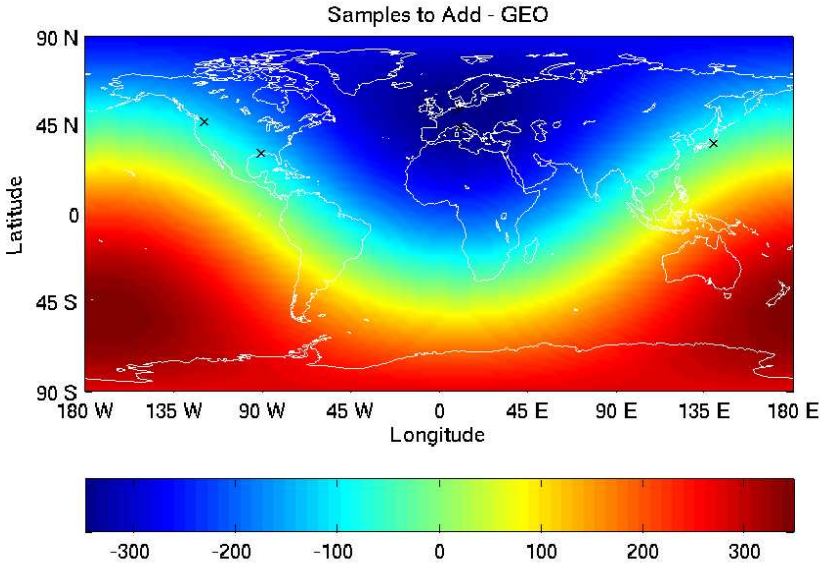


**Figure A.1.** The number of samples to add to signal start time with respect to the source sky location for GEO (sampling frequency = 16,384 samples/sec)

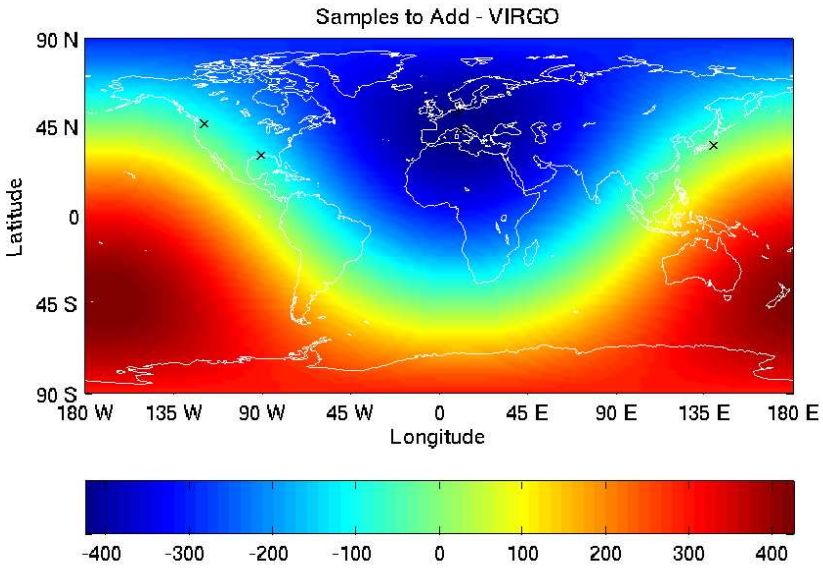


**Figure A.2.** The number of samples to add to signal start time with respect to the source sky location for VIRGO (sampling frequency = 20,000 samples/sec)

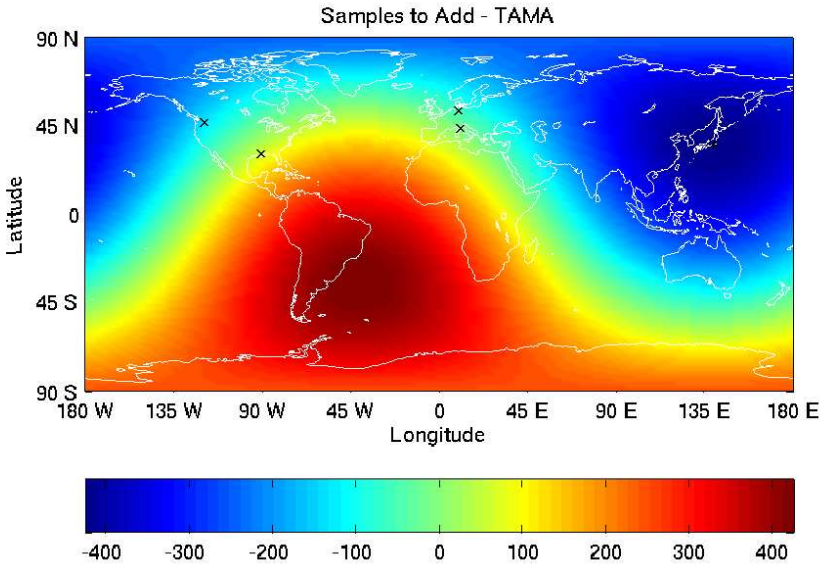


**Figure A.3.** The number of samples to add to signal start time with respect to the source sky location for TAMA (sampling frequency = 20,000 samples/sec)

## A.2 Antenna Patterns for Other Interferometric Gravitational Wave Observatories

Figures A.4, A.5 and A.6 are graphical representations of the antenna pattern for gravitational wave observatories other than LIGO. The theory behind these plots is explained in Section 2.6.

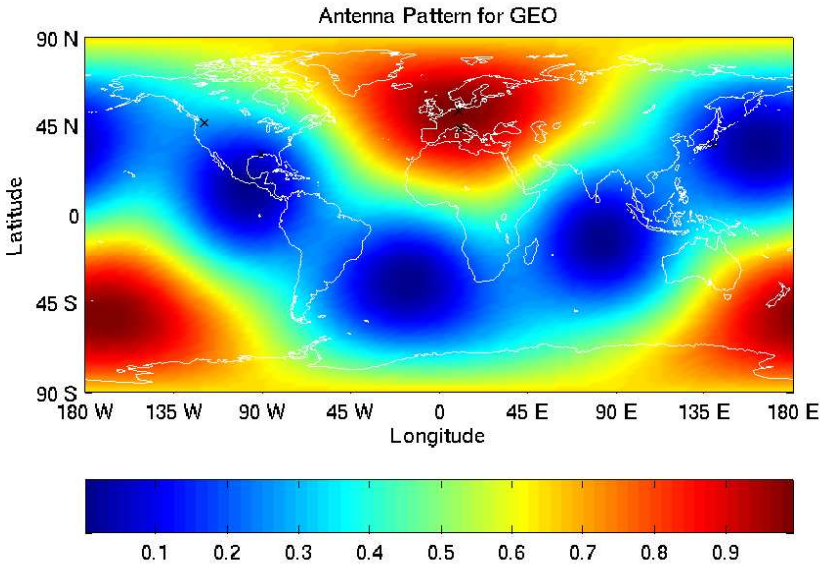


**Figure A.4.** Antenna pattern for GEO

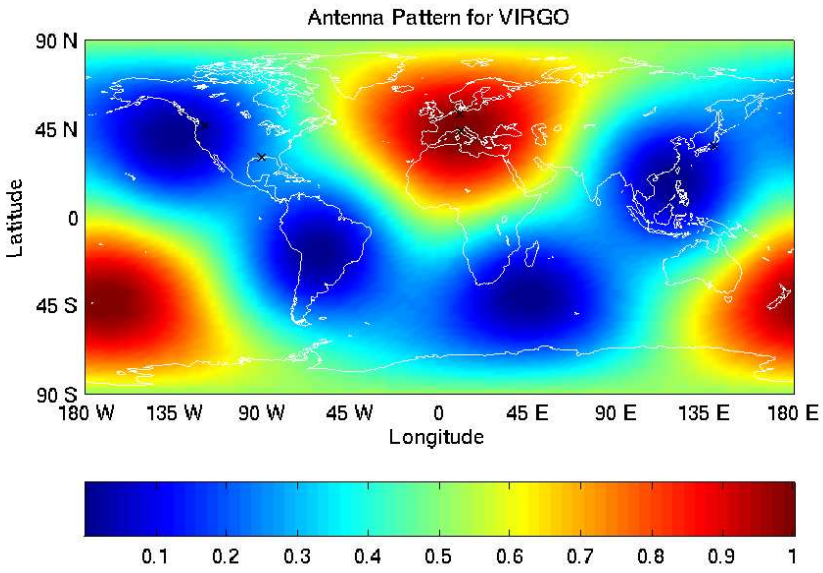


**Figure A.5.** Antenna pattern for VIRGO

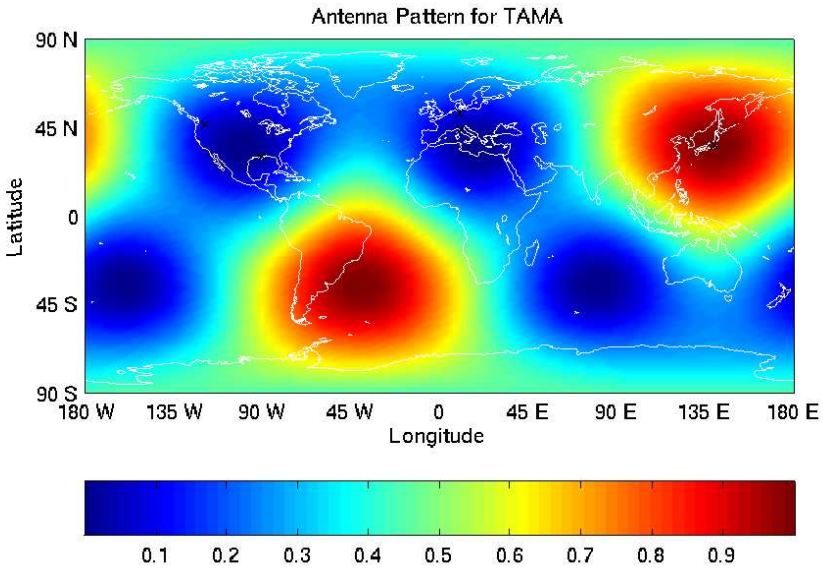


**Figure A.6.** Antenna pattern for TAMA

Appendix B

# Complete Derivation of Equation 3.9

Section 3.2.1 noted that the specific model of interest for the BlockNormal ETG is $\mathcal{M}_2$. This is the probability that the subsets, $X_j$ and $X_{N-j}$ are both described by a single normal distribution function, that is, they are each described by model $\mathcal{M}_1$. The explicit definition of $\mathcal{M}_2$ is given as:

$$P(X_N|\mathcal{M}_1) = \int_0^\infty \frac{\alpha\beta}{\sigma}(2\pi\sigma^2)^{-\frac{N}{2}}\mathrm{d}\sigma \int_0^\infty \prod_{k=0}^{N-1} \exp\left(-\frac{(x[k]-\mu)^2}{2\sigma^2}\right)\mathrm{d}\mu \qquad \text{(B.1)}$$

In the above integral, the product of $N$ exponentials can be expressed as the sum of a single exponential to the power $\sum_{i=1}^{N} x_i$, where $x_i$ represents the power of the $i^{th}$ exponential term:

$$P(X_N|\mathcal{M}_1) = \int_0^\infty \frac{\alpha\beta}{\sigma}(2\pi\sigma^2)^{-\frac{N}{2}}\mathrm{d}\sigma \int_0^\infty \exp\left(-\frac{1}{2\sigma^2}\sum_{k=0}^{N-1}(x[k]-\mu)^2\right)\mathrm{d}\mu \qquad \text{(B.2)}$$

Solving the sum in the exponential gives:

$$\begin{aligned} P(X_N|\mathcal{M}_1) \;=\; & \int_0^\infty \frac{\alpha\beta}{\sigma}(2\pi\sigma^2)^{-\frac{N}{2}}\mathrm{d}\sigma \int_0^\infty \exp\left(-\frac{1}{2\sigma^2}\sum_{k=0}^{N-1}(x^2[k] \;\ldots \right. \\ & \left. -2\mu x[k]+\mu^2)\right)\mathrm{d}\mu \end{aligned} \qquad \text{(B.3a)}$$

$$P(X_N|\mathcal{M}_1) = \int_0^\infty \frac{\alpha\beta}{\sigma}(2\pi\sigma^2)^{-\frac{N}{2}}\mathrm{d}\sigma \int_0^\infty \exp\left(-\frac{N}{2\sigma^2}(\overline{x^2} \ldots -2\mu\overline{x}+\mu^2)\right)\mathrm{d}\mu \quad \text{(B.3b)}$$

Completing the square in the exponential then gives:

$$P(X_N|\mathcal{M}_1) = \int_0^\infty \frac{\alpha\beta}{\sigma}(2\pi\sigma^2)^{-\frac{N}{2}}\mathrm{d}\sigma \int_0^\infty \exp\left(-\frac{N}{2\sigma^2}(\overline{x^2}-\overline{x}^2+\overline{x}^2 \ldots -2\mu\overline{x}+\mu^2)\right)\mathrm{d}\mu \quad \text{(B.4a)}$$

$$P(X_N|\mathcal{M}_1) = \int_0^\infty \frac{\alpha\beta}{\sigma}(2\pi\sigma^2)^{-\frac{N}{2}}\exp\left(-\frac{N}{2\sigma^2}(\overline{x^2}-\overline{x}^2)\right)\mathrm{d}\sigma \int_0^\infty \exp\left(-\frac{N}{2\sigma^2}(\overline{x} \ldots -\mu)^2)\right)\mathrm{d}\mu \quad \text{(B.4b)}$$

The integral over $\mathrm{d}\mu$ can be evaluated explicitly from an integral table as:

$$\int_0^\infty \exp\left(-\frac{N}{2\sigma^2}(\overline{x}-\mu)^2)\right)\mathrm{d}\mu = \sqrt{\frac{2\pi\sigma^2}{N}} \quad \text{(B.5)}$$

leaving:

$$P(X_N|\mathcal{M}_1) = \frac{\alpha\beta(2\pi)^{-\frac{N-1}{2}}}{\sqrt{N}}\int_0^\infty \sigma^{-N}\exp\left(-\frac{N}{2\sigma^2}(\overline{x^2}-\overline{x}^2)\right)\mathrm{d}\sigma \quad \text{(B.6)}$$

Now, consider only the integral in Equation B.6. Let:

$$\gamma \equiv N(\overline{x^2}-\overline{x}^2) \quad \text{(B.7a)}$$

$$z \equiv \frac{\sqrt{\gamma}}{\sigma} \quad \text{(B.7b)}$$

When making the substitution of $z$ for $\sigma$, the limits of integration on the integral in Equation B.6 must be reversed because as $\sigma$ tends toward infinity, $z$ tends toward zero:

$$\int_\infty^0 \frac{z^N}{\gamma^{N/2}}\exp\left(-\frac{z^2}{2}\right)\left(\frac{\sqrt{-\gamma}}{z}\right)\mathrm{d}z = \frac{-1}{\gamma^{(N-1)/2}}\int_\infty^0 z^{N-2}\exp\left(\frac{-z^2}{2}\right)\mathrm{d}z \quad \text{(B.8)}$$

Solving Equation B.8 using integration by parts leaves:

$$\int_{\infty}^{0} \frac{z^N}{\gamma^{\frac{N}{2}}} \exp\left(-\frac{z^2}{2}\right) \left(\frac{-\sqrt{\gamma}}{z}\right) \mathrm{d}z = \frac{1}{\gamma^{\frac{N-1}{2}}} \left( \left[ -z^{N-3} \exp\left(-\frac{z^2}{2}\right) \right|_0^{\infty} \cdots + (N-3) \int_0^{\infty} z^{N-4} \exp\left(-\frac{z^2}{2}\right) \mathrm{d}z \right) \quad \text{(B.9)}$$

Define a new quantity $I_N$ such that:

$$I_N \equiv \int_0^{\infty} z^N \exp\left(-\frac{z^2}{2}\right) \mathrm{d}z \quad \text{(B.10)}$$

which will make the integral in Equation B.9 $I_{N-4}$. Solving for various values of $N$ gives:

$$\begin{aligned}
I_0 &= \int_0^{\infty} \exp\left(-\frac{z^2}{2}\right) \mathrm{d}z = \sqrt{\frac{\pi}{2}} && \text{(B.11a)}\\
I_1 &= \int_0^{\infty} z \exp\left(-\frac{z^2}{2}\right) \mathrm{d}z = -\exp\left(-\frac{z^2}{2}\right|_0^{\infty} = 1 && \text{(B.11b)}\\
I_2 &= (2-1)I_0 && \text{(B.11c)}\\
I_3 &= (3-1)I_1 && \text{(B.11d)}\\
I_4 &= (4-1)I_2 = (4-1)(2-1)I_0 && \text{(B.11e)}\\
I_5 &= (5-1)I_3 = (5-1)(3-1)I_1 && \text{(B.11f)}\\
\vdots &= \vdots \qquad\qquad = \vdots && \text{(B.11g)}
\end{aligned}$$

The above pattern yields the recurrence relation:

$$I_N = (N-1)I_{N-2} = (N-1)(N-3)I_{N-4} = (N-1)(N-3)(N-5)I_{N-6} = \cdots \quad \text{(B.12)}$$

and the solution:

$$I_N = (N-1)!! \begin{cases} 1 & N \text{ odd} \\ \sqrt{\frac{\pi}{2}} & N \text{ even} \end{cases} \quad \text{(B.13)}$$

Therefore:

$$I_{N-4} = \frac{I_{N-2}}{(N-3)} \quad \text{(B.14)}$$

Substituting Equation B.14 into Equation B.9 simplifies to Equation 3.9:

$$P(X_N|\mathcal{M}_1) = \frac{\alpha\beta}{\sqrt{N}} \left(2\pi N \left(\overline{x^2} - \overline{x}^2\right)\right)^{-\frac{N-1}{2}} I_{N-2} \tag{B.15}$$

Appendix C

# S3 Playground Data Segments

So as not to bias analysis results by tailoring data conditioning and ETG parameters for individual data segments, a subset data, referred to as the playground data set, is used to tune the parameters and then excluded from the final science results. The playground data set consists of evenly spaced segments of triple coincidence data between 300 and 600 seconds long and comprised about 10% of the triple coincident data [81]. Specifically, the S3 data segment is defined to begin "at an integer multiple of 6370 seconds counted from GPS time 729293613 seconds (the start of the S2 run)." It is assumed that there are no (or very few) real gravitational wave bursts in the playground data.

Tables C.1, C.2, C.3 and C.4 list the data segment numbers (also known as a *lock*) from which the playground segment is drawn and the start and stop GPS times of the playground segments that have been used to tune the BlockNormal (q.v. section 3.4) and SLOPE (q.v. Section 4.5) ETGs and investigated in Chapter 6.

| Data segment no. | GPS start time | GPS end time |
|---|---|---|
| 10 | 751976293 | 751976760 |
| 26 | 752364863 | 752365320 |
| 29 | 752390343 | 752390943 |
| 35 | 752441340 | 752441400 |
| 45 | 752581443 | 752582043 |
| 47 | 752587813 | 752588343 |
| 48 | 752632403 | 752632440 |
| 50 | 752639043 | 752639220 |
| 55 | 752670928 | 752671223 |
| 57 | 752677008 | 752677263 |
| 59 | 752721660 | 752721780 |
| 60 | 752727953 | 752728553 |
| 61 | 752734844 | 752734923 |
| 62 | 752740693 | 752741293 |
| 64 | 752753433 | 752754033 |
| 66 | 752759834 | 752759898 |
| 74 | 752906313 | 752906684 |
| 78 | 752912683 | 752913283 |
| 88 | 752970013 | 752970613 |
| 92 | 753014603 | 753015203 |
| 95 | 753027343 | 753027943 |
| 123 | 753601043 | 753601243 |
| 127 | 753620041 | 753620353 |
| 133 | 753638863 | 753639463 |
| 163 | 754008323 | 754008923 |
| 165 | 754021063 | 754021167 |
| 169 | 754180513 | 754180913 |
| 170 | 754193053 | 754193653 |
| 174 | 754205943 | 754206393 |
| 177 | 754218533 | 754219133 |
| 178 | 754224903 | 754225104 |
| 180 | 754231273 | 754231404 |
| 181 | 754237643 | 754238243 |
| 185 | 754250383 | 754250983 |
| 188 | 754282233 | 754282440 |

**Table C.1.** S3 Playground data segments used to compare ETGs. (Continued in Table C.2.)

| Data segment no. | GPS start time | GPS end time |
|---|---|---|
| 208 | 754575253 | 754575853 |
| 214 | 754842793 | 754843393 |
| 219 | 754868273 | 754868873 |
| 221 | 754874643 | 754875243 |
| 224 | 754887383 | 754887983 |
| 231 | 754976563 | 754977163 |
| 233 | 754989303 | 754989747 |
| 235 | 754995884 | 754996273 |
| 238 | 755346023 | 755346623 |
| 239 | 755352393 | 755352993 |
| 246 | 755505273 | 755505758 |
| 254 | 755575343 | 755575943 |
| 255 | 755607488 | 755607720 |
| 260 | 755760073 | 755760404 |
| 265 | 755785553 | 755785941 |
| 298 | 755932511 | 755932663 |
| 301 | 755944803 | 755945384 |
| 304 | 755963913 | 755964513 |
| 308 | 755976653 | 755976718 |
| 309 | 755976964 | 755977064 |
| 312 | 755989393 | 755989993 |
| 315 | 755995980 | 755996059 |
| 316 | 755996262 | 755996363 |
| 318 | 756002460 | 756002733 |
| 320 | 756008503 | 756009103 |
| 322 | 756014988 | 756015473 |
| 326 | 756027613 | 756027824 |
| 328 | 756053093 | 756053268 |
| 329 | 756065833 | 756066433 |
| 330 | 756072203 | 756072803 |
| 332 | 756078573 | 756078704 |
| 335 | 756084943 | 756085543 |
| 337 | 756091313 | 756091724 |
| 341 | 756098088 | 756098283 |
| 344 | 756104053 | 756104653 |

**Table C.2.** S3 Playground data segments used to compare ETGs. (Continued in Table C.3.)

| Data segment no. | GPS start time | GPS end time |
|---|---|---|
| 346 | 756110808 | 756111023 |
| 347 | 756116793 | 756117393 |
| 350 | 756129734 | 756130054 |
| 354 | 756155013 | 756155088 |
| 356 | 756180493 | 756181008 |
| 360 | 756193233 | 756193560 |
| 363 | 756205973 | 756206328 |
| 364 | 756212343 | 756212943 |
| 368 | 756301608 | 756302123 |
| 371 | 756403443 | 756403750 |
| 373 | 756416183 | 756416753 |
| 380 | 756448328 | 756448440 |
| 382 | 756467143 | 756467743 |
| 384 | 756473513 | 756474113 |
| 385 | 756480353 | 756480483 |
| 386 | 756486253 | 756486404 |
| 387 | 756492623 | 756493223 |
| 388 | 756498993 | 756499100 |
| 390 | 756505380 | 756505521 |
| 395 | 756530843 | 756531443 |
| 402 | 756549953 | 756550488 |
| 406 | 756562693 | 756563293 |
| 407 | 756569063 | 756569663 |
| 410 | 756594543 | 756594768 |
| 424 | 756690613 | 756690693 |
| 425 | 756696905 | 756697063 |
| 427 | 756715573 | 756716173 |
| 430 | 756811123 | 756811723 |
| 431 | 756849343 | 756849720 |
| 436 | 756881193 | 756881640 |
| 439 | 756900303 | 756900903 |
| 440 | 756906673 | 756907273 |
| 442 | 756932153 | 756932268 |
| 474 | 757218803 | 757219403 |
| 476 | 757225186 | 757225773 |

**Table C.3.** S3 Playground data segments used to compare ETGs. (Continued in Table C.4.)

| Data segment no. | GPS start time | GPS end time |
|---|---|---|
| 480 | 757237913 | 757238384 |
| 487 | 757263393 | 757263993 |
| 488 | 757269763 | 757270300 |
| 491 | 757282503 | 757283103 |
| 493 | 757295686 | 757295843 |
| 494 | 757301613 | 757302213 |
| 496 | 757307986 | 757308583 |
| 504 | 757320826 | 757321323 |
| 506 | 757333463 | 757334063 |
| 507 | 757339833 | 757340433 |
| 508 | 757346203 | 757346760 |
| 509 | 757575788 | 757576123 |
| 510 | 757581893 | 757582493 |
| 511 | 757588263 | 757588863 |
| 512 | 757594633 | 757595233 |
| 513 | 757601003 | 757601568 |
| 514 | 757646100 | 757646193 |
| 515 | 757651963 | 757652040 |

**Table C.4.** S3 Playground data segments used to compare ETGs . (Concluded)

Appendix D

# Timeseries Comparison of Strongest Triggers Produced on White Noise

Section 6.3 characterized the timeseries characteristics of the strongest accidental triggers produced on S3 playground data. It is also investigated if these characteristics are dependent on the data analyzed. Presented here are the timeseries of the strongest three triggers (in red) along with the neighboring $\pm 1$ seconds of data (in black) as produced on white noise.

Overall, there were 135 simulated data segments of 600 seconds in length with a sampling frequency of 128 samples/sec. Each data segment (also known as a *lock*) was permitted to contribute 100 of its strongest triggers to be ranked among the triggers from the rest of the segments. Each ETG contributed a total of 13,500 triggers (except for BlockNormal which contributed one less) for the rankings shown here. The mean and variance from the strongest 10 triggers for BlockNormal and SLOPE are summarized in Table D.1. Because Q Pipeline is a frequency-domain ETG and does not have a well-defined trigger duration, the mean and variance of the trigger in the time-domain is not well defined.

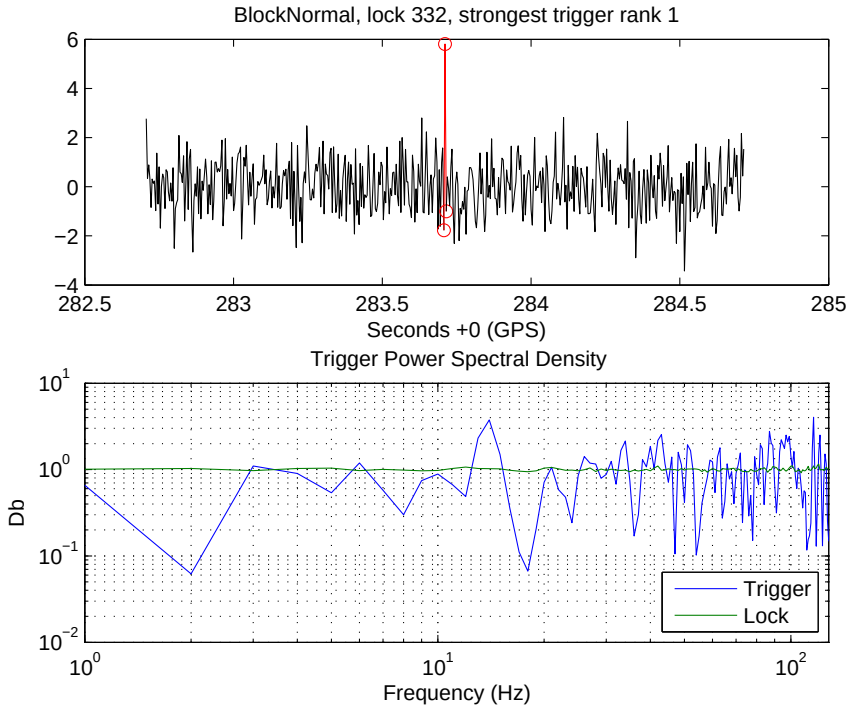


**Figure D.1.** Strongest BlockNormal trigger from all white noise data segments.

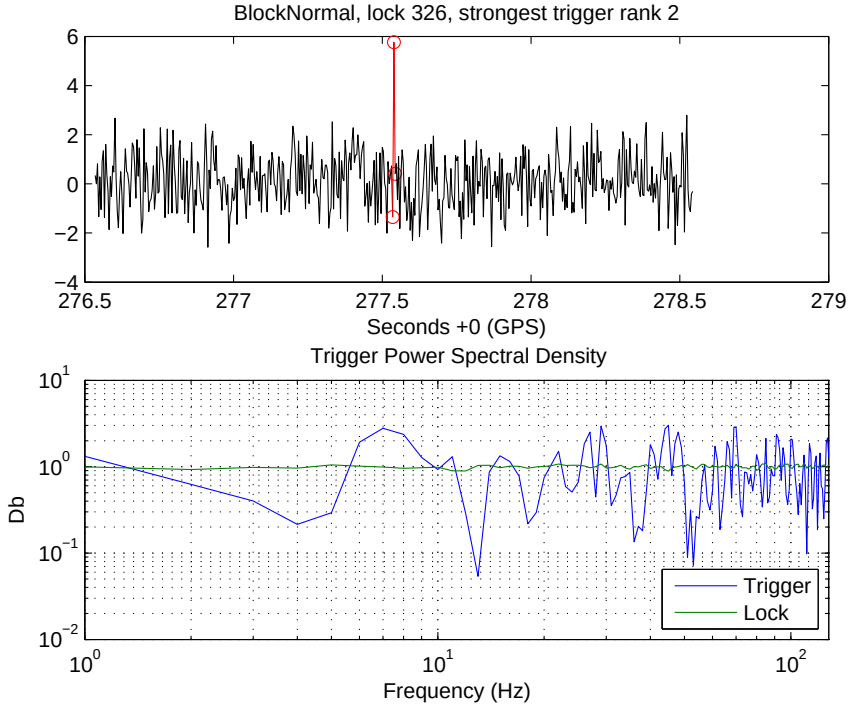


**Figure D.2.** Second strongest BlockNormal trigger from all whie noise data segments.

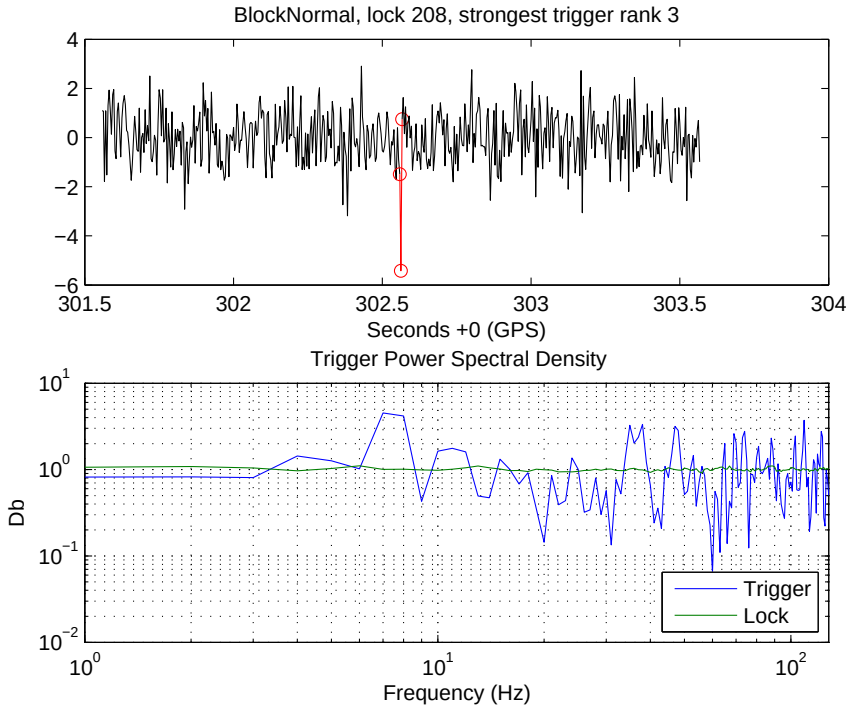


**Figure D.3.** Third strongest BlockNormal trigger from all white noise data segments.

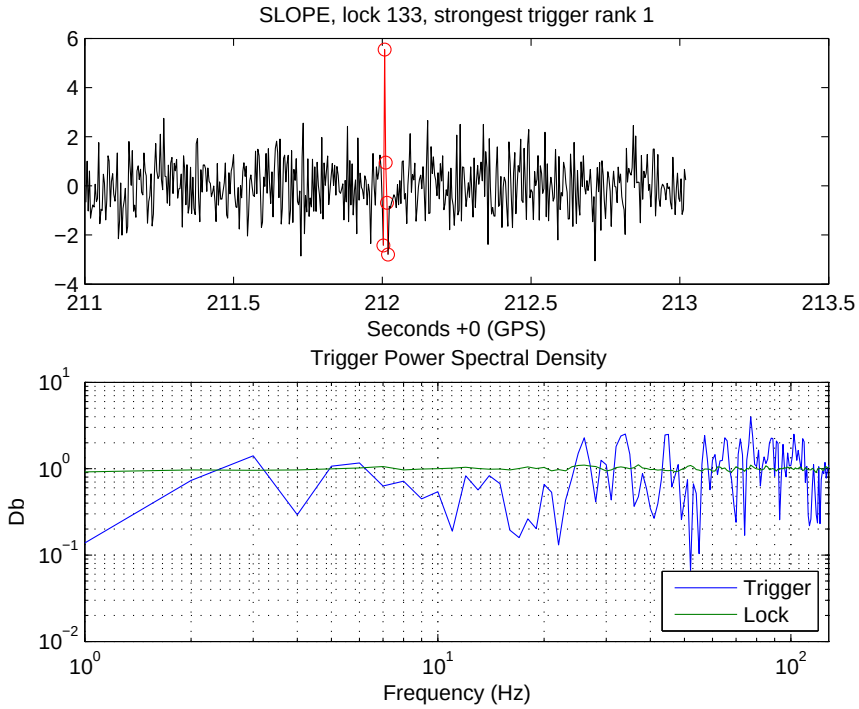


**Figure D.4.** Strongest SLOPE trigger from all S3 playground data segments.

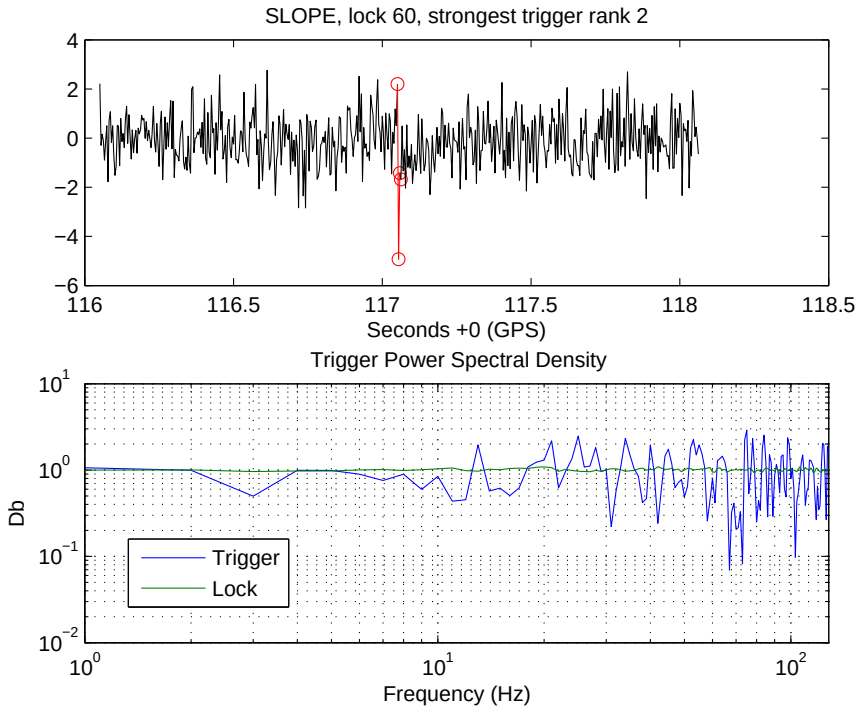


**Figure D.5.** Second strongest SLOPE trigger from all white noise data segments.

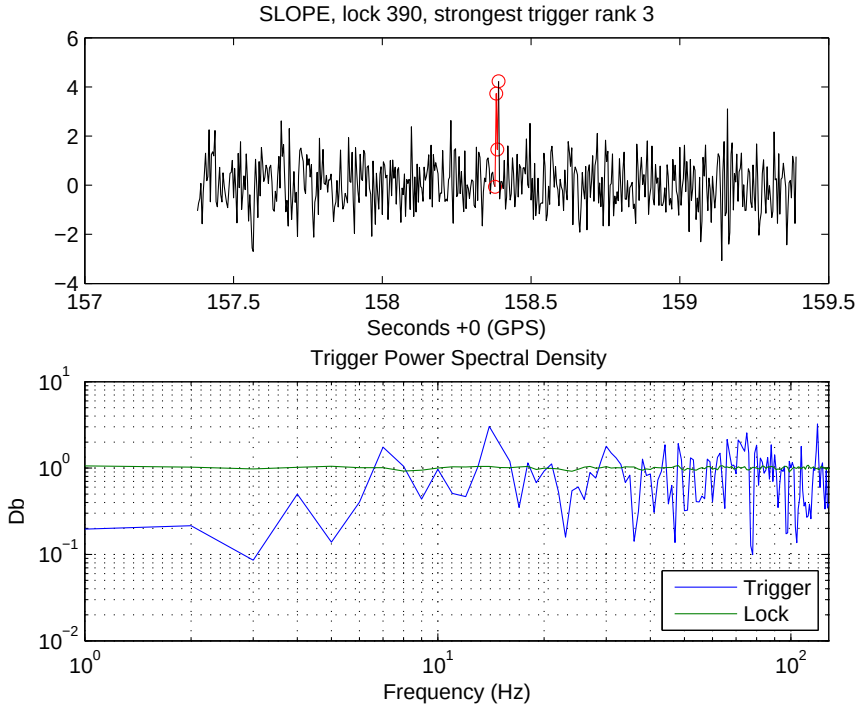


**Figure D.6.** Third strongest SLOPE trigger from all white noise data segments.

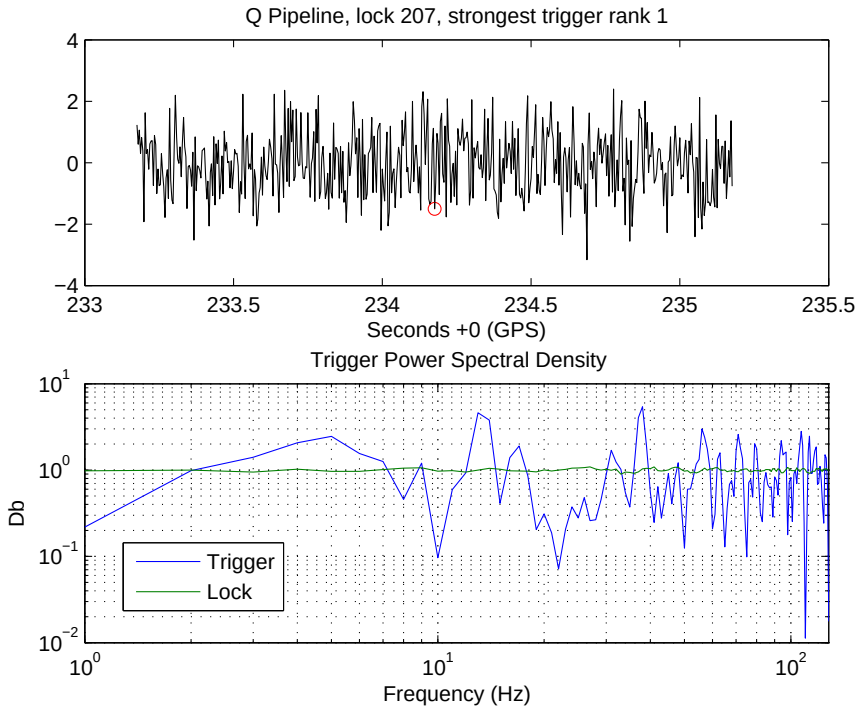


**Figure D.7.** Strongest Q Pipeline trigger from all white noise data segments.

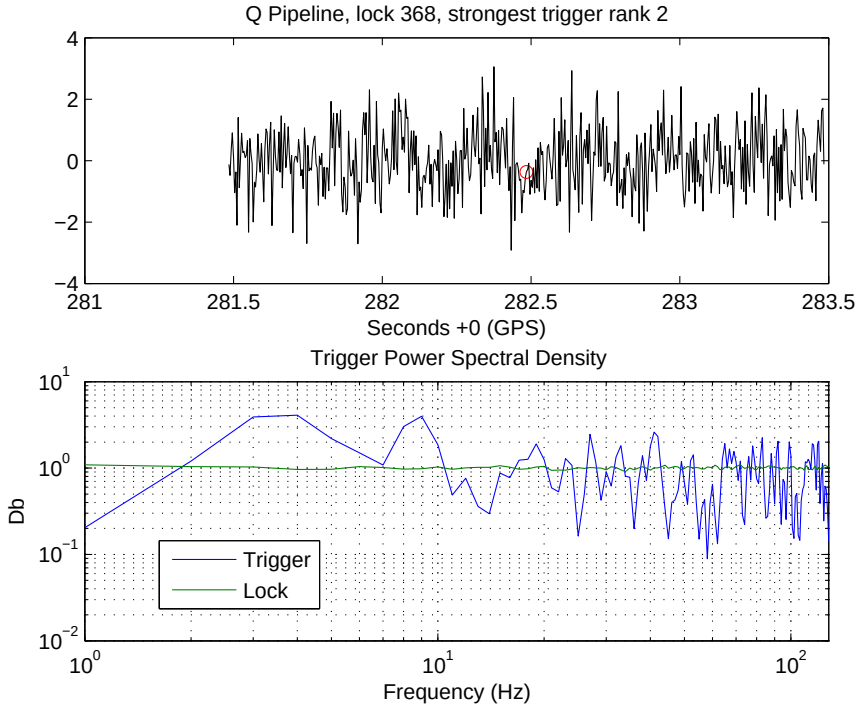


**Figure D.8.** Second strongest Q Pipeline trigger from all white noise data segments.

| **10 Strongest Triggers** | BlockNormal | SLOPE | Q Pipeline |
|---|---|---|---|
| Average duration | 17.188 msec | 15.625 msec | N/A |
| Average mean | 0.2416 | -0.01221 | N/A |
| Average variance | 11.368 | 8.7036 | N/A |

**Table D.1.** Characteristics of the data within the 10 strongest triggers from all white noise data segments (since Q Pipeline is a frequency-domain ETG, the duration of a trigger is not well defined, and therefore neither is the mean or variance of the trigger). The average mean and variance of all of the white noise data sets is 0 and 1, respectively.

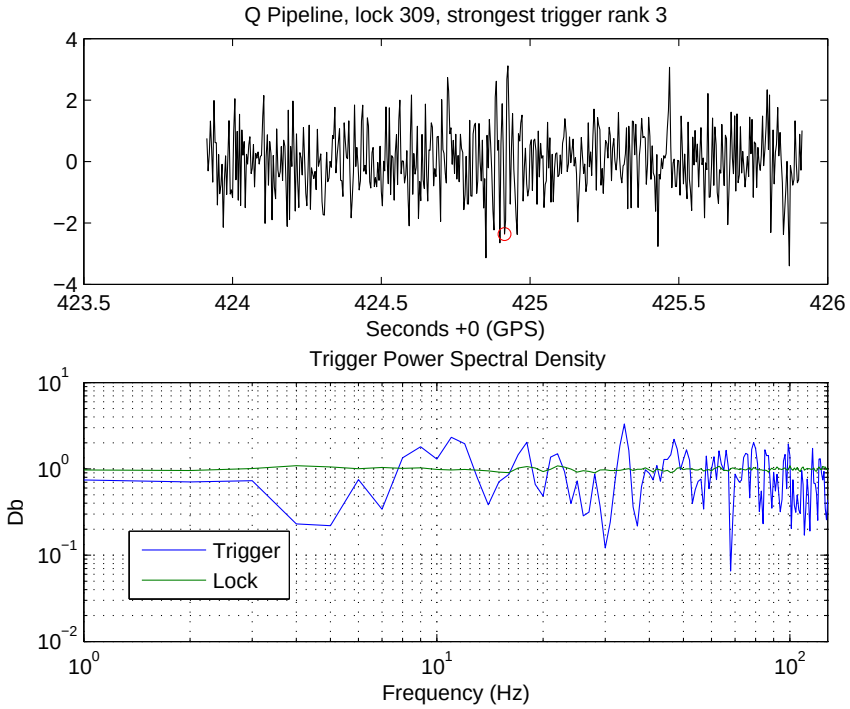


**Figure D.9.** Third strongest Q Pipeline trigger from all white noise data segments.

Appendix E

# Full Efficiency Profiles of ETG Performances With Respect to a Specific Signal

Measuring the efficiency of a signal of varying amplitude and duration produces a three dimensional surface which can be compared between ETGs. Efficiency profiles are the basis of the investigations of Chapter 7 and the profiles shown here are summarized by the $A_{50}$ curves of Figures 7.1, 7.3 and 7.5 and the sigmoid slope curves in Figures 7.2, 7.4 and 7.6.

The plots shown in this appendix show the efficiency profile for each ETG, *using its current practical tuning* (q.v. Sections 3.4, 4.5 and 5.6), as both a 3-dimensional surface and a contour plot. The 50% efficiency level on each plot is marked with '`x`'.

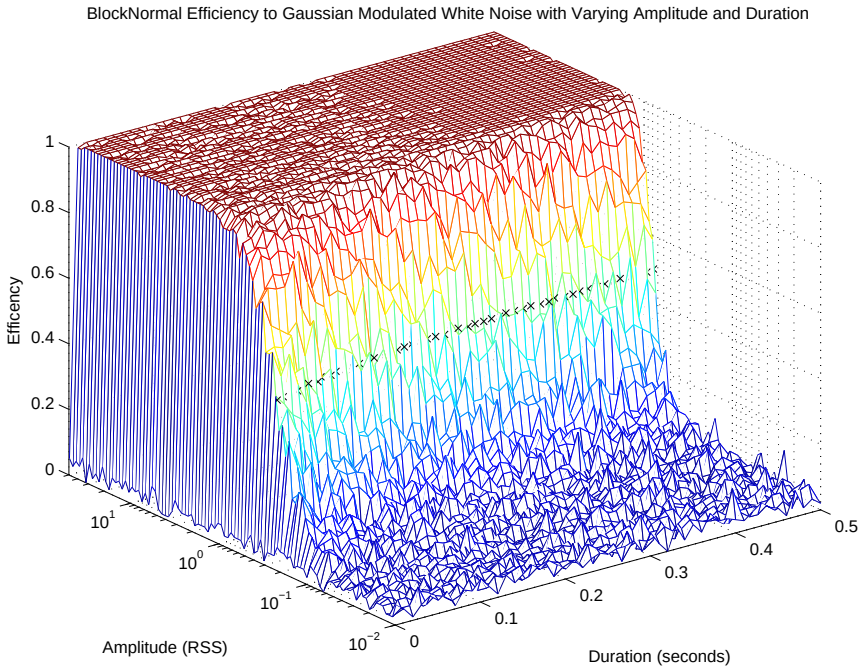


**Figure E.1.** BlockNormal efficiency to Gaussian modulated white noise with varying amplitude and duration (shown as a 3-dimensional surface).

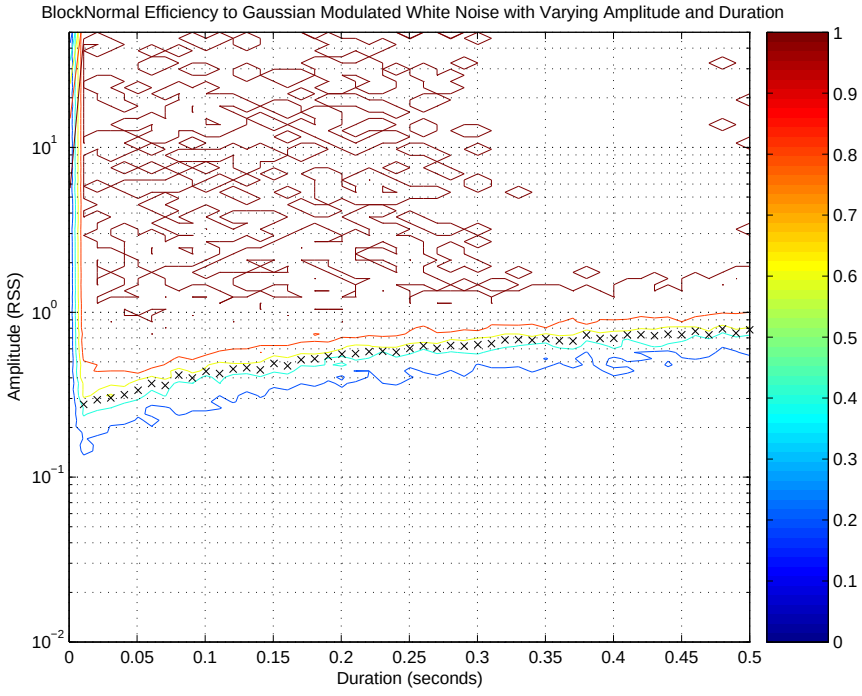


**Figure E.2.** BlockNormal efficiency to Gaussian modulated white noise with varying amplitude and duration (shown as a contour plot).

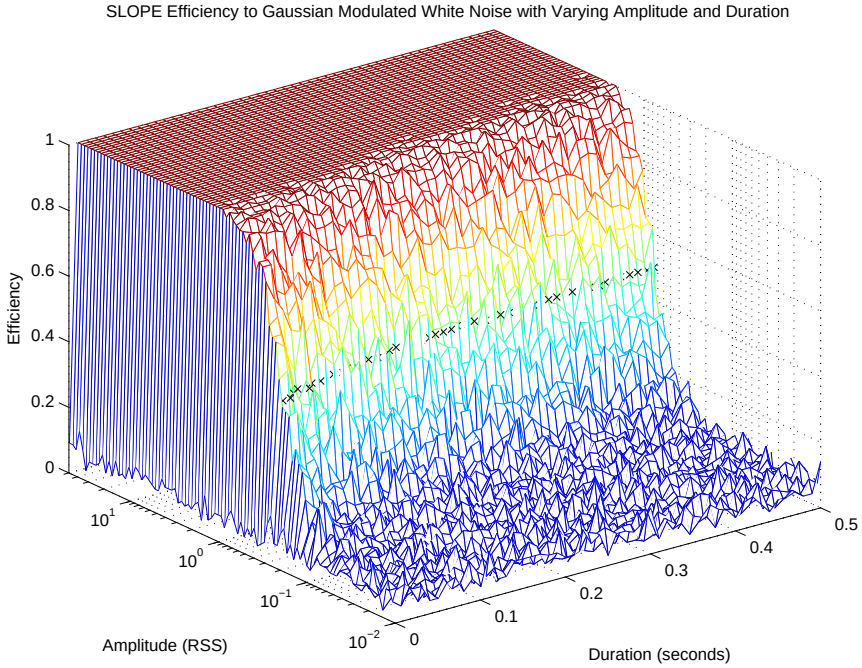


**Figure E.3.** SLOPE efficiency to Gaussian modulated white noise with varying amplitude and duration (shown as a 3-dimensional surface).

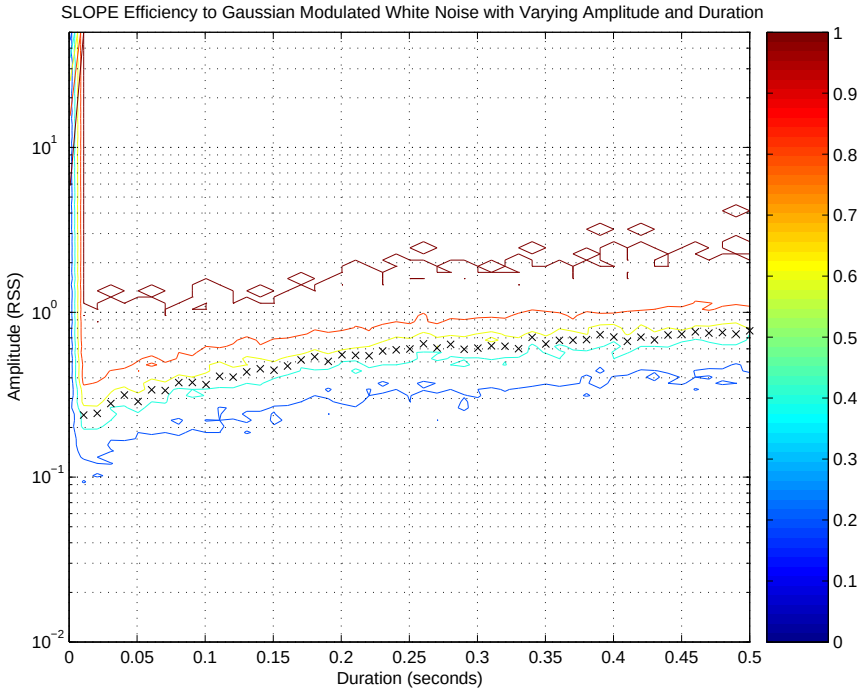


**Figure E.4.** SLOPE efficiency to Gaussian modulated white noise with varying amplitude and duration (shown as a contour plot).

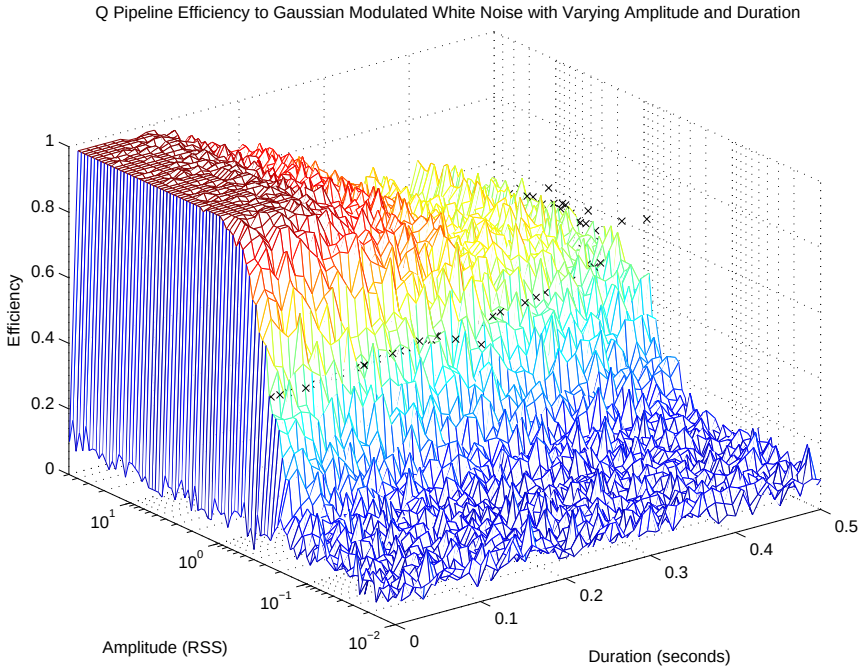


**Figure E.5.** Q Pipeline efficiency to Gaussian modulated white noise with varying amplitude and duration (shown as a 3-dimensional surface).

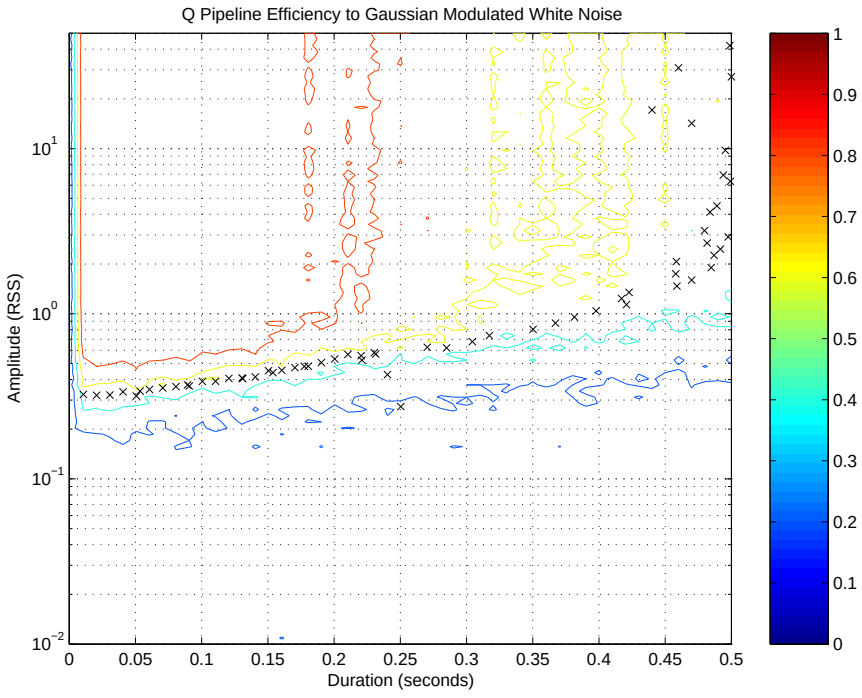


**Figure E.6.** Q Pipeline efficiency to Gaussian modulated white noise with varying amplitude and duration (shown as a contour).

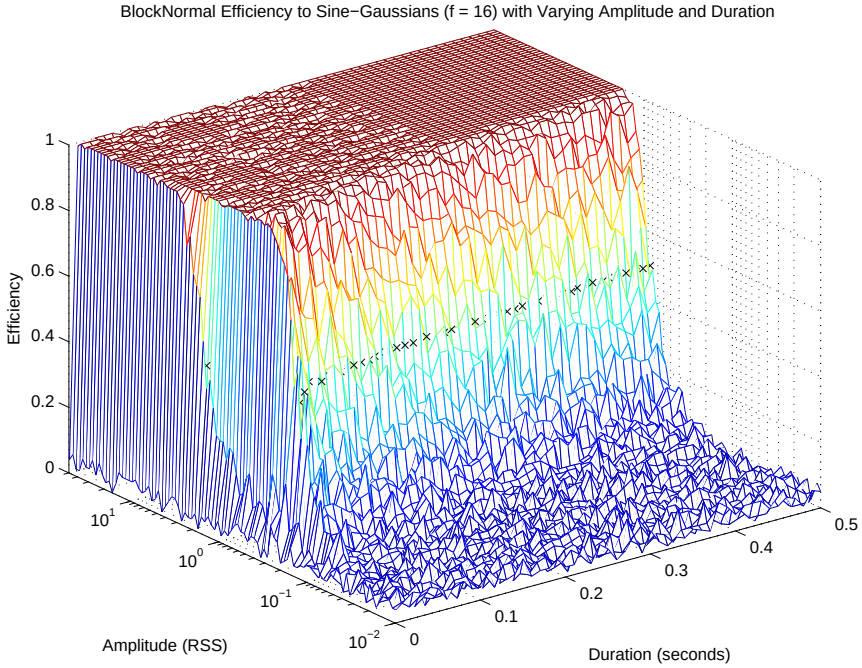


**Figure E.7.** BlockNormal efficiency to 16 Hz sine-Gaussians with varying amplitude and duration (shown as a 3-dimensional surface).

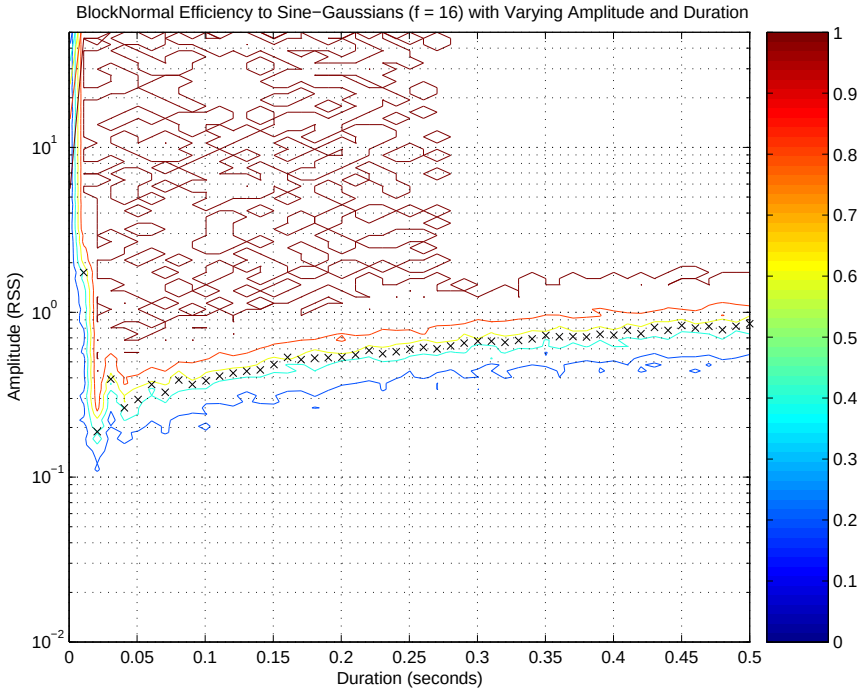


**Figure E.8.** BlockNormal efficiency to 16 Hz sine-Gaussians with varying amplitude and duration (shown as a contour plot).

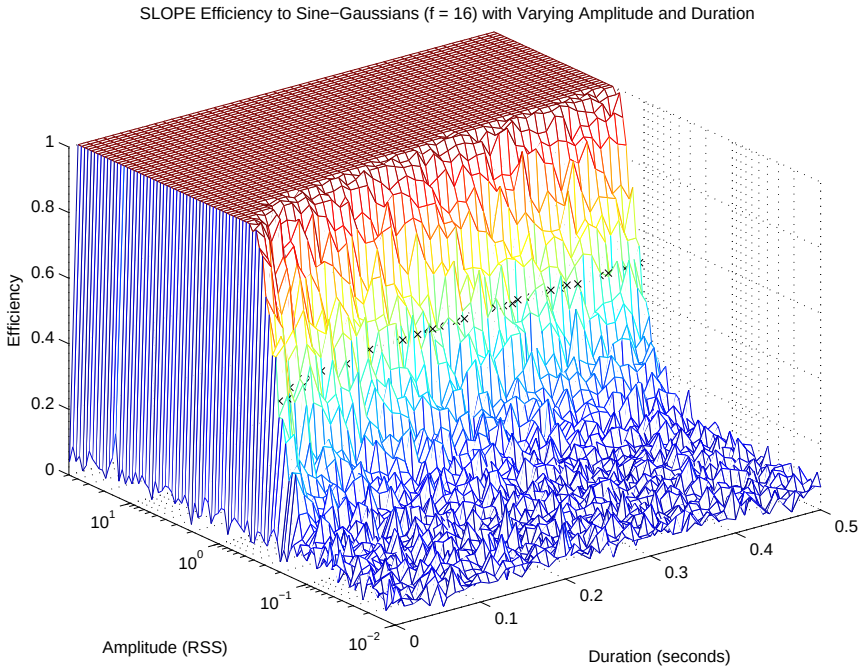


**Figure E.9.** SLOPE efficiency to 16 Hz sine-Gaussians with varying amplitude and duration (shown as a 3-dimensional surface).

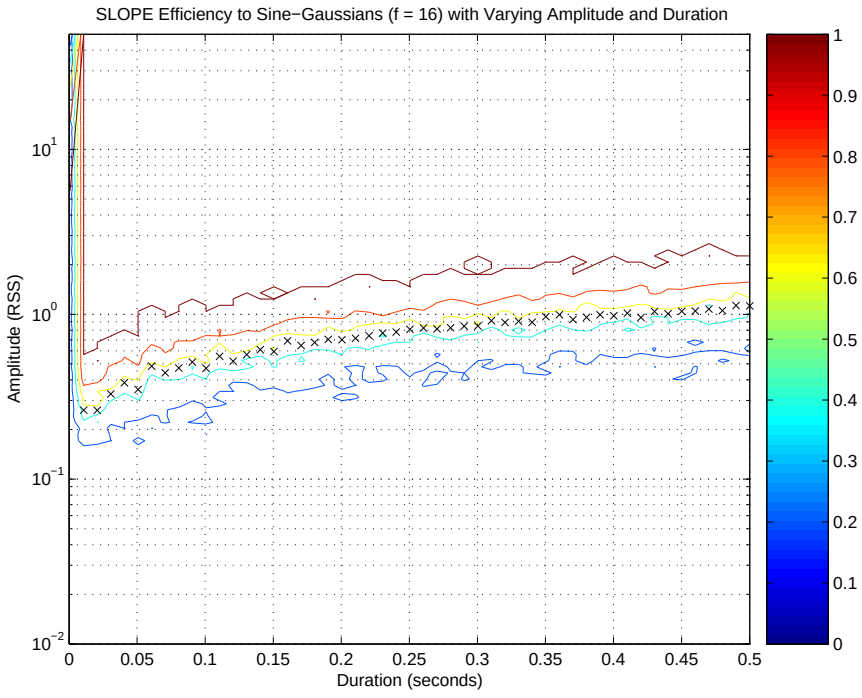


**Figure E.10.** SLOPE efficiency to 16 Hz sine-Gaussians with varying amplitude and duration (shown as a contour plot).

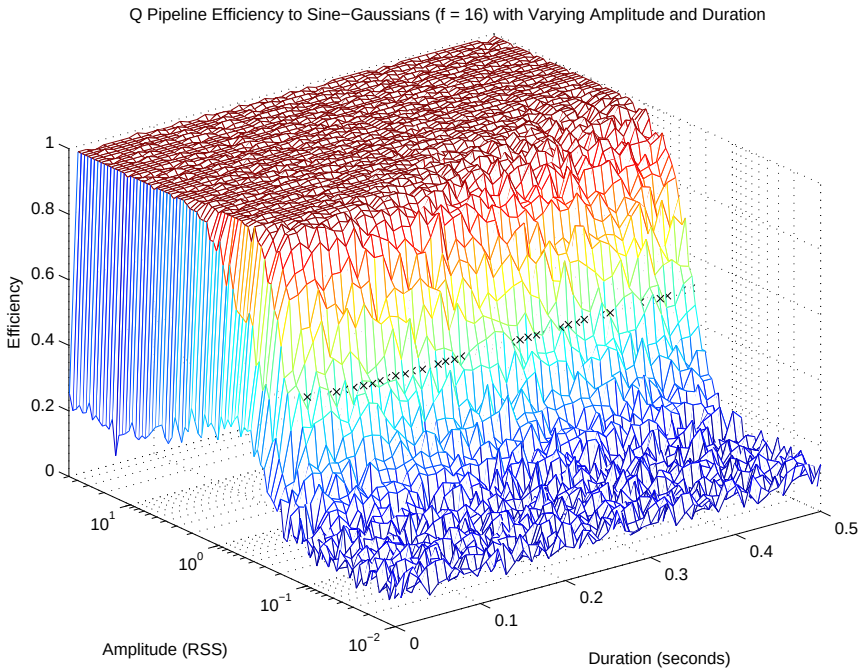


**Figure E.11.** Q Pipeline efficiency to 16 Hz sine-Gaussians with varying amplitude and duration (shown as a 3-dimensional surface).

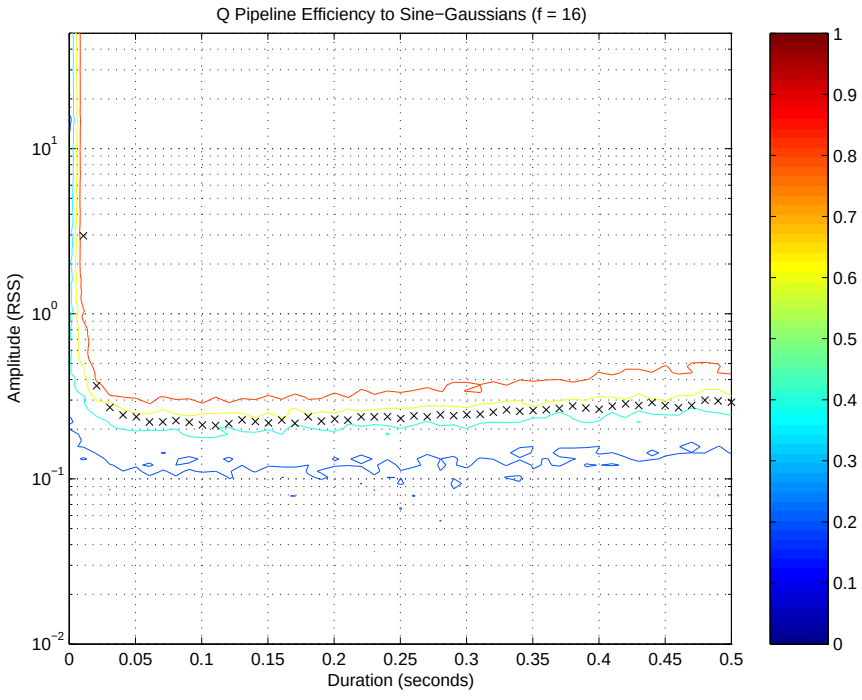


**Figure E.12.** Q Pipeline efficiency to 16 Hz sine-Gaussians with varying amplitude and duration (shown as a contour plot).

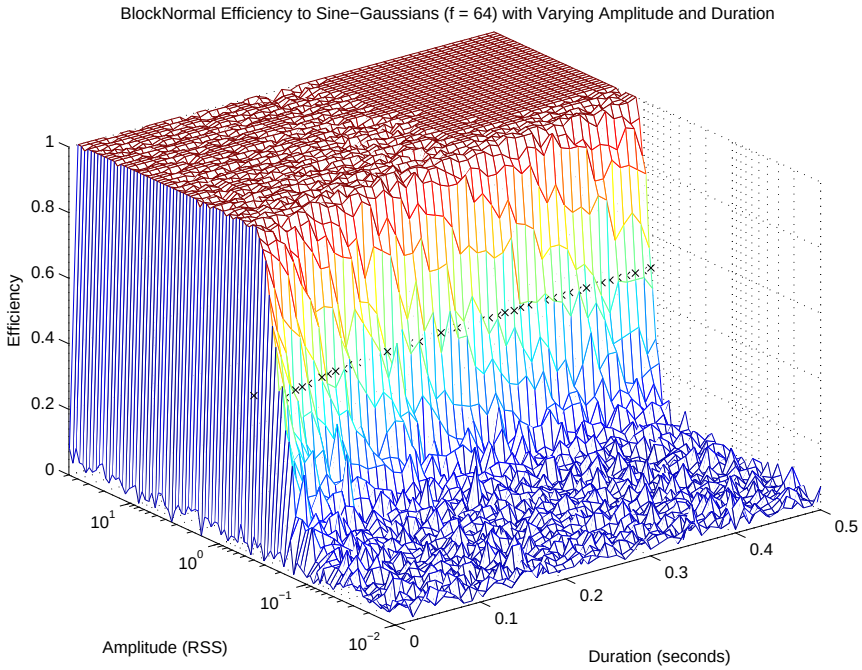


**Figure E.13.** BlockNormal efficiency to 64 Hz sine-Gaussians with varying amplitude and duration (shown as a 3-dimensional surface).

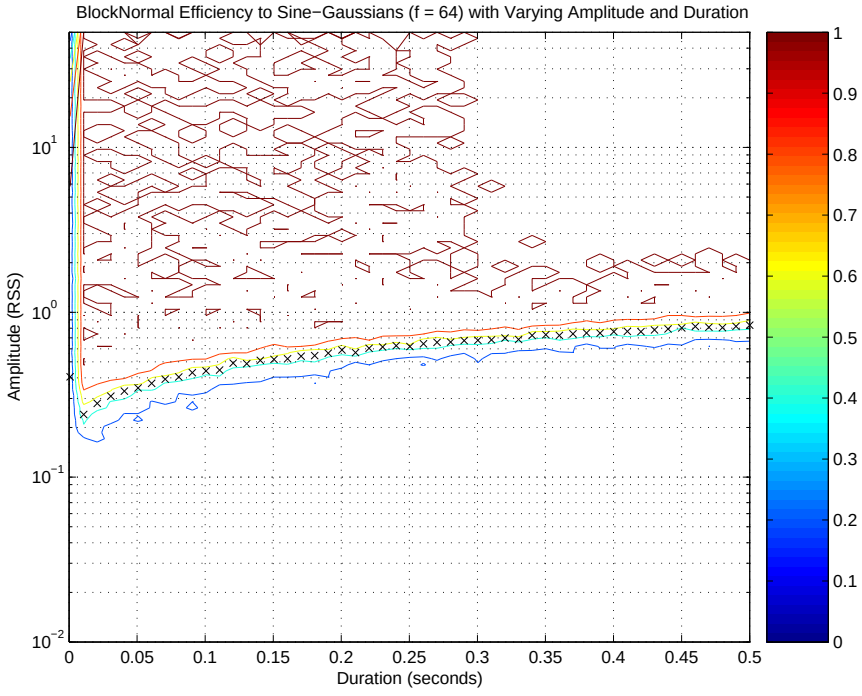


**Figure E.14.** BlockNormal efficiency to 64 Hz sine-Gaussians with varying amplitude and duration (shown as a contour plot).

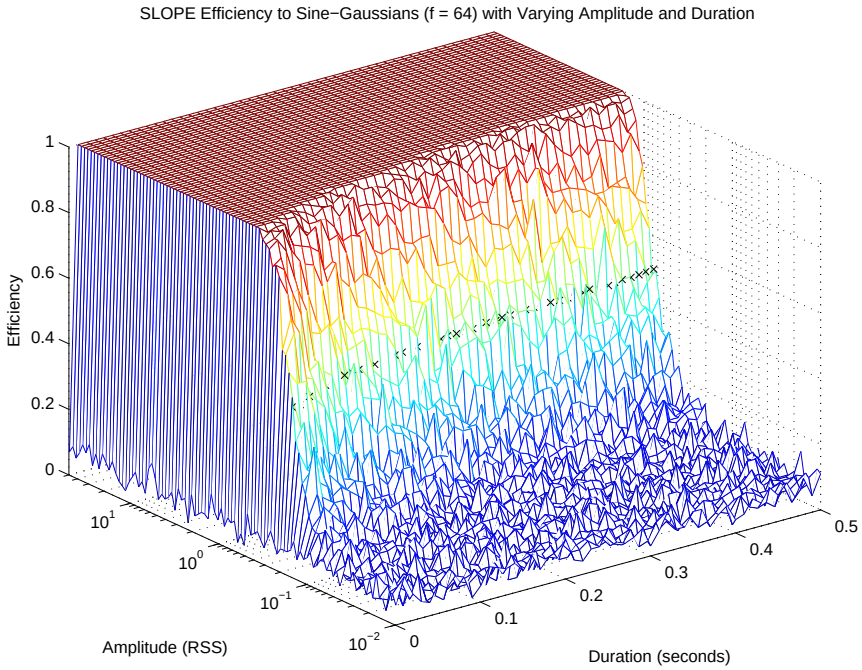


**Figure E.15.** SLOPE efficiency to 64 Hz sine-Gaussians with varying amplitude and duration (shown as a 3-dimensional surface).

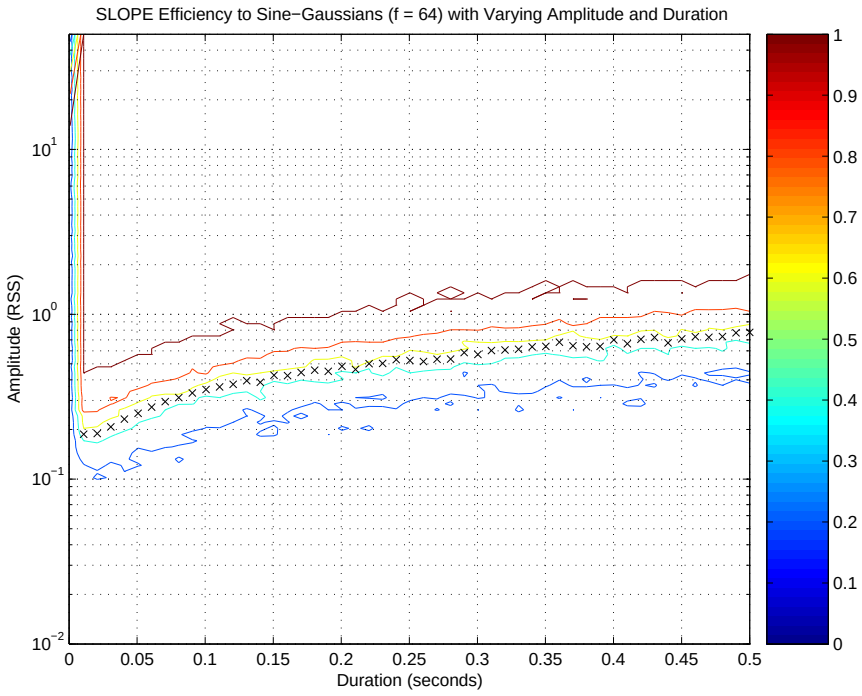


**Figure E.16.** SLOPE efficiency to 64 Hz sine-Gaussians with varying amplitude and duration (shown as a contour plot).

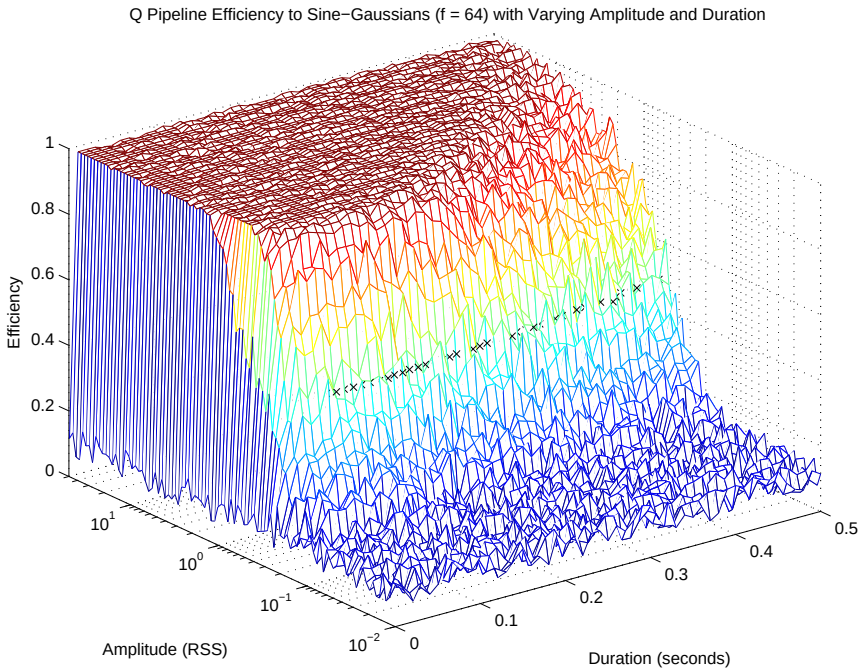


**Figure E.17.** Q Pipeline efficiency to 64 Hz sine-Gaussians with varying amplitude and duration (shown as a 3-dimensional surface).

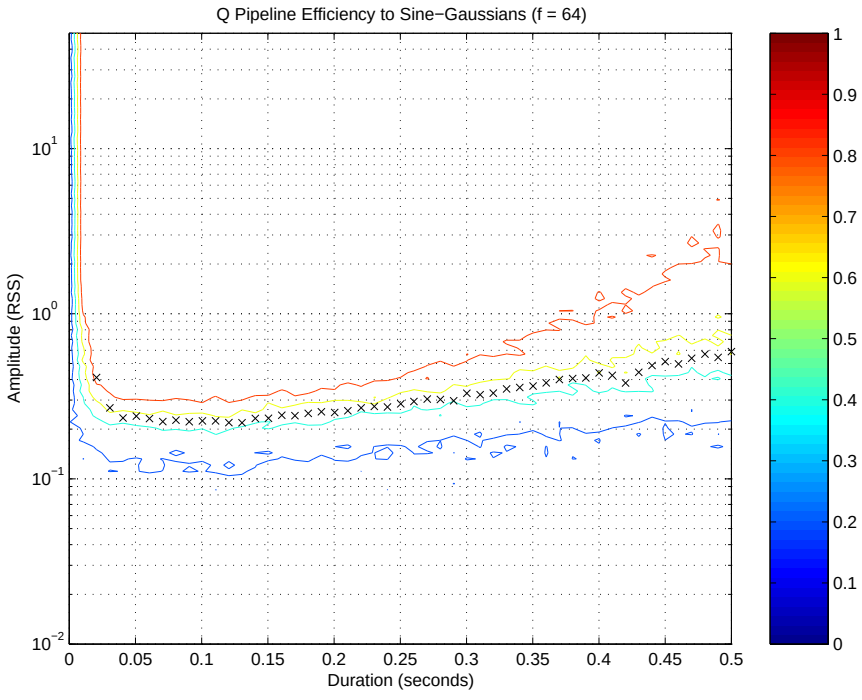


**Figure E.18.** Q Pipeline efficiency to 64 Hz sine-Gaussians with varying amplitude and duration (shown as a contour plot).

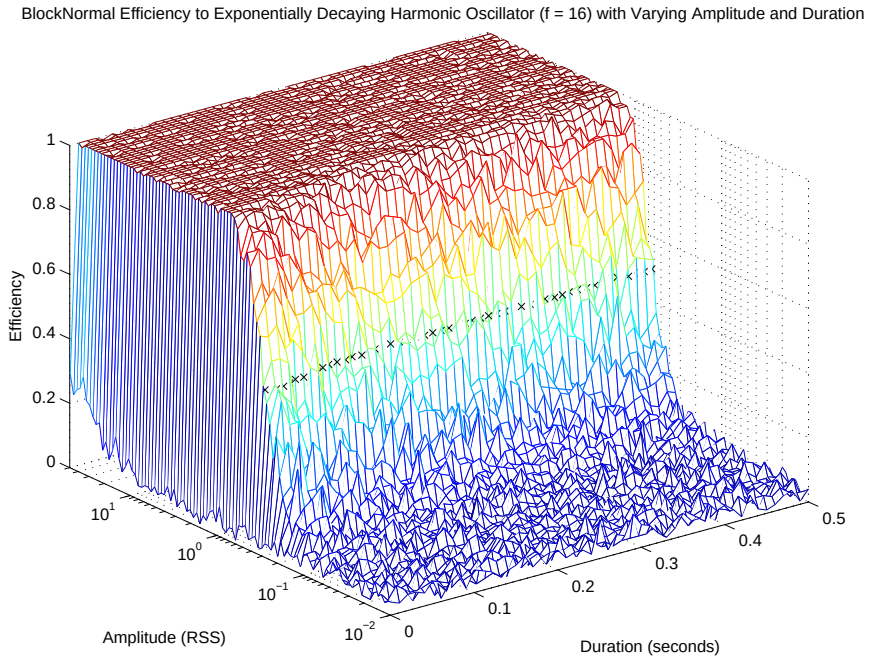


**Figure E.19.** BlockNormal efficiency to exponentially decaying harmonic oscillators of 16 Hz with varying amplitude and duration (shown as a 3-dimensional surface).

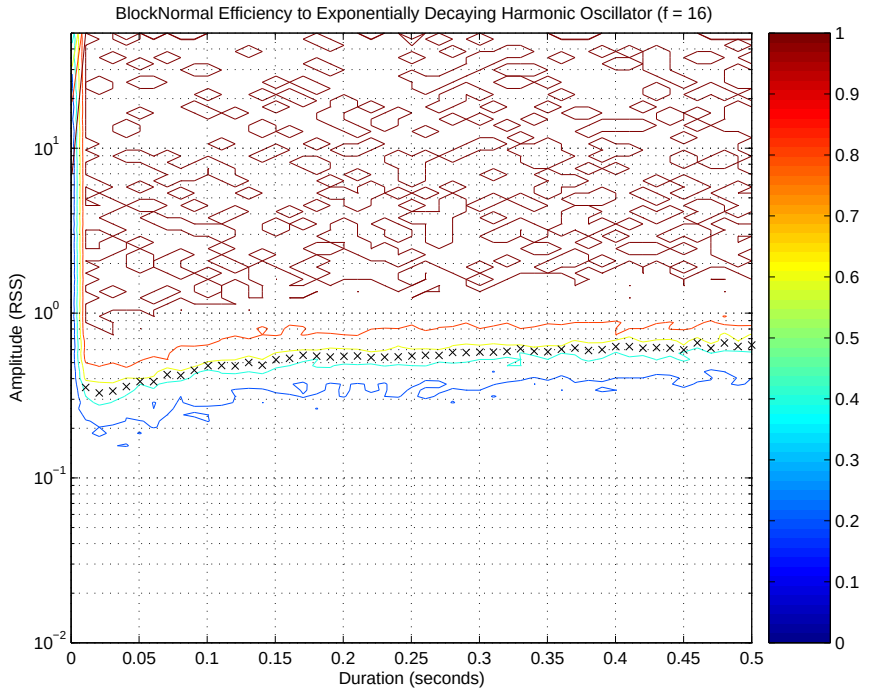


**Figure E.20.** BlockNormal efficiency to exponentially decaying harmonic oscillators of 16 Hz with varying amplitude and duration (shown as a contour plot).

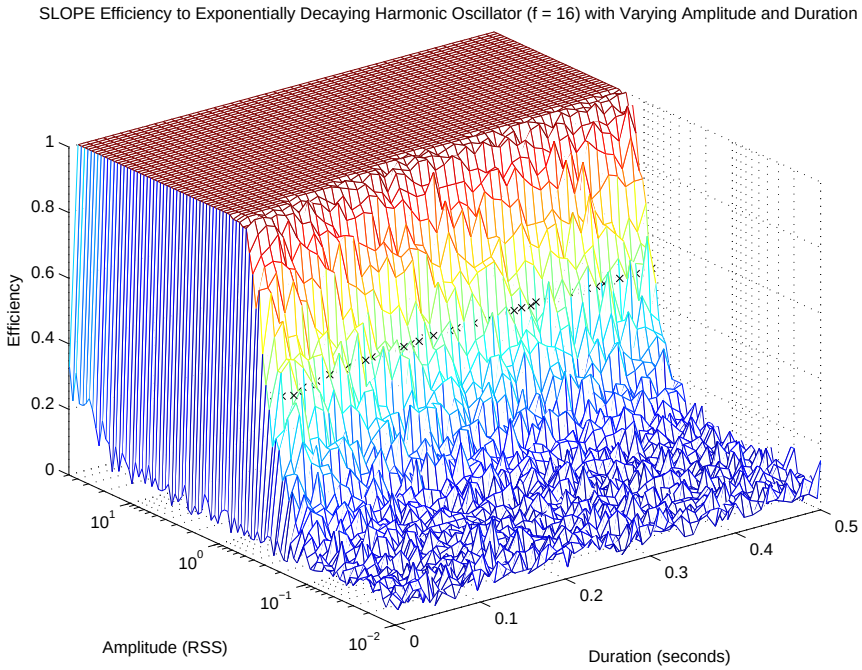


**Figure E.21.** SLOPE efficiency to exponentially decaying harmonic oscillators of 16 Hz with varying amplitude and duration (shown as a 3-dimensional surface).

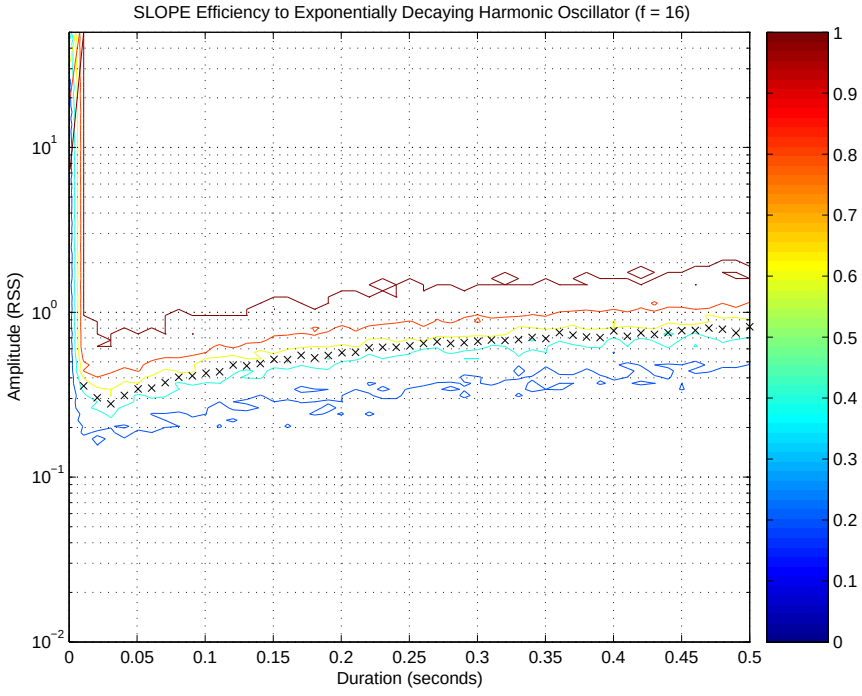


**Figure E.22.** SLOPE efficiency to exponentially decaying harmonic oscillators of 16 Hz with varying amplitude and duration (shown as a contour plot).

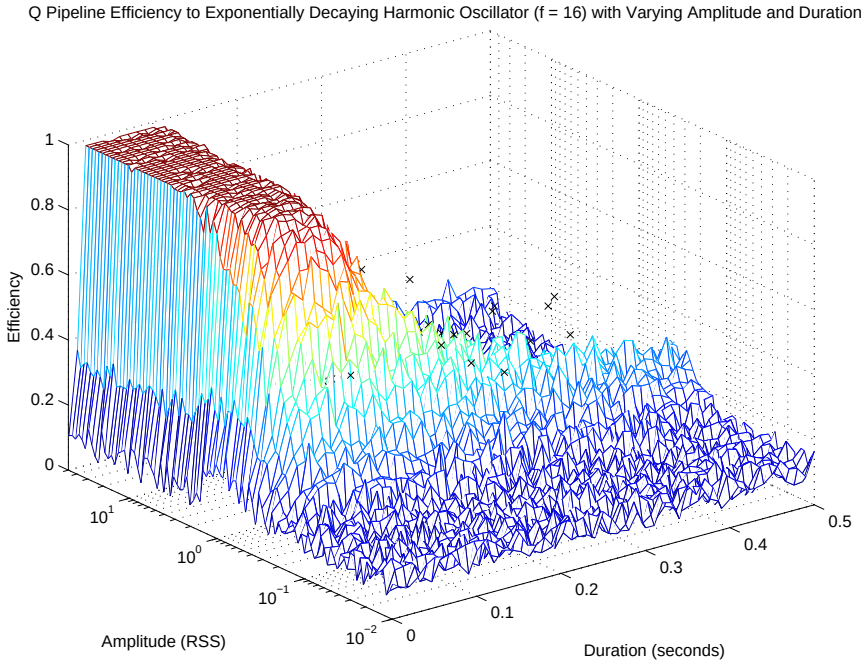


**Figure E.23.** Q Pipeline efficiency to exponentially decaying harmonic oscillators of 16 Hz with varying amplitude and duration (shown as a 3-dimensional surface).

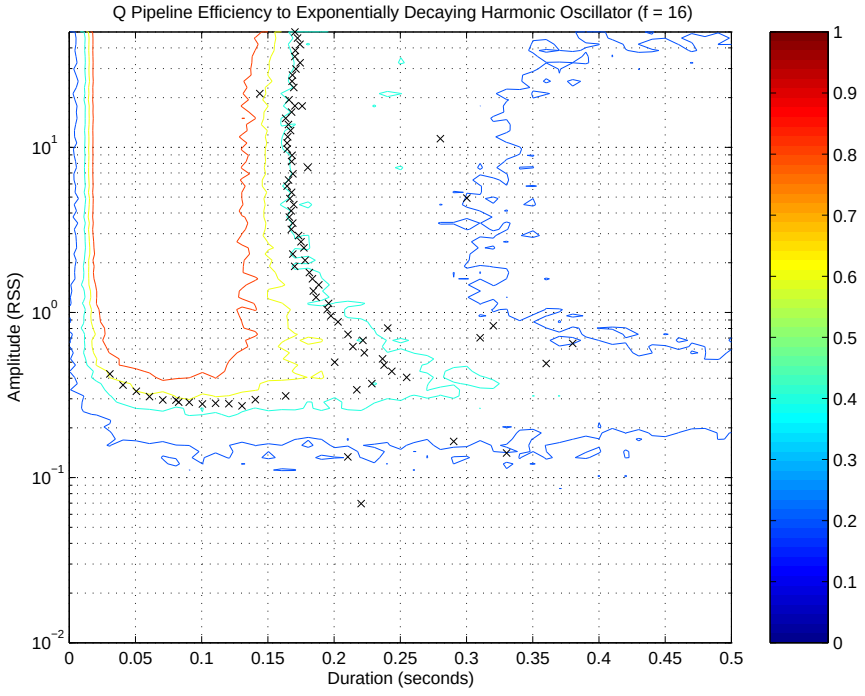


**Figure E.24.** Q Pipeline efficiency to exponentially decaying harmonic oscillators of 16 Hz with varying amplitude and duration (shown as a contour plot).

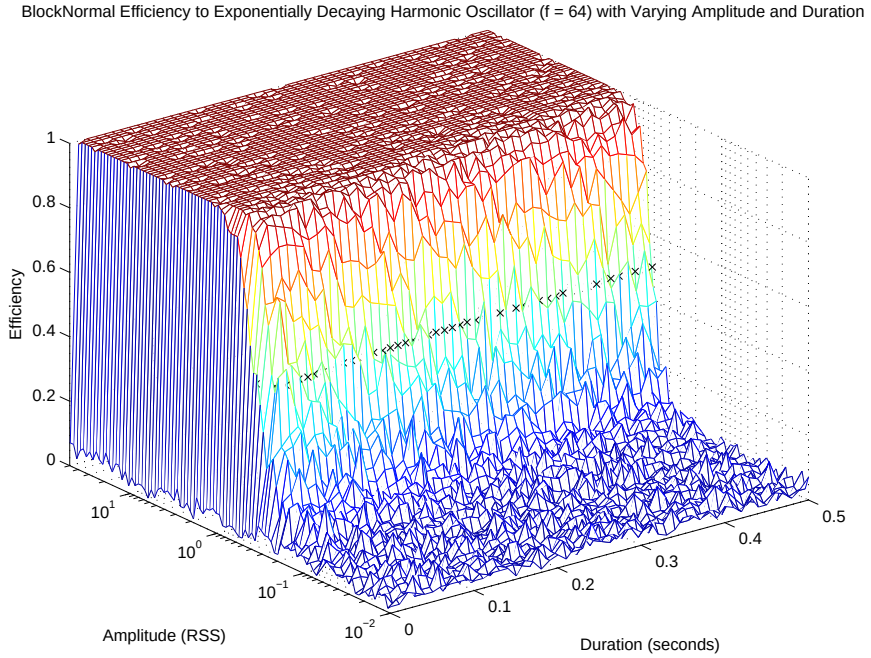


**Figure E.25.** BlockNormal efficiency to exponentially decaying harmonic oscillators of 64 Hz with varying amplitude and duration (shown as a 3-dimensional surface).

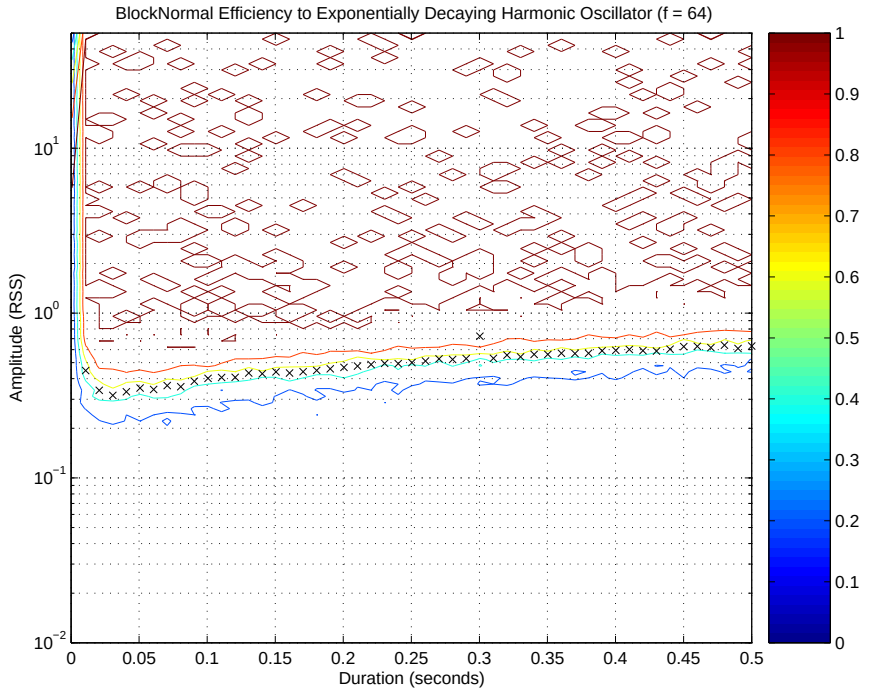


**Figure E.26.** BlockNormal efficiency to exponentially decaying harmonic oscillators of 64 Hz with varying amplitude and duration (shown as a contour plot).

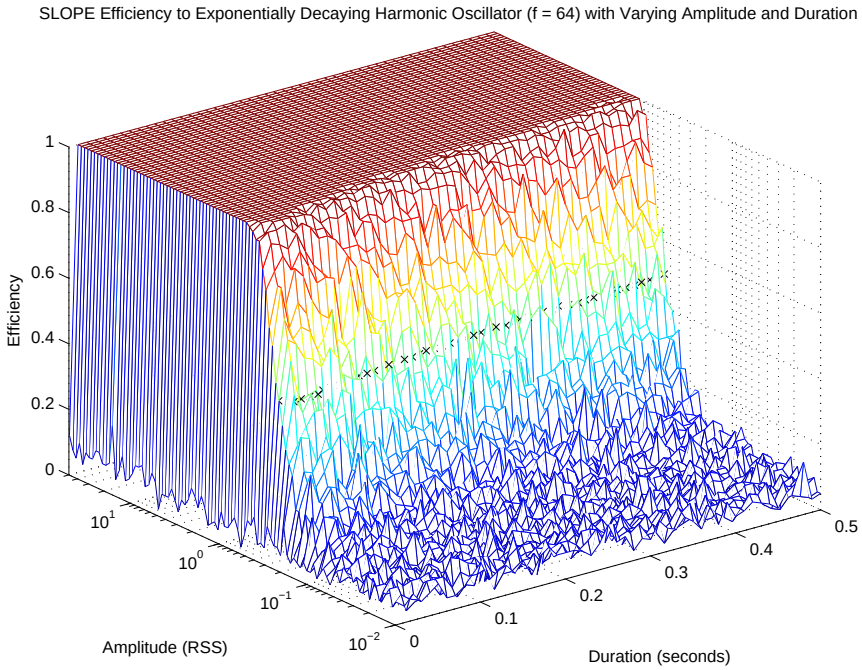


**Figure E.27.** SLOPE efficiency to exponentially decaying harmonic oscillators of 64 Hz with varying amplitude and duration (shown as a 3-dimensional surface).

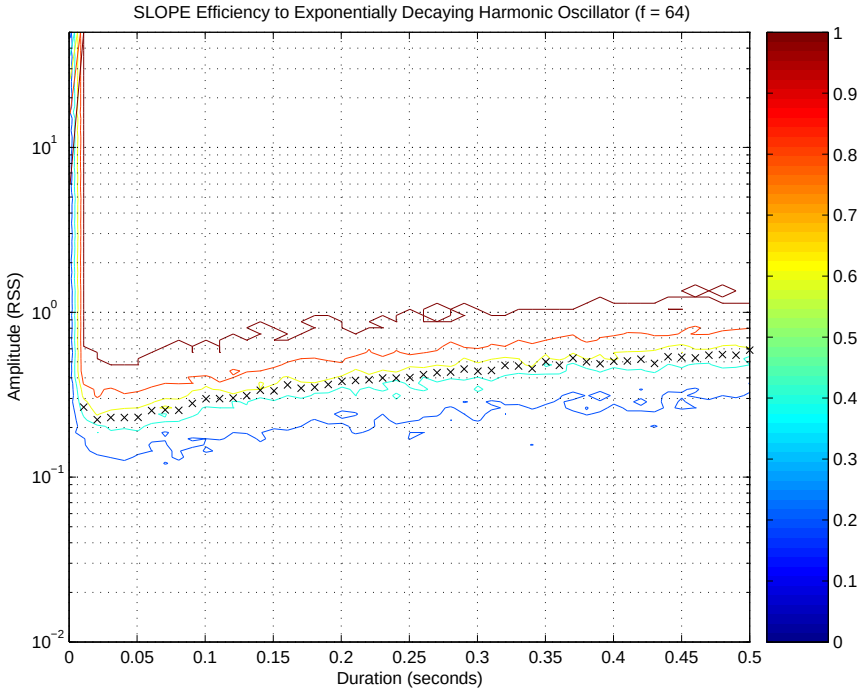


**Figure E.28.** SLOPE efficiency to exponentially decaying harmonic oscillators of 64 Hz with varying amplitude and duration (shown as a contour plot).

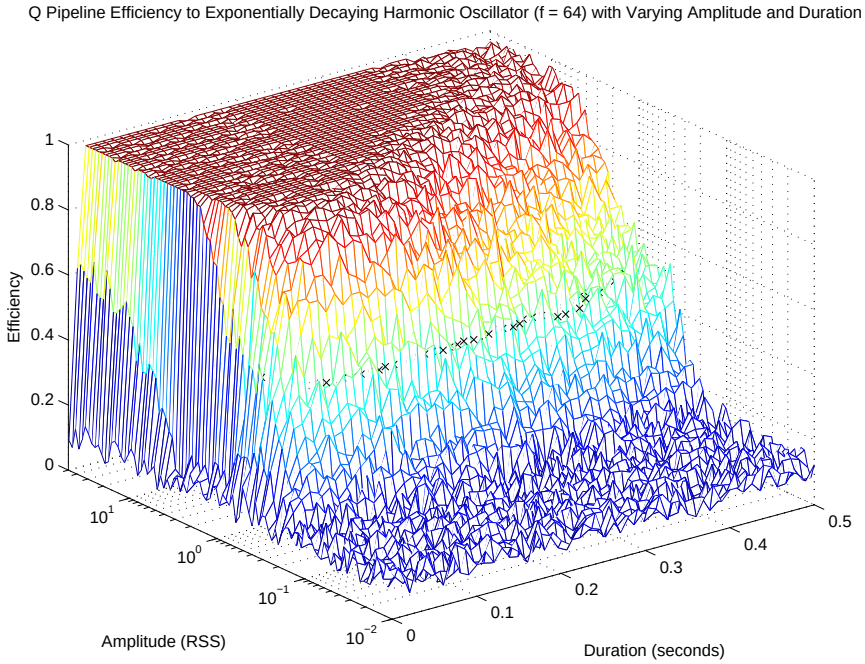


**Figure E.29.** Q Pipeline efficiency to exponentially decaying harmonic oscillators of 64 Hz with varying amplitude and duration (shown as a 3-dimensional surface).

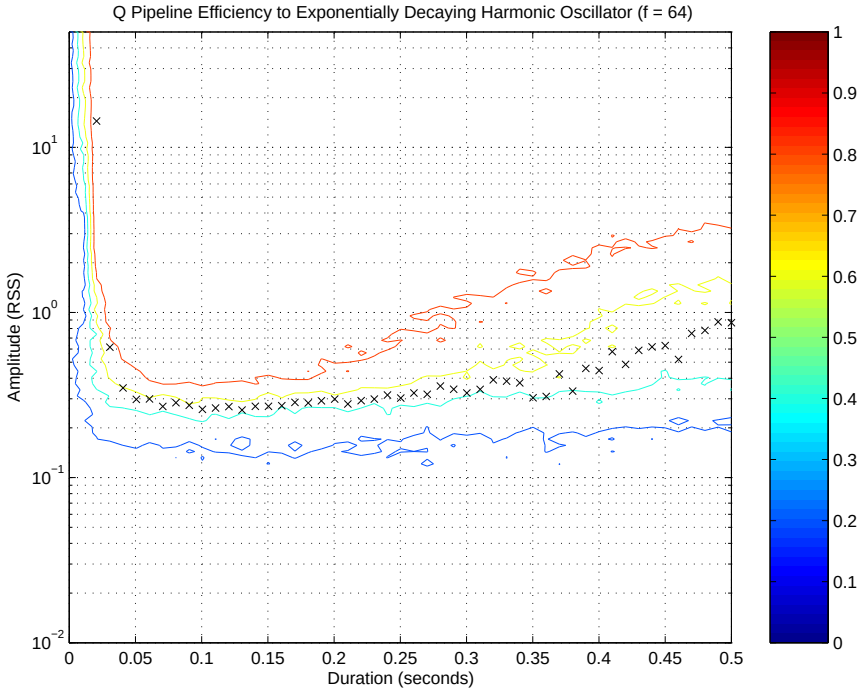


**Figure E.30.** Q Pipeline efficiency to exponentially decaying harmonic oscillators of 64 Hz with varying amplitude and duration (shown as a contour plot).

Appendix F

# Full Efficiency Profiles of BlockNormal and SLOPE Performances With Respect to a Specific Signal Using an Alternative Tuning

Measuring the efficiency of a signal of varying amplitude and duration produces a three dimensional surface which can be compared between ETGs. Efficiency profiles are the basis of the investigations of Chapter 7 and the profiles shown here are summarized in Section 7.4 by the $A_{50}$ curves of Figures 7.7 and 7.8.

The plots shown in this appendix show the efficiency profile of each signal type and frequency for each ETG, *using a previous, incorrect tuning* (q.v. Section 7.4), as both a 3-dimensional surface and a contour plot. The 50% efficiency level on each plot is marked with '`x`' and the label '[alt tune]' is applied to the figure captions to distinguish them from the figures in Appendix E .

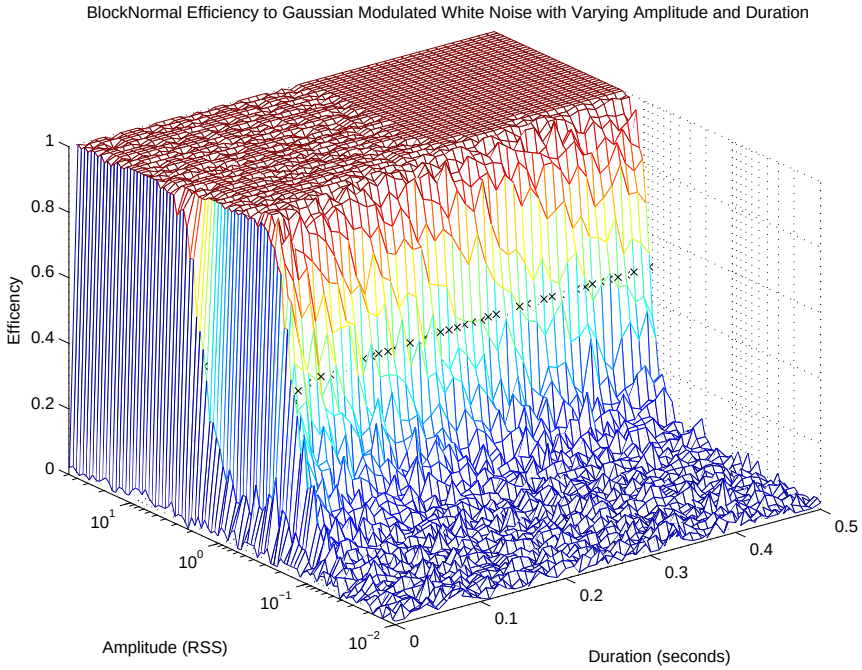


**Figure F.1.** BlockNormal efficiency to Gaussian modulated white noise with varying amplitude and duration (shown as a 3-dimensional surface) [alt tune].

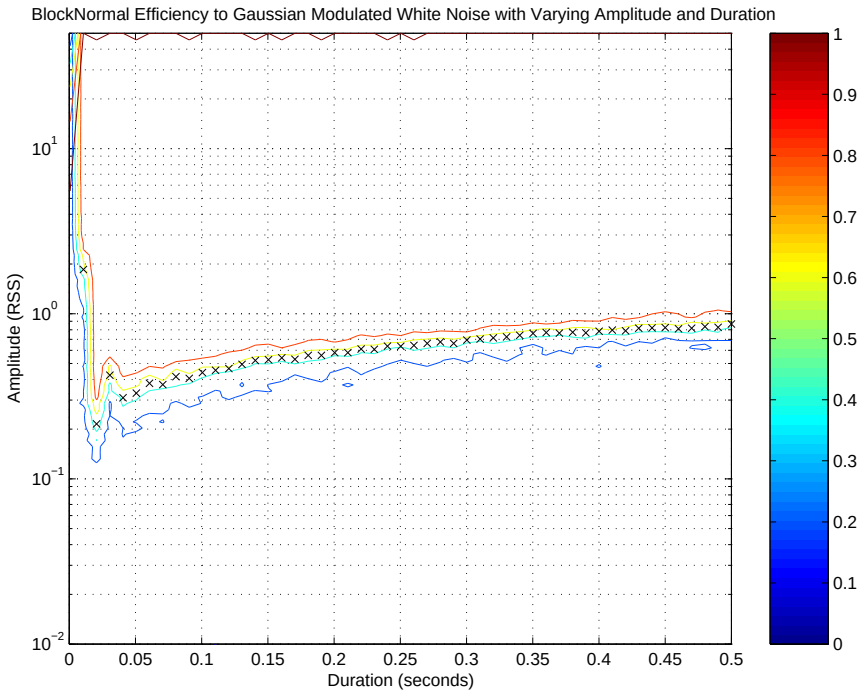


**Figure F.2.** BlockNormal efficiency to Gaussian modulated white noise with varying amplitude and duration (shown as a contour plot) [alt tune].

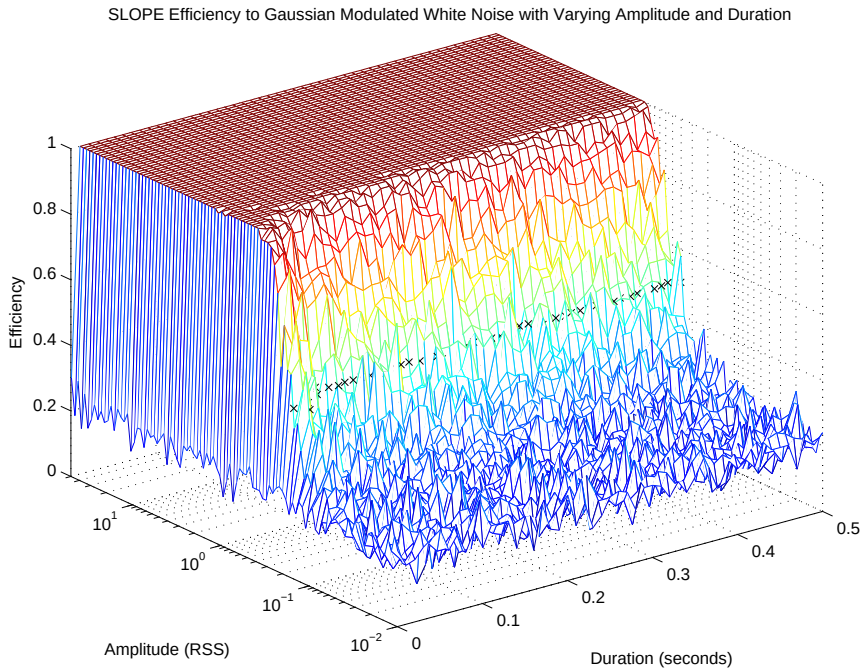


**Figure F.3.** SLOPE efficiency to Gaussian modulated white noise with varying amplitude and duration (shown as a 3-dimensional surface) [alt tune].

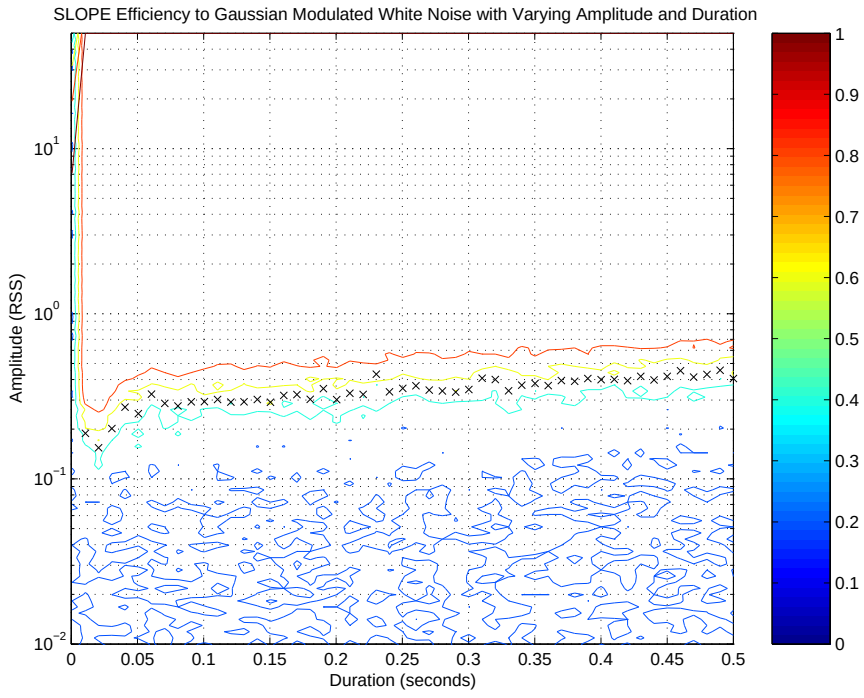


**Figure F.4.** SLOPE efficiency to Gaussian modulated white noise with varying amplitude and duration (shown as a contour plot) [alt tune].

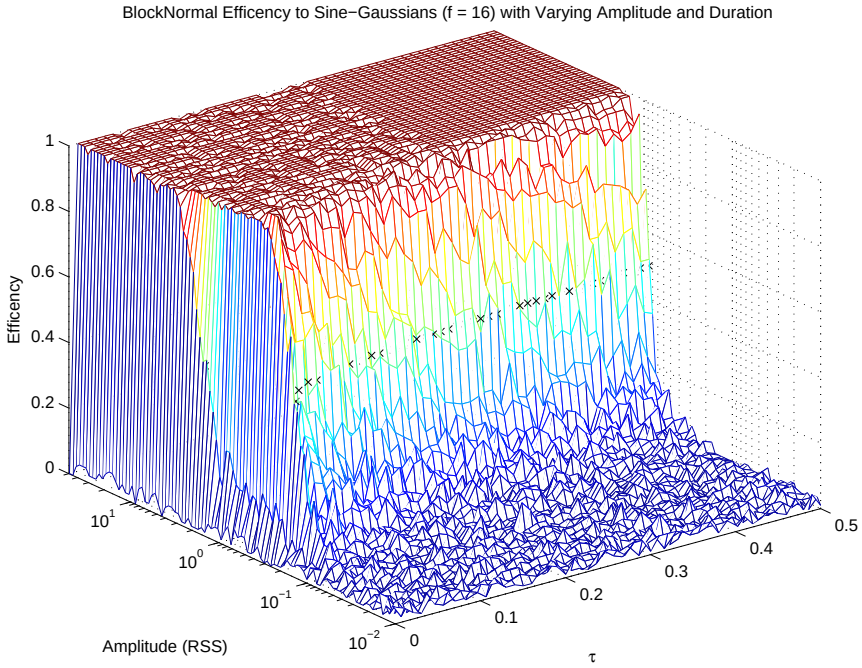


**Figure F.5.** BlockNormal efficiency to 16 Hz sine-Gaussians with varying amplitude and duration (shown as a 3-dimensional surface) [alt tune].

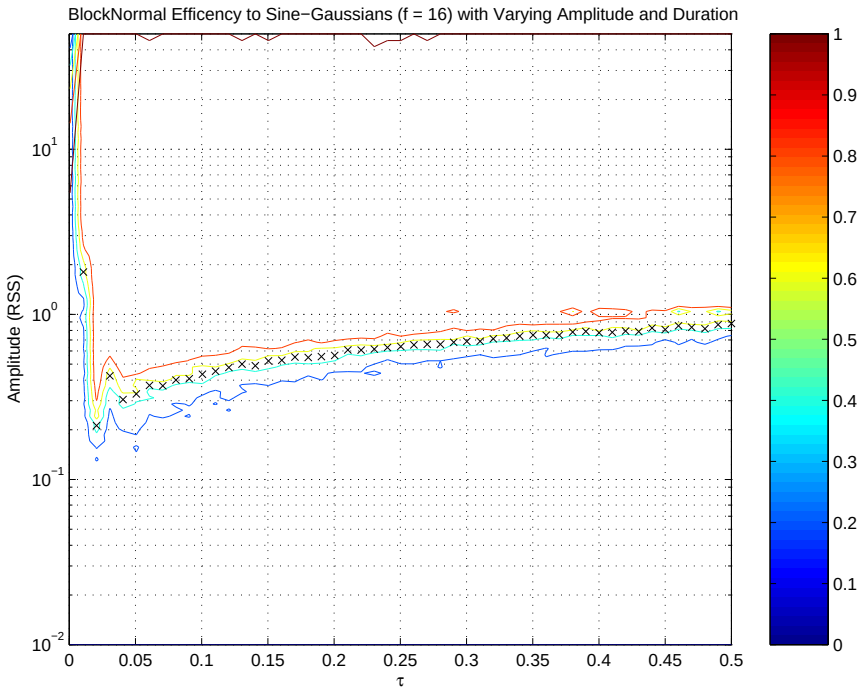


**Figure F.6.** BlockNormal efficiency to 16 Hz sine-Gaussians with varying amplitude and duration (shown as a contour plot) [alt tune].

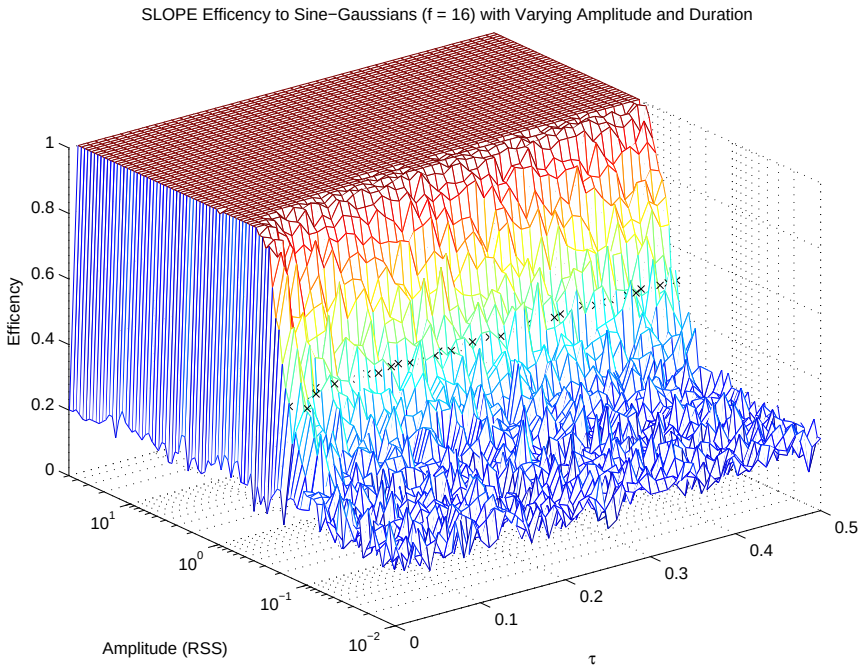


**Figure F.7.** SLOPE efficiency to 16 Hz sine-Gaussians with varying amplitude and duration (shown as a 3-dimensional surface) [alt tune].

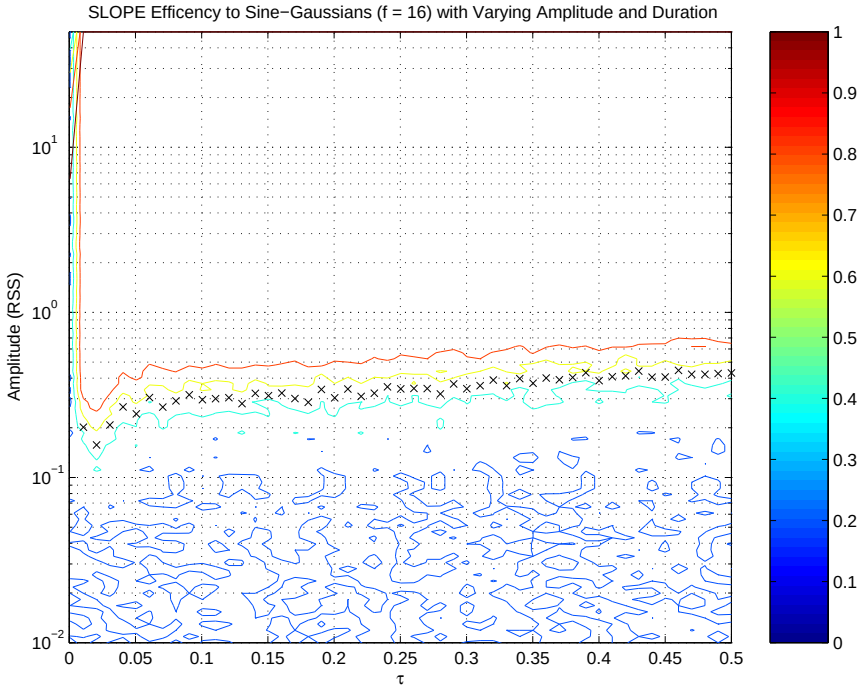


**Figure F.8.** SLOPE efficiency to 16 Hz sine-Gaussians with varying amplitude and duration (shown as a contour plot) [alt tune].

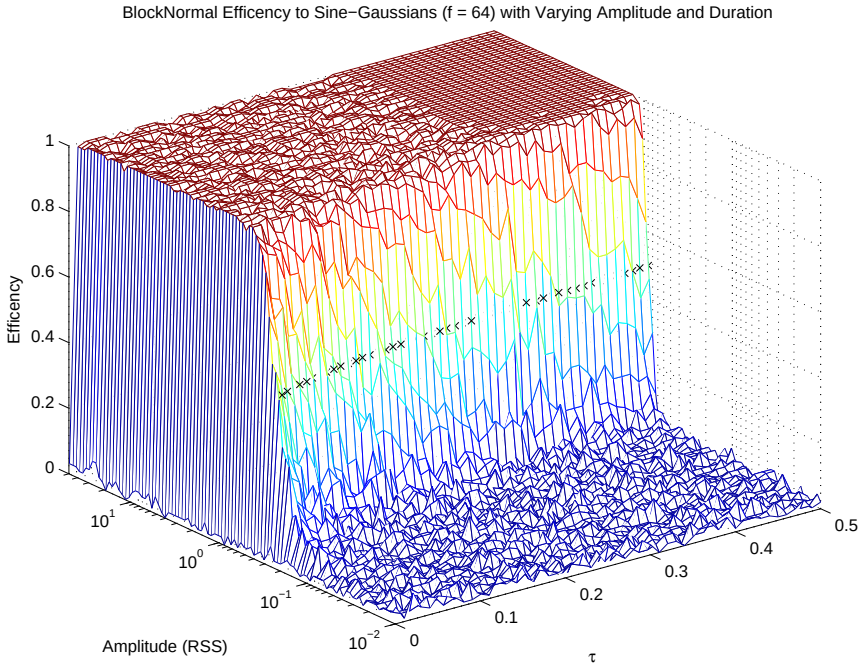


**Figure F.9.** BlockNormal efficiency to 64 Hz sine-Gaussians with varying amplitude and duration (shown as a 3-dimensional surface) [alt tune].

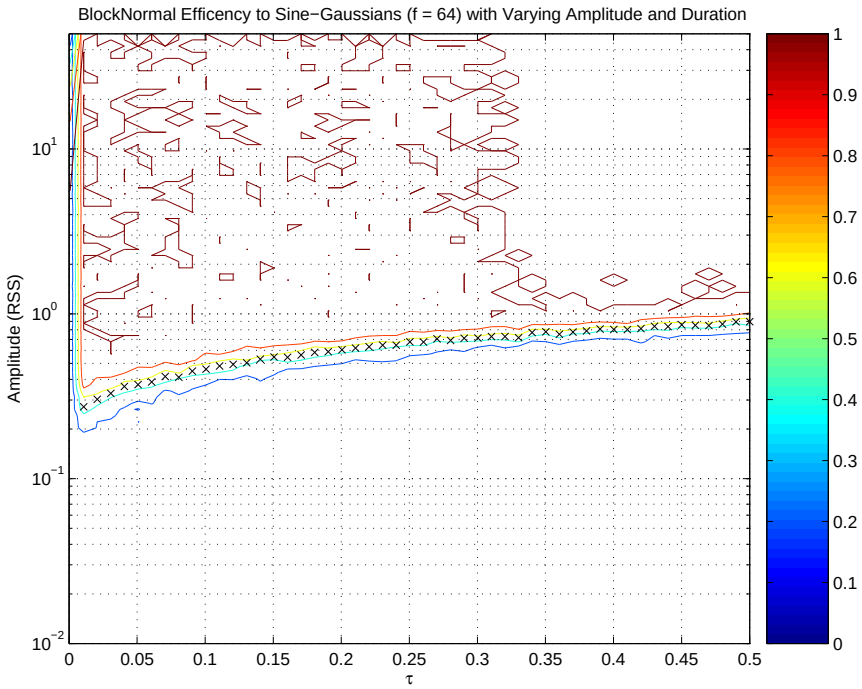


**Figure F.10.** BlockNormal efficiency to 64 Hz sine-Gaussians with varying amplitude and duration (shown as a contour plot) [alt tune].

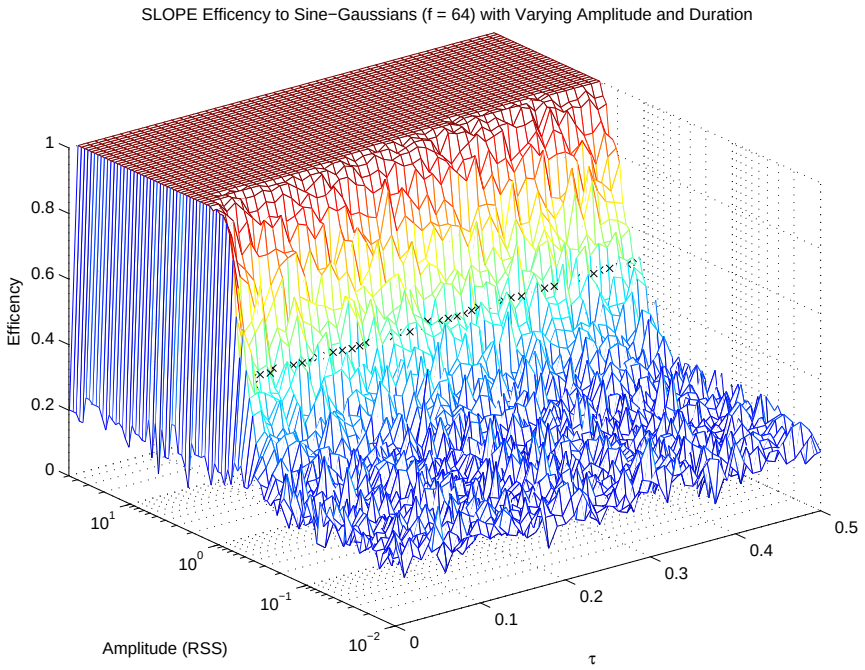


**Figure F.11.** SLOPE efficiency to 64 Hz sine-Gaussians with varying amplitude and duration (shown as a 3-dimensional surface) [alt tune].

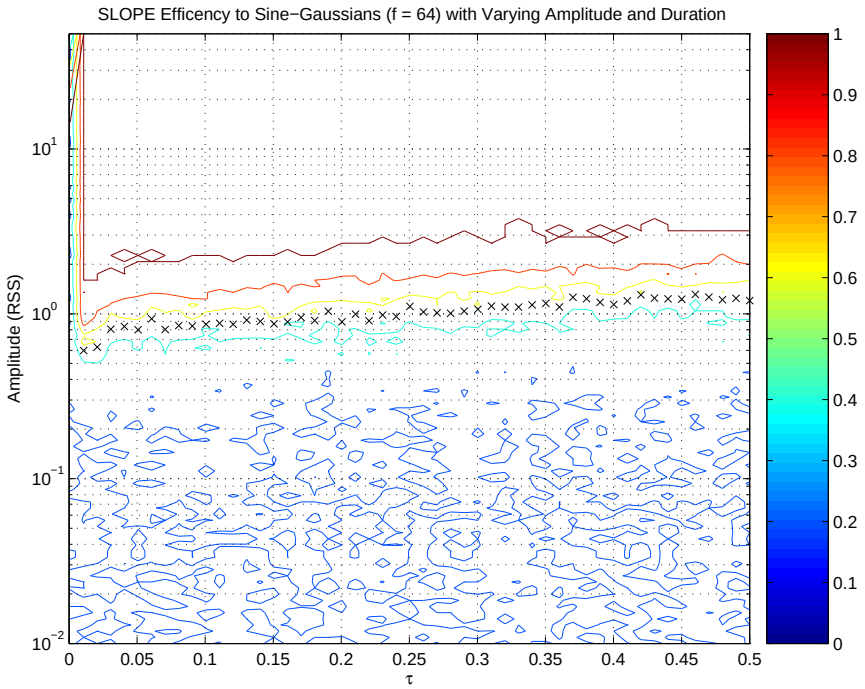


**Figure F.12.** SLOPE efficiency to 64 Hz sine-Gaussians with varying amplitude and duration (shown as a contour plot) [alt tune].

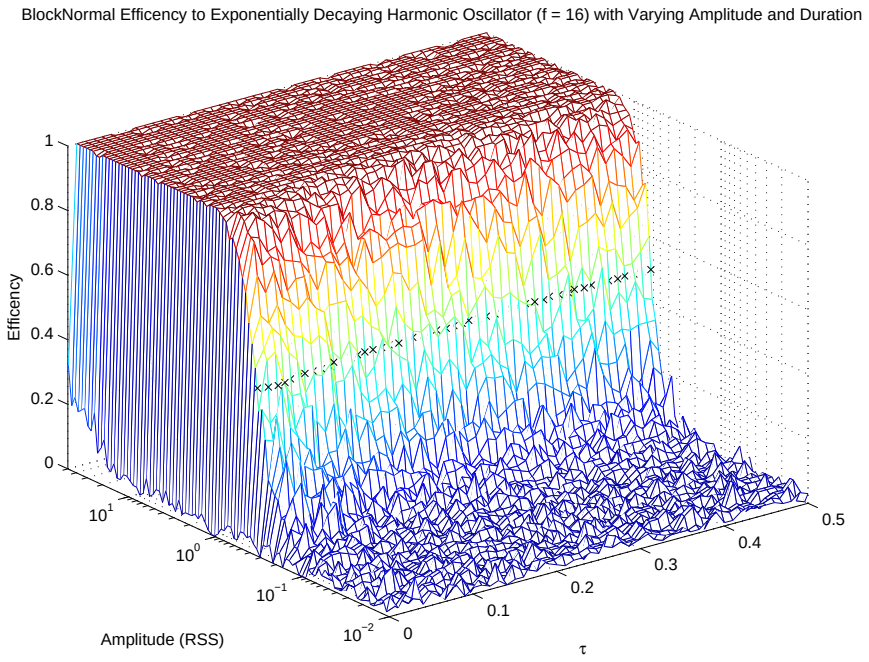


**Figure F.13.** BlockNormal efficiency to exponentially decaying harmonic oscillators of 16 Hz with varying amplitude and duration (shown as a 3-dimensional surface) [alt tune].

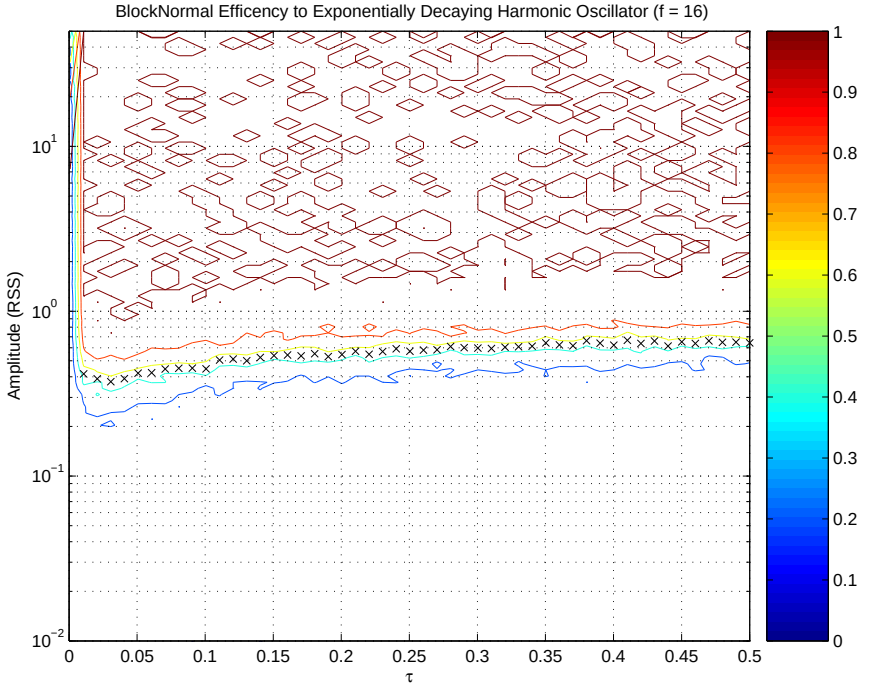


**Figure F.14.** BlockNormal efficiency to exponentially decaying harmonic oscillators of 16 Hz with varying amplitude and duration (shown as a contour plot) [alt tune].

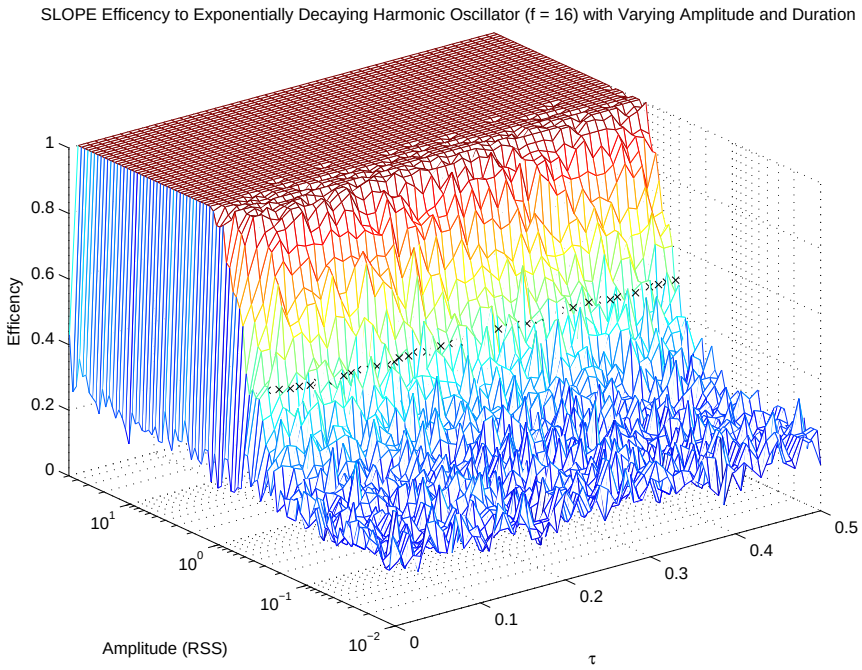


**Figure F.15.** SLOPE efficiency to exponentially decaying harmonic oscillators of 16 Hz with varying amplitude and duration (shown as a 3-dimensional surface) [alt tune].

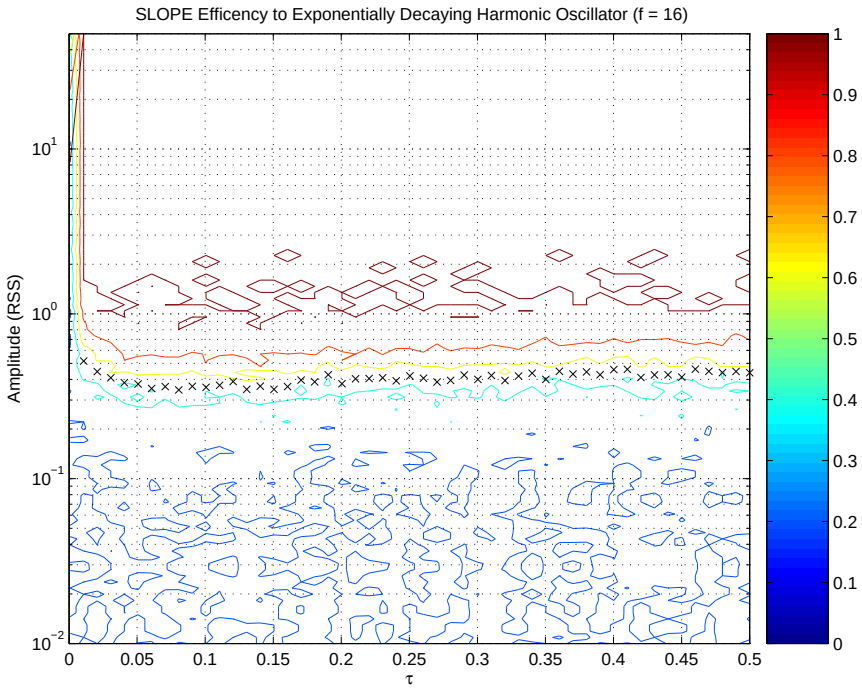


**Figure F.16.** SLOPE efficiency to exponentially decaying harmonic oscillators of 16 Hz with varying amplitude and duration (shown as a contour plot) [alt tune].

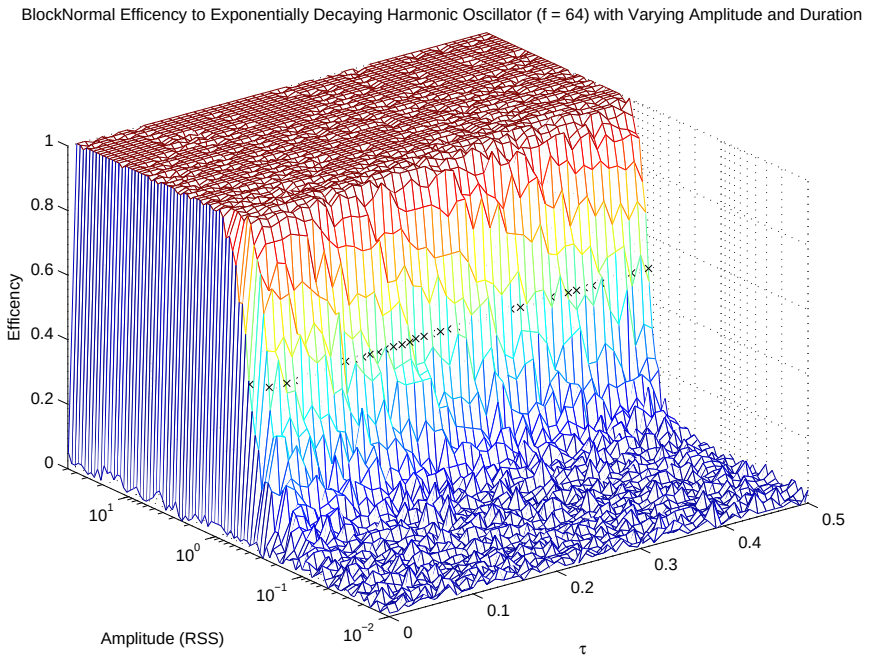


**Figure F.17.** BlockNormal efficiency to exponentially decaying harmonic oscillators of 64 Hz with varying amplitude and duration (shown as a 3-dimensional surface) [alt tune].

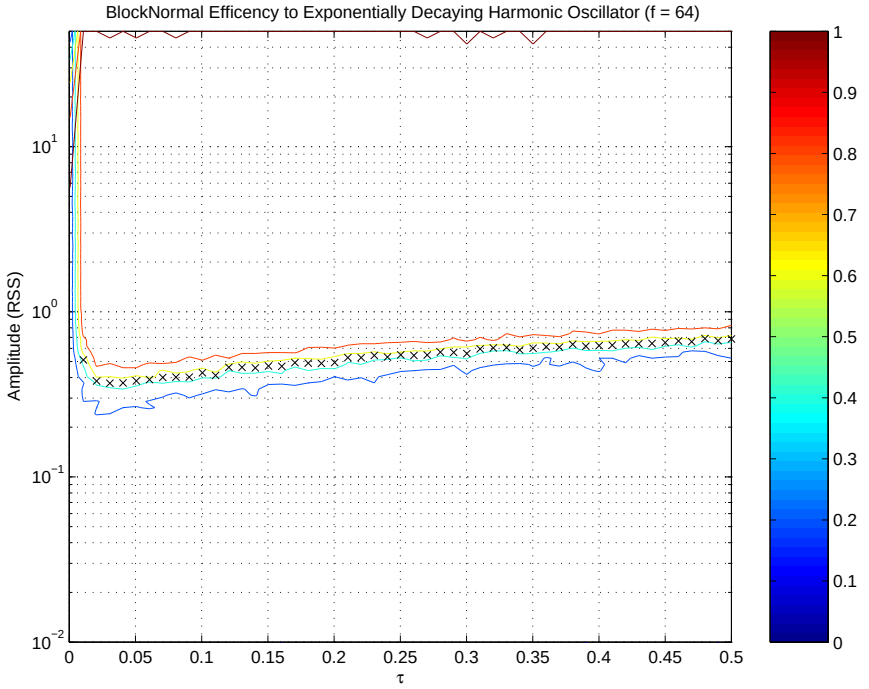


**Figure F.18.** BlockNormal efficiency to exponentially decaying harmonic oscillators of 64 Hz with varying amplitude and duration (shown as a contour plot) [alt tune].

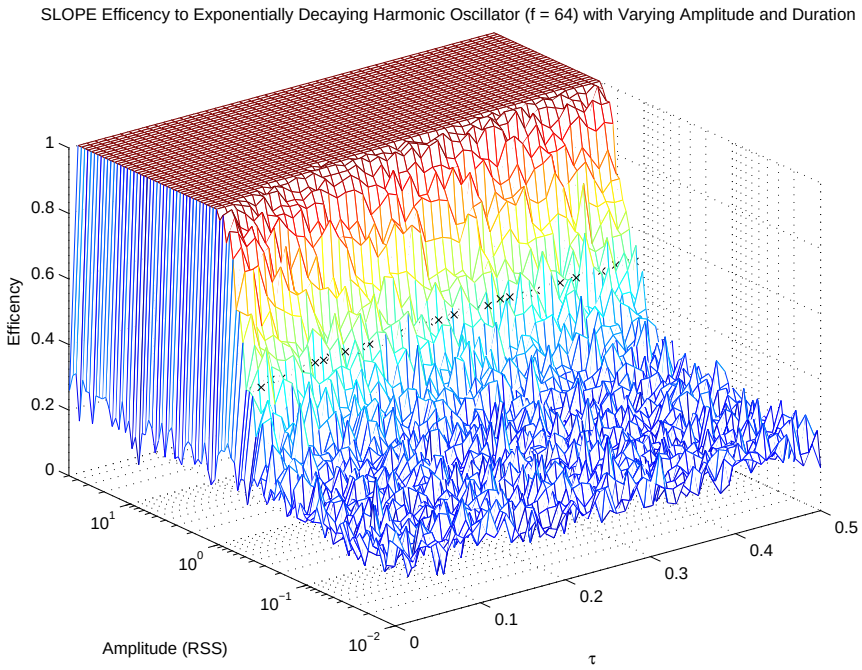


**Figure F.19.** SLOPE efficiency to exponentially decaying harmonic oscillators of 64 Hz with varying amplitude and duration (shown as a 3-dimensional surface) [alt tune].

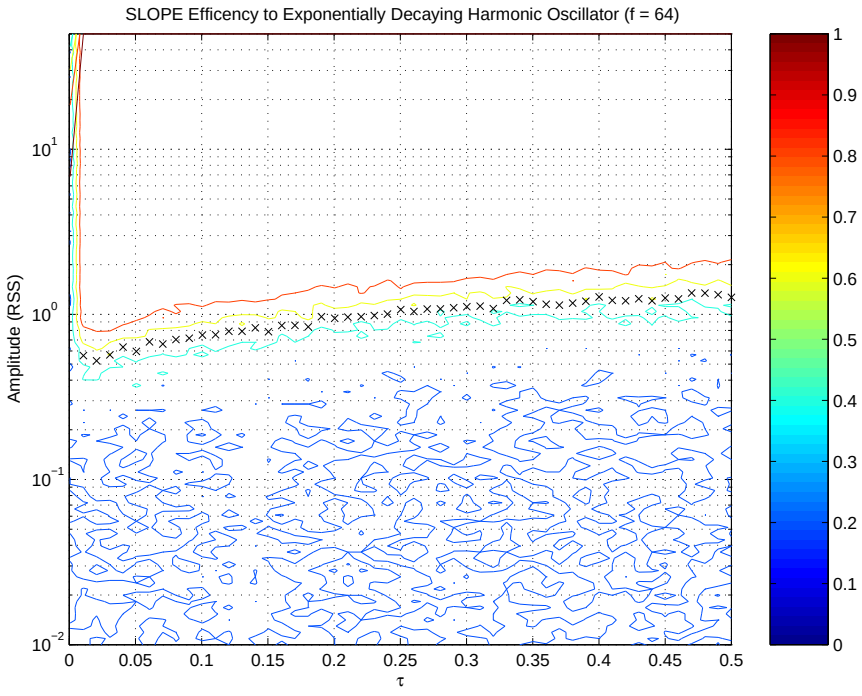


**Figure F.20.** SLOPE efficiency to exponentially decaying harmonic oscillators of 64 Hz with varying amplitude and duration (shown as a contour plot) [alt tune].

Appendix G

# Full Efficiency Profiles of ETG Performances With Respect to a Specific Signal Frequency-Domain Signal

Measuring the efficiency of a signal of varying amplitude and duration produces a three dimensional surface which can be compared between ETGs. Efficiency profiles are the basis of the investigations of Chapter 8 and the BlockNormal and SLOPE profiles shown here are summarized by the $A_{50}$ curves of Figures 8.1 and 8.3 and the sigmoid slope curves in Figures 8.2 and 8.4.

The plots shown in this appendix show the efficiency profiles for *each frequency-domain magnitude* (q.v. Section 8.1) of every signal type and frequency for each ETG, *using its current practical tuning* (q.v. Sections 3.4, 4.5 and 5.6), as both a 3-dimensional surface and a contour plot (Q Pipeline contour plots are shown in Section 8.2.3). The 50% efficiency level on each plot for BlockNormal and SLOPE is marked with '`x`' and the label '[const. magnitude]' is applied to the figure captions to distinguish them from the figures in Appendix E.

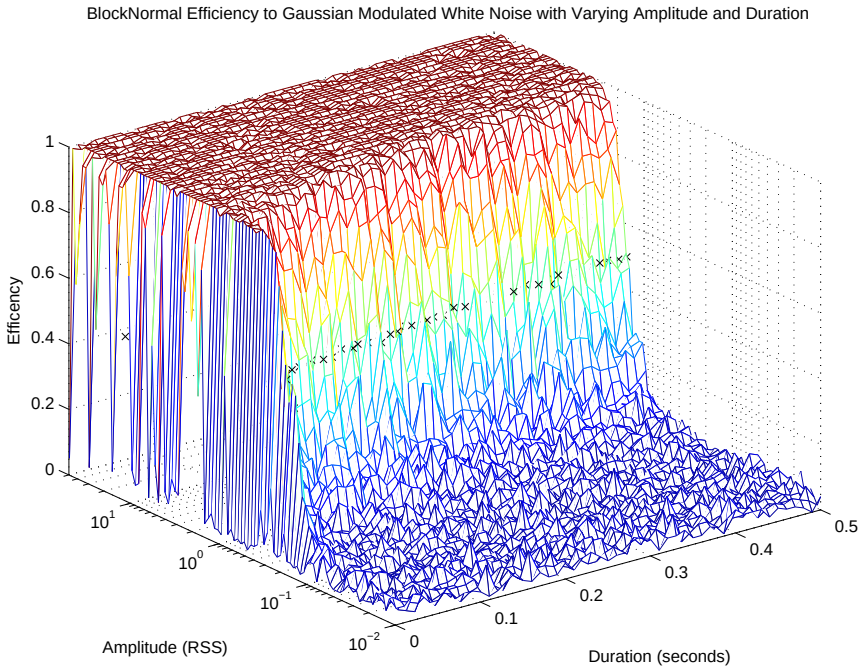


**Figure G.1.** BlockNormal efficiency to Gaussian modulated white noise with varying amplitude and duration (shown as a 3-dimensional surface) [const. magnitude].

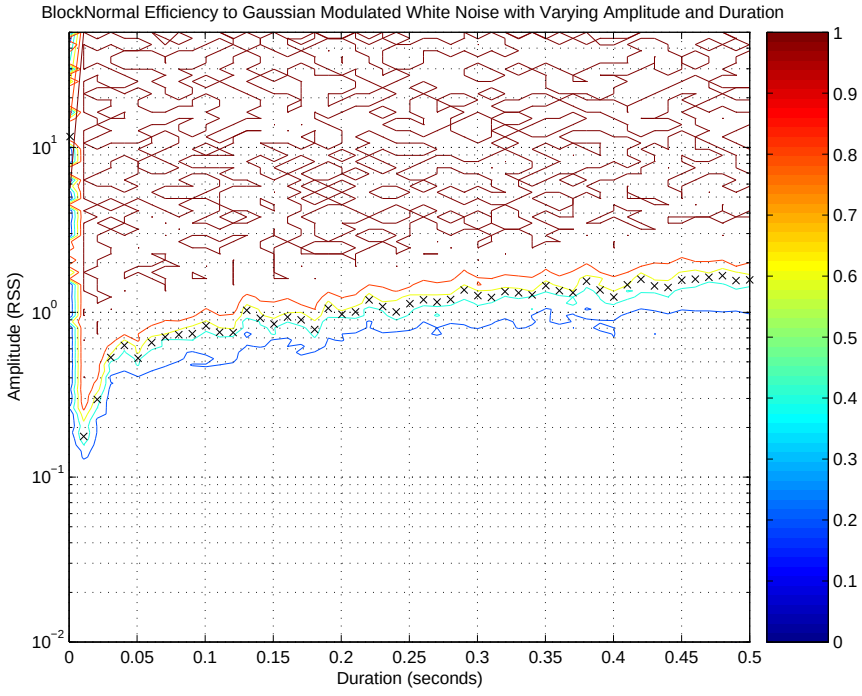


**Figure G.2.** BlockNormal efficiency to Gaussian modulated white noise with varying amplitude and duration (shown as a contour plot) [const. magnitude].

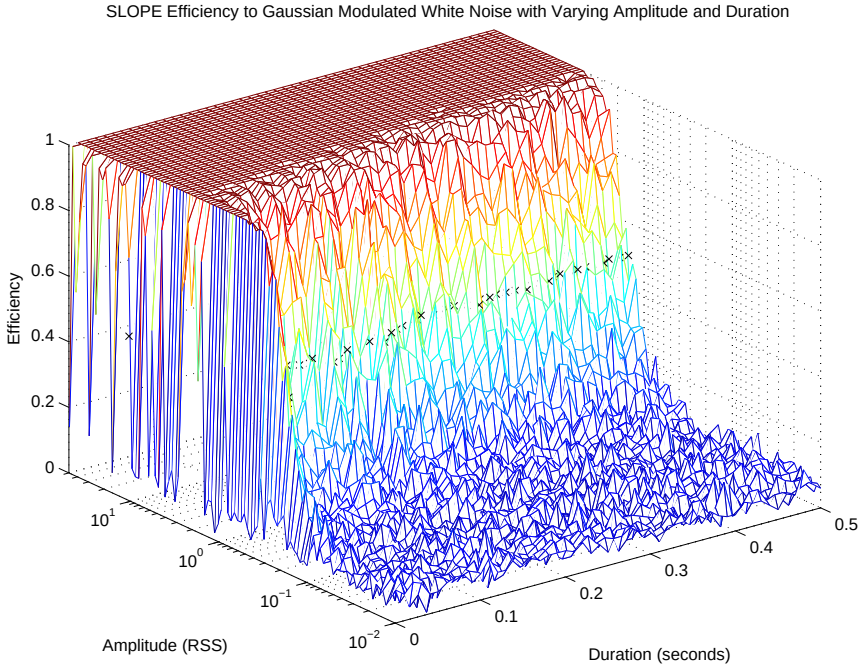


**Figure G.3.** SLOPE efficiency to Gaussian modulated white noise with varying amplitude and duration (shown as a 3-dimensional surface) [const. magnitude].

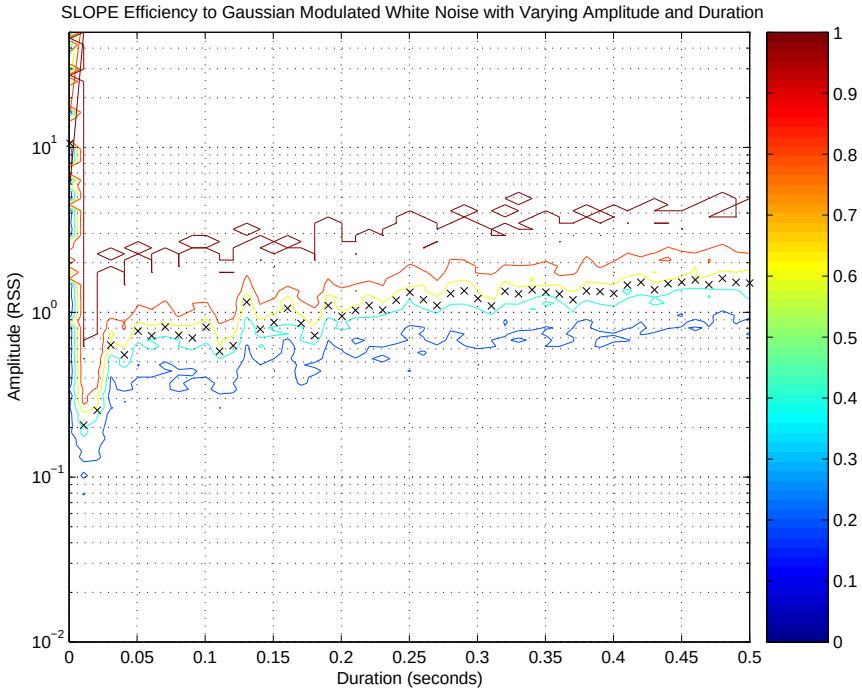


**Figure G.4.** SLOPE efficiency to Gaussian modulated white noise with varying amplitude and duration (shown as a contour plot) [const. magnitude].

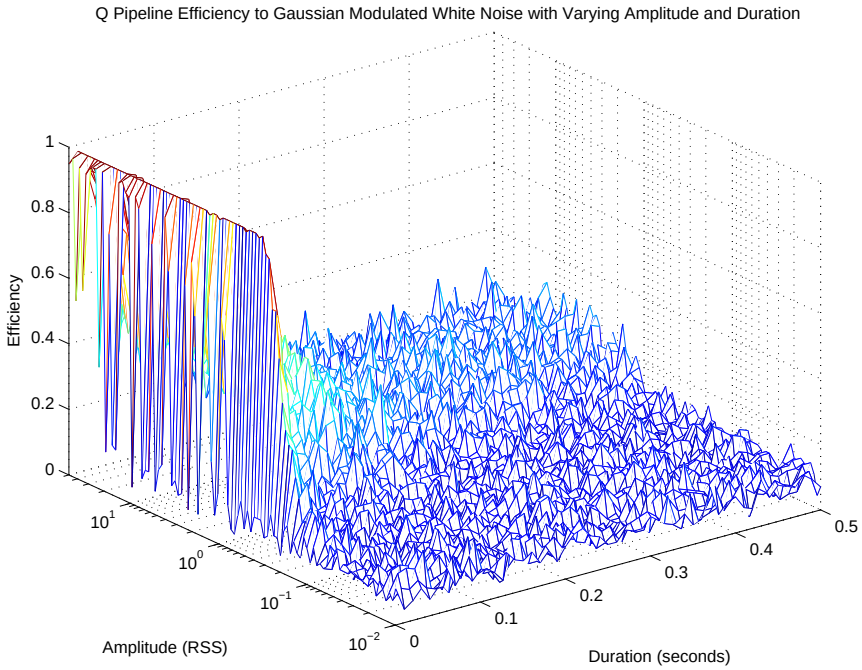


**Figure G.5.** Q Pipeline efficiency to Gaussian modulated white noise with varying amplitude and duration (shown as a 3-dimensional surface) [const. magnitude].

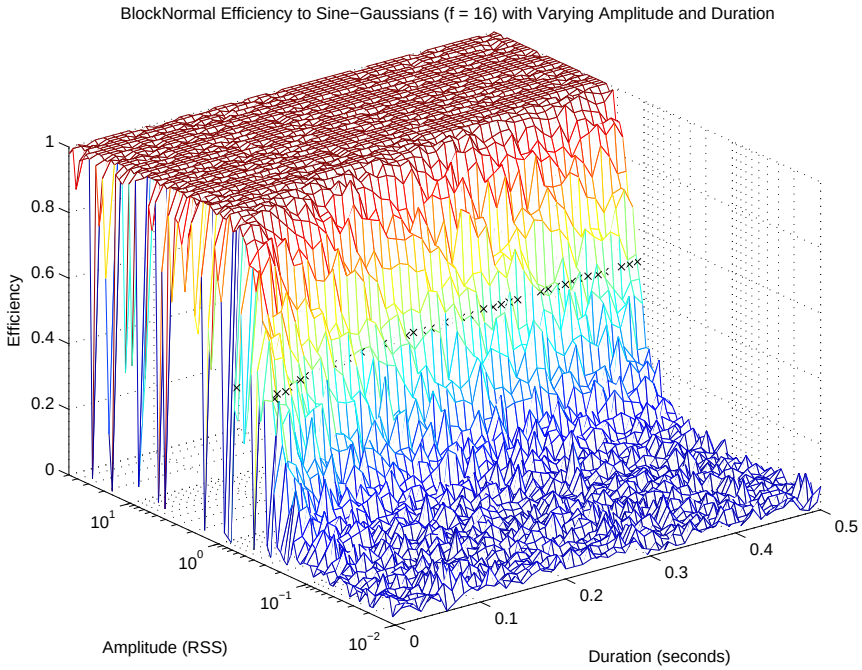


**Figure G.6.** BlockNormal efficiency to 16 Hz sine-Gaussians with varying amplitude and duration (shown as a 3-dimensional surface) [const. magnitude].

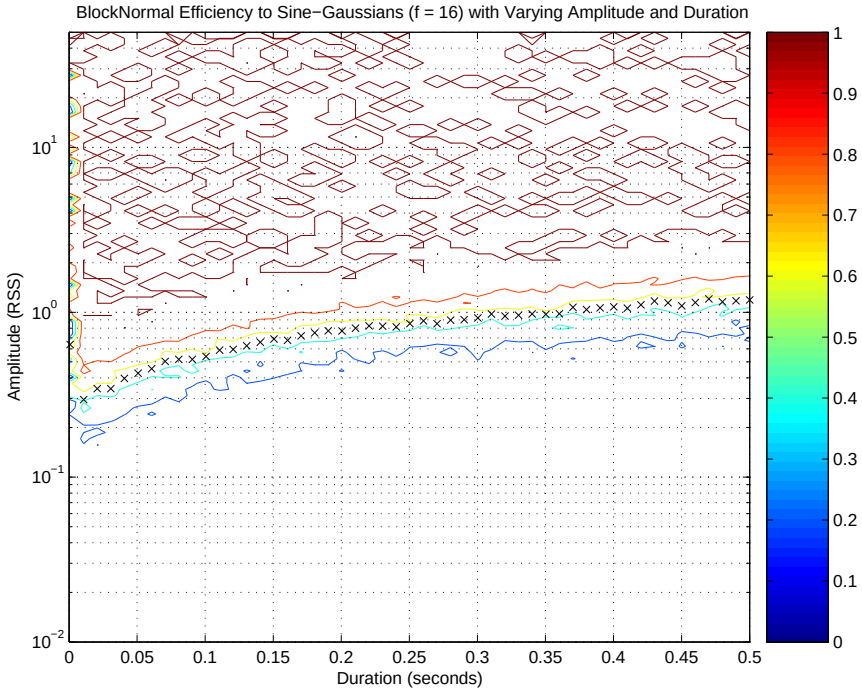


**Figure G.7.** BlockNormal efficiency to 16 Hz sine-Gaussians with varying amplitude and duration (shown as a contour plot) [const. magnitude].

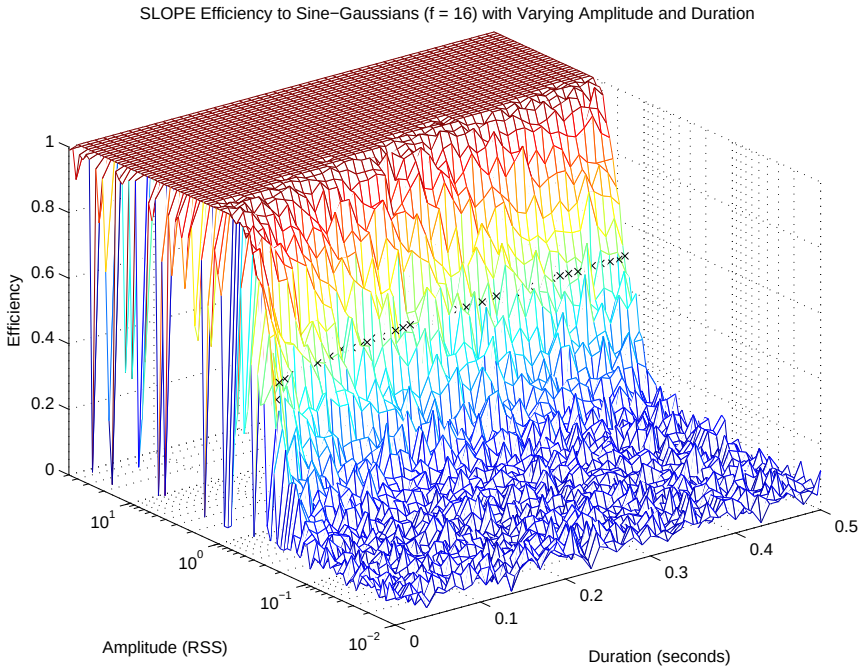


**Figure G.8.** SLOPE efficiency to 16 Hz sine-Gaussians with varying amplitude and duration (shown as a 3-dimensional surface) [const. magnitude].

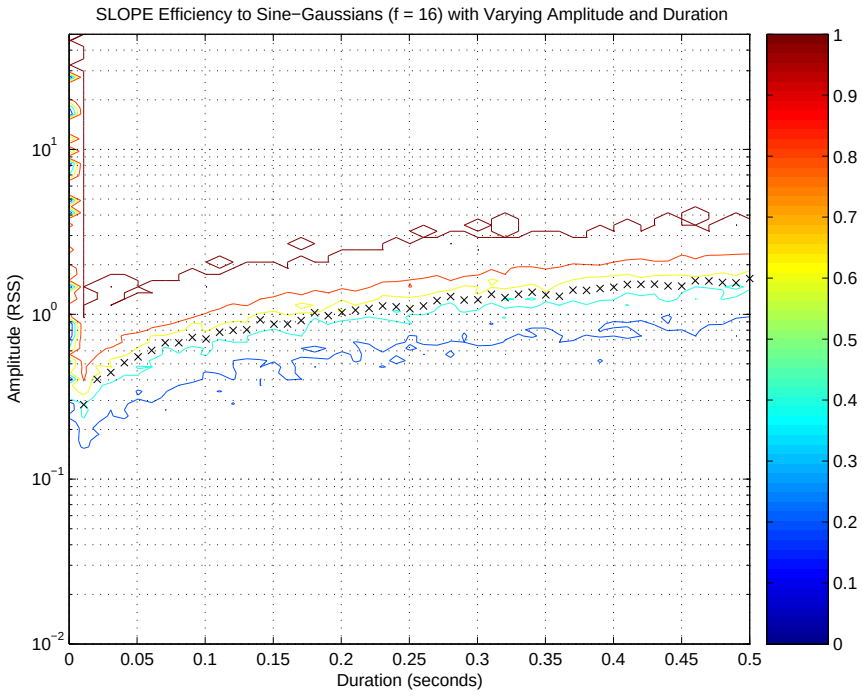


**Figure G.9.** SLOPE efficiency to 16 Hz sine-Gaussians with varying amplitude and duration (shown as a contour plot) [const. magnitude].

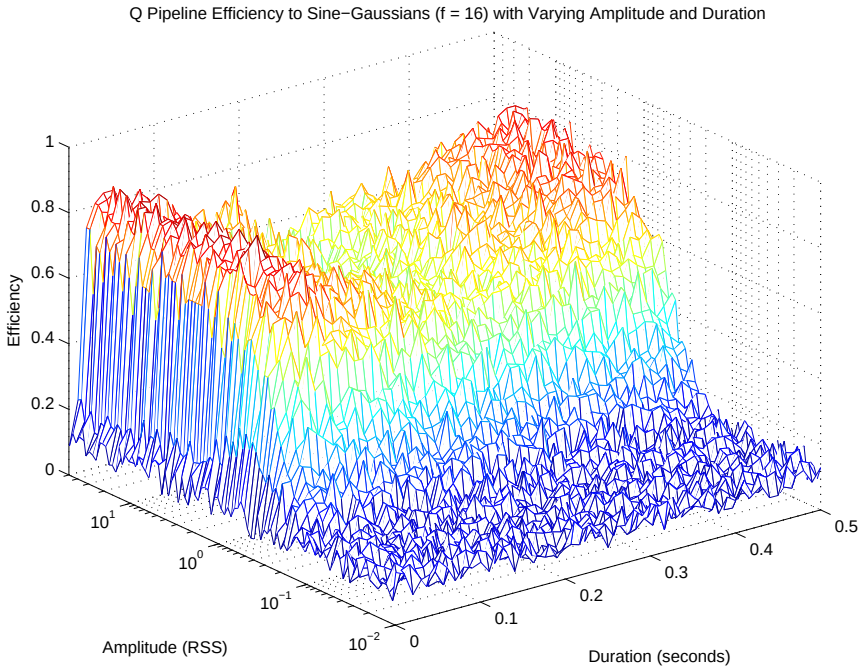


**Figure G.10.** Q Pipeline efficiency to 16 Hz sine-Gaussians with varying amplitude and duration (shown as a 3-dimensional surface) [const. magnitude].

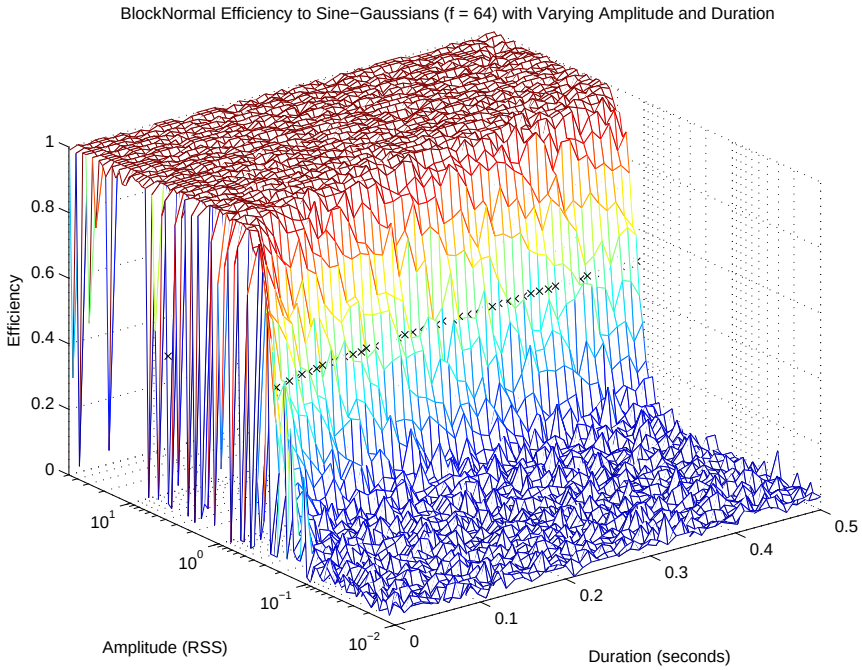


**Figure G.11.** BlockNormal efficiency to 64 Hz sine-Gaussians with varying amplitude and duration (shown as a 3-dimensional surface) [const. magnitude].

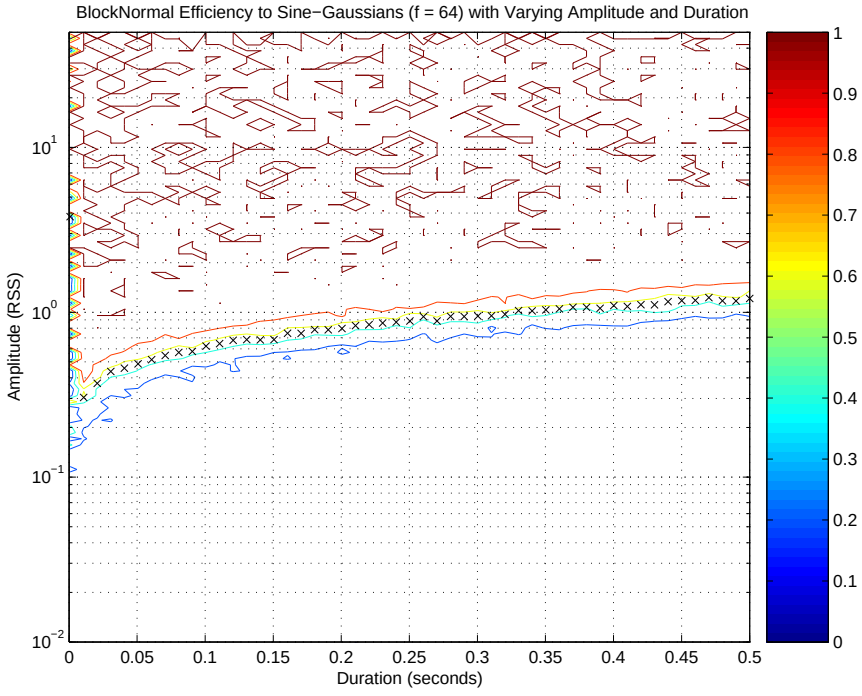


**Figure G.12.** BlockNormal efficiency to 64 Hz sine-Gaussians with varying amplitude and duration (shown as a contour plot) [const. magnitude].

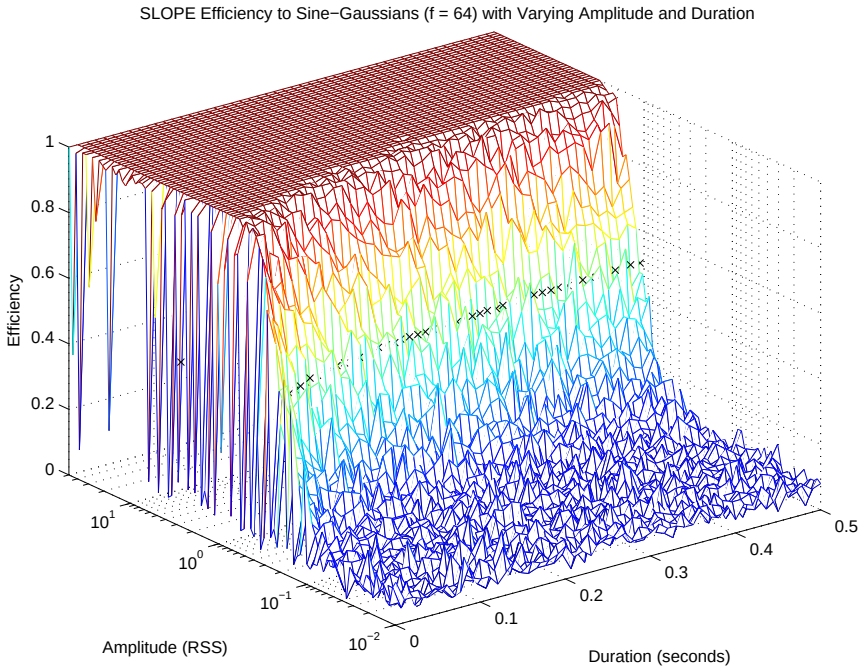


**Figure G.13.** SLOPE efficiency to 64 Hz sine-Gaussians with varying amplitude and duration (shown as a 3-dimensional surface) [const. magnitude].

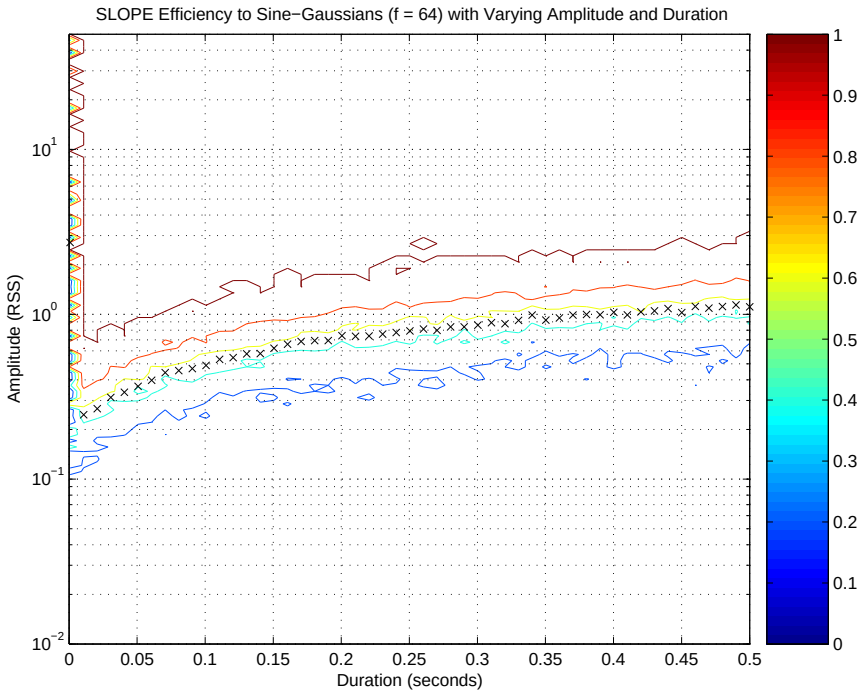


**Figure G.14.** SLOPE efficiency to 64 Hz sine-Gaussians with varying amplitude and duration (shown as a contour plot) [const. magnitude].

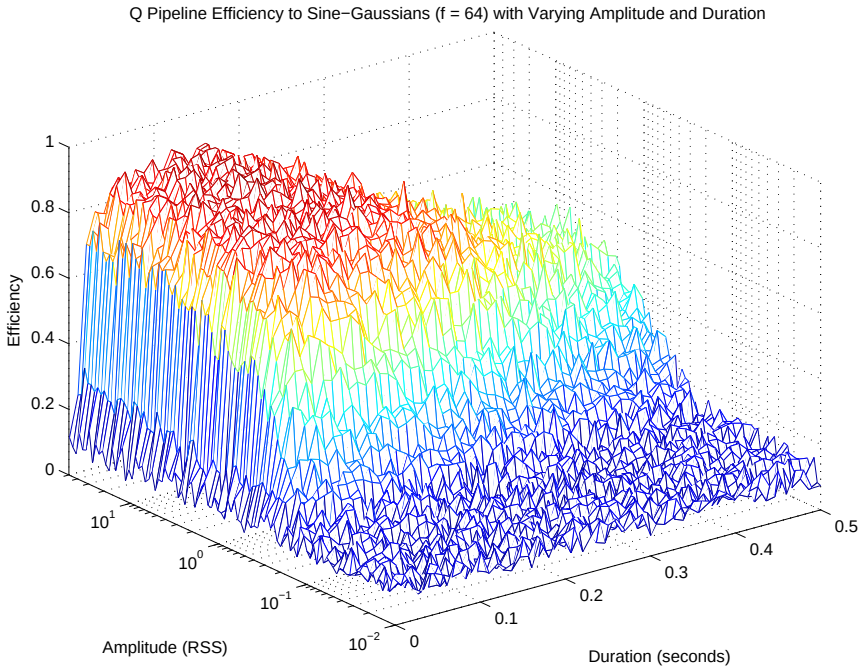


**Figure G.15.** Q Pipeline efficiency to 64 Hz sine-Gaussians with varying amplitude and duration (shown as a 3-dimensional surface) [const. magnitude].

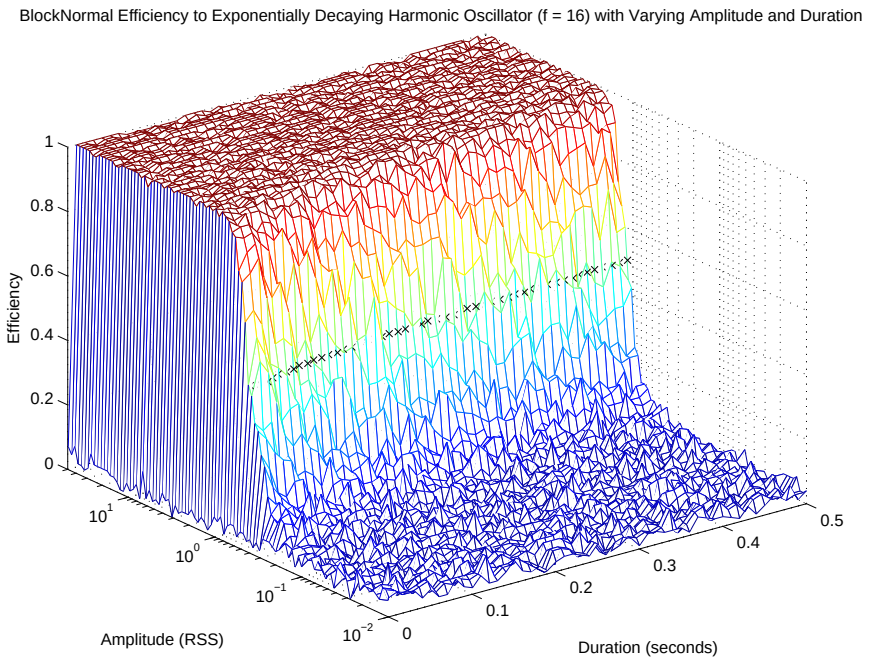


**Figure G.16.** BlockNormal efficiency to exponentially decaying harmonic oscillators of 16 Hz with varying amplitude and duration (shown as a 3-dimensional surface) [const. magnitude].

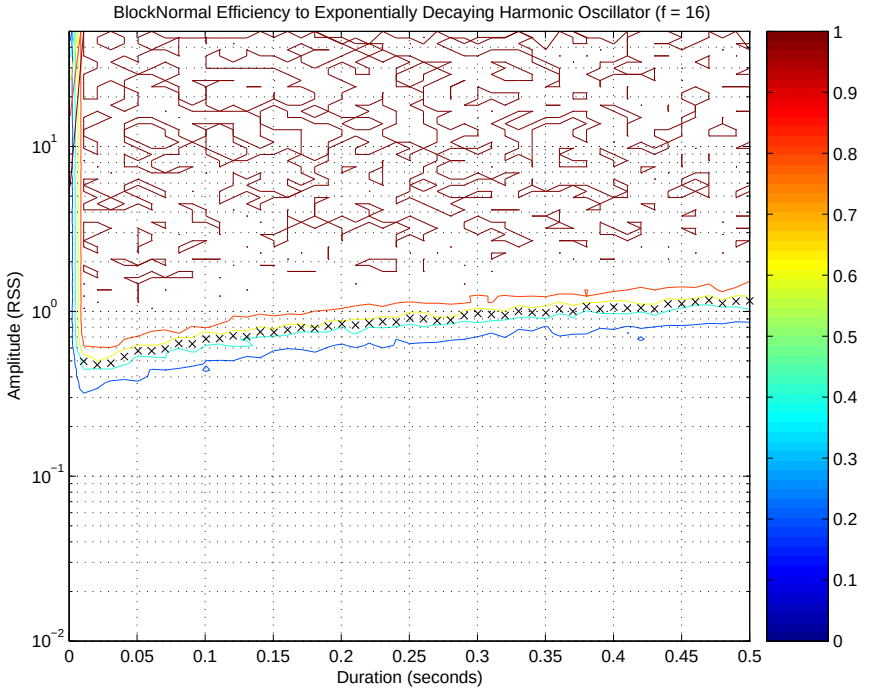


**Figure G.17.** BlockNormal efficiency to exponentially decaying harmonic oscillators of 16 Hz with varying amplitude and duration (shown as a contour plot) [const. magnitude].

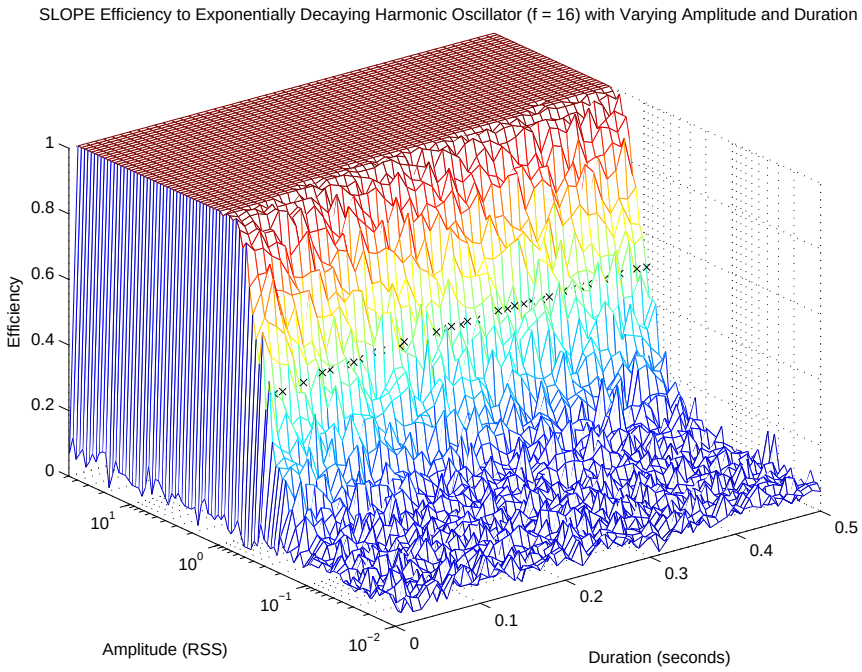


**Figure G.18.** SLOPE efficiency to exponentially decaying harmonic oscillators of 16 Hz with varying amplitude and duration (shown as a 3-dimensional surface) [const. magnitude].

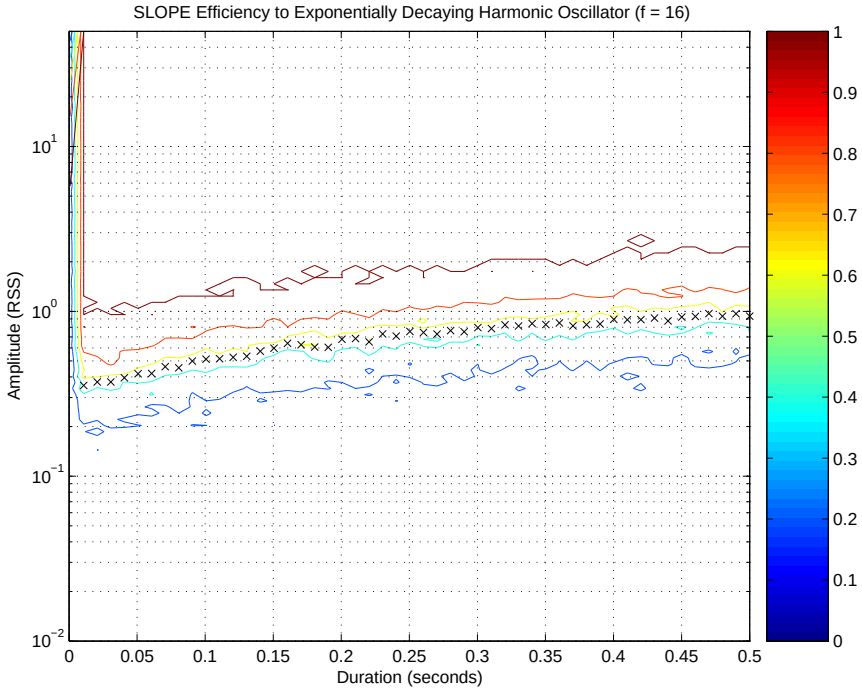


**Figure G.19.** SLOPE efficiency to exponentially decaying harmonic oscillators of 16 Hz with varying amplitude and duration (shown as a contour plot) [const. magnitude].

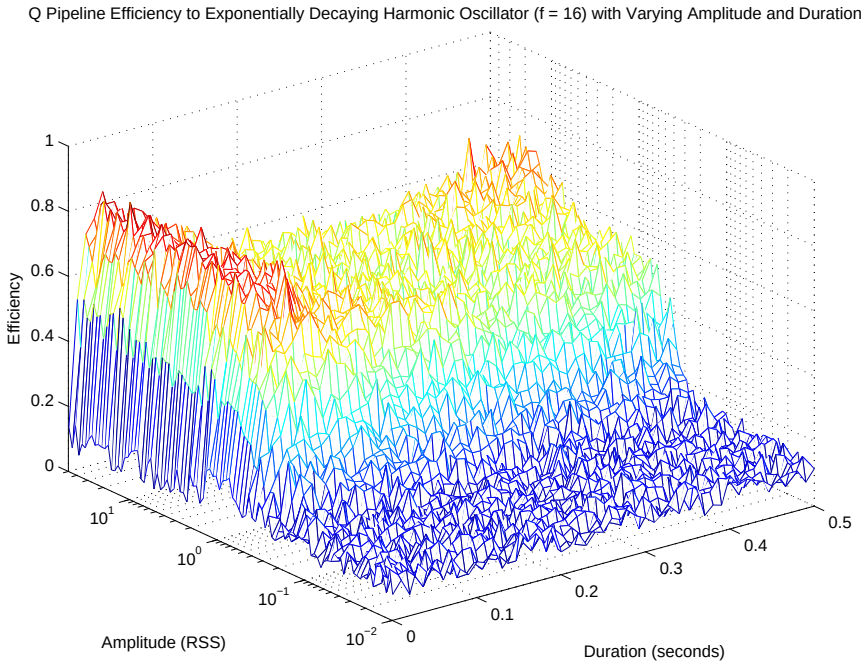


**Figure G.20.** Q Pipeline efficiency to exponentially decaying harmonic oscillators of 16 Hz with varying amplitude and duration (shown as a 3-dimensional surface) [const. magnitude].

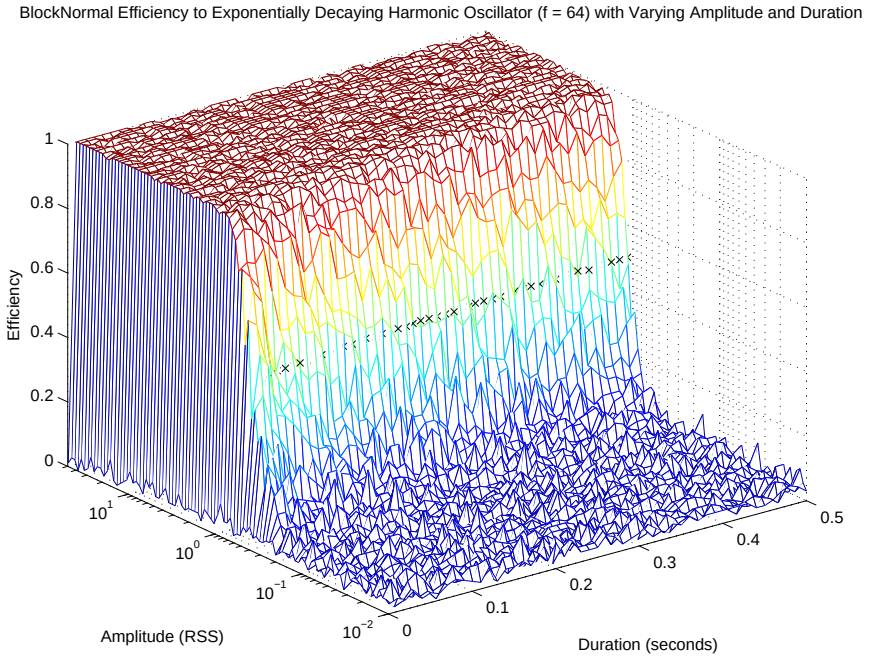


**Figure G.21.** BlockNormal efficiency to exponentially decaying harmonic oscillators of 64 Hz with varying amplitude and duration (shown as a 3-dimensional surface) [const. magnitude].

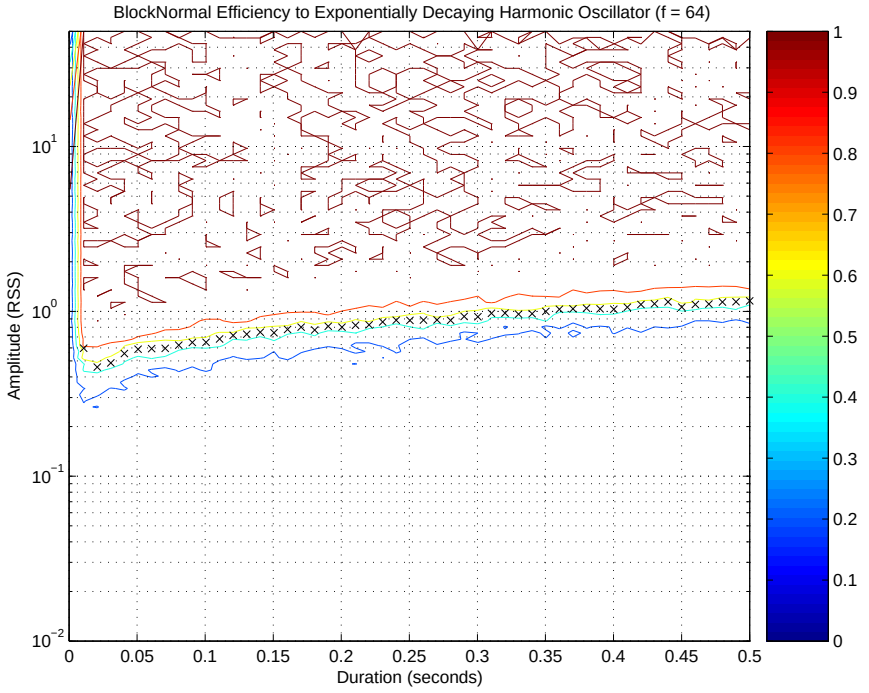


**Figure G.22.** BlockNormal efficiency to exponentially decaying harmonic oscillators of 64 Hz with varying amplitude and duration (shown as a contour plot) [const. magnitude].

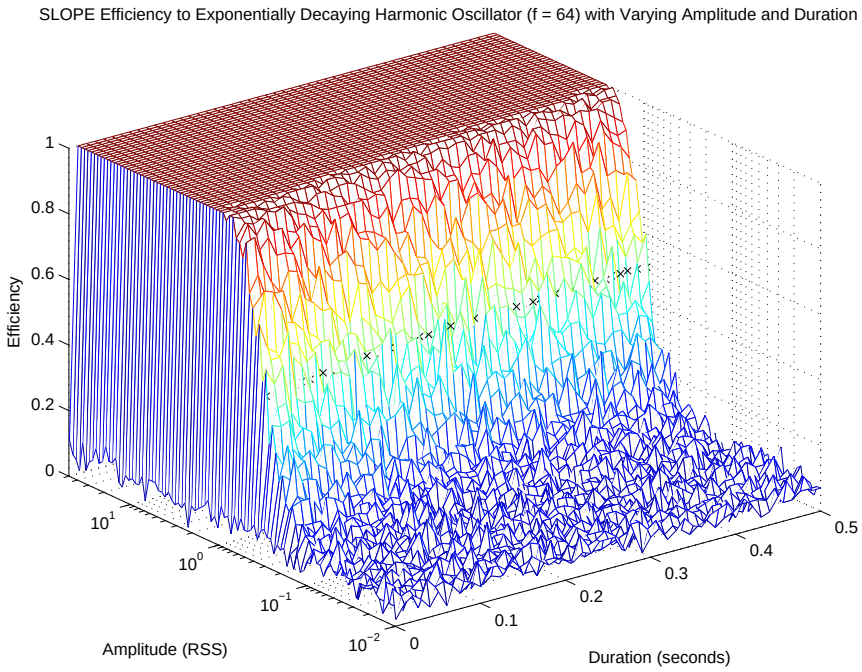


**Figure G.23.** SLOPE efficiency to exponentially decaying harmonic oscillators of 64 Hz with varying amplitude and duration (shown as a 3-dimensional surface) [const. magnitude].

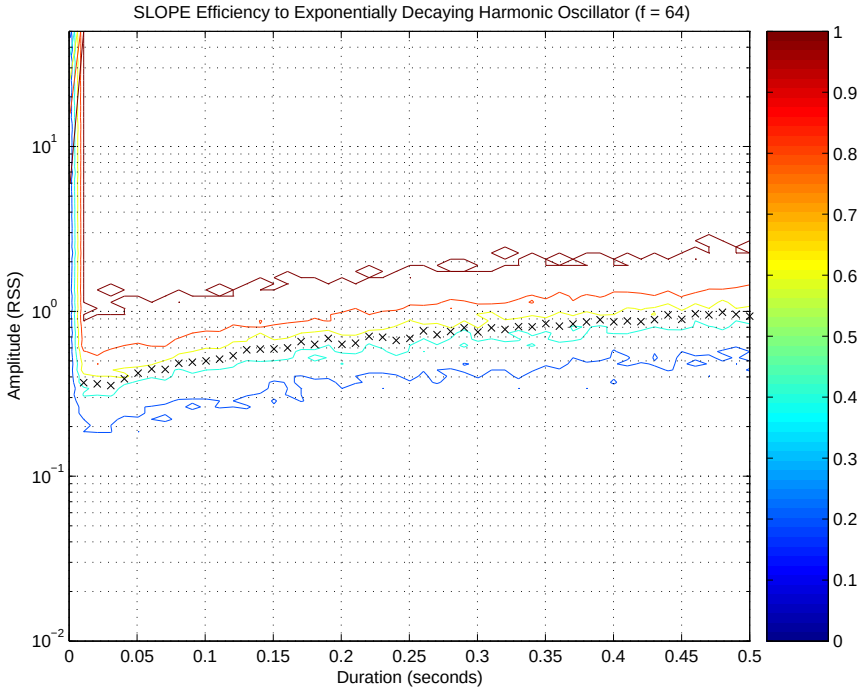


**Figure G.24.** SLOPE efficiency to exponentially decaying harmonic oscillators of 64 Hz with varying amplitude and duration (shown as a contour plot) [const. magnitude].

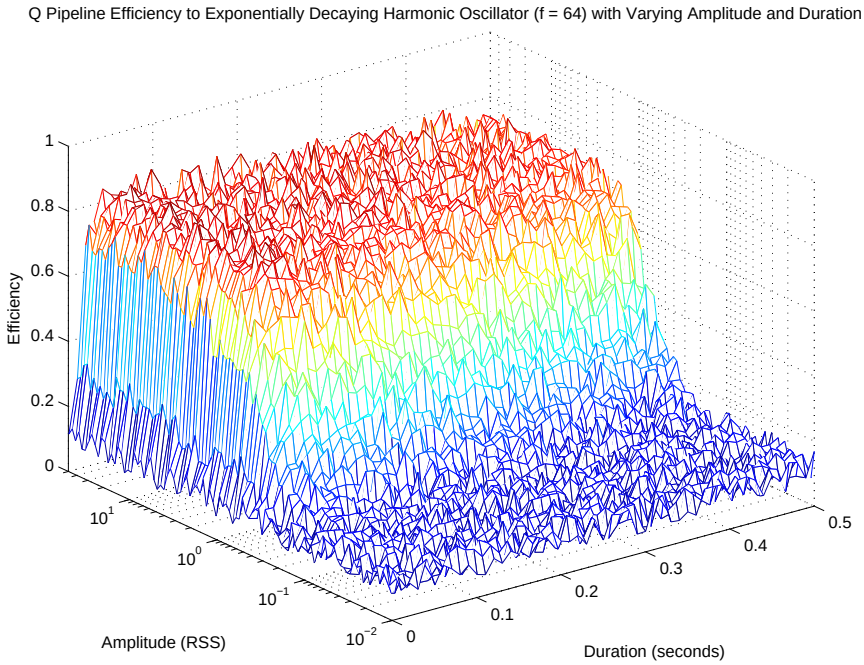


**Figure G.25.** Q Pipeline efficiency to exponentially decaying harmonic oscillators of 64 Hz with varying amplitude and duration (shown as a 3-dimensional surface) [const. magnitude].

# Bibliography


[1] J. M. Weisberg and J. H. Taylor, "The Relativistic Binary Pulsar B1913+16," in *Radio Pulsars, ASP Conference Proceedings, Vol. 302*, M. Bailes, D. J. Nice, and S. E. Thorsett, Eds. San Francisco: Astronomical Society of the Pacific, 2003, pp. 93–100. [Online]. Available: http://arxiv.org/abs/astro-ph/0211217

[2] "First Lock at Hanford Observatory." [Online]. Available: http://www.ligo.caltech.edu/LIGO_web/firstlock/ifo_sketch.html

[3] A. Lazzarini, "S3 Best Strain Sensitivities," LIGO, Tech. Rep. LIGO-G040023-00-E, 2004. [Online]. Available: http://admdbsrv.ligo.caltech.edu/dcc/

[4] G. González, M. Landry, B. O'Reilly, and H. Radkins, "Calibration of the LIGO detectors for S2," LIGO, Tech. Rep. LIGO-T030097-01-D, 2004. [Online]. Available: http://admdbsrv.ligo.caltech.edu/dcc/

[5] L. Cadonati, "Tuning slope thresholds," 2002. [Online]. Available: http://emvogil-3.mit.edu/~cadonati/S1/slopeThreshold/slopeThreshold.html [password required]

[6] S. K. Chatterji, "The search for gravitational wave bursts in data from the second LIGO science run," Ph.D. dissertation, Massachusetts Institute of Technology, 2005.

[7] C. W. Misner, K. S. Thorne, and J. A. Wheeler, *Gravitation*. San Francisco: Freeman, 1973.

[8] R. A. Hulse and J. H. Taylor, "Discovery of a pulsar in a binary system," *Astrophys. J.*, vol. 195, pp. L51–L53, Jan. 1975.

[9] J. H. Taylor and J. M. Weisberg, "A new test of general relativity - Gravitational radiation and the binary pulsar PSR 1913+16," *Astophys. J.*, vol. 253, pp. 908–920, Feb. 1982.

[10] ——, "Further experimental tests of relativistic gravity using the binary pulsar PSR 1913 + 16," *Astophys. J.*, vol. 345, pp. 434–450, Oct. 1989.

[11] J. Weber, "Detection and generation of gravitational waves," *Phys. Rev.*, vol. 117, pp. 306–313, 1960.

[12] E. Mauceli, Z. K. Geng, W. O. Hamilton, W. W. Johnson, S. Merkowitz, A. Morse, B. Price, and N. Solomonson, "The Allegro gravitational wave detector: Data acquisition and analysis," *Phys. Rev. D*, vol. 54, no. 2, pp. 1264–1275, 1996. [Online]. Available: http://arxiv.org/abs/gr-qc/9609058

[13] G. A. Prodi, et al., "Initial operation of the gravitational wave detector AURIGA," in *Gravitational Waves - Proceedings of the 2nd Edoardo Amaldi conference on gravitational wave experiments*, E. Coccia, G. Veneziano, and G. Pizzella, Eds. World Scientific, 1998, pp. 148–158.

[14] P. Astone, et al., "Long-term operation of the Rome "Explorer" cryogenic gravitational wave detector," *Phys. Rev. D*, vol. 47, no. 2, pp. 362–375, 1993.

[15] ——, "The gravitational wave detector NAUTILUS operating at T = 0.1 K," *Astropart. Phys.*, vol. 7, pp. 231–243, 1997.

[16] D. G. Blair, E. N. Ivanov, M. E. Tobar, P. J. Turner, F. van Kann, and I. S. Heng, "High sensitivity gravitational wave antenna with parametric transducer readout," *Phys. Rev. Lett.*, vol. 74, pp. 1908–1911, 1995.

[17] P. Astone, et al., "Increasing the bandwidth of resonant gravitational antennas: the case of EXPLORER," *Phys. Rev. Lett.*, vol. 91, no. 11, 2003. [Online]. Available: http://www.lnf.infn.it/esperimenti/rog/collaboration/pdf/10_expllbw.pdf

[18] B. Abbott, et al., "Detector Description and Performance for the First Coincidence Observations between LIGO and GEO," *Nucl.Instrum.Meth.A*, vol. 517, p. 154, 2004. [Online]. Available: http://arxiv.org/abs/gr-qc/0308043

[19] B. C. Barish and R. Weiss, "LIGO and the Detection of Gravitational Waves," *Physics Today*, vol. 52, pp. 44–50, October 1999. [Online]. Available: http://www.ligo.caltech.edu/docs/P/P990039-00.pdf

[20] P. R. Saulson, "If light waves are stretched by gravitational waves, how can we use light as a ruler to detect gravitational waves?" *Am. J. Phys.*, vol. 65, pp. 501–505, 1997. [Online]. Available: http://www.ligo.caltech.edu/docs/P/P960059-00.pdf

[21] ——, *Fundamentals of Interferometric Gravitational Wave Detectors.* Singapore: World Scientific, 1994.

[22] A. Lazzarini, "Strain Sensitivities for the LIGO Interferometers for S1," LIGO, Tech. Rep. LIGO-G020461-01-E, 2003. [Online]. Available: http://admdbsrv.ligo.caltech.edu/dcc/

[23] ——, "Strain Sensitivities for the LIGO Interferometers during S2," LIGO, Tech. Rep. LIGO-G030379-00-E, 2003. [Online]. Available: http://admdbsrv.ligo.caltech.edu/dcc/

[24] ——, "S4 Strain Sensitivities for the LIGO Interferometers," LIGO, Tech. Rep. LIGO-G050230-02-E, 2005. [Online]. Available: http://admdbsrv.ligo.caltech.edu/dcc/

[25] B. Willke, et al., "Status of GEO 600," *Class. Quantum Grav.*, vol. 21, pp. S417–S423, 2004.

[26] R. Takahashi, et al., "Status of TAMA300," *Class. Quant. Grav.*, vol. 21, pp. S403–S408, 2004.

[27] F. Acernese, et al., "The present status of the VIRGO central interferometer," *Class. Quantum Grav.*, vol. 19, pp. 1421–1428, 2002.

[28] H. Tagoshi, et al., "The first search for gravitational waves from inspiraling compact binaries using TAMA300 data," *Phys. Rev. D*, vol. 63, no. 062001, 2001. [Online]. Available: http://arxiv.org/abs/gr-qc/0012010

[29] B. Abbott, et al., "Setting upper limits on the strength of periodic gravitational waves from PSR J1939+2134 using the first science data from the GEO 600 and LIGO detectors," *Phys. Rev. D*, vol. 69, no. 082004, 2004. [Online]. Available: http://arxiv.org/abs/gr-qc/0308050

[30] ——, "Analysis of LIGO data for gravitational waves from binary neutron stars," *Phys. Rev. D*, vol. 69, no. 122001, 2004. [Online]. Available: http://arxiv.org/abs/gr-qc/0308069

[31] ——, "First upper limits from LIGO on gravitational wave bursts," *Phys. Rev. D*, vol. 69, no. 102001, 2004. [Online]. Available: http://arxiv.org/abs/gr-qc/0312056

[32] ——, "Analysis of first LIGO science data for stochastic gravitational waves," *Phys. Rev. D*, vol. 69, no. 122004, 2004. [Online]. Available: http://arxiv.org/abs/gr-qc/0312088

[33] H. Takahashi, et al., "Coincidence analysis to search for inspiraling compact binaries using TAMA300 and LISM data," *Phys. Rev. D*, vol. 70, no. 042003, 2004. [Online]. Available: http://arxiv.org/abs/gr-qc/0403088

[34] M. Ando, et al., "Observation results by the TAMA300 detector on gravitational wave bursts from stellar-core collapses," *Phys. Rev. D*, vol. 71, no. 082002, 2005. [Online]. Available: http://arxiv.org/abs/gr-qc/0411027

[35] B. Abbott, et al., "Upper limits on gravitational wave bursts in LIGO's second science run," *Phys. Rev. D*, vol. 72, no. 062001, 2005. [Online]. Available: http://arxiv.org/abs/gr-qc/0505029

[36] ——, "Search for gravitational waves associated with the gamma ray burst GRB030329 using the LIGO detectors," *Phys. Rev. D*, vol. 72, no. 042002, 2005. [Online]. Available: http://arxiv.org/abs/gr-qc/0501068

[37] ——, "Limits on gravitational-wave emission from selected pulsars using LIGO data," *Phys. Rev. Lett.*, vol. 94, no. 181103, 2005. [Online]. Available: http://arxiv.org/abs/gr-qc/0410007

[38] ——, "First all-sky upper limits from LIGO on the strength of periodic gravitational waves using the Hough transform," *Phys. Rev. D*, vol. 72, no. 102004, 2005. [Online]. Available: http://arxiv.org/abs/gr-qc/0508065

[39] LIGO, TAMA, "Upper limits from the LIGO and TAMA detectors on the rate of gravitational-wave bursts," *Phys. Rev. D*, vol. 72, no. 122004, 2005. [Online]. Available: http://arxiv.org/abs/gr-qc/0507081

[40] B. Abbott, et al., "Search for gravitational waves from galactic and extra-galactic binary neutron stars," *Phys. Rev. D*, vol. 72, no. 082001, 2005. [Online]. Available: http://arxiv.org/abs/gr-qc/0505041

[41] ——, "Search for gravitational waves from primordial black hole binary coalescences in the galactic halo," *Phys. Rev. D*, vol. 72, no. 082002, 2005. [Online]. Available: http://arxiv.org/abs/gr-qc/0505042

[42] ——, "Upper limits on a stochastic background of gravitational waves," *Phys. Rev. Lett.*, vol. 95, no. 221101, 2005. [Online]. Available: http://arxiv.org/abs/astro-ph/0507254

[43] ——, "Search for gravitational-wave bursts in ligo's third science run," *Class. Quant. Grav*, vol. 23, pp. S29–S39, 2006. [Online]. Available: http://arxiv.org/abs/gr-qc/0511146

[44] MATLAB® is a product of The MathWorks, Inc.

[45] W. G. Anderson, P. R. Brady, J. D. E. Creighton, and É. É. Flanagan, "An Excess power statistic for detection of burst sources of gravitational radiation," *Phys. Rev. D*, vol. 63, no. 042003, 2001. [Online]. Available: http://arxiv.org/abs/gr-qc/0008066

[46] ——, "A Power Filter for the Detection of Burst Sources of Gravitational Radiation in Interferometric Detectors," *International Journal of Modern Physics D*, vol. 9, pp. 303–307, 2000. [Online]. Available: http://arxiv.org/abs/gr-qc/0001044

[47] J. Sylvestre, "Time-frequency detection algorithm for gravitational wave bursts," 2002. [Online]. Available: http://arxiv.org/abs/gr-qc/0210043

[48] S. Klimenko, I. Yakushin, M. Rakhmanov, and G. Mitselmakher, "Performance of the WaveBurst algorithm on LIGO data," vol. 21, 2004, pp. S1685–S1694. [Online]. Available: http://arxiv.org/abs/gr-qc/0407025

[49] S. Klimenko, I. Yakushin, and G. Mitselmakher, "WaveBurst," LIGO, Tech. Rep. LIGO-T040040-00-Z, 2004. [Online]. Available: http://admdbsrv.ligo.caltech.edu/dcc/

[50] L. Blackburn, et al., "A first comparison of search methods for gravitational wave bursts using LIGO and Virgo simulated data," vol. 22, 2005, pp. S1293–S1302. [Online]. Available: http://arxiv.org/abs/gr-qc/0504060

[51] N. Arnaud, M. Barsuglia, M.-A. Bizouard, V. Brisson, F. Cavalier, M. Davier, S. Hello Patrice, Kreckelbergh, E. K. Porter, and T. Pradier, "Comparison of filters for detecting gravitational wave bursts in interferometric detectors," *Phys. Rev. D*, vol. 67, no. 062004, 2003. [Online]. Available: http://arxiv.org/abs/gr-qc/0210098

[52] "Full source MATLAB® programming repository for GravEn." [Online]. Available: http://www.lsc-group.phys.uwm.edu/cgi-bin/cvs/viewcvs.cgi/matapps/src/simulation/GravEn/?cvsroot=lscsoft

[53] A. L. Stuver, "GravEn Simulation Engine Primer," LIGO, Tech. Rep. LIGO-T040020-01-Z, 2005. [Online]. Available: http://admdbsrv.ligo.caltech.edu/dcc/

[54] C. D. Ott, A. Burrows, E. Livne, and R. Walder, "Gravitational Waves from Axisymmetric, Rotational Stellar Core Collapse," *Astrophys. J.*, vol. 600, pp. 834–864, 2004. [Online]. Available: http://arxiv.org/abs/astro-ph/0307472

[55] National Imagery and Mapping Agency, "Department of Defense World Geodetic System 1984: Its Definition and Relationships with Local

Geodetic Systems," NIMA, Tech. Rep. NIMA TR8350.2, January 2000, Third Edition, Amendment 1. [Online]. Available: http://earth-info.nga.mil/GandG/publications/tr8350.2/tr8350_2.html

[56] K. S. Thorne, "Multipole expansions of gravitational radiation," *Rev. Mod. Phys.*, vol. 52, no. 2, pp. 299–339, 1980.

[57] ——, S. Hawking and W. Israel, Eds. New York, NY: Cambridge University Press, 1987.

[58] W. E. Althouse, S. D. Hand, L. K. Jones, A. Lazzarini, and R. Weiss, "Precision alignment of the LIGO 4 km arms using the dual-frequency differential global positioning system," *Rev. Sci. Instrum.*, vol. 72, pp. 3086–3094, 2001. [Online]. Available: http://www.ligo.caltech.edu/docs/P/P000006-D.pdf

[59] GEO Collaboration, "The Location of GEO 600," GEO, Tech. Rep., 2006. [Online]. Available: http://www.geo600.uni-hannover.de/geo600/project/location.html

[60] B. F. Schutz and M. Tinto, "Antenna patterns of interferometric detectors of gravitational waves. I: Linearly polarized waves," *Mon. Not. R. astr Soc.*, vol. 224, pp. 131–154, 1987.

[61] R. Adhikari, G. González, M. Landry, and B. O'Reilly, "Calibration of the LIGO detectors for the first LIGO science run," *Class. Quantum. Grav.*, vol. 20, pp. S903–S914, 2003. [Online]. Available: http://www.ligo.caltech.edu/docs/T/T030097-00.pdf

[62] G. González, M. Landry, B. O'Reilly, and X. Siemens, "Calibration of the LIGO detectors for S3," LIGO, Tech. Rep. LIGO-T050059-01-D, 2005. [Online]. Available: http://admdbsrv.ligo.caltech.edu/dcc/

[63] A. Dietz, J. Garofoli, G. González, M. Landry, B. O'Reilly, and M. Sung, "Calibration of the LIGO detectors for S4," LIGO, Tech. Rep. LIGO-T050262-00-D, 2005. [Online]. Available: http://admdbsrv.ligo.caltech.edu/dcc/

[64] T. Z. Summerscales, "Gravitational Wave Astronomy with LIGO: From Data to Science," Ph.D. dissertation, The Pennsylvania State University, 2006. [Online]. Available: http://etda.libraries.psu.edu/theses/approved/WorldWideIndex/ETD-1198/index.html

[65] J. W. C. McNabb, M. Ashley, L. S. Finn, E. Rotthoff, A. Stuver, T. Summerscales, P. Sutton, M. Tibbits, K. Thorne, and K. Zaleski, "Overview of the BlockNormal event trigger generator," vol. 21, 2004, pp. S1705–S1710. [Online]. Available: http://arxiv.org/abs/gr-qc/0404123

[66] "Full source MATLAB® programming repository for BlockNormal." [Online]. Available: http://www.lsc-group.phys.uwm.edu/cgi-bin/cvs/viewcvs.cgi/matapps/src/searches/burst/BlockNormal/?cvsroot= ... lscsoft

[67] T. J. Loredo, *Statistical Challenges in Modern Astronomy*, E. D. Feigelson and G. J. Babu, Eds. New York: Springer-Verlag, 1992.

[68] L. S. Finn, "Issues in gravitational wave data analysis," in *Gravitational Waves - Proceedings of the 2nd Edoardo Amaldi conference on gravitational wave experiments*, E. Coccia, G. Veneziano, and G. Pizzella, Eds. World Scientific, 1998, pp. 180–191. [Online]. Available: http://arxiv.org/abs/gr-qc/9709077

[69] A. F. M. Smith, "A Bayesian approach to inference about a change-point in a sequence of random variables," *Biometrika*, vol. 62, pp. 407–416, 1975.

[70] J. D. Scargle, "Studies in Astronomical Time Series Analysis. V. Bayesian Blocks, A New Method to Analyze Structure in Photon Counting Data," *Astrophys. J.*, vol. 504, pp. 405–418, 1998. [Online]. Available: http://arxiv.org/abs/astro-ph/9711233

[71] L. J. Vostrikova, "Detecting 'disorder' in multidimensional random processes," *Soviet Math. Dokl.*, vol. 24, pp. 55–59, 1981.

[72] "Full source MATLAB® programming repository for SLOPE." [Online]. Available: http://www.lsc-group.phys.uwm.edu/cgi-bin/cvs/viewcvs.cgi/matapps/src/searches/burst/SLOPE/?cvsroot=lscsoft

[73] N. Arnaud, F. Cavalier, M. Davier, and P. Hello, "Detection of gravitational wave bursts by interferometric detectors," *Phys. Rev. D.*, vol. 59, no. 082002, 1999. [Online]. Available: http://arxiv.org/abs/gr-qc/9812015

[74] "Full source MATLAB® programming repository for Q Pipeline." [Online]. Available: http://www.lsc-group.phys.uwm.edu/cgi-bin/cvs/viewcvs.cgi/matapps/src/searches/burst/Q_Pipeline/matlab/ ... ?cvsroot=lscsoft

[75] S. Chatterji, L. Blackburn, G. Martin, and E. Katsavounidis, "Multiresolution techniques for the detection of gravitational-wave bursts," *Class. Quant. Grav.*, vol. 21, pp. S1809–S1818, 2004. [Online]. Available: http://arxiv.org/abs/gr-qc/0412119

[76] J. W. Tukey, *Exploratory Data Analysis (Limited Preliminary Edition)*. Reading, MA: Addison-Wesley, 1970, vol. 1.

[77] ——, *Exploratory Data Analysis (First)*. Reading, MA: Addison-Wesley, 1977.

[78] R. McGill, J. W. Tukey, and W. A. Larsen, "Variations of Box Plots," *Am. Statistician*, vol. 32, no. 1, pp. 12–16, February 1978.

[79] J. G. Zweizig, "S3 Data Quality Investigation," LIGO, Tech. Rep. LIGO-G040136-00-E, 2004. [Online]. Available: http://admdbsrv.ligo.caltech.edu/dcc/

[80] ——, "S3 Data Quality Review." [Online]. Available: http://www.ligo.caltech.edu/∼jzweizig/S3_Data_Quality/index.html

[81] L. S. Finn, "S3 Playground Selection," LIGO, Tech. Rep. LIGO-T030256-00-Z, 2003. [Online]. Available: http://admdbsrv.ligo.caltech.edu/dcc/

[82] C. Spearman, "The proof and measurement of association between two things," *Am. J. of Psychology*, vol. 15, pp. 72–101, 1904.

[83] K. Thorne, "Towards an Astrophysics-Based Burst ETG Tuning," LIGO, Tech. Rep. LIGO-G040349-00-Z, 2004. [Online]. Available: http://admdbsrv.ligo.caltech.edu/dcc/

# Vita

## Amber L. Stuver

### *Education*

- The Pennsylvania State University, University Park, PA 16802 *(Fall 1999 – August 2006)*
  - Ph.D. Physics, August 2006
    - Thesis Title: *Burst Gravitational Wave Data Analysis Methods: Design, Development and Comparison*
    - Advisor: Lee Samuel Finn
  - M.Ed. Physics; Educational Minor in Higher Education, August 2001
    - Thesis Title: *Analysis of the Undergraduate Curriculum Department of Physics The Pennsylvania State University, University Park*
    - Advisor: Gabriela González
- Frostburg State University, Frostburg, MD 21532 *(Fall 1997 – Spring 1999)*
  - B.S. Physics and General Science; Minor in Mathematics, May 1999, Magna Cum Laude
    - Thesis Title: *CCD Variable Star Photometry*
    - Advisor: Gregory Latta
- Westmoreland County Community College, Youngwood, PA 15697 *(Spring 1997 – Summer 1997, Summer 1998)*
- Hempfield Area Senior High School, Greensburg, PA 15601 *(Fall 1993 – Spring 1997)*
  - Diploma, June 1997

### *Teaching* **The Pennsylvania State University, University Park**

- Instructor, PHYS 001 (The Science of Physics [conceptual]), Summer 2004
- Lecturer, PHYS 251 (Introduction to Physics II [algebra]), Spring 2003, 2004, 2005 and 2006
- Grader, PHYS 419 (Theoretical Mechanics), Spring 2001
- Teaching Assistant, PHYS 215 (Introduction to Physics I [algebra]) -*discontinued*, Fall 2000
- Teaching Assistant, PHYS 265 (Introduction to Physics II [algebra]) -*discontinued*, Fall 1999 and Spring 2000

### *Service* **The Pennsylvania State University, University Park**

- WISE (Women in Science and Engineering) Advisory Committee Graduate Student Representative, Fall 2005 – Spring 2006
- PAW (Physics and Astronomy for Women) Group coordinator and mentor for undergraduate female students in introductory physics sequence, Spring 2003 – Spring 2006
- Graduate Student Representative to the Physics Department Climate Committee, Fall 2000 – Spring 2001 and Fall 2002 – Summer 2004
- Graduate Student representative to the Eberly College of Science Diversity and Climate Committee, Fall 2000 – Spring 2004

### *Honors and Awards*

- Elected to the American Physical Society's Forum on Graduate Student Affairs Executive Board as Member-at-Large, January 2005 to January 2007
- Graduated from Frostburg State University (FSU) with departmental honors in Physics (first in class rank) and elected as the School of Natural and Social Sciences Student Commencement Speaker, Spring 1999
- Scholarships: Tam Memorial Scholarship (FSU, Physics), Fall 1998 – Spring 1999; University Scholarship and Residential Scholarship (FSU, Admissions) , Fall 1997 – Spring 1999
- Honor Society Memberships: Sigma Pi Sigma (Physics), Spring 1999; Kappa Mu Epsilon (Mathematics), Spring 1999; Phi Eta Sigma (Freshman), Spring 1998